12-2015

HIGH TEMPERATURE SYNTHESIS AND CHARACTERIZATION OF REDUCED POLYOXOMETALATE SALT-INCLUSION SOLIDS

Dino Sulejmanovic
Clemson University, dsulejm@clemson.edu

HIGH TEMPERATURE SYNTHESIS AND CHARACTERIZATION OF REDUCED POLYOXOMETALATE SALT-INCLUSION SOLIDS

A Dissertation
Presented to
the Graduate School of
Clemson University

In Partial Fulfillment
of the Requirements for the Degree
Doctor of Philosophy
Chemistry

---

by
Dino Sulejmanovic
December 2015

Accepted by:
Dr. Shiou-Jyh Hwu, Committee Chair
Dr. Stephen Creager
Dr. Andrew Tennyson
Dr. Jian He

ABSTRACT

Herein, several new salt-inclusion solids (*SIS*s) featuring electronically reduced Keggin polyoxometalate (POM) clusters were isolated for the first time using molten-salt high temperature (> 500 ^{o}C) synthetic method. These POM-based *SIS*s are novel all-inorganic materials featuring an integrated lattice of ionic halide salt and covalent metal oxide clusters. Due to the weak interactions at the interface between these two chemically dissimilar lattices, these POM *SIS*s are soluble in aqueous and polar solvents. While POM compounds are well-studied and are routinely synthesized in solution, the synthetic method presented in this dissertation yielded several POM solids with interesting structures and infrequently observed, reduced oxidation states of the transition metal cations. This dissertation focuses on describing the high temperature (> 500 ^{o}C), salt-inclusion synthesis of several all-inorganic, reduced polyoxometalate clusters. Four chapters with different chemical systems are presented. Chapters 3, 4, and 5 feature related Keggin-based POM compounds: namely the one electron reduced, $Cs_6I_3Na(PMo_{12}O_{40})$, POM compound in Chapter 3; the two electron reduced family of compounds, $Cs_6X_2Na(PMo_{12}O_{40})$ where X_2 = Cl_2, ICl, Br_2, and I_2 in Chapter 4; and the highly reduced family of compounds, $Cs_6X_2M(PMo_{12}O_{40})$ where M^{3+} = Ti, V, Mn, Fe and X_2 = Cl_2, Br_2 and I_2 in Chapter 5. In addition, a series of hybrid inorganic-organic compounds based on reduced polyoxovanadates (POVs) are presented in Chapter 6 where a novel method using pre-synthesized soluble POVs was used. These results demonstrate the utility of salt-inclusion chemistry in regards to water-soluble POM salts that can be used for various transformative studies of biomedical and catalytic relevance. Antibacterial tests in aqueous solution of the

two electron reduced POMs (Chapter 4) show that the *Staph. A.* bacterial strains (SA1199, SA1199B, MRSA) are more susceptible to inhibition by the reduced POMs, presented herein, compared to their fully oxidized counterparts (*e.g.* $Na_3PMo^{VI}_{12}O_{40}\bullet 2H_2O$). Replacing the Na^+ cation in the two electron reduced POM with transition metals (Ti, V, Mn and Fe) resulted in the isostructural highly reduced family of compounds in Chapter 5. These novel POM *SIS*s feature infinite one-dimensional (1D) transition metal-oxide chains with interlinked Keggin clusters, $\{\text{-M-}(PMo_{12}O_{40})\text{-}\}_\infty$. These chains feature unusual square antiprismatic eight-coordinate environments of the transition metals chelated by the Keggin clusters and forming chains along the tetragonal (*P4/ncc*), *c* crystallographic direction. The unusual eight-coordination of the first-row transition metals is the first such example in an all-inorganic compound with oxo-based ligand environment. The compounds presented in this dissertation were characterized by several solid-state and solution-based characterization techniques including: single crystal and powder X-ray diffraction, biomedical properties of soluble POMs, magnetic susceptibility, spectroscopy (UV-vis and IR), electrochemical properties, and thermogravimetric analysis. The work presented in this dissertation is significant for several reasons: 1) this opens up a new method for synthesis of POM solids; 2) isolation of electronically reduced POMs is favored using the high-temperature, molten-salt method; 3) this method produced novel POM-based *SIS*s that are otherwise unattainable using conventional methods; 4) unusual structures and local geometry (*e.g.* metal-oxide connectivity along *c* and eight-coordination of transition metals) could give rise to interesting properties, including water-soluble clusters, to be studied in the near future; 5) in regards to the solids synthesized in Chapter

6, a new understanding of the interaction between anionic POV clusters and organic ligands with respect to the nature of bonding is learned; 6) finally, the synthesis of POM *SIS*s illustrated, once more, the versatility and utility of the salt-inclusion synthetic method.

DEDICATION

I dedicate the efforts presented in this dissertation to the person who has taught me the value of hard work and the importance of having a purpose in life. Though I was too little to understand everything at the time, looking back I will never forget the bedtime stories and valuable times I spent with my grandmother, Dzuma Sulejmanovic.

I also dedicate this work to my loving family, my mother Edvina, my father Memo and my two lovely sisters, Amela and Amina. Without their support and sacrifices this work would not have been possible.

ACKNOWLEDGMENTS

First and foremost, I would like to thank my advisor, Dr. Shiou–Jyh Hwu, for allowing me to join his group and study solid state chemistry under his wing. His knowledge, teachings, patience, support, and encouragement during my graduate studies at Clemson have shaped me to be a better scientist and a better person. My gratitude goes out to my committee members Dr. Stephen Creager, Dr. Andrew Tennyson and Dr. Jian He for their help and discussions regarding my research.

A special thank you goes out to our collaborators across different disciplines. I thank Dr. Jian He and his former graduate student Dr. Dale Hitchcock from the Department of Physics and Astronomy at Clemson for their help with the property measurements of the solids presented herein related to magnetism and transport measurements. Also, I thank Dr. Jeremy Tzeng and his graduate student Yash Raval from the Biological Sciences Department at Clemson University for conducting biomedical experiments related to the compounds presented herein. I thank Dr. Andrew Tennyson and his graduate student Yamin Htet for running tedius electrochemical experiments on some of my compounds.

I thank the past Hwu group members, Dr. Matthew Williams, Dr. Palmer J. West, Dr. Duminda Sanjeewa and Mr. Riyadh Alshammari for their support and for teaching me everything I needed to know about in-lab, experimental side of solid state chemistry. In addition I would like to thank the current Hwu group members Justin Talbert and Yu Shen.

A special thanks goes out to Dr. Don Vanderveer, Chemistry Department, Clemson University for teaching me X-ray crystallography theory and how to solve crystal

structures. In addition, I would like to thank Dr. Colin McMillen for his technical support in X-ray crystallography.

I would like to thank all of my professors, friends, office staff, and building workers in the Chemistry Department at Clemson University.

I also want to thank my 'lunch crew': Yamin Htet, Craig Goodman, and Amir Jafariyan for their friendship.

Outside of the chemistry department, I want to thank my friends who have been a big part of my PhD journey. First and foremost, I'd like to thank Sarah Calle for being there for me at the start of my journey when the road seemed to be the toughest. The times and her support will never be forgotten. I thank my best friends Senad Sinanovic and Ismet Handzic, and my Balkan friends Beta Dumancic, Mel Shehu, Uros Zecevic, Marija Vukicevic and Milica Stamenic for the relaxing times away from school. I am also greatful for my current and past roommates: Jordan, Michael and Jason.

I also want to acknowledge and thank all of my cousins, aunts, uncles, and extended family whom I have seen very rarely during my PhD journey.

Finally, I'd like to thank all of my soccer friends from Nettles park and those with whom I played in different leagues over the past few years.

TABLE OF CONTENTS

Table of Contents (Continued) Page

LIST OF TABLES

List of Tables (Continued) Page

List of Tables (Continued) Page

LIST OF FIGURES

List of Figures (Continued) Page

CHAPTER ONE

INTRODUCTION

Personally, before delving into solid state chemistry, my understanding of the chemistry of solids was very limited. Prior to going on this journey, I hadn't even considered that solids react. When we think of chemical reactions, at least from my prior personal limited knowledge, we tend to think of reactions only occurring in solutions and gases. We rarely ever consider a rock being able to react with another rock to make a new useful material. However, as the time went on, the more I learned about solid state chemistry, the more I wanted to get involved and contribute to the field. Along the way I realized that there were plenty of motivations for me to study solid state chemistry. Among them were: interesting properties of superconductors (*e.g.* zero electrical resistivity, magnetic levitation, etc.), advancements in energy storage materials (*e.g.* batteries, capacitors, hydrogen storage, etc.), properties of semiconductors that have revolutionized the electronic industry (*e.g.* continued miniaturization of devices), the development of solar cells that can potentially remove our dependence on fossil fuels, and even materials featuring low-dimensional nanomagnets that show promise in quantum computing applications, just to name a few.

Solid State Chemistry

Chemistry is a dynamic field of science. Traditionally, chemistry has been divided into three general areas: organic, physical and inorganic chemistry with some arguments to include analytical chemistry as the fourth branch.[1] Solid state chemistry is the study of

synthesis, structure, bonding, and properties of solids. It has often been regarded as being a part of inorganic chemistry branch. Since the invention of X-ray crystallography in the early 1900's by William Lawrence Bragg solid state chemistry has flourished and our understanding of solids with respect to their structure, composition, and nature of bonding has led to many advancements in the study of properties of solids. X-ray crystallography enabled to survey different structures of solids and to come to an important realization that structure dictates function/properties of solids. From this realization, researchers were able to chemically modify existing structures and compositions of solids in order to obtain desired properties in new materials. Driven by the use of solids in technologically important applications, solid state chemistry has seen increased interest among researchers over the last century.

Solid state chemistry can be classified into two broad general areas based on the nature of bonding in solids: molecular and non-molecular solid state chemistry. In molecular solids, individual molecules are held together by van der Waals forces and their properties largely depend on the structure of a single molecule. Take for example a molecule of naphthalene, the simplest polycyclic aromatic hydrocarbon. In naphthalene, its formula is fixed at $C_{10}H_8$ and defects in its structure are not allowed. If one atom is misplaced or replaced by another atom, the overall composition would lead to a completely new molecule. Doping in naphthalene solid is also not allowed as it would produce a completely new material with different properties. The way we study the structure of molecular solids is also different compared to non-molecular solids. Molecular structure of naphthalene can be determined spectroscopically from NMR / Mass Spectrometry and/or

IR. The bond distances between atoms, the angles, and packing of molecular solids is determined by single crystal X-ray crystallography. The properties of molecular solids largely depend on the structure and composition of the molecule itself and not so much on the overall packing of molecules.

Non-molecular solids, on the other hand, can be classified into two categories: crystalline (extended) or non-crystalline (amorphous), based on the packing of atoms and their periodicity in a three-dimensional (3D) space. Non-molecular solids are held by relatively stronger ionic and/or covalent bonds extending in 3D space. An example of a non-molecular crystalline solid is aluminum oxide, Al_2O_3. The formula of Al_2O_3 is usually fixed but vacancies and imperfections of the lattice with respect to the atomic sites and composition are unavoidable. Dislocations of atoms, interstitial impurities and small concentration of vacancies in the solid are always present. Doping, or replacement of elements by different elements is possible. Take for example, ruby crystal which is commonly used in lasing applications. Ruby is a chromium-doped Al_2O_3 solid. Small amount (usually less than 1%) of Cr^{3+} ion is doped into the Al^{3+} atomic sites. Pure Al_2O_3 solid is a white solid but when doped with Cr^{3+}, it is red in color. The small amount of doped Cr^{3+} is responsible for its color, due to *d-d* transitions, and lasing properties. Because properties are governed by structure on a range of length-scales, complete structure studies of non-molecular solids such as the Cr^{3+}-doped Al_2O_3 involve characterizations across length scales from local (*i.e.* Cr^{3+} octahedra), to unit cell (packing of atoms and their composition), nano and micro scales (porosity). From different structures across length scales in non-molecular solids, many technologically useful properties arise. When we

consider the properties across different length-scales of Al_2O_3 solid, its films and ceramics are used as electronic insulators, Cr^{3+}-doped Al_2O_3 is used in lasing applications, porous Al_2O_3 solids are used in catalysis as supports.[1]

In crystalline (extended) non-molecular solids, the way the atoms pack inside a unit cell (defined as the simplest repeating unit in a crystal) is extremely important. Take for example another inorganic solid, calcium silicate, Ca_2SiO_4. In calcium silicate, the three elements can pack inside a unit cell differently resulting in two different structures (or polymorphs) of Ca_2SiO_4. One of the two polymorphs, β-Ca_2SiO_4, reacts with water to produce a hydrated calcium silicate and results in a rock solid material that is used as the main ingredient of concrete in the construction industry. Another polymorph of calcium silicate (γ-Ca_2SiO_4), with the same composition of elements as the β polymorph, does not react with water and hence it is not useful in making of concrete materials. Even though both polymorphs contain the same composition of elements, this simple example shows the importance of the structure of a solid on the unit cell scale size, and how the structure, not just the composition, dictates properties.[1]

Throughout the history, some of the most important discoveries in solid state chemistry were influenced and motivated by the need for technologically important materials such as ferroelectric perovskites in 1940's,[2] catalysts used in petroleum industry featuring zeolites and platinum materials,[3] semiconductors for electronic industry in the 1960's,[4] high temperature superconductors in 1980's,[5] colossal magnetoresistance of materials in 1990's, energy driven discoveries ranging from solar cells,[6] batteries and hydrogen storage materials in the recent years.[7] With the broad range of solid state

materials and their diverse properties, oftentimes solid state chemistry encompasses other areas of science such as physics, biology, materials science, metallurgy, geology and mineralogy. These broad areas of study related to properties of solids can all be classified into a field called solid state science in which solid state chemistry plays an important role in synthesis and the study of structure of solids.

The main focus of this dissertation is on the synthesis and characterization of extended solids featuring electronically reduced polyoxometalate (POM) clusters. The efforts presented in this dissertation produced many new POM containing solids. In addition, the methods used in the synthesis of these new POM materials are unconventional based on the hitherto published literature of POMs. This unique approach to synthesis of POM materials provides a new synthetic method that can open doors to synthesis and isolation of otherwise unattainable POM compounds. The motivation for synthesis of electronically reduced POM materials stems largely from the interesting properties which arise due to unpaired valence *d* electrons in magnetism and electronic properties, for example. The following few sections will have some introductory paragraphs on topics relevant to the materials presented in this dissertation.

Polyoxometalates

Polyoxometalates (POMs) or transition-metal oxide clusters have been known since 1826 when Berzilius noticed a yellow solid form from a reaction between molybdate and phosphoric acid. The formed solid was the $(NH_4)_3(PMo_{12}O_{40})$ compound.[8] POM ions are chemically diverse early transition-metal oxides with discrete geometry and high

nuclearity. The sizes and shapes of POMs range from small and spherical to large and wheel-like having up to 172 metal centers. The metal polyhedra are joined together by sharing of common oxide bridges. The metal polyhedra are typically octahedra of Jahn-Teller distorted ions such as $V^{4+, 5+}$, $Mo^{5+, 6+}$ $W^{5+, 6+}$, etc., where the connection between the neighboring polyhedra is manifested through edge- and corner-sharing of oxygen bridges. Due to their size, spherical and cluster-like geometry, POMs can be thought of as inorganic analogues of carbon-containing fullerenes.

Up to date, the most studied POM is the Keggin anion with the general formula $(XM_{12}O_{40})^{n-}$ where X = Si, P, As and M = Mo^{6+}, W^{6+}. The name of the anion is derived from the person who solved its structure using X-ray crystallography in 1933.[9] Keggin solved the structure of the heteropoly acid, ($H_3PW_{12}O_{40}$), and found that the Keggin POM or cluster features twelve distorted octahedra of tungsten, one central tetrahedral PO_4^{3-} anion and four different types of oxygen sites. One of those oxygen sites connects the central main-group anion with the early-transition metal *via* a long metal-oxygen bond (typically 2.2~2.5 Å). Another oxygen site is the short metal-oxygen bond pointing away from the center of the Keggin cluster with a typical distance of about 1.6~1.7 Å. The remaining two oxygen sites are the metal-oxygen-metal bridges which are defined as μ-2 (having two metal atomic sites connected to a common oxygen) and μ-3 (having three metal sites connected to a common oxygen site).

For the reader's sake, given that the Keggin heteropolyanion is presented in this dissertation, its detailed structure is shown in Figure 1.1. The ubiquitous α-Keggin anion, $(XM_{12}O_{40})^{n-}$, with T_d symmetry is composed of four M_3O_{13} groups or 'triads' having edge-

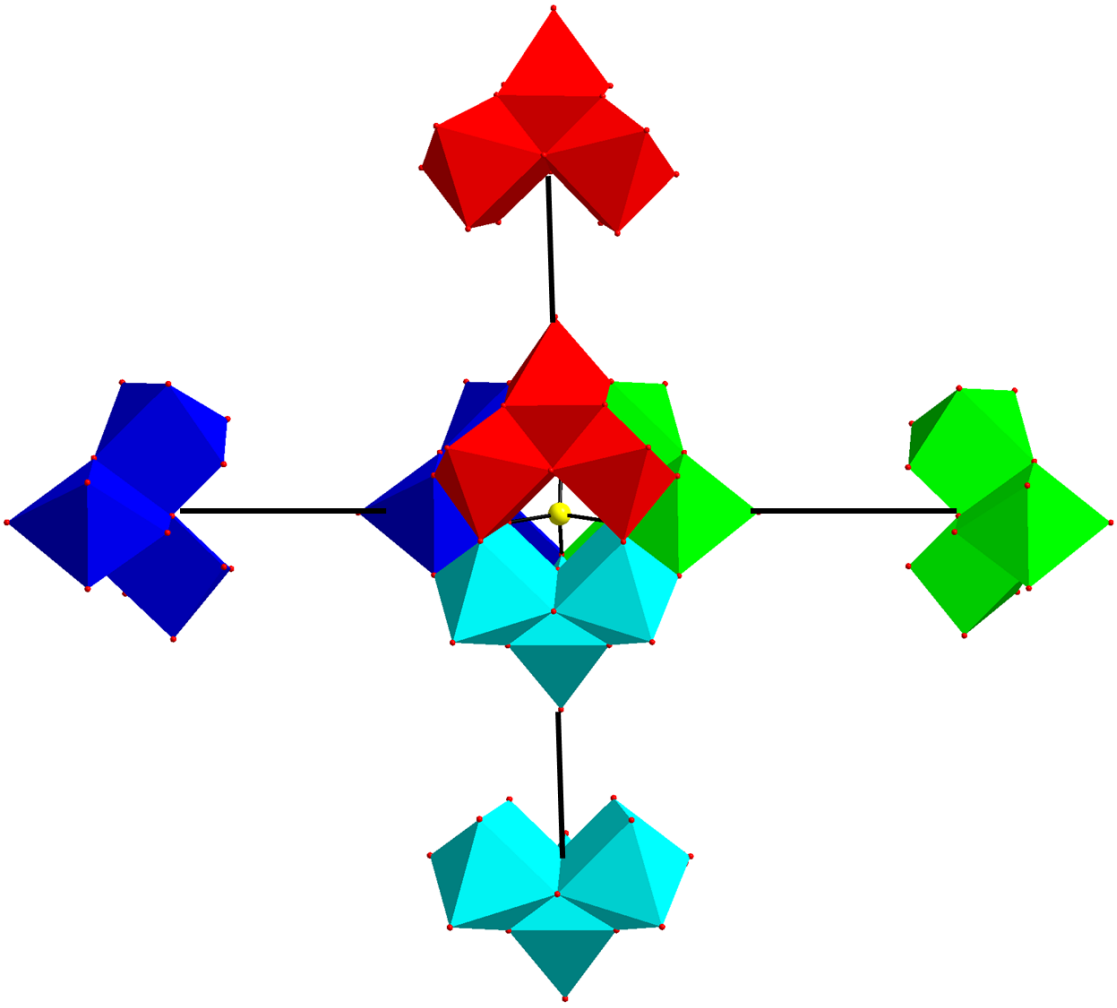

Figure 1.1: Four M_3O_{13} triads connected to each other by corner-sharing of octahedra to generate the $(XM_{12}O_{40})^{n-}$, Keggin anion. In addition each triad is connected to the central tetrahedral anion by corner-sharing. The central tetrahedral main group element is represented by a yellow sphere in the center. The different colors of triads are used for clarity purposes and they all represent the same MO_6 octahedra.

sharing MO_6 octahedra. These four M_3O_{13} groups are connected together by corner-sharing of MO_6 octahedra and by corner-sharing to the central heteroatom XO_4 tetrahedron.

Compositionally, POMs are divided into two classes: isopolyanions and heteropolyanions. Keggin cluster is an example of a heteropolyanion due to the incorporation of a 'hetero' atom, X, in the center of the cluster, $(XM_{12}O_{40})^{n-}$. Heteropolyanions can be represented by the general formula $(X_zM_mO_z)^{n-}$ where X is the hetero element, typically main group P, As, Si, Ge. Isopolyanions are POMs in which only the early transition-metal (addenda) and oxygen make up the framework of the cluster. Their general formula can be written as $(M_mO_y)^{n-}$ with M being molybdenum or tungsten and less frequently vanadium, niobium and tantalum. In both isopolyanions and heteropolyanions, the restrictions of the addendum metal (M) are confined to those with a suitable combination of the metal characteristics including ionic radius, charge, and the presence of empty *d* orbitals which can form strong π overlaps with the oxygen p (π) orbitals to result in M-O bond formation.[10]

A large number of different structures of POMs is attributed to the way their pyramidal MO_5 and octahedral MO_6 units or building blocks are packed in a 3D array to form discrete geometries. These MO_n polyhedra are connected by sharing edges or corners with very rare instances of face-sharing. The first reported POM in which the metal centers are connected by face-shared polyhedra was reported in the structure of $(CeMo_{12}O_{42})^{8-}$ by Dexter in 1968.[11] The reason for the rare occurrence of face-shared polyhedra of metal centers in POMs is due to the instability of such connectivities due to coulombic repulsions of neighboring highly charged (most oxidized) metal cation centers. The connectivities

featuring edge- and corner-sharing polyhedra have relatively smaller coulombic repulsions between the neighboring metal cation centers. On the other hand, face-sharing polyhedra result in the closest M-M distances causing instability and coulombic repulsions between the metal centers. Looking at the M-M distances between the corner-, edge-, and face-shared polyhedra in POMs, the shortest distances are found in face-shared polyhedra, as mentioned above, with the mean separations of about 3.2 Å. On the other hand, the corner-shared polyhedra typically have distances between the metal centers of about 3.8 Å. Intermediate distances between the neighboring metal centers are found in edge-sharing polyhedra of about 3.4 Å.[10]

Synthesis of Polyoxometalates

Polyoxometalates have been routinely prepared in aqueous and non-aqueous solutions. The most common method to synthesize POMs is to acidify a solution of early-transition metal oxides, for isopolyanions, and in the presence of hetero main group anions, for heteropolyanions. General process of acidification and formation of the Keggin POM is shown below. The building block MO_n polyhedra combine to form intermediate secondary building units (*e.g.* M_3O_{13} in Keggin clusters). The secondary building units then combine and form final discrete POM anions which can be isolated in the solid state by the

$$12MO^{2-}_4 + H_3PO_4 + 21H^+ \longrightarrow (PM_{12}O_{40})^{3-} + 12H_2O$$

addition of counter-cations that readily form insoluble salts in the reaction mixure.[10] The condensation of simple oxides of the early transition metals and the formation of POM

anions is illustrated in Figure 1.2. Several reaction parameters play important roles in the synthesis of POMs using solution-based methods including: pH, temperature, reactants used, concentrations of reactants, pressure, solvent, and even the order in which the reactants are added.[10] Naturally, the selection of such reaction conditions for designed synthesis of POMs is seemingly critical, but not easily defined due mostly to the complexity of these chemical systems, especially when specific POMs are targeted.

Other common methods for synthesis of POM anions exist and have been used in the past few decades. One such method is the use of hydro/solvothermal processing in which the reactants are heated to mild temperatures (< 200 ^{o}C). This method relies on the autogeneous pressure being generated when the solution is heated and typically results in metastable or intermediate phases being synthesized leading to the isolation of kinetic products[12]. Similar to the hydro/solvothermal method is the use of ionic liquids in the ionothermal synthesis. Ionothermal synthesis is a relatively new approach to synthesis of extended solids which was first described by Morris and coworkers and, in the recent years, has also been effective for synthesis of POMs.[13] What makes this approach very intriguing is that the ionic liquids are significantly less volatile than water or organic solvents given that the ionic liquids are composed of ions resulting in higher energy needed to vaporize them compared to water or organic solvents.[12] As such, ionic liquids have high chemical and thermal stabilities making them useful in intermediate temperature (< 400 ^{o}C) synthesis. In addition, ionic liquids are able to dissolve many different types of inorganic compounds including oxides which is beneficial for synthesis of POMs. However, the main drawback of ionothermal approach is the poor controllability of the composition of the

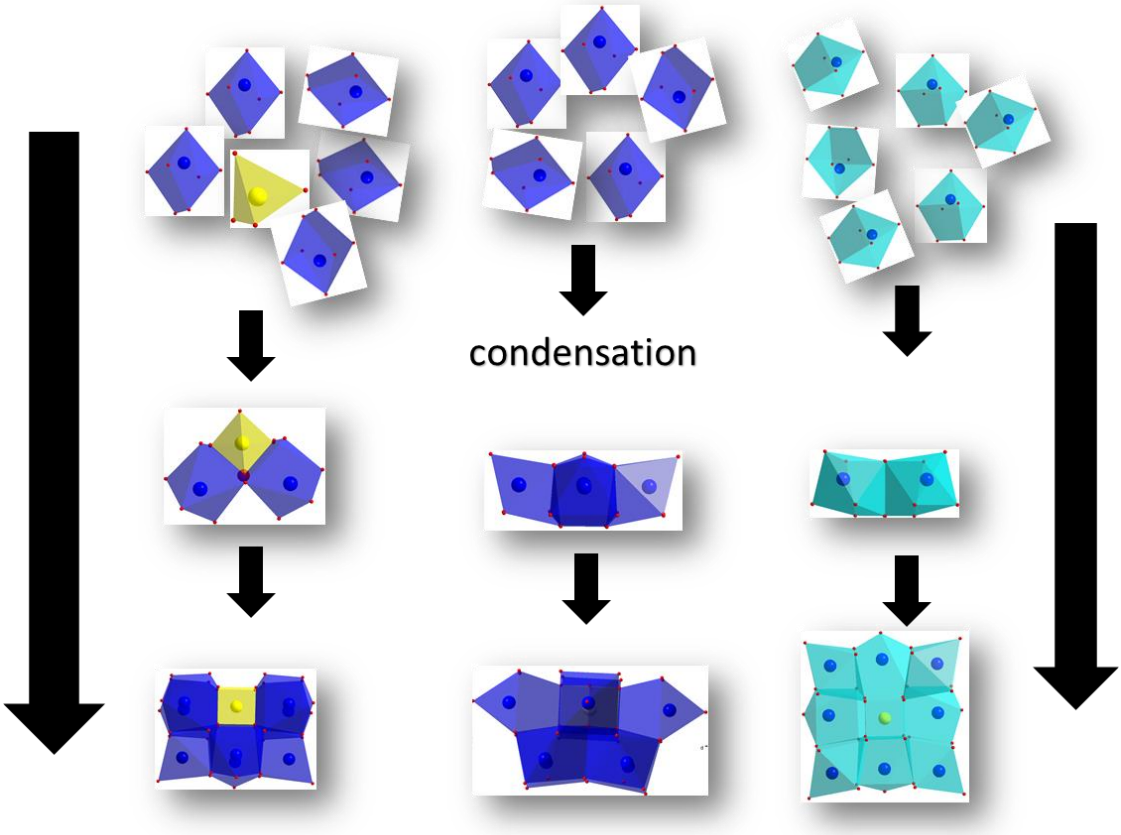

Figure 1.2: Illustration showing the condensation pathway of early transition metal oxides to form secondary building units and eventually condense into polyoxometalate anions.

crystallized phases due in part by the high concentration of solvent cations and anions. This is especially evident when high yield stoichiometric synthesis is attempted. Another disadvantage of ionothermal synthesis is the difficulty of controlling the reaction pH which shows to be crucial in conventional solution-based POM synthesis.

Generally, unless strong reducing agents (*e.g.* hydrazine) are used, all of the above synthetic methods result in synthesis of fully oxidized POMs. On the other hand, synthesis of electronically reduced POMs, which are of interest to the magnetic and electronic research communities, using conventional methods is rare in literature. To exemplify the interest in electronically reduced POMs, one example deals with POM-based cathode materials for Li-ion batteries. It is well-known that the daunting task for synthesis of Li-ion cathodes is to make materials which would allow for access of more than one Li atom per transition-metal in order to increase the energy density of the cathode material.[14] With this respect, reduced polyoxometalates (POMs) are perfect candidates given their high negative charge. In addition, if the transition-metals used in POMs can be accessed for more than one redox couple. For example, reducing Mo^{6+} to Mo^{5+} and finally to Mo^{4+} in $(PMo_{12}O_{40})^{3-}$, the overall anionic charge would result in a charge of 27- which would allow for 27 Li atoms (*i.e.* $Li_{27}(PMo_{12}O_{40})$) to be incorporated into the structure and hence increasing the energy density of the material.[15,16] Similarly, structures in which vanadium is used as part of the POM anion, redox couples of $V^{5+}/V^{4+}/V^{3+}$ can potentially be exploited. The most commonly used vanadium redox couple V^{4+}/V^{3+} is located around 4 V with respect to Li and offers higher theoretical gravimetric energy densities compared to those in the iron-containing materials.

Given their stability under redox conditions, POMs could potentially offer the much anticipated third redox couple and increased energy density in cathode materials. For this reason, the study of reduced Li-containing polyoxometalates would be of interest if such materials can be isolated in the solid state.[15, 16]

In addition to the potential electronic applications of reduced POMs, the idea of confined electrons in a zero-dimensional (0D) molecular cage has always intrigued researchers in the magnetic communities. This intrigue largely stems from materials that are analogous to POMs (at least with regard to 0D or low dimensionality) in which interesting properties are exhibited by low-dimensional magnets such as single molecule magnets (SMMs), single chain magnets (SCMs) and even single ion magnets (SIMs).[17,18,19] These low-dimensional magnets exhibit slow relaxation of magnetization and quantum tunneling effects at low temperatures.[20] Spin-based electronics (or so-called spintronics) in which spin degrees of freedom of charge carriers can be manipulated actively, is the most active area of research in nanomagnetism in which low-dimensional magnets mentioned above have potential applications for data storage and quantum computing.[21] In the case of SMMs, for example, they are single molecules acting as individual magnetic particles which is rather different than what is observed in conventional bulk magnets in which cooperative effects (magnetization or alignment with the magnetic field) of 'many' spins are needed. This requirement for 'many' spins (also called domains) to be magnetized in bulk magnets results in limitations of data storage densities. In SMMs, the spins of a single molecule show magnetization and magnetic hysteresis which means that a single molecule can be used to store data resulting in relatively higher data storage densities.[22] For a

material to exhibit SMM-like behavior, two requirements need to be met: 1) the molecule needs to contain magnetic ion (ions) with a large spin ground state and 2) significant anisotropy or 'easy' axis of magnetization should exist. In the original discovery of SMM behavior, the Mn_{12} cluster-containing molecule meets both of the requirements in which a large spin ground state of $S = 10$ exists for the mixed-valent manganese sites with the anisotropy being induced by the crystal electric field in the structure of the compound.[17]

However, the need for low temperatures for SMM materials to exhibit slow relaxation of magnetization and quantum tunneling effects limits their immediate use in spintronic devices. Attempts to increase the blocking temperature (temperature below which these molecules exhibit SMM behavior) have been attempted to be increased through chemical modification of the SMM molecules. Because thermal energy (*i.e.* above blocking temperature) breaks up the magnetized state in SMMs, making the structure of the SMM more rigid can potentially lead to higher blocking temperatures as a result of decreased phonon interactions.[23]

In theory, polyoxometalates are ideal for potential SMM-like behavior due to their molecular nature and the large number of potential magnetic ions incorporated into the structure. Compared to their organic coordination compound counterparts, POMs have some intrinsic advantages: 1) they exhibit robust, stable, all-inorganic structures; 2) they have multiple metal sites with potential for inclusion of magnetic ions; 3) they possess the ability to accept a number of electrons without a significant change in structure.[24]

To study the properties of a novel material, such as the electronically reduced POMs presented in this dissertation, the first step is to develop a method by which the

material can be synthesized in pure yield and large enough amounts. The work presented herein largely is focused on the synthesis of electronically reduced POMs using the high-temperature, molten-salt synthesis method. Based on the survey of POM literature, this method for preparation of POMs is unconventional and was only observed recently in two instances published by our group.[25, 26] Not only does this method present a new platform for synthesis of POMs with novel structures, it also seems to enable the isolation of electronically reduced POMs that are otherwise infrequently found in conventional solution-based synthetic approaches. The use of high-temperature synthesis (*i.e.* > 500 ^{o}C) for isolation of POMs is not intuitive at first, due to the tendency of high-temperature synthesis to result in condensed metal-oxide frameworks which preclude the formation of discrete anionic 'molecular' clusters. However, the use of molten-salt in the reaction mixture provides a 'break' in the covalent metal-oxygen connectivity and templates the formation of discrete anionic clusters.[25-27] Recently in our group, we have shown that through salt-inclusion reactions, metal oxides with dimensionally reduced lattices can be synthesized under relatively high temperature conditions in favor of electronic reduction. This is due to the high-temperature equilibrium between the release of oxygen from the metal oxide and the reaction atmosphere (oxygen) aiding in the reduction (or prevention of oxidation) of metal centers. Our approach has thus far produced a good number of new inorganic solids including some recent reports containing all-inorganic compositions featuring reduced POMs.[25-32]

The main emphasis of my research is in the synthesis of electronically reduced polyoxometalates *via* high-temperature, molten-salt method. These reduced

polyoxometalates (r-POMs) are otherwise less accessible using solution-based approaches. The main idea is that by using high-temperature (> 500 ^{o}C) in combination with the right stoichiometries, these conditions would potentially assist in the formation of electronically reduced POMs. Further, the presence of alkali and alkali-earth halide salts in the reaction mixture, acting both as reactants and as high-temperature solvents, can help form discrete metal-oxide frameworks. In addition, due to the chemically dissimilar nature in bonding (*i.e.* ionic *vs.* covalent) in the salt-templated POMs, these solids are expected to be soluble in polar solvents. As such they can be used as building blocks for solution-based reactions in which organic ligands can be introduced and new organic-inorganic frameworks can potentially be found.

One recent area of interest in the synthesis of hybrid organic-inorganic compounds is in the formation of metal-organic frameworks or MOFs. The proposed idea herein was to use POMs in place of single ion metal centers in MOFs to potentially create larger voids in the so-called polyoxometalate-organic frameworks (POMOFs) yielding structures that would be suitable for energy storage applications. Just like in MOFs, the organic ligand would serve as a spacer to help create three-dimensional porous frameworks in which chemical energy can be stored or substrates can be catalyzed by the POM redox centers. Essentially, the POM can be thought of as occupying the corners of a cube while the organic ligands are the edges and the created void space of a cube can be thought of as a micro vessel for gas storage and a micro beaker for catalytic reactions of substrates. Synthesis of POMOFs is difficult using bottom-up, one-pot synthetic routes due to the formation of undesirable non-POM containing phases. Moreover, it is difficult to control

the *in situ* formation of POMs and in turn designed synthesis of final POMOF products is almost impossible. In order to target desired materials and gain more control over the formation of the final products, I proposed to use pre-synthesized soluble POMs which can be used as building blocks to facilitate self-assembly of hybrid POMOF materials. This research employed the existing, water-soluble POM-containing salts, including the ones that were newly discovered *via* salt-inclusion chemistry in our laboratory.[25, 26] From the proposed research efforts, it was believed that a new understanding would be gained with respect to the bonding interactions at the interface between the anionic POMs and the organic entities. In addition, solution stability of reduced POMs would be revealed from the reactions targeting proposed POM-based inorganic-organic hybrids.

The following chapters of this dissertation will present several new electronically reduced polyoxometalate clusters synthesized using molten-salt high temperature method, with the exception of compounds synthesized using solution-based approaches presented in Chapter 6. General experimental procedures are presented in Chapter 2 while more specific experimental approaches are described in each individual chapter where appropriate. New salt-inclusion solids (*SISs*) featuring Keggin POMs are described in Chapters 3~5. These solids all share common structural features (*i.e*. Keggin anion) and given that they have very similar overall structures, they can be regarded as derivative compounds of one another. With slight chemical manipulation of their structures, reduced Keggin POMs are able to be isolated in which a one-electron (Chapter 3), two-electron (Chapter 4) and four-electron (Chapter 5) reduced Keggin anions are isolated. In addition, in Chapter 5, the Keggin anions are connected by an unusual eight-coordinated transition

metal resulting in infinite chains along the *c* crystallographic direction. This pseudo-one-dimensional metal-oxygen connectivity is of interest to the condensed matter physics communities due to the existence of potential electron conductance pathway along *c*. Chapter 6 features the hybrid inorganic-organic POM-based solids synthesized using solution based approaches. The solids presented in Chapter 6 feature non-covalent, van der Waals interactions at the interface between the anionic clusters and organic ligand. Chapter 7 summarizes the findings presented in this dissertation with some suggestions for future directions related to the work described herein.

Literature Cited

1. West, A. R. *Solid State Chemistry and Its Applications*, 2nd ed.; Wiley: New York, 2014.

2. Cross, L.E., Newnham, R.E. *Ceramics and Civilization: History of Ferroelectrics*; The American Ceramic Society Inc. **1987**, *111*. 290-291.

3. Rabo, J.A, Schoonover, M.W. *Appl. Catal*., A **2001**, *222*, 261–275.

4. Safa, O., Kasap, P.C. *Springer Handbook of Electronic and Photonic Materials* Springer. **2006**, Chapter 13.

5. (a) Bednorz, J.G., Müller, K.A., Z. *Phys. B*, **1986**, *64*, 189-193.

   (b) Wu, M. K, Ashburn, J.R., Torng, C.J., Hor, P.H., Meng, R.L., Gao, L., Huang, Z.J., Wang, Y.Q., Chu, C.W. *Phys. Rev. Lett*. **1987**, *58*, 908-910.

   (c) Beno, M.A., Soderholm, L., Capone II, D.W., Hinks, D.G., Jorgensen, J.D., Grace, J.D., Shculler, I.K., Segre, C.U., Zhang, K., *Appl. Phys. Lett*. **1987**, *51*, 57-59.

6. Dresselhaus, M. S.; Thomas, I. L. *Nature* **2001**, *414*, 332.

7. Stock, N.; Biswas, S. *Chem. Rev.* **2012**, *112*, 933–969.

8. Berzelius, J. J. *Pogg. Ann. Phy*. **1826**, *6*, 369.

9. (a) Keggin, J. F. *Nature* **1933**, *131*, 908.

   (b) Keggin, J. F. *Proc. Roy. Soc. A* **1934**, *144*, 75.

10. M. T. Pope in *Heteropoly and Isopoly Oxometalates*, Springer-Verlag, Berlin, 1983.

11. Dexter, D. D.; Silverton, J. V. J. *Am. Chem. Soc*. **1968**, *90*, 3589.

12. Ahmed, E.; and Ruck, M. *Angew. Chem. Int. Ed*. **2012**, *51*, 308-309.

13. Cooper, E. R.; Andrews, P. S.; Wheatley, P. S.; Webb, P. B.; Wormald, P.; and Morris, R. E. *Nature*. **2004**, *430*, 1012-1016.

14. Goodenough, J. B.; Kim Y. *Chem. Mater*. **2010**, *22*, 587-603.

15. Nishimoto, Y.; Yokogawa, D.; Yoshikawa, H.; Awaga, K.; Irle, S. *J. Am. Chem. Soc*. **2014**, *136*, 9042-9052.

16. Wang, H.; Hamanaka, S.; Nishimoto, Y.; Irle, S.; Yokoyama, T.; Yoshikawa, H.; Awaga, K. *J. Am. Chem. Soc*. **2012**, *134*, 4918-4924.

17. Christou, G.; Gatteschi, D.; Hendrickson, D. N.; Sessoli, R. *MRS Bulletin* **2000**, *25*, 66–71.

18. Caneschi, A.; Gatteschi, D.; Lalioti, N.; Sangregorio, C.; Sessoli, R.; Venturi, G.; Vindigni, A.; Rettori, A.; Pini, M. G.; Novak, M. A. *Angew. Chem. Int. Ed*. **2001**, *40*, 1760–1763.

19. Craig, G. A.; Murrie, M. *Chem. Soc. Rev*. **2015**, *44*, 2135.

20. Gatteschi D.; Sessoli, R. *Angew. Chem*., *Int. Ed*., **2003**, *42*, 268.

21. Bogani L.; Wernsdorfer, W. *Nat. Mater*., **2008**, *7*, 179.

22. Langley, S. K.; Le, C.; Ungur, L.; Moubaraki, B.; Abrahams, B. F.; Chibotaru, L. F.; Murray, K. S. *Inorg. Chem*. **2015**, *54*, 3631-3642.

23. West, J. Ph.D. Dissertation, Clemson University, Clemson, SC, **2012**.

24. Clemente-Juan, J. M.; Coronado, E.; Gaita-Arino, A. *Chem. Soc. Rev*., **2012**, *41*, 7464–7478.

25. Queen, W.L.; West, J.P.; Hudson, J.; Hwu, S.–J. *Inorg. Chem.* **2011**, *50*, 11064–11068.

26. Queen, W.L.; West, J.P.; Hwu, S.–J.; Tran, T.T.; Halasyamani, P.S.; VanDerveer, D. *Chem. Commun.* **2012**, *48*, 1665–1667.

27. Huang, Q.; Ulutagay, M.; Michener, P. A.; Hwu, S.-J. *J. Am. Chem. Soc*., **1999**, *121*, 10323-10326.

28. Hwu, S.–J. Chem. Mater. **1998**, *10*, 2846–2859.

29. Huang, Q.; Hwu, S-J.; Mo, X. *Angew Chem Int Ed*., **2001**, *40* (9), 1690-1693.

30. Huang, Q.; Hwu, S-J. *Inorg. Chem*. **2003**, *42* (3), 655-657.

31. Gao, J.; Li, J.; Sulejmanovic, D.; Hwu, S.-J. Inorg. Chem., **2015**, *54* (3), 1136-1144.

32. West, J. P.; Sulejmanovic, D.; Becht, B.; He, J.; Hitchcock, D.; Yan, Y.; Hwu, S.-J. J. Solid State Chem., **2013**, *206*, 51-59.

CHAPTER TWO

EXPERIMENTAL METHODS

The synthesis of inorganic, non-molecular solids can be done by a variety of methods. The oldest and simplest of such methods is the conventional, high-temperature solid-state approach to synthesis of inorganic solids. This method is still most widely used especially in synthesis of thermodynamically stable solids. In fact, most technologically important solids, including the high-T_c superconductors, were first synthesized by using conventional solid-state synthetic method. Typical approach to make inorganic solids using the conventional high-temperature method is to mix together powdered starting materials or press them into pellets and heat the reaction mixture for a prolonged time (typically a few days). Intermediate grindings of the solid reaction mixtures are oftentimes required due to poor diffusion of solids. Although the ground mixture may appear homogenous (*e.g.* on a scale down to ~1 μm), on the atomic scale the mixture is largely inhomogeneous which results in non-desired local non-stoichiometry. For this reason, solid-state synthetic method has been termed as not being very sophisticated. Other names have been used to describe the method such as 'shake and bake' or 'beat and heat'. To improve the diffusion and to increase the chance of homogenous mixing on the atomic scale between reactants, solid state counter-diffusion of ions is necessary. To increase counter-diffusion of ions, high temperatures and/or very long heating are necessary.[1] Additionally, liquid- or gas-phase transport of ions has been used to speed up the diffusion and bring together atoms in desired stoichiometric ratios for reaction to occur. A variety of new synthetic techniques have been

developed to overcome the intrinsic drawbacks of the solid state synthetic technique related to poor diffusion. Recent developments in synthesis of solids have utilized solution-based approaches such as solvo-/hydrothermal, sol-gel, microwave processing, electrochemical, molten-salt flux, and ionic liquid techniques. These new methods have afforded many interesting solids that are kinetically stable rather than being thermodynamic products. Such meta-stable or kinetic products were previously unattainable using traditional solid-state methods. Of particular interest, as they relate to this dissertation, are the molten-salt flux and solvo-/hydrothermal synthetic methods which will be discussed in further detail below.

The exciting discoveries in solid state chemistry have provided a motivation for researchers to improve the old synthetic methods and develop new methods that would lead to discovery of previously unattainable materials. When these new solids are formed, an equally important step in discovery is the characterization of said materials in order to determine the structure, first and foremost, and to reveal chemical and physical properties of these materials. The most widely used structure characterization method of crystalline solid materials is X-ray diffraction (XRD) technique. After revealing the atomic arrangement and the overall structure of the solid, predictions on potential property characterizations can be done based on close analysis of the structure alone. Further, once the chemical and physical properties are studied in depth, a close interplay between structure and properties can be correlated. Finally, based on the structure-property correlation, predictions of chemical and physical properties can be made upon chemical manipulation and alteration of the structure of the material.

Chapter 2 of this dissertation will focus on describing the general synthetic methods used to synthesize new solids presented herein. A heavy focus on synthesis will be placed in this chapter with some additional descriptions of property characterization measurements. Detailed and non-general synthetic and property measurement procedures will be pointed out in each individual chapter where appropriate. This chapter serves as a reader's guide describing the experimental approaches taken to synthesize the materials and how their chemical and physical properties were studied.

Synthetic Procedures

A large majority of the starting materials used in synthesis of new salt-inclusion polyoxometalate solids are sensitive to air and/or oxygen. For this reason, air-/moisture-free conditions had to be used. A nitrogen-purged drybox (solvent-free glovebox), manufactured by MBraun, was used to reduce the exposure of air-/moisture-sensitive starting materials to air. It should be noted that air-/moisture-sensitive materials were stored inside the drybox soon after they were purchased. However, before the starting materials were brought inside the drybox, they had to be dried as surface water or hydrated water may be present in such materials. These reactants were dried using either of the two methods. The first method, which was most commonly used was vacuum oven drying using elevated temperature (typically at 200 ^{o}C for at least 24 hours) to help drive off surface water. The second method for drying the starting materials was using the vacuum line with attached test tubes with adapters for smaller size samples. The test tube with reactants was wrapped with a heating tape in order to heat the starting materials for quicker drying.

After the starting materials were dried, they were quickly transferred (generally while still hot to prevent condensation of water upon cooling) into the antechambers of the drybox which are connected to a vacuum pump and a nitrogen tank. The nitrogen source and vacuum are controlled by opening or closing of the respective valves. The antechambers work by evacuating the antechamber after the supplies are brought in and eventually allowing nitrogen (which is inert and moisture free) in to equilibrate the pressure between the drybox and the antechamber to allow for opening of the antechamber door from the inside of the drybox. The antechambers serve as a way to bring in supplies and chemicals without exposing the drybox atmosphere to air. The MBraun drybox has two antechambers; one small and one large. Depending on the size and amount of supplies/chemicals being brought in large or small antechambers were used. In the case of large amount of supplies, large antechamber was used. To ensure that all of air/moisture was removed from the chamber, two vacuum pumping cycles were done. Each pumping cycle was consisted of 30 minutes of evacuation of the antechamber. After the first cycle, the antechamber was purged with nitrogen in order to help remove, or dilute, air that may have still remained in the antechamber. The second pumping cycle, also for 30 minutes, was conducted after which the antechamber was filled with nitrogen. At this point, the antechamber was able to be opened and the supplies were brought in. Finally, the antechamber was closed and the vacuum valve was opened. Similar procedure was followed for the small antechamber except that each pumping cycle was shorter, 15 minutes per cycle. It should be noted that when drybox was not in operation, the antechambers were kept under dynamic vacuum (*i.e*. valve always opened to the vacuum

pump) in order to prevent any possibility of air entering through the antechamber door seals.

The reactants were weighed on an OHAUS analytical microbalance with a precision of 0.1 mg. After weighing, the reactants were ground using an agate mortar and pestle. Typical grinding time was about five minutes or until the reaction mixture was visibly homogenous and reactants were intimately mixed. The mixture of reactants was then transferred into fused-silica ampoules (about six inches in length) and a glass transfer adapter was connected to the ampoules to minimize exposure of reactants to air while being transferred to the vacuum line. It should be noted that the fused-silica ampoules used as reaction containers were made in-house by cutting a larger piece of fused-silica and using a flame torch to cut and shape the tubes with a test tube end. Fused-silica ampoules were cleaned by washing with deionized water and rinsing with acetone before being dried and brought inside the antechambers. In some cases the fused-silica tubes were carbon-coated by burning acetone inside the tube and forming a homogenous coat of carbon in order to protect the starting materials from reacting with the silica glass. This was especially the case for synthesis of polyoxovanadate starting materials as presented in Chapter 6.

The fused-silica ampoules containing reactants were attached to the vacuum line and were evacuated. Then, the ampoules were sealed and cut using a flame torch. The sealed ampoules were wrapped in insulating heating blankets in order to prevent physical damage and protect the furnace integrity in case tubes fail or explode. Specific heating program was chosen based on whether the reaction was targeting crystal growth or stoichiometric yield products. In most cases where single crystal growth was targeted, a

molten-salt flux was employed which served as a high temperature solvent. The heating program in such reactions was chosen to heat the mixture at 1 ^{o}C/min and typically 150 ^{o}C above the melting point of the eutectic point of the salt flux to ensure that the entire mixture melted for improved diffusion of reactants. Generally, the reactions were allowed to isotherm at the highest set temperature for a few days before being cooled down. The set cooling temperature was chosen to be 150 ^{o}C below the eutectic melting point of the salt flux in order to give a wide enough window for crystal formation and growth to occur. To improve the growth of crystals and allow for greater size growth, slow cooling rate, generally 0.1 ^{o}C per minute was chosen. It is believed that these conditions entice the formation of single crystal growth which is vital for structural characterization using single crystal X-ray diffraction (SXRD).

Unlike the single crystal growth described above, stoichiometric reactions targeted polycrystalline products and were generally done without the use of salt flux. The heating conditions were changed by speeding up the cooling rate as single crystal growth was not targeted. Typically, the cooling rate was chosen to be the same as the heating rate, 1 or 2 ^{o}C per minute. When the required oxides are unavailable, such as 'Cs_2O', stoichiometric reactions of A_2CO_3 and MO_x targeting A-M-O (where A is Cs or Rb and M is early transition metal in question such as Mo and V) were loaded to synthesize precursor starting materials. The use of these precursors provided an oxide source of Cs which otherwise would not be readily available. The synthetic procedures for A-M-O precursors are discussed in detail in Chapters 3 and 4.

Given the targeted systems mentioned in Chapter 1, A-X-L-M-O (where A is alkali and alkaline-earth metal; X is Cl, Br, I; L is P, Ge or As; and M is an early transition metal, V, Mo, W), the reactions targeting such systems involve the use of refractory or high melting oxides. The starting materials list is included in Table 2.1 showing the names of reactants and their respective melting points. From this table, it can be observed that relatively high-melting oxide materials are used in targeted reactions. The diffusion rates of these refractory oxides in a given reaction are extremely slow unless high temperature reaction conditions are employed. In order to increase the diffusion rates of otherwise refractory oxides, alkali/alkaline-earth metal halides in eutectic mixtures were used in excess (usually at least 3 times the mass of oxide reactants). The reason for this excess amount of eutectic halide mixtures is to promote the digestion or 'solvation' of the refractory oxide reactants.[2] It is believed that the halide eutectic flux mixtures help crystal growth of desired phases by allowing for closer-to-stoichiometric intimate mixing of oxide reactants on the atomic scale. The 'solvation' of refractory oxides via halide eutectic flux coupled with slow cooling rate helps promote the crystal growth of desired phases. In addition to the advantageous 'solvation' of refractory oxides by halide eutectics, upon the completion of reactions, these halide salts can easily be washed away using deionized water due to their high solubility in water. However, given that the halide flux eutectics not only act as high temperature solvents, inevitably they are also capable of behaving as reactants and can easily be incorporated into the products resulting in a class of compounds known as salt-inclusion solids or *SIS*s. In case *SIS*s are formed, oftentimes these solids are also soluble in water and as such the reactions where halide salts are used require careful

analysis of products with keen observation while washing away the eutectic halide salts. Using eutectic halide salts, several classes of *SIS*s have been formed including three-dimensional $(3D)^3$ oxide frameworks with occasional channels where halide salts are found; two-dimensional $(2D)^4$ layered oxide solids in which the halide salts reside between the covalent oxide sheets and finally, zero-dimensional $(0D)^5$ covalent oxide frameworks in which the halide salts surround such networks resulting in cluster of transition-metal oxides which are commonly known as polyoxometalates.

Solvo-/Hydrothermal Reactions

In Chapter 6, several inorganic-organic polyoxometalate containing solids are presented. These solids were synthesized using solvo-/hydrothermal synthetic method. Generally, hydrothermal (water is used as the solvent) or solvothermal (solvent other than water is used) reactions involve the use of sealed containers in mild (up to 220 ^oC) to high temperature (700 ^oC) region. The research presented herein employed mild conditions where Teflon-lined stainless steel hydrothermal/solvothermal reaction vessel was used. To synthesize compounds presented in Chapter 6, reactants were weighed in open air (outside of drybox) and were stirred in appropriate solvents before being transferred to the Teflon cup containers. The pH of the reaction mixture was adjusted by dropwise addition of 1M HCl solution. Total volume of the solution was about 10 mL for each reaction. After the solutions with the starting materials were transferred into Teflon cups, the vessels were sealed and placed inside standard box furnaces for the heating step. The heating program was generally set to heat the reaction at a rate of 1 ^oC per minute to temperatures between

100 ^{o}C and 200 ^{o}C. To preserve the integrity of Teflon stainless steel vessels, temperatures above 200 ^{o}C were not used. The reactions were allowed to isotherm at the elevated temperature for a few days before being slow cooled at a rate of 0.1 ^{o}C per minute. Upon opening the reaction vessels, solid products were filtered and washed with deionized water. Powder X-ray diffraction (PXRD) was used to analyze overall solid products. Suitable single crystals were collected and mounted for single crystal X-ray diffraction (SXRD).

Starting Materials

Table 2.1 reports all of the chemicals used in synthesis of compounds presented in this dissertation as well as the chemicals used for exploratory synthesis. Additionally Table 2.1 reports the purities, sources and the melting points of the chemicals.[6] Table 2.2 shows the halide salts used in exploratory synthesis of polyoxometalate salt-inclusion solids. In addition, Table 2.2 also shows the eutectic mixtures of halide salts and their respective molar ratios and melting points. All materials were purchased commercially except for two cesium molybdate precursors which were prepared using Cs_2CO_3 and MoO_3 in open-air reactions. Namely, Cs_2MoO_4 and $Cs_2Mo_5O_{16}$ were prepared according the literature procedures as will be discussed in chapters to follow.[7, 8]

Table 2.1: Chemicals used for exploratory and synthesis of compounds presented in this dissertation

Compounds	Chemical Formula	Source, purity	FW, g/mol	M.P. (˚C)
Arsenic tri-oxide	As_2O_3	Aldrich, 98%	197.84	312
Barium Chloride	$BaCl_2$	Aldrich, 99.9%	208.25	963
Barium Oxide	BaO	Aldrich, 97%	153.34	1920
Cesium Carbonate	Cs_2CO_3	Alfa Aesar, 99.9%	325.82	610
Cesium Chloride	CsCl	Alfa Aesar, 99.99%	168.36	646
Cobalt (II, III) Oxide	Co_3O_4	Alfa Aesar, 99%	240.79	900(dec.)
Iron (III) Oxide	Fe_2O_3	Alfa Aesar, 99.945%	159.69	1565
Gadolinium Oxide	Gd_2O_3	Alfa Aesar, 99%	362.50	2339
Lithium Chloride	LiCl	J. T. Baker, 99.8%	133.84	449
Manganese (III) Oxide	Mn_2O_3	Aldrich, 99%	157.86	940
Molybdenum(IV) Oxide	MoO_2	Alfa Aesar, 99.98%	127.94	1100 (dec.)
Molybdenum(VI) Oxide	MoO_3	Alfa Aesar, 99.99%	143.95	795
Molybdenum(V) Chloride	$MoCI_5$	Alfa Aesar, 99.6%	273.21	194
Phosphorus Penta-oxide	P_2O_5	Aldrich, 98%	141.94	580
Potassium Carbonate	K_2CO_3	Mallinckrodt, 99%	138.21	891
Potassium Chloride	KCl	Alfa Aesar, 99.9%	74.55	776
Potassium Superoxide	KO_2	Alfa Aesar, 96.5%	71.10	380
Rubidium Carbonate	Rb_2CO_3	Alfa Aesar, 99.8%	230.95	837
Rubidium Chloride	RbCl	Alfa Aesar, 99.8%	120.92	718
Silver Oxide	Ag_2O	Cerac, 99.5%	231.74	300(dec.)
Sodium Oxide	Na_2O	Alfa Aesar, 85%	61.98	1275
Sodium Peroxide	Na_2O_2	Aldrich, 97%	77.98	460
Sodium Carbonate	Na_2CO_3	Alfa Aesar, 99.95%	105.99	851
Sodium Chloride	NaCl	Alfa Aesar, 99.9%	58.44	801
Strontium Chloride	$SrCl_2$	Alfa Aesar, 99.9%	158.33	874
Strontium Oxide	SrO	Alfa Aesar, 99.9%	103.62	2531
Titanium(IV) Oxide	TiO_2	Alfa Aesar, 99.9%	79.87	1843
Titanium(III) Oxide	Ti_2O_3	Alfa Aesar, 99.99%	143.76	2130
Vanadium (III) Oxide	V_2O_3	Alfa Aesar, 99.9%	149.12	1970
Vanadium (IV) Oxide	VO_2	Alfa Aesar, 99.8%	82.94	1967
Vanadium (V) Oxide	V_2O_5	Alfa Aesar, 99.6%	181.88	690

Table 2.2: Halide salts used in exploratory synthesis of polyoxometalate compounds. Eutectic mixtures and their respective molar ratios and melting points are shown below.

Halide Salts	Chemical Formula	Source, purity	FW, g/mol	M.P. (˚C)
Cesium Bromide	CsBr	Alfa Aesar, 99.9%	212.81	636
Cesium Chloride	CsCl	Alfa Aesar, 99.99%	168.36	646
Cesium Iodide	CsI	Alfa Aesar, 99.9%	259.81	632
Potassium Chloride	KCl	Alfa Aesar, 99.9%	74.55	790
Potassium Iodide	KI	Alfa Aesar, 99.9%	166.00	681
Rubidium Bromide	RbBr	Alfa Aesar, 99.8%	165.37	693
Rubidium Chloride	RbCl	Alfa Aesar, 99.8%	120.92	725
Rubidium Iodide	RbI	Alfa Aesar, 99.8%	212.37	656
Sodium Bromide	NaBr	Alfa Aesar, 99.9%	102.89	747
Sodium Chloride	NaCl	Alfa Aesar, 99.9%	58.44	810
Sodium Iodide	NaI	Alfa Aesar, 99.9%	149.89	661

Mixture	Molar ratio	Melting Point (˚C)
NaCl/CsCl	35:65	493
NaCl/NaI	35:65	575
NaI/CsI	45:55	435
NaCl/CsI	35:65	497
KCl/KI	50:50	598
KCl/RbCl	60:40	750
RbCl/RbI	50:50	555
CsBr/CsI	50:50	578
CsBr/RbBr	37:63	615
CsBr/NaBr	41:59	465

Characterization Techniques

The motivation for synthesis of new materials is driven primarily by the potential discovery of interesting and new properties that can be exploited in many aspects of technology. One of the most important steps in discovery of new materials is structural characterization which entails finding of how the atoms and/or molecules are arranged in a three-dimensional (3D) space. Knowing the arrangement of atoms in 3D space enables scientists to understand, through experiments and structure comparisons, the underlying chemical principles and processes which are responsible for given properties of materials (*e.g*. conductivity, energy storage, etc.). The understanding of the structure of materials, in terms of bonding and oxidation states, for instance, allows researchers to chemically modify known materials and discover new materials with improved properties.

In this dissertation study, we routinely focus on structural characterization of newly discovered crystalline solids using single crystal X-ray (SXRD) and powder X-ray (PXRD) diffraction. In addition to the structural characterizations, the compounds presented in chapters to follow were also characterized by other characterization techniques as appropriate. These characterization methods include UV-vis spectroscopy, IR spectroscopy, elemental analysis using SEM-EDX microscopy, CHN elemental analysis, and thermal analysis (*i.e*. DSC, TGA). Besides the above-mentioned characterization methods, several collaborative efforts were done in which magnetic characterizations were done by Dr. Jian He of the Clemson Physics Department while the microbiology experiments presented in Chapter 4 were done in collaboration with Dr. Jeremy Tzeng of the Clemson Biological Sciences Department.

Single Crystal X-ray Diffraction (SXRD): In solid state materials, the atoms and molecules can be arranged in a non-periodic (*i.e.* amorphous) or periodic fashion (*i.e.* crystalline or extended solids). Crystalline solids are most commonly characterized using both single crystal and powder X-ray diffraction techniques. SXRD is a ubiquitous method used for a precise determination of atomic positions, crystal structures, and the overall composition of a crystalline solid. As mentioned above, given that the atomic arrangement dictates properties of materials, it is extremely important to know the structure before further property characterizations are done.

To be able to use SXRD for structure characterization, one has to have, not only a crystalline material, but also sizable (greater than 0.2 mm in any dimension) single crystals of the material in question. The atomic arrangement in a single crystal follows a periodic trend where the smallest volume of a three-dimensional unit cell repeats throughout the crystal in 3D space until the edge of the crystal boundaries. While this is also the case with polycrystalline materials (*i.e.* their crystals have a periodic arrangement of atoms), the crystallites in a polycrystalline material are oriented in 'all' directions resulting in average orientation of the unit cells. Suppose a polycrystalline material is packed in a cube in which the crystallites are oriented randomly, as would be expected. Observing the cube from one side and getting on the unit cell scale, one would 'see' the same, or average, orientation of unit cells from each of the crystallites irrespective of from which side of the cube one is looking. Unlike in polycrystalline materials where the observer sees the average or all orientations of the unit cells, single crystals may have different orientations of their unit cells depending on how the crystal is oriented with respect to the observer and the

symmetry of the unit cell itself. Controllably rotating a single crystal allows to 'observe' different orientations of the unit cell. While rotating a single crystal in essentially all directions with respect to the X-ray source, the incident X-rays are diffracted by the planes of atoms of the crystal and result in diffraction patterns that are recorded by a detector. These diffraction patterns depend on the angles at which the incident X-rays come in and can then be systematically interpreted to give a 3D map of the unit cell contents. Similar approach is done with polycrystalline materials but due to the average orientation of crystallites and therefore an average orientation of unit cells with respect to the X-ray source, PXRD is less commonly used to solve the structure. Rather, PXRD is most commonly used for phase matching to existing phases and confirmation of the synthesis of desired compounds whose structure was previously solved using SXRD.

Single crystals of newly discovered compounds were prepared by reaction conditions discussed in Chapters 3, 4, 5, and 6. Their preparation for SXRD was done using a general approach in which the crystals were quickly placed in mineral oil to prevent moisture sensitive crystals from decomposing in air. Then, these crystals were mounted on a thin (~ 1 mm diameter) glass fibers using epoxy glue. The glue itself also served as a protective film to prevent any possible decomposition of the single crystals in air. Single crystals were then used for collection of SXRD data using a four circle AFC8 diffractometer with a Mercury CCD area detector.

In most cases, data were collected at room temperature except for a few compounds presented in Chapter 6 due to the large number of light elements in those compounds. Mo Kα radiation ($\lambda = 0.71073$ Å) produced by a graphite monochromator was used as the X-

ray source. The distance between the crystals and the detector was by default 27.6 mm unless otherwise specified. The crystal quality and the reduced unit cell parameters were initially examined by first collecting four frames. Once the unit cell dimensions were discovered, the Inorganic Crystal Structure Database (ICSD) was searched for any existing compounds with similar unit cell dimensions. In case of similar (or the same within experimental error) values of the unit cell parameters, the single crystals were generally not subjected to full data collection. When no match in ICSD database or the internal group database was found, a full data collection was performed. For most scans, data collection was done on 480 frames which took approximately three hours per single crystal. In case of poor diffracting crystals and/or poor crystalline samples, longer scans, up to 60 hours per crystal, were performed.

After the data collection was complete, *CrystalClear*[9] software (written by *Rigaku*) was used to process the data and a multi-scan absorption correction was applied using *REQABS*[10] subroutine of the *CrystalClear* program. Data reduction was also done using *CrystalClear* where the data was integrated, merged and averaged on F^2 for each frame to create a list of intensities and their respective *hkl* values. The structure of the crystals was solved using direct methods with *SHELXTL 6.1*[11] program which involved the input of the resulting reduction file from CrystalClear and the reduced unit cell. A list of possible unit cells with crystal systems and their corresponding centering conditions were given. Choosing a space group based on the input data, centering conditions and the symmetry of the unit cell allowed for the elimination of systematic absences. At this point, a potential atom assignment containing the user-defined unit cell contents was predicted by

SHELXTL 6.1. Using a Fourier difference map, atom assignment of the incorrectly assigned and unassigned atoms can be done. Repeated refinements and corrections of incorrectly assigned atoms resulted in feasible structure solutions. *PLATON*[12] was used to check the symmetry of the chosen crystal system and the space group. In case of incorrectly solved structures, *PLATON* was used for suggestion of more feasible crystal system and/or space group. Finally, upon generating a chrystallographic information file (cif), *checkCIF* analysis using *checkCIF* service provided by the International Union of Crystallography (IUC) was used to reveal any systematic errors and omissions in the structure solution process. *CheckCIF* results will be included in the appendix section of this dissertation. In case of poorly solved crystals, structures were attempted to be solved in the least symmetric space groups *P*1 (no.1) and *P*-1 (no. 2) in order to lift the constraint of symmetry of atomic sites associated with higher symmetry space groups. If all of the above described attempts resulted in unsatisfactory crystals structure solutions, different single crystals were mounted in hopes of collecting better quality data. In addition, longer scans and low temperatures (-80 ^{o}C) were also used to improve the quality of SXRD data. The drawings of structures throughout this dissertation were done using *Diamond 2.1*[13] visualization software.

Powder X-ray Diffraction (PXRD): As mentioned above, the crystallites in a polycrystalline powder are oriented randomly and show average orientation of atomic planes with respect to the incident X-ray source. When sizeable single crystals are unable to be synthesized and when purity of a stoichiometric yield synthesis is to be determined, PXRD can be a powerful technique which can provide a fingerprint pattern of the average

hkl (atomic planes) reflections and as such can be used to match the patterns of powder samples to those of the existing phases found in the ICSD database or internal (*i.e*. Dr. Hwu group) database. PXRD is almost exclusively used for phase identification. However, in rare cases, provided a significant amount of information about the compound in question is known, PXRD can also be used to solve a structure. In case very little or no information is known about a particular phase, PXRD, unlike SXRD, cannot be used to solve structures due to the intrinsic drawback of the technique where symmetry-equivalent reflections having the same spacing of atomic planes (*d*) cannot be resolved. However, the use of high-intensity X-ray sources which provide large resolutions in X-ray powder patterns could be used to solve structures in which some information of the unit cell is known. The high-intensity X-ray sources are not readily available on campuses, but they can be accessed through national laboratory facilities through user submitted proposals. These resources are invaluable to solid state chemists as they provide information about the phases in which large crystals are unable to be synthesized. Advanced Photon Source at Argonne National Laboratory in Argonne, IL, is one facility which readily accepts outside user proposals. Using the 11-BM high intensity X-ray beamline, users can get access to high intensity X-rays by on-site experiments or convenient mail-in program which generally has a quick turnaround time for data retrieval. Detailed description of the mail-in program is outlined in reference 14 below.[14]

When preparing the PXRD samples, powder samples were ground and placed on an aluminum sample holder. The powder was pressed and leveled with a glass slide to provide a leveled surface for incident X-rays. The PXRD data were collected using Rigaku

Ultima IV diffractometer equipped with Cu Kα radiation of 1.5406 Å generated using a graphite monochromator. Typically PXRD patterns were collected in the range of 5-65° *2θ* with step size of 0.02° and a duration of two hours per sample. In some cases, longer patterns were collected for profile refinement and extraction of unit cell parameters. *PDXL*[15] software provided by Rigaku was used for further data analysis and for database search. *PCW23*[16] program was utilized to obtain the calculated PXRD pattern based on the SXRD data previously collected. For some highly pure samples, profile refinements were done using GSAS[17] and/or FullProf[18] software suites. The profile refinements provide the unit cell parameters of the polycrystalline samples and can be compared to those of the single crystal structure solution.

Magnetic Measurements: Magnetic susceptibility measurements were performed on polycrystalline samples using a VSM (Vibrating Sample Magnetometer) from the Physics Department at Clemson University. DC magnetic measurements were performed in the temperature range of 10-300 K with an applied field of 100-500 Oe. Specific conditions are outlined in each chapter.

SEM and EDS Analysis: Scanning electron microscopy (SEM) was used for microscopy characterizations of crystals. The chemical compositions were characterized by energy dispersive spectroscopy (EDS). These characterizations were done using a table-top SEM-EDS TM 3000 instrument. Typically, single crystals were characterized but also powder samples were subjected to SEM-EDS for semi-quantitative chemical composition analysis.

Spectroscopic Characterization: For chemists, spectroscopy is one of the most valuable tools conveniently used to probe the structure of materials through the interaction of electromagnetic radiation with matter. Infrared (IR) spectroscopy is used to study the vibrations occurring between atoms when infrared radiation is absorbed. By measuring characteristic vibrations occurring in a material, information about the makeup of the material can be obtained. For example, O-H bond stretching vibration is characteristic to samples containing O-H bonds and can be used to indicate the presence of water or alcohols based on its distinctive IR shift in a given sample. On the other hand, UV-Vis spectroscopy can be used to study the electronic changes in solids or liquid samples occurring upon the absorption of UV-Vis radiation. In transition metal compounds, electronic transitions occur upon the absorption of UV-Vis radiation. For example, ligand to metal charge transfer (LMCT) and *d-d* transitions occur in the UV-Vis region. Transition metal derivatives in an octahedral field with different electronic configurations such as Mn^{2+} (high spin, d^5) vs. Fe^{2+} (high spin, d^6) can be distinguished based on the *d-d* transitions. In Mn^{2+} complex, *d-d* transitions are spin forbidden and are very weak or not observed at all. For this reason Mn^{2+} transition metal compounds are typically white or pale pink color.

IR Spectroscopy: The IR data were collected on a NICOLET Magna IR Spectrometer 550. Initial sample preparation procedures were done by isolating and weighing approximately 10 mg of single crystals or polycrystalline samples. Each sample was then mixed in with dry KBr salt. KBr was typically dried in a vacuum oven at 150 ^{o}C overnight and was kept in a desiccator. The amount of KBr salt used was approximately 100 mg. The single crystals, along with KBr, were ground in an agate mortar until the

mixture appeared homogenous. Then, the ground mixtures were pressed into disk-like pellets using a standard hydraulic pellet press dye. The obtained pellets were translucent and approximately 2 mm thick. The pellets were attached to the sample holder using scotch tape with only a small portion of the pellet being attached to the tape to hold the sample in place during the measurements. The samples, including the KBr blank, were measured in the frequency range of 400 cm^{-1} to 4000 cm^{-1}.

UV-Vis Spectroscopy: Optical absorption spectra (UV-Vis) were obtained from a PC-controlled SHIMADZU UV-3100 UV-Vis-NIR spectrometer equipped with an integrating sphere. The data of solid samples was collected in the reflectance mode between 200 nm (6.2 eV) and 2500 nm (0.5 eV). The reflectance data was converted to absorbance by using the Kubelka-Munk Function[19] embedded in the *UVProbe* software package. The solution UV-Vis spectroscopy was also done using a PC-controlled SHIMADZU UV-3101 UV-Vis-NIR instrument in the range of 250-800 nm using plastic square cuvettes for data collection. Baseline was collected using the solvent in which the analyte was dissolved (typically deionized water).

Thermal Analysis: Thermal analysis of newly discovered compounds was used to study their thermal stability. When compounds are heated several temperature-dependent changes can occur. For example, decomposition of compounds into more stable ones occurs when the temperature is sufficient enough. Typically, decomposition of compounds results in loss of gaseous species which can be indirectly observed by monitoring of the weight change as the decomposition is happening. In addition, phase changes and transformations can also be studied by measuring the amount of heat that is absorbed or

released by a sample. For example, crystallization of solids results in a release of energy while melting requires input of energy.

Differential Scanning Calorimetry (DSC) and Thermal-Gravimetric Analysis (TGA): measurements were done on ground powders (~10 mg) using a SDT Q600 TA Instruments calorimeter. A 110 μL platinum or alumina sample and reference pans were used for data collection. The heating profile for each measurement is included in descriptions of DSC/TGA experiments in the experimental sections of each chapter, where appropriate. A typical nitrogen gas flow of 75 ml/min was used in each measurement unless otherwise specified.

Other Characterization Methods: Other non-routine characterization methods such as Cyclic Voltammetry (Dr. Tennyson's lab, Clemson Chemistry Department), microbiology experiments including antibacterial properties presented in Chapter 4 (Dr. Tzeng, Clemson Biological Sciences Department) were done. Their detailed experimental procedures are outlined in specific chapters where appropriate.

Literature Cited

1. Rao, C. N. R.; Gopalakrishnan, *J. New Directions in Solid State Chemistry, 2nd ed.*; Cambridge University Press: New York, **1997**.

2. Bugaris D. E.; Loye, H-C. *Angew. Chem. Int. Ed.* **2012**, *51*, 3780-3811.

3. For example: Huang, Q.; Hwu, S.-J. *Inorg. Chem*. **2003**, *42*, 655-657.

4. For example: Mo, X.; Hwu, S.-J. *Inorg. Chem*. **2003**, *42*, 3978-3980.

5. For example: Queen, W.L.; West, J.P.; Hwu, S.-J.; Tran, T.T.; Halasyamani, P.S.; VanDerveer, D. *Chem. Commun*. **2012**, 48, 1665–1667.

6. *CRC Handbook of Chemistry and Physics*, 87th ed.; CRC Press: Boca Raton, FL, **2006-2007**.

7. Kool, F. X. N. M.; Koster, A. S.; and Rieck, G. D. *Acta Cryst*. **1970**, *B26*, 1974.

8. Gatehouse, B.M.; Miskin, B.K. *Acta Cryst*. **1975**, *B31*, 1293.

9. *CrystalClear*, Rigaku/MSC: The Woodlands, TX, USA, **1999**.

10. Jacobson, R. A. *REQABS Empirical Absorption Correction*, v. 1.1-03101998, Molecular Structure Corporation: Research Forest, TX, **1996-1998**.

11. Sheldrick, G. M. *SHELXTL, Version 6.1 Structure Determination Software Programs*, Bruker Analytical X-ray Systems Inc.; Madison, WI, **2001**.

12. Spek, A.L. *Acta Cryst*. **1990**, *A46*, C34.

13. Brandenburg, K.; Putz, H. *Diamond*, v. 2.1, Crystal Impact: GbR., **2001**.

14. Wang, J.; Toby, B. H.; Lee, P. L.; Ribaud, L.; Antao, S. M.; Kurtz, C.; Ramanathan, M.; Dreele, R. B. V.; Beno, M. Review of Scientific Instruments, 2008, 79, 085105.

15. *The Rigaku Journal* **2010**, *26*, 23-27.

16. Kraus, W.; Nolze, G. *PCW*, v. 2.4, Federal Institute for Materials Research and Testing: Berlin, Germany, **2000**.
17. Toby, B.; H. “EXPGUI', a graphical user interface for GSAS”, *J. Appl. Cryst.* **2001**, *34*, 210-213.

18. Rodrıguez-Carvajal, *J. Physica B*, **1993**, *192*, 55-69.

19. Kubelka, P. *J. Opt. Soc. Am.* **1948**, *38*, 448-457.

CHAPTER THREE

SOLID STATE SYNTHESIS AND CHARACTERIZATION OF A REDUCED KEGGIN-BASED SALT-INCLUSION POLYOXOMETALATE COMPOUND, $Cs_6I_3Na(PMo_{12}O_{40})$

Introduction

Salt inclusion chemistry (*SIC*) has proven to be a useful inorganic synthetic method for formation of new compounds related to nonlinear optics,[1] transition metal (TM)-oxide magnetic structures,[2] porous zeolite-type materials[3] and recently, water-soluble polyoxometalate (POM) clusters.[4] POMs are discrete nano-sized aggregates of transition metal oxides which are more commonly observed for the early transition metals such as V, Mo, W, Nb and Ta. They can vary in composition, shape and size with the number of early transition metals ranging from six to all the way up to 172 metals. Polyoxometalates in which the framework is solely composed of early transition metals and oxygen are called isopolyanions and are designated as $(M_xO_y)^{n-}$. Besides the isopolyanions, POM clusters can include the so-called heteroatoms such as main group elements (*i.e.* P, Si, Ge, As, etc.) such as in the case of the Keggin-type polyoxometalate $(XM_{12}O_{40})^{n-}$ that encapsulate is the heteroatom X. POMs that contain a heteroatom are called heteropolyanions.

The local coordination geometry of the transition metals in POM clusters is typically square pyramidal with five oxygen atoms and/or distorted octahedral geometry with six oxygen atoms surrounding the transition metal. In case of the heteroatoms, the local geometry can differ depending on if the heteroatom is encapsulated by the framework

(*e.g.* $(XM_{12}O_{40})^{n-}$) or is a part of the framework as is the case with $(As_8V_{14}O_{42}Cl)^{n-}$ polyoxometalate.[4a]

Up to date, synthesis of polyoxometalates (POMs) has almost exclusively relied upon the use of the solution-based synthetic methods such as the solvent evaporation method, crystallization technique, and precipitation methods where ambient pressure and temperature conditions have been used. In a typical solution-based reaction, transition metal oxide starting materials are dissolved in the presence of an inorganic acid under aqueous conditions. The acidification of the solution results in the formation of metal oxide fragments which undergo nucleation processes to form discrete anionic clusters. Solution-based approaches have thus far resulted in synthesis of a large number of POM compounds with applications found in catalysis,[5] photocatalysis,[6] magnetism,[7] biomedicine.[8]

Despite its success, the conventional solution-based synthetic method has some intrinsic drawbacks such as low solubility of metal-oxide starting materials, inclusion or co-crystallization of water and/or solvent molecules, difficulty with reproducibility, low reaction pressure and temperature, and poor controllability of reaction parameters such as the oxidation state of the early transition metals.[9] Some of these drawbacks are particularly evident in the attempts to make high yield synthesis of the desired compounds. Consequently, researchers have focused on looking for new synthetic methods which could alter the way polyoxometalates are formed to lead to synthesis of new compounds with novel structures and emergent properties.

In literature pertaining to the synthesis of polyoxometalate-containing extended solids, there are examples of other non-conventional or less common synthetic methods.

One such method is the use of hydro/solvothermal processing in which the reactants are heated to mild temperatures (< 200 ^{o}C) to presumably assist in the dissolution of otherwise less soluble metal oxides. This method relies on the autogeneous pressure being generated when the solution is heated and typically results in metastable or intermediate phases being synthesized, as is the case with conventional solution methods, leading to the isolation of kinetic products.[10]

Similar to the hydro/solvothermal method is the use of ionic liquids in the ionothermal synthesis. Using the simplest definition, ionic liquids are salts that are in the liquid state at or below the reaction temperature conditions. One example of an ionic liquid commonly employed in ionothermal synthesis of POMs is 1-butyl-3-methylimidazolium hexafluorophosphate which has a melting range between 6 ^{o}C and 10 ^{o}C. Ionothermal synthesis is a relatively new approach to synthesis of extended solids which was first described by Morris and coworkers and, in the recent years, has also been effective for synthesis of POMs.[11] What makes this approach intriguing is that the ionic liquids are significantly less volatile than water or organic solvents given that the ionic liquids are composed of ions resulting in higher energy needed to vaporize them compared to water or organic solvents.[10] As such, ionic liquids have high chemical and thermal stabilities making them useful in intermediate temperature (< 400 ^{o}C) synthesis. In addition, ionic liquids are able to dissolve many different types of inorganic compounds including oxides which is beneficial for synthesis of POMs. However, the main drawback of ionothermal approach is the poor controllability of the composition of crystallized phases due in part by

the high concentration of solvent cations and anions. This is especially evident when high yield stoichiometric synthesis is attempted.

Solid state synthesis method, on the other hand, has largely been disregarded in the synthesis of POMs due to some intrinsic disadvantages of high temperature (> 500 ^{o}C) synthesis such as the special requirement of reaction containers and the necessity for inert/vacuum environment in case of air sensitive reactants. In addition, the major drawback for POM synthesis using this method is the formation of condensed phases which are known to form at high temperatures (> 600 ^{o}C). However, employing salt-inclusion chemistry (*SIC*) where the salt can act as a high temperature solvent and/or reactant can preclude the formation of condensed phases and can aid in the formation of high nuclearity clusters as evidenced by the three recent POM reports.[4] Prior to the most recent three reports describing high temperature synthesis of polyoxovanadates (POVs) synthesized in our group, hitherto, there have not been other instances of synthesis of POMs using the high temperature solid state method. The report by Margret and coworkers,[12] for instance, features the $[Nb_6O_{12}]O_6$-type cluster with the overall composition of $Rb_4Al_2Nb_{35}O_{70}$ and illustrates that high temperature can lead to reduced oxidation states of transition metal cations. In addition, high temperature generally leads to extended networks of structures which is the case with $Rb_4Al_2Nb_{35}O_{70}$. This compound was synthesized by mixing Na_3NbO_4 and NbO in 1:1 molar ratio, excess RbCl flux and heating the reactants to 1050 ^{o}C. From the formula composition it can be noticed that the Nb atoms are not in their highest oxidation state with average formal charge of $Nb^{3.7+}$. Also, upon the analysis of the structure, it can be seen that $Rb_4Al_2Nb_{35}O_{70}$ features several buildings blocks including the

Nb_6 cluster described above. Even though the cluster formation is evident, this compound does not feature distinct high-nuclearity M_xO_y clusters as is commonly observed in polyoxometalates. Instead, extended networks of metal-oxygen are seen. This example of isolation of reduced cluster species using high temperature method exemplifies both the reducing, as well as the condensing nature of high temperature synthesis. Other similar examples which describe Nb_6 clusters have been isolated using similar approaches.[13]

From our recent results in high temperature POM synthesis,[4] we have reasons to believe that high-nuclearity, reduced polyoxometalate (r-POM) compounds can preferentially be isolated using the solid state salt inclusion synthesis method where temperatures between 500 ^oC and 700 ^oC are typically used. Chapter 3 will focus on salt inclusion synthesis and characterization of the one-electron reduced $Cs_6I_3Na(PMo_{12}O_{40})$ polyoxometalate compound featuring a Keggin-based high nuclearity cluster isolated for the first time using high temperature solid state method. This chapter will also discuss in detail the synthetic parameters under which the title compound formed. Further, discussion of structure with respect to the integrated ionic salt lattice and its role in the formation of the solid will be evaluated. Lastly, property characterizations will be discussed and correlated to the structure and the nature of bonding.

Synthetic Procedure and Discussion

Single Crystal Growth of $Cs_6I_3Na(PMo_{12}O_{40})$: Original reaction that led to the serendipitous formation of single crystals of $Cs_6I_3Na(PMo_{12}O_{40})$ was an exploratory reaction in which $SrMoO_4$:MoO_3:MoO_2:P_4O_{10} were loaded in a molar ratio of 3:10:10:1 targeting a composition to potentially isolate an unknown "$Sr_3(P_4Mo_{20}O_{72})$" reduced POM solid. (0.25 g of oxide reactants) in a eutectic CsCl/NaI (55:45 mol %, mp ~ 460 ^oC) that was used in excess; three times the mass of the oxide reactants (0.75g). The starting reactants were weighed and ground inside a nitrogen-purged glovebox (drybox) until the powder appeared homogeneous under close observation. The reactants were loaded into a carbon-coated fused silica ampoule and sealed under vacuum. The reaction was heated to 650 ^oC at a rate of 1 ^oC/min and was allowed to stay at high temperature for three days (72 hours) before being slow cooled at 0.1 ^oC/min to 400 ^oC (~ 150 ^oC below the eutectic melting point). Finally, the reaction was furnace cooled (> 5 ^oC/min) to room temperature. Upon opening the reaction ampoule, small brown columns were able to be identified. Half of the product was rinsed with deionized water in order to wash away excess salt flux while the other half was kept unwashed in case the synthesized crystals were soluble in water. The identified products of this reaction were the title phase, $Cs_6I_3Na(PMo_{12}O_{40})$ (visual yield of ~ 10 %) and $Cs_3(PMo_{12}O_{40})$ (yield of about 20 %). The latter phase features fully oxidized Mo^{6+} transition metal. This fully oxidized compound was previously synthesized using hydrothermal synthetic route.[14] Once the composition of the title phase was determined, reactions targeting a closer to stoichiometric composition (with salt flux added for crystal growth) were attempted. Initially, due to the lack of a Cs-O source, reactions

that targeted a fully stoichiometric composition were unable to be loaded. However, synthesis of two Cs-Mo-O precursors, namely Cs_2MoO_4 and $Cs_2Mo_5O_{16}$, allowed for stoichiometric reactions as discussed below in high yield synthesis.

The analysis of products involved breaking of the fused silica ampoules and observing the products under an optical microscope. In case of soluble or moisture sensitive phases being synthesized, the observation and characterization of products was further complicated by the instability of such products at ambient conditions. With assumptions that such phases are always synthesized in salt inclusion synthesis, generally only half of the product was washed with water while the other half was left unwashed. This unwashed half of the product was quickly examined under the microscope to see if any moisture sensitive phases had formed. Crystals of such phases were quickly engulfed in grease or epoxy to prevent any further decomposition under ambient conditions. In case of some moisture sensitive products, the reactions were opened inside the nitrogen-purged glovebox and were examined under a microscope attached to the glovebox window.

High Yield Synthesis of $Cs_6I_3Na(PMo_{12}O_{40})$: The high yield synthesis of $Cs_6I_3Na(PMo_{12}O_{40})$ required the use of a Cs-O source as mentioned above. Two precursors, namely Cs_2MoO_4 and $Cs_2Mo_5O_{16}$ were synthesized using the solid state reaction approach from Cs_2CO_3 and MoO_3 starting materials. For synthesis of Cs_2MoO_4, the molar ratio of Cs_2CO_3 to MoO_3 was 1:1. Reaction was done in open air according to the reported synthetic procedure at 950 ^oC.[15] Synthesis of $Cs_2Mo_5O_{16}$ was also done using the solid state approach[16] with Cs_2CO_3 to MoO_3 molar ratio of 1:5. The reaction was loaded and ground in a nitrogen-purged glovebox before being transferred into an open-to-air crucible. The

heating program consisted of a heating at a rate of 2 ^{o}C/min to 750 ^{o}C and isotherming for 48 hours after which the reaction was cooled to 250 ^{o}C at a rate of 2 ^{o}C/min. In order to prevent any moisture absorption by the final product, the reaction was taken out of the furnace at 250 ^{o}C and quickly transferred to the evacuation chamber of the glovebox. The final product was stored inside the glovebox where it was used as a Cs-Mo-O precursor for the below-described reaction. Figure 3.1 shows the powder X-ray diffraction for the as-prepared $Cs_2Mo_5O_{16}$. After the successful synthesis of the Cs-Mo-O precursors, stoichiometric reaction targeting the title compound was then able to be loaded. As an example, $Cs_2Mo_5O_{16}$, CsI, NaI, MoO_3, MoO_2, and P_4O_{10} were loaded in molar ratios of 8:8:4:6:2:1, respectively. The reaction was ground in a nitrogen-purged drybox and the resulting homogeneous mixture was transferred to a fused silica ampoule. The ampoule was then sealed under vacuum and was heated to 500 ^{o}C at a rate of 2 ^{o}C/min. It was isothermed at 500 ^{o}C for 48 hours and cooled back down to room temperature at a rate of 2 ^{o}C/min. Notice that slow cooling was not necessary here as the goal was not to grow single crystals. Figure 3.2 shows the calculated powder pattern (pink color) obtained from the single crystal X-ray diffraction solution along with the observed powder pattern (blue) from a stoichiometric high yield reaction as described above. It is important to note that the observed powder pattern from Figure 3.2 is a result of a product that was reground and reheated. As is the case with most solid state reactions, regrinding and reheating allowed for secondary intermixing of particles which can promote the reaction of any unreacted starting materials.

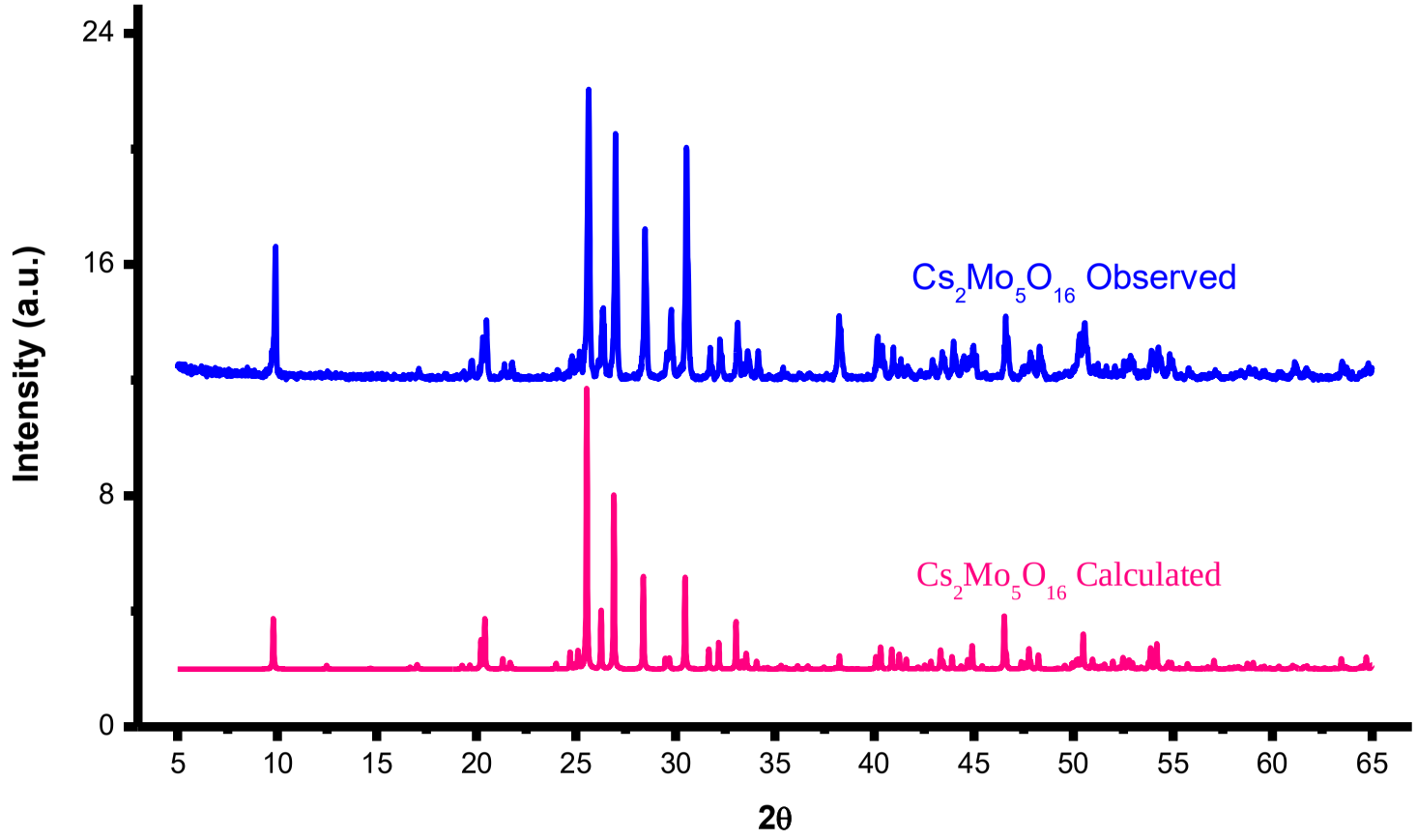

Figure 3.1: PXRD pattern of the reaction where $Cs_2Mo_5O_{16}$ precursor was targeted.

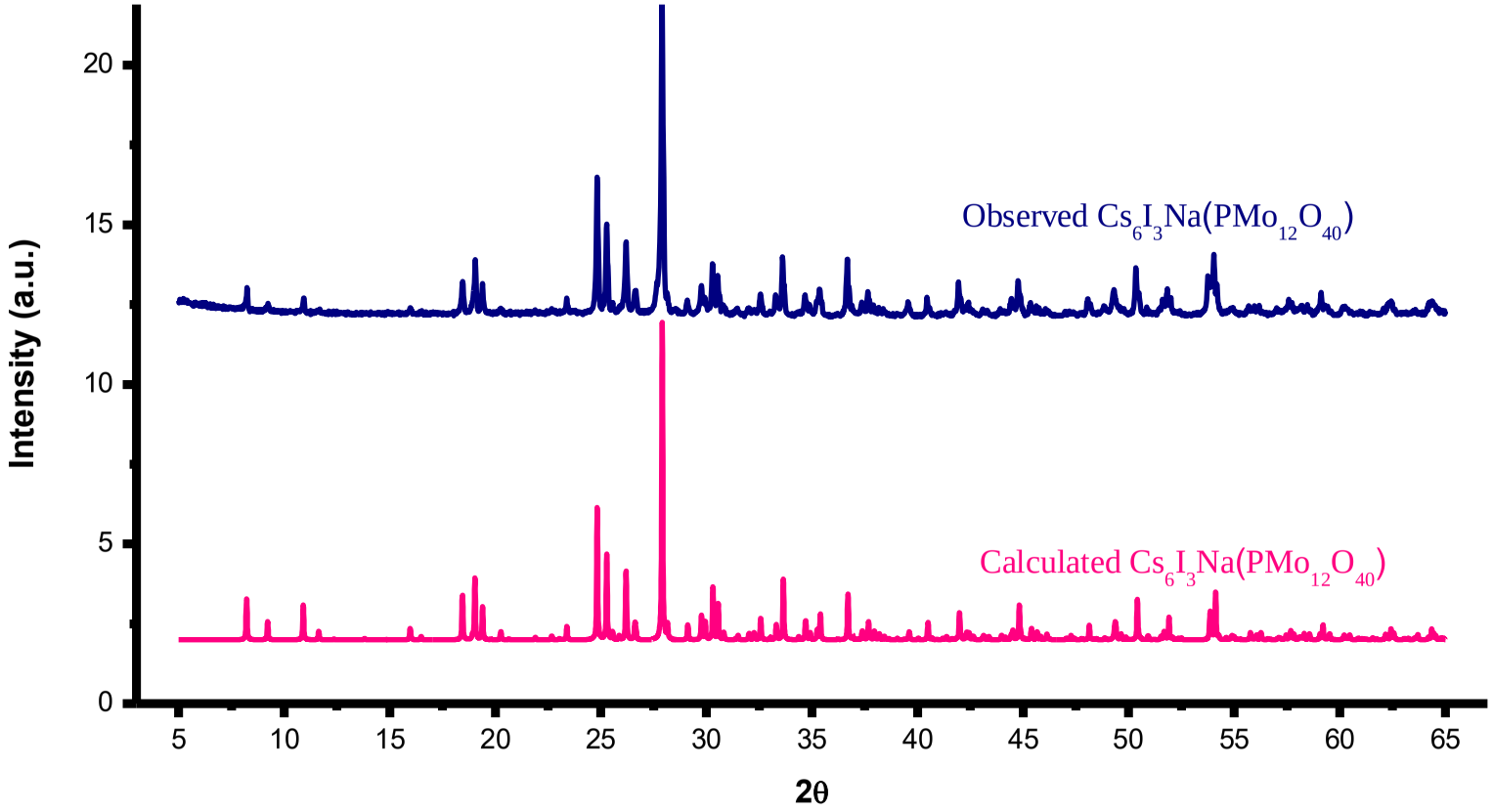

Figure 3.2: PXRD pattern of a high yield synthesis attempt of $Cs_6I_3Na(PMo_{12}O_{40})$ showing a successful high yield synthesis of the title phase.).

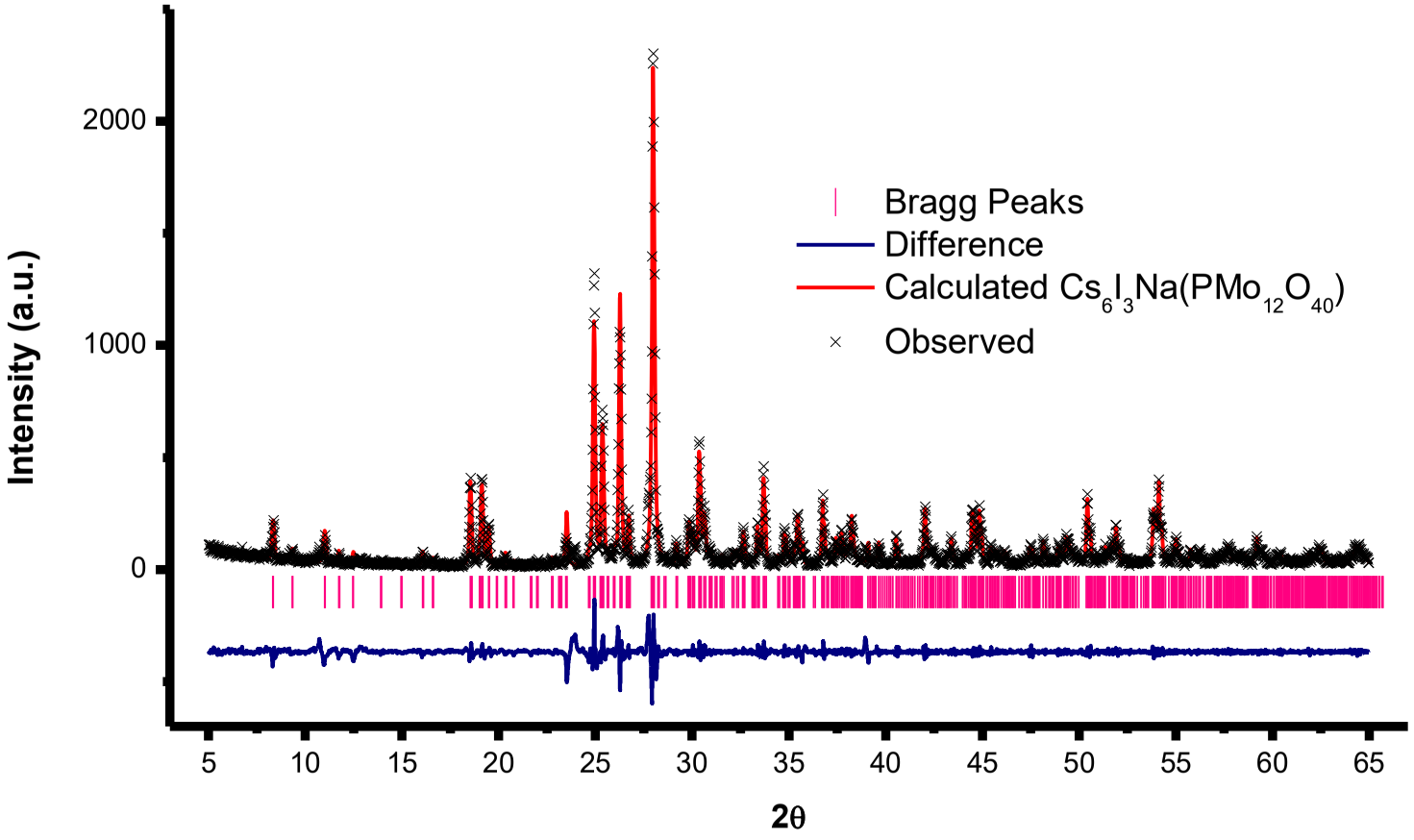

Figure 3.3: PXRD refinement pattern of a stoichiometric yield synthesis attempt reaction for $Cs_6I_3Na(PMo_{12}O_{40})$. The figure shows the calculated, observed, difference between calculated and observed patterns and the Bragg reflections.

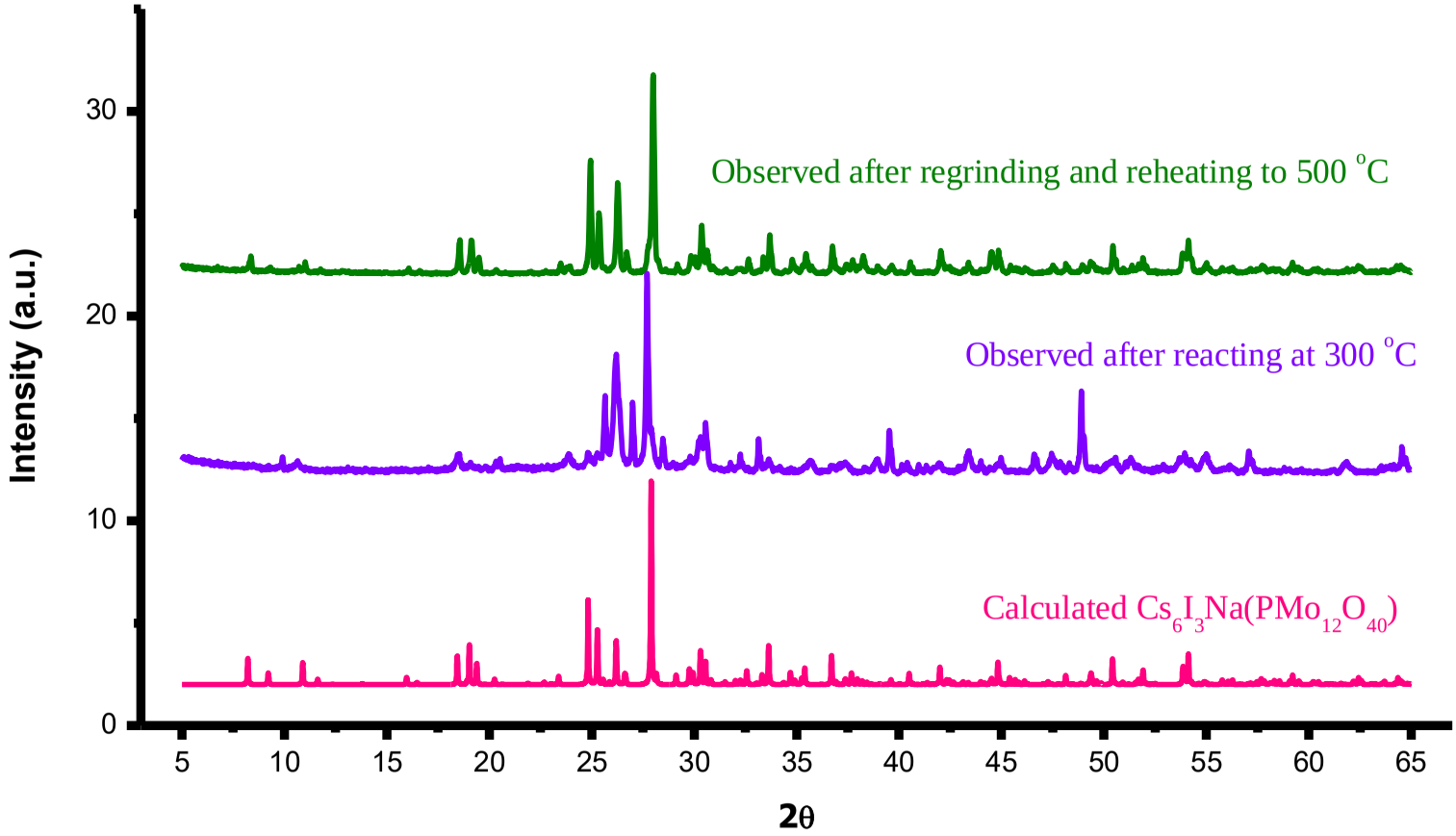

Figure 3.4: PXRD pattern of a different high yield synthesis reaction of $Cs_6I_3Na(PMo_{12}O_{40})$ where the reaction was initially heated to 300 ºC (violet color) and subsequent regrinding and reheating of the same powder to 500 ºC (green).

It should also be noted that the reaction temperatures for single crystal growth and for high yield stoichiometric synthesis were different. In the case of single crystal growth, the general practice was to use a eutectic flux that can act as a high temperature solvent. While it is difficult to predict whether all of the reactants will melt (or be dissolved) at a given temperature, increasing the temperature above the melting point of the employed flux surely increases the chances of reactants melting. For the single crystal growth reactions discussed in this chapter, the temperature therefore was set to approximately 150 ^{o}C above the eutectic halide salt flux melting temperature. In the case of high yield synthesis, lower temperatures were used given that large single crystal formation was not targeted. In such reactions, solid state or "shake and bake" method with intermittent grindings was employed.

Characterization

Elemental Analysis, Energy Dispersive Spectroscopy (EDS): EDS was used to qualitatively confirm the presence of elements comprised in the compositions of $Cs_6I_3Na(PMo_{12}O_{40})$. Elemental analysis was performed on the single crystals used for the SXRD structure determination of $Cs_6I_3Na(PMo_{12}O_{40})$.

Powder X–ray Diffraction (PXRD): PXRD was used to confirm the phase formations of the precursor, $Cs_2Mo_5O_{16}$ and the title phase, $Cs_6I_3Na(PMo_{12}O_{40})$. Powder diffraction patterns for a select few synthetic approaches can be seen in Figures 3.1~3.4. The powder X–ray diffraction data were collected at room temperature in the 2θ range of 5–65° with a step size of 0.02° and a scan rate of 0.25°/min.

Single Crystal X–ray Diffraction (SXRD): Dark brown, needle/column crystals of $Cs_6I_3Na(PMo_{12}O_{40})$ were selected under an optical microscope equipped with a polarizing light attachment. SXRD data were collected on these single crystals at room temperature using Mo Kα radiation (λ = 0.71073 Å) produced by a graphite monochromator. The crystallographic data can be seen in Table 3.1. The atomic coordinates, anisotropic thermal parameters, selected bond distances and angles and bond valence sums calculations can be seen in Tables 3.2~3.6. A *CheckCif* result is included in the appendix.

Profile refinement of PXRD patterns: Polycrystalline powder synthesized using high-yield stoichiometric reaction was used for profile refinement to provide the unit cell parameters for comparison to the SXRD unit cell constants. GSAS software package was used for profile refinement.[17] Figure 3.3 shows the refinement plot of the PXRD.

Table 3.1: Crystallographic data for $Cs_6I_3Na(PMo_{12}O_{40})$.

empirical formula	$Cs_6I_3NaPMo_{12}O_{40}$
formula wt, g/mol	3023.36
crystal system	tetragonal
space group	*P* 4/ncc (no. 130)
a , Å	15.203(2)
c , Å	19.181(4)
volume, $Å^3$	4433.33(13)
Z	4
D_{calc}, g/cm^3	4.529
abs coeff	10.357
crystal size, mm	0.14 x 0.08 x 0.07
theta range, deg	2.38 - 25.04
relns collected	26172
indep reflns	1966
R (int)	0.141
obsd ($I > 2s(I)$)	1743
goodness-of-fit on F^2	1.091
$R_1[I > 2s(I)]$[a]	0.057
wR_2 (all data)[b]	0.063

[a] $R = \Sigma||F_o| ? |F_c||/\Sigma|F_o|$. [b] $R_w = [\Sigma w(F_o^2 ? F_c^2)^2/\Sigma w(F_o^2)^2]^{1/2}$, w = 1/[σ2(Fo2) + (0.056P)2 + 207.8028P] where P = (Fo2 + 2Fc2)/3

Table 3.2: Atomic parameters for $Cs_6I_3Na(PMo_{12}O_{40})$.

Atom	Wyckoff notation	sof	x	y	z
Mo(1)	16g	1.0	0.18087 (6)	0.40179 (6)	0.44796 (5)
Mo(2)	16g	1.0	0.09830 (6)	0.31920 (7)	0.21263 (5)
Mo(3)	16g	1.0	0.16995 (7)	0.46815 (7)	0.08005 (5)
P	4c	1.0	1/4	1/4	0.5804 (3)
Na	4c	1.0	1/4	1/4	0.3308 (5)
Cs(1)	8f	1.0	0.08575 (6)	0.58575 (6)	1/4
Cs(2)	16g	1.0	0.40551 (5)	0.58141 (6)	0.40874 (4)
I(1)	8e	1.0	1/4	3/4	0.33424 (9)
I(2)	4b	1.0	1/4	3/4	1/2
O(1)	16g	1.0	0.3498 (7)	0.4721 (5)	0.2706 (4)
O(2)	16g	1.0	0.1311 (6)	0.5699 (6)	0.0791 (5)
O(3)	16g	1.0	0.1462 (7)	0.4696 (6)	0.3855 (5)
O(4)	16g	1.0	0.0950 (6)	0.4160 (8)	0.0106 (6)
O(5)	16g	1.0	0.0964 (7)	0.4153 (9)	0.1492 (6)
O(6)	16g	1.0	0.2595 (7)	0.4769 (9)	0.1493 (6)
O(7)	16g	1.0	0.1359 (9)	0.2922 (7)	0.4138 (6)
O(8)	16g	1.0	0.1357 (8)	0.2091 (6)	0.2471 (6)
O(9)	16g	1.0	0.2582 (7)	0.4781 (8)	0.0102 (6)
O(10)	16g	0.5	0.1706 (9)	0.2801 (10)	0.6271 (7)
O(11)	16g	0.5	0.1707 (9)	0.2794 (10)	0.5340 (8)

Table 3.3: Anisotropic thermal parameters (Å^2) for $Cs_6I_3Na(PMo_{12}O_{40})$.

Atom	U_{11}	U_{22}	U_{33}	U_{12}	U_{13}	U_{23}
Mo(1)	0.0209(5)	0.0137(5)	0.0107(5)	0.0049(4)	-0.0004(4)	0.0008(3)
Mo(2)	0.0157(5)	0.0223(5)	0.0102(5)	0.0055(4)	0.0019(4)	-0.0005(4)
Mo(3)	0.0156(5)	0.0109(5)	0.0232(6)	0.0017(4)	0.0003(4)	-0.0003(4)
P	0.0118(16)	0.0118(16)	0.012(3)	0.000	0.000	0.000
Na	0.021(3)	0.021(3)	0.022(5)	0.000	0.000	0.000
Cs(1)	0.0449(5)	0.0449(5)	0.0174(6)	-0.0080(6)	0.0075(4)	-0.0075(4)
Cs(2)	0.0245(5)	0.0331(5)	0.0229(4)	-0.0022(3)	0.0029(3)	-0.0009(3)
I(1)	0.0236(7)	0.0281(7)	0.0761(11)	-0.0003(5)	0.000	0.000
I(2)	0.0239(5)	0.0239(5)	0.0367(9)	0.000	0.000	0.000
O(1)	0.067(7)	0.008(4)	0.017(4)	-0.009(4)	0.013(4)	-0.002(3)
O(2)	0.025(5)	0.015(4)	0.049(6)	0.005(4)	0.008(4)	0.000(4)
O(3)	0.063(7)	0.028(5)	0.025(5)	0.037(5)	-0.012(5)	-0.001(4)
O(4)	0.028(5)	0.076(8)	0.048(6)	-0.025(5)	0.023(5)	-0.053(6)
O(5)	0.031(6)	0.089(9)	0.052(7)	-0.031(6)	-0.028(5)	0.054(7)
O(6)	0.029(5)	0.101(10)	0.054(7)	-0.035(6)	-0.017(5)	0.067(7)
O(7)	0.086(9)	0.022(5)	0.056(7)	-0.015(6)	0.064(7)	-0.017(5)
O(8)	0.080(8)	0.025(5)	0.052(7)	0.025(5)	-0.056(6)	-0.017(5)
O(9)	0.025(5)	0.089(9)	0.060(7)	-0.022(6)	0.019(5)	-0.061(7)
O(10)	0.015(7)	0.019(7)	0.009(7)	-0.003(6)	-0.005(6)	-0.003(6)
O(11)	0.015(7)	0.018(7)	0.009(7)	0.007(6)	0.005(6)	0.002(6)

Table 3.4: Selected bond distances in Angstroms (Å) for $Cs_6I_3Na(PMo_{12}O_{40})$.

$Mo(1)O_7$	
Mo1—O3	1.666(10)
Mo1—O4	1.901(12)
Mo1—O7	1.903(11)
Mo1—O9	1.905(12)
Mo1—O7	1.916(11)
Mo1—O11	2.486(15)
Mo1—O11	2.492(15)

$Mo(2)O_7$	
Mo2—O1	1.612(8)
Mo2—O8	1.887(10)
Mo2—O6	1.899(12)
Mo2—O5	1.901(13)
Mo2—O8	1.935(10)
Mo2—O10	2.477(14)
Mo2—O10	2.486(14)

$Mo(3)O_7$	
Mo3—O2	1.656(9)
Mo3—O9	1.902(11)
Mo3—O6	1.907(11)
Mo3—O5	1.912(12)
Mo3—O4	1.924(11)
Mo3—O11	2.414(14)
Mo3—O10	2.417(14)

$PO_8 \equiv PO_4$	
P—O11	1.564(15)
P—O11	1.564(15)
P—O11	1.564(15)
P—O11	1.564(15)
P—O10	1.571(14)
P—O10	1.571(14)
P—O10	1.571(14)
P—O10	1.571(14)

NaO_8	
Na—O7	2.440(14)
Na—O7	2.440(14)
Na—O7	2.440(14)
Na—O7	2.440(14)
Na—O8	2.446(13)
Na—O8	2.446(13)
Na—O8	2.446(13)
Na—O8	2.446(13)

$Cs(1)O_{10}I_2$	
Cs1—O5	3.237(13)
Cs1—O5	3.237(13)
Cs1—O3	3.274(10)
Cs1—O3	3.274(10)
Cs1—O2	3.358(10)
Cs1—O2	3.358(10)
Cs1—O6	3.667(12)
Cs1—O6	3.667(12)
Cs1—O1	3.714(11)
Cs1—O1	3.714(11)
Cs1—I1	3.884(1)
Cs1—I1	3.884(1)

$Cs(2)O_{10}I_4$	
Cs2—O5	3.108(11)
Cs2—O4	3.185(12)
Cs2—O6	3.207(12)
Cs2—O1	3.240(8)
Cs2—O4	3.27(1)
Cs2—O2	3.319(10)
Cs2—O9	3.390(11)
Cs2—O9	3.528(11)
Cs2—O3	3.622(11)
Cs2—O7	3.727(13)
Cs2—I1	3.768(1)
Cs2—I2	3.902(1)
Cs2—I2	3.902(1)
Cs2—I2	3.902(1)

Table 3.5: Selected bond angles (degrees) for $Cs_6I_3Na(PMo_{12}O_{40})$.

∠O-Mo(1)-O		∠O-Mo(2)-O		∠O-Mo(3)-O	
O3—Mo1—O4	101.16(47)	O1—Mo2—O8	102.38(49)	O2—Mo3—O9	99.76(48)
O3—Mo1—O7	102.71(51)	O1—Mo2—O6	100.34(46)	O2—Mo3—O6	101.37(50)
O3—Mo1—O9	103.16(48)	O1—Mo2—O5	102.09(46)	O2—Mo3—O5	101.05(52)
O3—Mo1—O7	100.32(46)	O1—Mo2—O8	103.89(40)	O2—Mo3—O4	99.56(48)
O3—Mo1—O11	160.41(48)	O1—Mo2—O10	159.15(43)	O2—Mo3—O11	157.89(46)
O3—Mo1—O11	156.72(48)	O1—Mo2—O10	157.54(43)	O2—Mo3—O10	158.68(46)

Table 3.6: Bond valence sums calculations for $Cs_6I_3Na(PMo_{12}O_{40})$.[19]

	r_0 Mo^{5+}	r_0 Mo^{6+}		r_0 Mo^{5+}	r_0 Mo^{6+}		r_0 Mo^{5+}	r_0 Mo^{6+}
$Mo(1)O_7$			**$Mo(2)O_7$**			**$Mo(3)O_7$**		
Mo1—O3	1.77	1.92	Mo2—O1	2.05	2.22	Mo3—O2	1.82	1.97
Mo1—O4	0.94	1.02	Mo2—O8	0.98	1.06	Mo3—O9	0.94	1.01
Mo1—O7	0.93	1.01	Mo2—O6	0.94	1.02	Mo3—O6	0.92	1.00
Mo1—O9	0.93	1.01	Mo2—O5	0.94	1.02	Mo3—O5	0.91	0.99
Mo1—O7	0.90	0.98	Mo2—O8	0.86	0.93	Mo3—O4	0.88	0.96
Mo1—O11 x 1/2	0.10	0.10	Mo2—O10 x 1/2	0.10	0.11	Mo3—O11 x 1/2	0.12	0.13
Mo1—O11 x 1/2	0.10	0.10	Mo2—O10 x 1/2	0.10	0.10	Mo3—O10 x 1/2	0.12	0.13
$\sum (Mo^{5,6+})$	**5.67**	**6.13**		**5.97**	**6.45**		**5.71**	**6.18**

	r_0 P^{5+}		r_0 Na^+		r_0 Cs^+
$PO_8 \equiv PO_4$		**NaO_8**		**$Cs(1)O_{10}$**	
P—O11 x 4 x 1/2	2.31	Na—O7 x 4	0.72	Cs1—O5 x 2	0.22
P—O10 x 4 x 1/2	2.26	Na—O8 x 4	0.70	Cs1—O3 x 2	0.20
				Cs1—O2 x 2	0.16
				Cs1—O6 x 2	0.07
				Cs1—O1 x 2	0.06
$\sum (P^{5+})$	**4.57**	$\sum (Na^+)$	**1.42**	$\sum (Cs^+)$	**0.70**

	r_0 Cs^+
$Cs(2)O_{10}$	
Cs2—O5	0.15
Cs2—O4	0.13
Cs2—O6	0.12
Cs2—O1	0.11
Cs2—O4	0.10
Cs2—O2	0.09
Cs2—O9	0.07
Cs2—O9	0.05
Cs2—O3	0.04
Cs2—O7	0.03
$\sum (Cs^+)$	**0.88**

Magnetic Studies: Magnetic susceptibility measurements were performed on $Cs_6I_3Na(PMo_{12}O_{40})$ polycrystalline sample using a Quantum Design PPMS magnetometer. Temperature–dependent magnetic susceptibility measurements of $Cs_6I_3Na(PMo_{12}O_{40})$ were performed on ground powder sample. Quantity of sample used for measurements consisted of 50.0 mg for $Cs_6I_3Na(PMo_{12}O_{40})$. The temperature–dependent studies of $Cs_6I_3Na(PMo_{12}O_{40})$ were measured in applied fields of 100 Oe at temperatures ranging from 10–300 K.

Thermal analysis, TGA and DSC: DSC/TGA measurements were done on ground powders (~10 mg) using a SDT Q600 TA Instruments calorimeter. A 110 μL platinum sample and reference pans were used for data collection. The heating profile for the measurement included a heating rate of 20 °C/min from room temperature to 700 °C, followed by a return cooling rate of 20 °C/min in the presence of 75 mL/min nitrogen gas flow.

Results and Discussion

A new salt inclusion polyoxometalate compound has been synthesized in molten salt media. The title compound, $Cs_6I_3Na(PMo_{12}O_{40})$, crystallizes in the tetragonal space group, *P* 4/*ncc* (no. 130), *Z* = 4. The crystallographic data is presented in Table 3.1 which includes the unit cell parameters and other relevant information. Tables 3.2 and 3.3 provide the atomic and anisotropic displacement parameters for the title compound, respectively. Figures 3.5~3.8 illustrate the structure of the $Cs_6I_3Na(PMo_{12}O_{40})$.

$Cs_6I_3NaPMo_{12}O_{40}$ consists of the α-Keggin anion which has the general formula of $(XM_{12}O_{40})^{n-}$, where X is the heteroatom and M is the early transition metal. In the title compound, the heteroatom is P and the early transition metal is Mo. The Keggin anion is composed of three crystallographically unique molybdenum atoms. The framework of the Keggin anion can be decomposed into three parts as shown in Figure 3.6. The two Mo_4 caps (blue polyhedra in Figure 3.6) consisting of Mo(1) and Mo(2) atoms are connected by an additional Mo_4 equatorial belt composed of crystallographically unique Mo(3) atoms (cyan polyhedra in Figure 3.6). The connection between the Mo(1) cap and the Mo(3) belt is made possible through the μ_2-oxo bridges *via* 4 × O(4) and 4 × O(9). The distances of these connections are shown in Table 3.4 and are comparable to the sum of the crystal radii for Mo^{6+} and O^{2-} (0.73 Å and 1.24 Å, respectively).[19] The Mo(2) cap connects to the Mo(3) belt through 4 × μ_2-O(5) and 4 × μ_2-O(6). As is the case with the previously reported, fully oxidized $(PMo_{12}O_{40})^{3-}$ clusters,[14] each molybdenum site in $Cs_6I_3NaPMo_{12}O_{40}$ adopts the MoO_6 distorted octahedral coordination with comparably short apical molybdenyl (M=O) bonds, ranging from 1.612(10) Å to

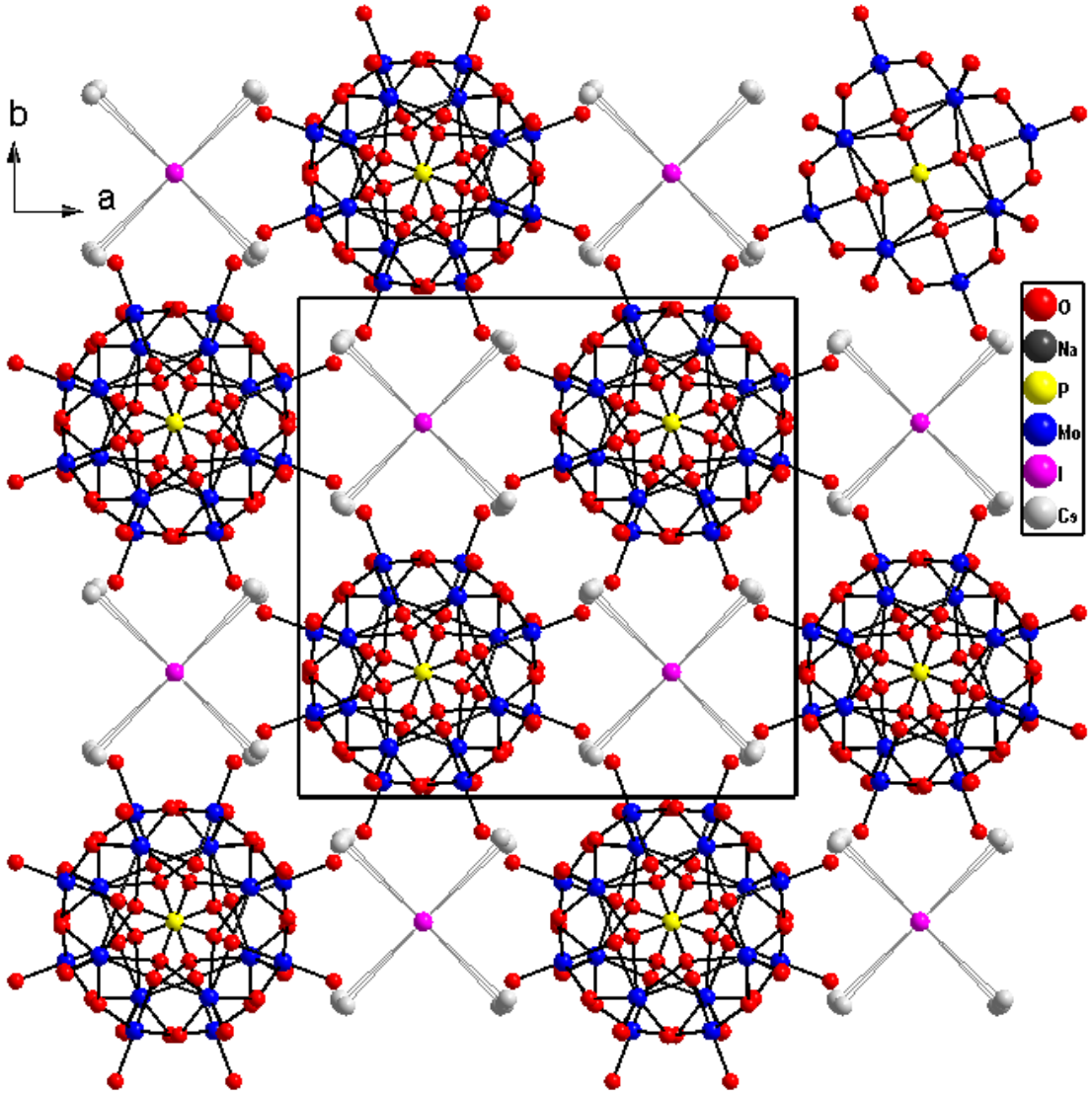

Figure 3.5: Perspective view along the *c*–axis of $Cs_6I_3Na(PMo_{12}O_{40})$ showing the 4–fold symmetry. The $(PMo_{12}O_{40})^{4-}$ clusters are surrounded by the $[Cs_2I]_\infty$ salt lattice. The Na^+ ions reside in an anti–prismatic eight–coordinate environment between the neighboring clusters along *c* (not seen in this picture).

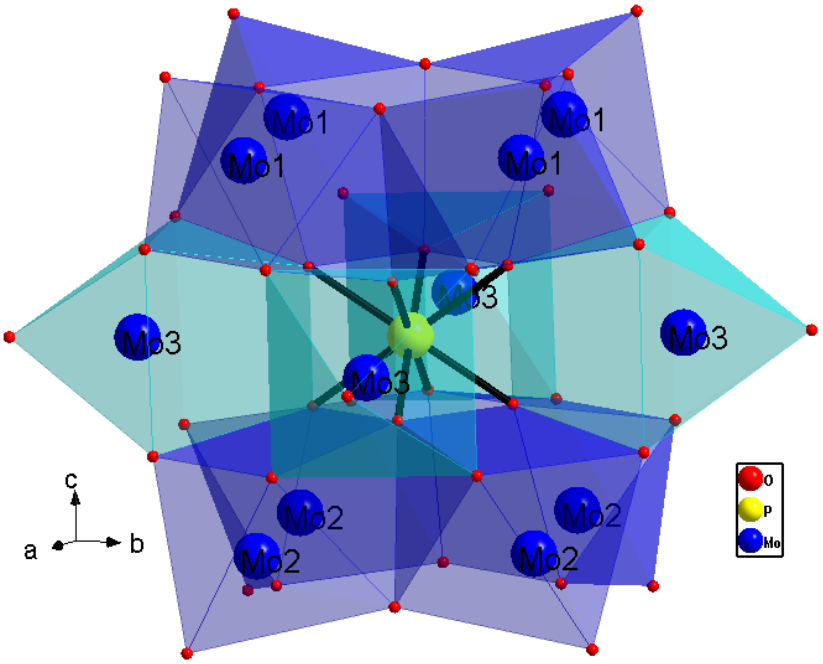

Figure 3.6: Structure of the Keggin anion $(PMo_{12}O_{40})^{4-}$ showing the four-fold symmetry of the three crystallographically unique Mo atoms; Mo(1), Mo(2) (blue polyhedra), and Mo(3) (cyan polyhedra).

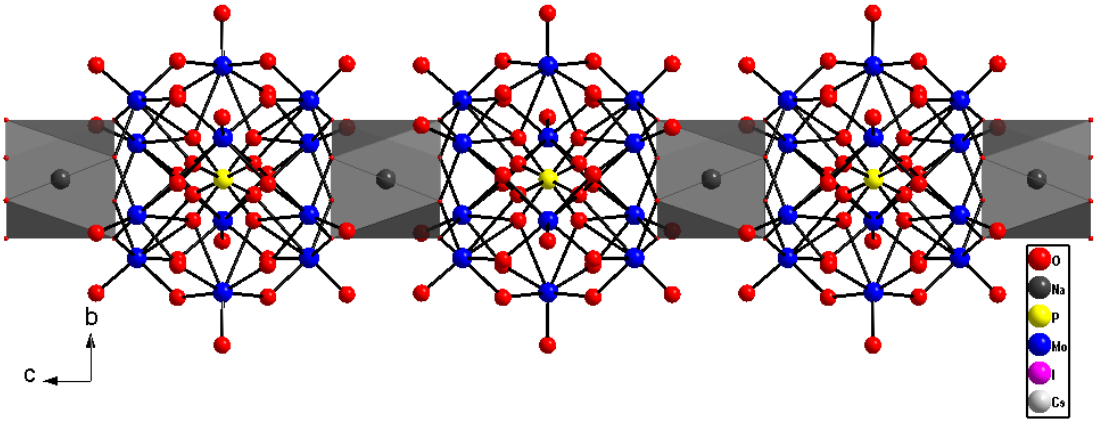

Figure 3.7: Partial structural view along the *c*–axis showing the [-Na-($PMo_{12}O_{40}$)-] infinite chain. The Na^+ ions are represented by dark grey polyhedra.

a)

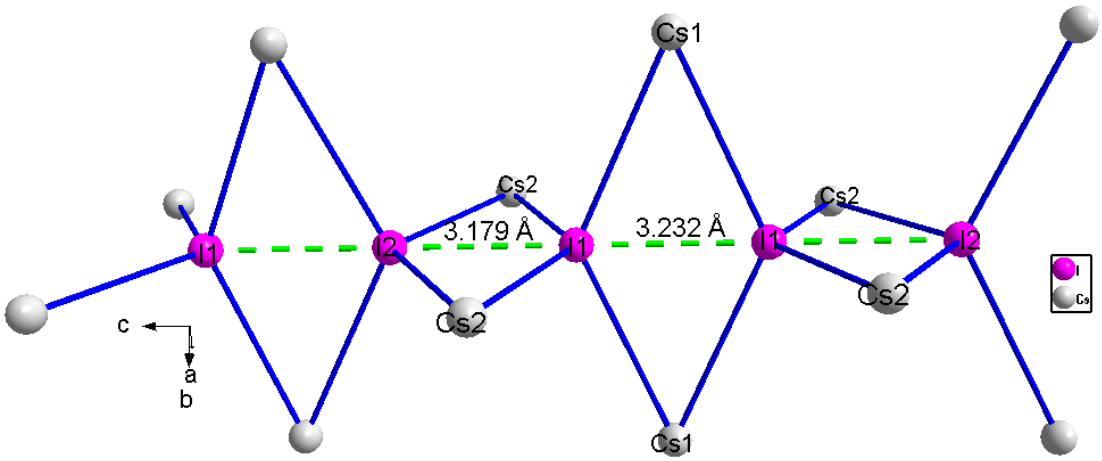

b)

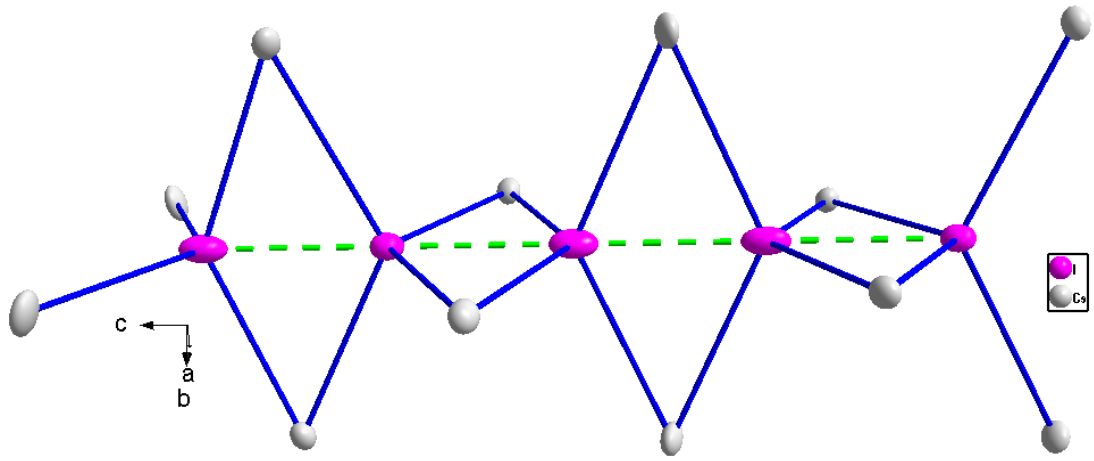

Figure 3.8: a) $[Cs_2I]_\infty$ salt lattice showing the tetrahedral geometry and the bond lengths between the neighboring I^- atoms. b) Ellipsoidal view showing the elongation of I^- atoms along the *c* crystallographic direction.

1.666(9) Å, and pointing away from the center of the cage. It should be noted that the Mo atoms are seemingly coordinated to seven oxygen atoms instead of six, but due to the disorder of the oxygen atoms inside the cluster, only one of the two oxygen atoms coordinates to Mo at a given instance. This is due to the crystallographic occurrence when one of the superimposed Keggin anions is rotated about the C_4 axis.[18] As a result of this crystallographic occurrence, the $(PO_4)^{3-}$ anion residing inside the cage of the cluster is disordered given the surrounding oxygen atoms (4 × O(10) and 4 × O(11)) are half-occupied as shown in Table 3.2.

The rest of the observed Mo−O bond distances, 1.95~1.97 Å as listed in Table 3.4, are comparable to the sum of the Shannon crystal radii, 1.97 Å, for a 6-coordinate $Mo^{5,6+}$ and O^{2-} (1.22 Å).[19] The shortest Mo-Mo distance is 3.540(1) Å. The expected anionic charge, based on the counter-cations, on the cluster is 4-, $(PMo_{12}O_{40})^{4-}$, with one Mo^{5+} and eleven Mo^{6+} cations. The charges of the Mo atoms are largely delocalized as indicated by the bond valence sums calculations shown in Table 3.6. The bond valence sums of Mo(1) and Mo(3) are slightly lower than those of Mo(2). However, such small differences are likely insignificant and as a result, it is difficult to conclude if any localization of the single Mo^{5+} exists.

As shown in Fig. 3.8, the antifluorite-type salt chain, $[Cs_2I]_\infty$, is featured in which the iodine atoms adopt tetrahedral geometry with respect to the Cs atoms. This salt chain likely has a templating or structure-directing effect on the overall formation of the extended solid. Recent reports have highlighted the importance of the salt lattices and their structure-directing and dimensionality reducing effects on the metal-oxide frameworks.[20] The bond

distances between Cs and I range from 3.768(1) Å to 3.902(1) Å and are comparable to the sum of their Shannon radii, 3.94 Å (~1.88 Å for Cs^+, CN = 8 and 2.06 Å for I^-, CN=6).[19] The bond valence sums calculations of the Cs sites show a slightly lower than expected bond valence sums. This is most likely due to the fact that only Cs-O distances were used in the calculation of bond valence sums. In addition to oxygen bonds, Cs is also connected to iodides, as mentioned above.

It is interesting to point out that the salt chain in $Cs_6I_3NaPMo_{12}O_{40}$ is stabilized by the presence of halogen bonding between the adjacent iodine atoms along the *c* crystallographic direction as shown in the partial representation of the salt chain in Figure 3.8. The bond distances between the two neighboring iodine atoms in $Cs_6I_3NaPMo_{12}O_{40}$ are, to the best of our knowledge, the shortest I···I non-covalent halogen bonds reported and they range from 3.179(2) Å to 3.232(3) Å. These distances are significantly shorter than the sum of the two ionic Shannon radii for I^- (~4.12 Å for CN=6).[19] Figure 3.8 (b) shows the ellipsoidal representation of the atoms in the $[Cs_2I]_\infty$. It can be noticed that the iodine atoms show slight elongation or cigar shape along the *c* crystallographic direction. This preferential elongation along the *c* crystallographic direction also suggests that an interaction between the neighboring iodine atoms likely exists. Similar halogen bonding is observed between the intermolecular iodine atoms in the crystalline I_2 solid with significantly longer I···I distances of about 3.50 Å.[21] The existence of the short halogen bonding between the neighboring iodine atoms in $Cs_6I_3NaPMo_{12}O_{40}$ is likely the reason for its insolubility in water due to the increased stabilization of the I···I interaction. Changing from water to relatively less polar solvents, ethanol and dimethylformamide (DMF), small

amount of $Cs_6I_3NaPMo_{12}O_{40}$ is able to dissolve (see Figure 3.9). Similar observation is noted in iodine solid where only slight solubility of I_2 is observed in water while higher amounts can be dissolved in non-polar solvents.[22] These observations further support the fact that an unusually short interaction between iodine atoms exists in $Cs_6I_3NaPMo_{12}O_{40}$.

Nevertheless, the Keggin ions are interconnected through a single Na^+ ion (Na) residing between the neighboring $(PMo_{12}O_{40})^{4-}$ anions. The Na^+ is coordinated to two crystallographically unique oxygen atoms, 4 x O(7) and 4 x O(8) resulting in an eight coordinate square antiprismatic geometry as represented by dark grey polyhedra in Figure 3.6. The distances between the Na^+ and the oxygen atoms range from 2.440(14) Å to 2.446(13) Å. The resulting $[-(PMo_{12}O_{40})-Na-]_\infty$ pseudo-1D chain extends in the *c* crystallographic direction. The bond valence sums from Table 3.6 show a slightly higher than expected value for Na^+.

Figure 3.10 shows the magnetic susceptibility plots for the title compound. The data were collected with an applied magnetic field of 0.5 T. As can be seen from the χ *vs. T* plot, as the temperature is decreased, the number of spins aligning with the field increased resulting in increased magnetic susceptibility which is representative of what is expected for paramagnetic materials. In order to obtain some information about the paramagnetic ions including the magnetic moment, the magnetic susceptibility data were fitted using the Curie-Weiss law. A linear behavior in the χ^{-1} *vs. T* plot is observed and was fitted above 100 K. Using the equation for effective magnetic moment, $2.82(\chi_M T)^{1/2}$, the effective magnetic moment was able to be plotted as a function of varying temperature (inset in Figure 3.10). At room temperature the value for effective magnetic moment was found to

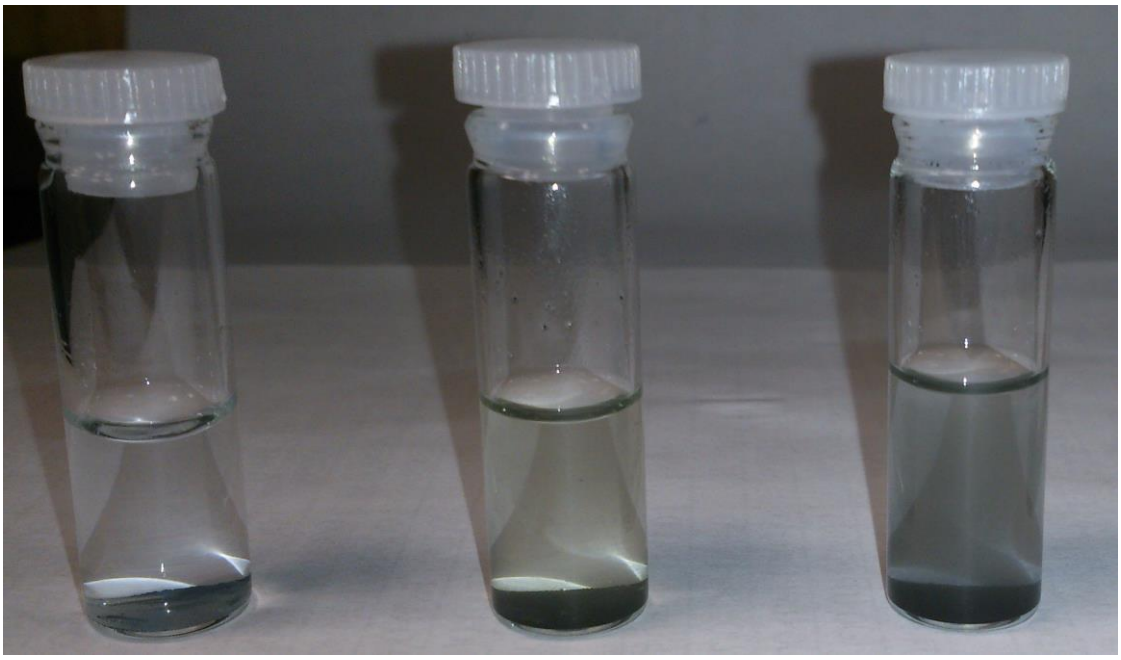

Figure 3.9: Solubility of $Cs_6I_3NaPMo_{12}O_{40}$ in different solvents. 10 mg were placed in water, ethanol and dimethylformamide (DMF), respectively from left to right. With decreasing polarity of the solvent, more of the title compound can be dissolved.

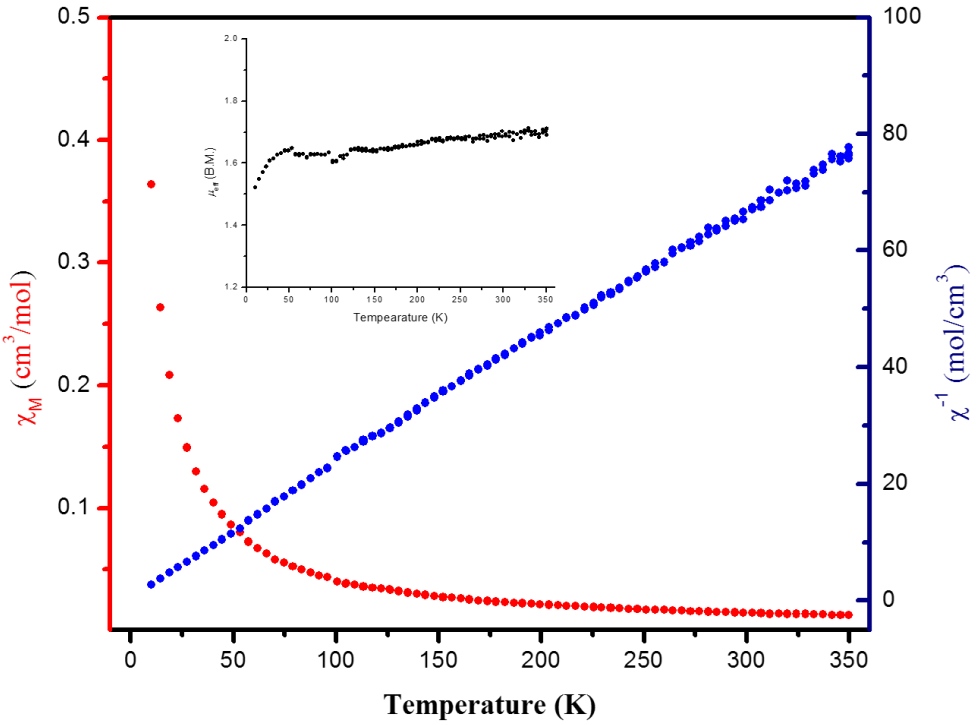

Figure 3.10: Molar magnetic susceptibility, χ_M (red), and the inverse molar magnetic susceptibility, χ^{-1} (blue) collected with the applied field of 0.5 T. The inset shows the magnetic moment, μ_{eff}, plotted as function of temperature.

be 1.69 μ_B which is slightly lower than the expected value, 1.73 μ_B for Mo^{5+}, S = ½. The susceptibility plot in Figure 3.10 shows no evidence of long range order. The lack of any evidence of long range order is likely due to the insulating nature of the ionic salt lattices. Looking at the magnetic moment *vs*. temperature plot (inset in Figure 3.10), the magnetic moment starts to sharply decrease below 50 K. Above this temperature, thermal energy is sufficient enough to make the unpaired (paramagnetic-like).

DSC and TGA measurements illustrated in Figure 3.11 show that $Cs_6I_3NaPMo_{12}O_{40}$ is thermally stable up to about 200 ^oC at which point about 5% weight loss starts to occur. This ~5% loss of mass was observed between 200 ^oC and 300 ^oC and is likely the result of a loss of ½ I_2 which corresponds to approximately 4.2% of the total formula weight. The second drop occurs continuously from 300 ^oC and onsets with a sharp drop from 475 ^oC to about 550 ^oC corresponding to about 8% of the total mass. This 8% loss of mass could be due to the loss of the remaining I_2. The total loss at about 550 ^oC is approximately 13% which is comparable to three moles of I per formula unit equaling about 12.6% of I. Given that I^- was oxidized to I_2, the likely scenario is that the remaining molybdenum species were further reduced which explains the presence of a dark blue solid at the bottom of the sample pan. DSC plot shows an endothermic peak around 530 ^oC which is likely due to the melting of the resulting species after the iodine loss and the recrystallization of the same around 430 ^oC. Based on the TGA/DSC results, a possible decomposition pathway can be formulated according to the equation shown.

$$Cs_6I_3Na(PMo_{12}O_{40}) \xrightarrow{300\ oC} \tfrac{1}{2}\ I_2 + Cs_6I_2Na(PMo_{12}O_{40}) \xrightarrow{600\ oC} I_2 + \text{“}Cs_6Na(PMo_{12}O_{40})\text{”}$$

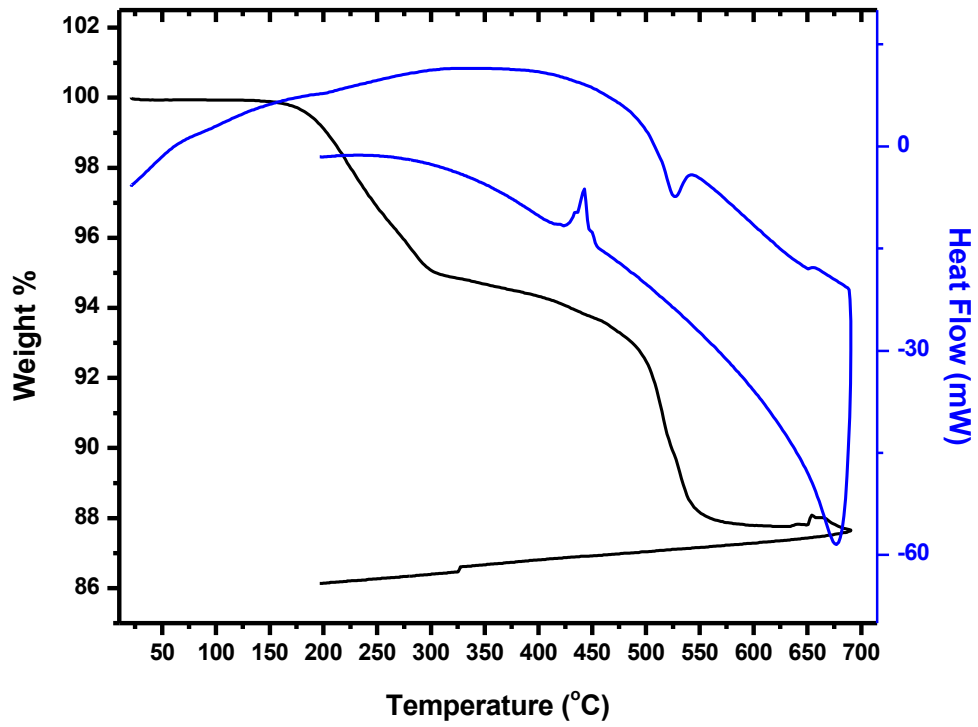

Figure 3.11: Thermogravimetric analysis (TGA) (black line) and differential scanning calorimetry (DSC) (blue line) plots for $Cs_6I_3NaPMo_{12}O_{40}$ under N_2 gas flow.

In order to confirm the decomposition pathway of $Cs_6I_3Na(PMo_{12}O_{40})$, small amount of the powdered form of the compound was heated in various conditions. Figure 3.12 shows the PXRD patterns showing the decomposition of $Cs_6I_3Na(PMo_{12}O_{40})$ at 300 ^oC. First, the compound was heated in a sealed ampoule at 300 ^oC for 15 minutes (third line from the bottom in Figure 3.12). The ampoule was opened and the powder was subjected to XRD for phase identification. Given that the TGA/DSC experimental condition involved a steady flow of inert N_2 gas, similar condition was set up using a tube furnace where N_2 gas flowed during the 15 minute-long heating at 300 ^oC. Based on the obtained PXRD patterns, $Cs_6I_3Na(PMo_{12}O_{40})$ likely decomposes to $Cs_6I_2Na(PMo_{12}O_{40})$ which is a two electron reduced compound belonging to a family of $Cs_6X_2Na(PMo_{12}O_{40})$ (X = Cl, Br, I) compounds described in Chapter 4. Looking at the second line from the top in Figure 3.12 (labeled "open tube N_2 flow 300 ^oC") and comparing it to the calculated powder patterns of $Cs_6I_3Na(PMo_{12}O_{40})$ (bottom line) and $Cs_6I_2Na(PMo_{12}O_{40})$ (top line), one can identify the peaks corresponding to both $Cs_6I_3Na(PMo_{12}O_{40})$ and $Cs_6I_2Na(PMo_{12}O_{40})$. The likely reason for the incomplete conversion of $Cs_6I_3Na(PMo_{12}O_{40})$ to $Cs_6I_2Na(PMo_{12}O_{40})$ is that a significantly large amount of powder was used which was converted mainly on the surface due to inhomogeneous heating. For TGA/DSC experiment on the other hand, only a few milligrams of the powder were used.

Heating the powder to the decomposition temperature in the presence of N_2 flow, a dark blue powder was formed. When comparing the PXRD of the 650 ^oC decomposition product and the available calculated PXRDs, a match cannot be seen which indicates that a new four-electron reduced compound, "$Cs_6Na(PMo_{12}O_{40})$", is likely to exist. However,

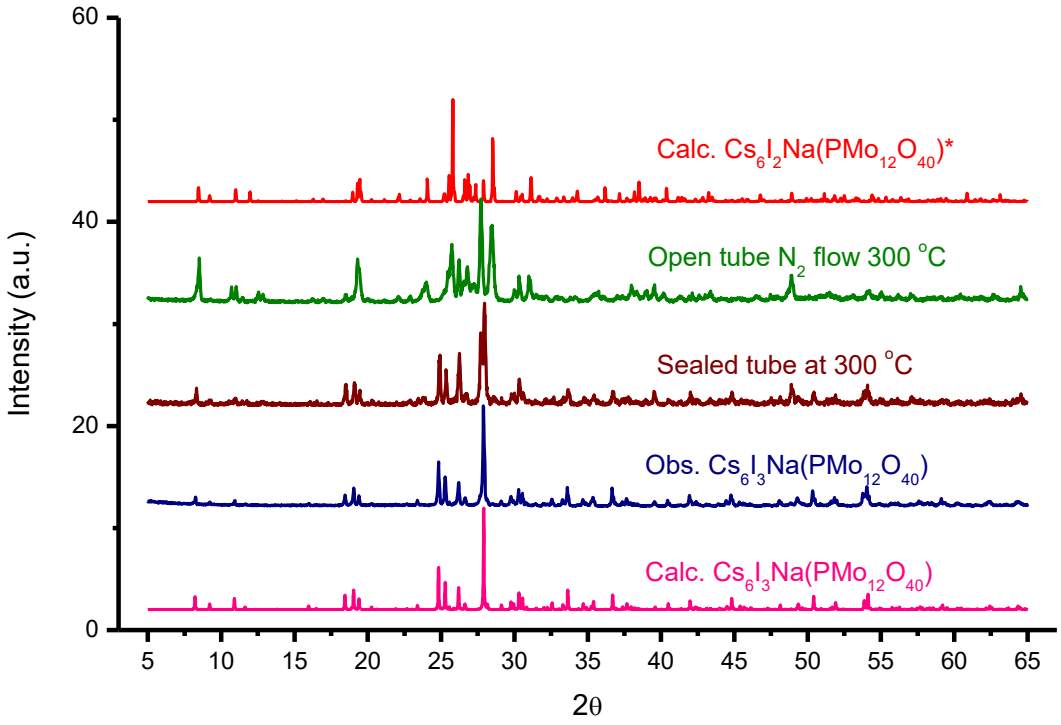

Figure 3.12: PXRD patterns showing the decomposition after 300 °C. From bottom to top: calculated $Cs_6I_3Na(PMo_{12}O_{40})$, observed $Cs_6I_3Na(PMo_{12}O_{40})$, observed after heating in sealed tube at 300 °C, observed after heating at 300 °C under N_2 flow, calculated $Cs_6I_2Na(PMo_{12}O_{40})$. *$Cs_6I_2Na(PMo_{12}O_{40})$ is a two electron reduced compound discussed in Chapter 4.

single crystals were unable to be isolated for single crystal structure analysis. Possible future reactions using a similar approach in which iodide is oxidized to iodine to grow further reduced solids could be used.

Another indication of the above described decomposition pathway is the formation of I_2 solid on the upper portion of the glass ampoule after a regrind/reheat step in the initial synthesis of $Cs_6I_3Na(PMo_{12}O_{40})$. This is easily seen if a larger fused silica ampoule is used in the regrind/reheat step which is caused by the temperature gradient inside the tube. However, keeping the ampoule length to less than 10 cm reduces the temperature gradient inside the tube and prevents the decomposition of $Cs_6I_3Na(PMo_{12}O_{40})$ and the formation of I_2 solid on the side of the tube.

UV-vis reflectance data was collected on the solid powder sample of $Cs_6I_3Na(PMo_{12}O_{40})$ and a optical band gap was obtained by plotting the Tauc plot from the Kubelka-Munk function[23] of the obtained reflectance data, shown in Figure 3.13. The linear region at the lowest eV range was extrapolated to the *x*-axis (at y = 0). Using this method the obtained optical band gap for $Cs_6I_3Na(PMo_{12}O_{40})$ was 2.91 eV by extrapolating the linear region between 5.0 and 5.5 eV. However, it is clear that no obvious platoue can be seen at energies lower than 5.0 which indicates that the absorption edge is even lower. This likely suggests that $Cs_6I_3Na(PMo_{12}O_{40})$ has an even lower band gap which would need to be obtained using alternative methods, such as four-point probe electrical resistivity method. Based on literature search, the band gap of 2.91 eV seems higher compared to other Keggin-based solids. For example, the fully oxidized $H_3(PMo_{12}O_{40})$ shows a HOMO-LUMO gap of about 2.0 eV.[24]

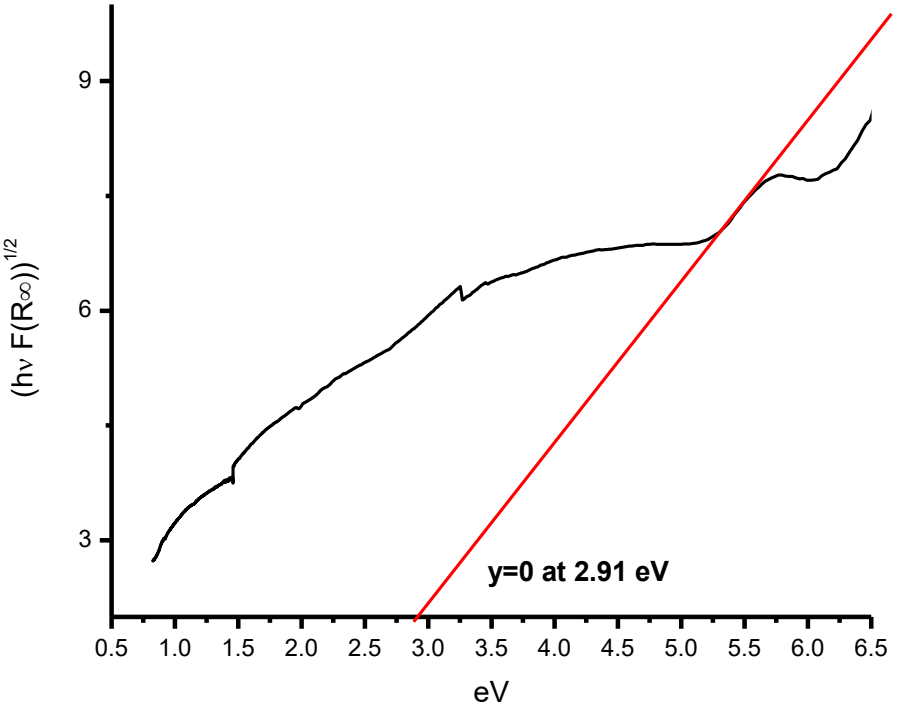

Figure 3.13: Kubelka-Munk[23] plot showing the experimental band gap obtained from UV-vis diffuse reflectance for $Cs_6I_3Na(PMo_{12}O_{40})$.

Conclusions

Here, a new salt inclusion solid containing discrete polyoxometalate clusters is presented. This new compound has the composition of $Cs_6I_3NaPMo_{12}O_{40}$ in which the one electron reduced Keggin-based polyoxometalate is featured. To the best of our knowledge, this is the first time a Keggin-based polyoxometalate has been isolated using conventional, high-temperature molten-salt methods. From previous reports, and the compounds presented in this dissertation, we have reasons to believe that high temperature synthesis of polyoxometalates promotes the isolation of reduced species which is not generally the case with the solution-based low temperature synthetic routes. Upon the investigation of the structure and bonding, it can be noticed that the neighboring iodine atoms in the $[Cs_2I]_\infty$ antifluorite salt chain are unusually close in proximity. This suggests that there exists a non-covalent halogen interaction between the two neighboring iodine atoms which further stabilizes the overall structure. This additional stabilizing feature is likely one of the reason for insolubility of the title compound in water and increased solubility in less polar solvents. This similar trend was observed in iodine solid which also features non-covalent interactions between the intermolecular neighboring iodine atoms. The TGA data shows that the title compound is thermally stable under N_2 gas flow up to about 200 ^oC and has two sharp weight losses corresponding to about 13% weight loss attributed to oxidation and loss of iodine. The magnetic susceptibility measurements show distinctive paramagnetic behavior which suggests that any long range order is likely suppressed by the insulating nature of the ionic salt lattices.

Future Work

Even though the Keggin cluster is embedded in an ionic matrix featuring $[Cs_2I]_\infty$ antifluorite type salt chain and the Na^+ ions residing between the neighboring clusters, the title compound is not soluble in water. It is suspected that the halogen bonding between the neighboring iodine atoms is one of the stabilizing factors which prevents the solubility of $Cs_6I_3Na(PMo_{12}O_{40})$ in water. It would be interesting to see if the solubility of the title compound could essentially be tuned by replacing the large Cs^+ ions with smaller A-site cations which would result in comparably poorer size matching between the large iodine and smaller A-site cations resulting in a relatively more ionic-type interaction. If similar water soluble clusters can be isolated, they could potentially be used as building blocks for conventional solution-based synthesis of extended solids featuring polyoxometalate clusters. In addition, their properties with respect to biological systems could be investigated and compared to those of fully oxidized clusters previously studied. If a soluble one-electron reduced Keggin compound could be isolated, its biomedical properties, including antibacterial effects, could be studied as was done with the two-electron family of Keggin-based compounds in the next chapter.

It is thought that the thermal decomposition of $Cs_6I_3Na(PMo_{12}O_{40})$ results in oxidation of I^- to I_2. A better understanding of the decomposition process could potentially be exploited for synthesis of new similar phases. If the oxidation of I^- is indeed occurring, the likely result is that Mo^{6+} is being reduced which can potentially lead to synthesis of further reduced cluster species likely to be interesting for their electronic and magnetic

properties. The title compound illustrates, once more, the importance of salt-inclusion synthesis and the vast utility of this synthetic method in formation of novel frameworks.

Literature Cited

1. Yu, H.; Wu, H.; Pan, S.; Wang, Y.; Yang, Z. and Su, X. *Inorg. Chem*. **2013**, 52 (9), 5359-5365.

2. (a) Ranmohotti, K. G. S.; Queen, W. L.; West, J. P.; VanDerveer, D. and Hwu, S.-J. *J. Chem. Crystallogr*. **2009**, 39, 303.

   (b) Hwu, S.–J.; Ulutagay–Kartin, M.; Clayhold, J.A.; Mackay, R.; Wardojo, T.A.; O'Connor, C.T.; Krawiec, M. *J. Am. Chem. Soc.* **2002**, *124*, 12404–12405.

   (c) Huang, Q.; Kartin, M.; Mo, X. and Hwu, S.-J. *Mater. Res. Soc. Symp. Proc*., **2002**, 459.

   (d) Ulutagay, M.; Schimek, G. L.; Hwu, S.-J. and Taye, H. *Inorg. Chem*. **1998**, 37, 1507.

3. (a) Queen, W. L.; Hwu S.-J. and Reighard, S. *Inorg. Chem*. **2010**, 49, 1316.

   (b) Huang, Q.; Hwu, S.-J. and Mo, X. *Angew. Chem. Int. Ed*. **2001**, 40, 1690.

   (c) Huang, Q.; Ulutagay, M.; Michener, P. A. and Hwu, S.-J. *J. Am. Chem. Soc*. **1999**, 121, 10323.

   (d) Etheredge, K. M. S. and Hwu, S.-J. *Inorg. Chem*. **1995**, 34, 3123.

4. (a) Queen, W.L.; West, J.P.; Hwu, S.-J.; Tran, T.T.; Halasyamani, P.S.; VanDerveer, D. *Chem. Commun*. **2012**, 48, 1665–1667.

   (b) Queen, W.L.; West, J.P.; Hudson, J.; Hwu, S.-J. *Inorg. Chem*. **2011**, 50, 11064–11068.

   (c) Queen, W. L.; Hwu, S.-J.; and Reighard, S. *Inorg. Chem*. **2011**, 49, 1316-1318.

5. Kozhevnikov I. *Chem. Rev.* **1998**, *98* (1), 171–198.

6. (a) Papaconstantinou, E. *Chem. Soc. Rev.* **1989**, *18*, 1.

   (b) Yamase, T. *Chem. Rev*. **1998**, *98*, 307.

7. Compain, J-D.; Mialane, P.; Dolbecq, A.; Mbomekalle, I. M.; Marrot, J.; Secheresse, F.; Riviere, E.; Rogez, G.; Wernsdorfer, W. *Angew. Chem. Int. Ed.* **2009**, *48* (17), 3077-3081.

8. (a) Yamase, T.; Fukuda, N.; Tajima, Y. *Biol. Pharm. Bull.* **1996**, *19*, 459-465.

(b) Yamase, T.; Fujita, H.; Fukushima K. *Inorg. Chim. Acta.* **1988**, *151*, L15-L18.

9. Miras, H. N.; Yan, J.; Long, D-L.; and Cronin, L. *Chem. Soc. Rev.* **2012**, *41*, 7403-7430.

10. Ahmed, E.; and Ruck, M. *Angew. Chem. Int. Ed*. **2012**, *51*, 308-309.

11. (a) Cooper, E. R.; Andrews, P. S.; Wheatley, P. S.; Webb, P. B.; Wormald, P.; and Morris, R. E. *Nature*. **2004**, *430*, 1012-1016.

(b) Aidoudi, F. H.; Aldous, D. W.; Goff, R. J.; Slawin, A. M. Z.; Attfield, J. P.; Morris, R. E.; and Lightfoot, P. *Nature Chem*. **2011**, *3*, 801-806.

(c) Lin, S.; Liu, W.; Li, Y.; Wu, Q.; Want, E.; and Zhang, Z. *Dalton Trans*. **2010**, *39*, 1740-1744.

(d) Fu, H.; Li, Y.; Lu, Y.; Chen, W.; Wu, Q.; Meng, J.; Wang, X.; Zhang, Z.; and Wang, E. *Cryst. Growth Des*. **2011**, *11*, 458-465.

12. Geselbracht, M. J.; Stacy, A. M. *J. Solid State Chem.* **1994**, *110*, 1–5.

13. (a) Köhler, J.; Simon, A. *Z. Anorg. Allg. Chem.* **1987**, *553*, 106.

(b) Köhler, J.; Simon, A. *Z. Anorg. Allg. Chem.* **1989**, *572*, 7.

(c) Kersting, K. B.; Jeitschko, *J. Solid State Chem*. **1991**, *93*, 350.

14. McGarvey, G. B.; and Moffat, J.B. *J. Catal*. **1991**, *132*, 100-116.

15. Kool, F. X. N. M.; Koster, A. S.; and Rieck, G. D. *Acta Cryst.* **1970**, *B26*, 1974.

16. Gatehouse, B.M.; Miskin, B.K. *Acta Cryst*. **1975**, *B31*, 1293.

17. Toby, B. H. *J. Appl. Cryst.* **2001**, *34*, 210-213.

18. (a) Evans, H. T. Jr.; Pope, M. T. *Inorg. Chem*. **1984**, *23*, 501-504.

(b) Niu, J-Y.; Shan, B-Z.; and You, X-Z. *Transition Met. Chem*. **1999**, *24*, 108-114.

19. Shannon, R.D. *Acta Cryst*. **1976**, *A32*, 751-767.

20. Hwu, S-J. *Chem. Mater*. **1998**, *10*, 2846-2859.

21. Van Bolhuis, F.; Koster, P.B.; and Migchelsen, T. *Acta Cryst*. **1967**, 23, 90-91.

22. Nakanishi, K. and Asakura, S. *J. Phys. Chem*. **1977**, 81 (18), 1745-1746.

23. (a) Kubelka, P.; Munk, F. *Z. Tech. Phys*. **1931**, *12*, 593.

(b) Kubelka, P. *J. Opt. Soc. Am*. **1948**, *38*, 448-457.

24. Kim, H.; Youn, M. H.; Jung, J. C.; Song, I. K. *J. Mol. Catal. A: Chem*. **2006**, *252*, 252.

CHAPTER FOUR

SYNTHESIS, CHARACTERIZATION AND IN VITRO BIOMEDICAL ACTIVITY OF REDUCED, WATER-SOLUBLE SALT-INCLUSION POLYOXOMETALATE SOLIDS BASED ON $Cs_6X_2Na(PMo_{12}O_{40})$ (X = Cl, Br, I)

Introduction

Polyoxometalates (POMs) are well-studied inorganic high nuclearity clusters. They are aggregates of early transition metals typically occurring in their highest oxidation states such as W^{6+}, Mo^{6+}, V^{5+}, etc. The chemistry and properties of these fully oxidized materials have been studied extensively in the past few decades. However, electronically reduced POMs are not well-studied, especially in the biomedical applications. Given their structural similarities and 0-dimensionality (0D), POMs can be considered as inorganic analogues of fullerenes. They occupy an intermediate place between nano-sized particles and infinite extended metal oxide frameworks providing a platform as building blocks for functional crystalline solids. As mentioned in the previous chapters, POMs come in a variety of shapes and sizes ranging from small, six transition metals, to large, up to 172 transition metals.[1] One of the reasons for the large variety in shapes and sizes can be attributed to the conformational changes of POMs due to the ability of early transition metals to adopt multiple oxidation states and different local geometries such as tetrahedral, octahedral and square pyramidal. Although the early work with POMs dates back to 1860s, these materials have not been extensively studied until the past few decades.[2] What makes these materials so interesting to chemists, and potentially physicists and material scientists is their ability

to undergo multiple reduction-oxidation (redox) reactions due to the presence of multiple transition metal centers. In addition, the structure and consequently the stability of POMs is largely unchanged under redox conditions which makes them very robust and useful for a variety of applications. The redox properties of POMs can be exploited in the fields of catalysis, magnetism and biomedical applications.[1]

Over the years, researchers have shown that POMs have exhibited a vast number of electronic properties, structural motifs, and chemical compositions all of which are a motivation for exploring the synthesis of POMs in order to target novel and useful functional materials.[3] POMs have shown to be effective in aqueous and non-aqueous media. Due to their high negative charge and comparatively lower lattice energies, POMs are often soluble in aqueous solvents. This environmentally-friendly property of POMs makes them particularly useful in homogenous catalysis, building block approach synthesis of extended POM-containing solids, and in biomedical applications in which aqueous physiological conditions are desired.

The study of POMs in biologically relevant chemotherapeutic applications such as antitumor, antiviral and antibiotic activities is well established.[4] Most prevalent examples of POMs with biological activity are the W-containing POMs in which tungsten atoms are usually in their highest oxidation states.[5] Few examples of the chemotherapeutic studies of V- (POVs) and Mo-containing (POMos) polyoxometalates also exist.[5] However, due to the elusiveness and synthetic challenges of reduced POMs under conventional solvent-based methods (as discussed in Chapter 3), there have been very few chemotherapeutic studies of POMs in which the early transition metals are not in their highest oxidation states. To

highlight a few biomedically relevant POM studies that can be found in literature, the next section will focus on anti-tumor, antiviral and antibacterial properties of POMs.

Historically, some of the first studies of POMs inhibiting biological systems were reported about 40 years ago when $(SiW_{12}O_{40})^{4-}$ was shown to inhibit various non-retro RNA and DNA viruses.[6] These studies were performed both in vitro and in vivo. Also, Friend leukemia virus and Moloney murine sarcoma virus were shown to be inhibited by the silicotungstate POM in vitro and by $[NH_4]_{17}Na[Na(SbW_7O_{24})_3(Sb_3O_7)_2]\cdot 14H_2O$ in vivo.[7] The latter compound is known as a French drug and is historically called HPA-23. HPA-23 was also shown to be effective at inhibiting the human immunodeficiency virus (HIV) in some animal models. However, due to its high cytotoxicity, the clinical trials of the drug were never carried out.

Examples of POMs inhibiting tumors are common in recent POM literature. In particular, the Anderson-type $(Mo_7O_{24})^{6-}$ POM showed anti-tumor activity at non cytotoxic concentrations of *in vitro* studies.[8] In addition to the *in vitro* studies, the Anderson-type POM suppressed the methylcholantrene-induced tumors (Meth-A sarcoma), adenocarcinoma and human cancer xenographs on tumor-bearing mice. The growth suppression of the tumors by Anderson-type POMs was surprisingly higher compared to some clinically approved anti-tumor drugs as further illustrated below.[9]

The effect of reduced POMs on anti-tumor activity is largely unknown. Only a few examples of anti-tumor activity of reduced POM species are known. Namely, $[Me_3NH]_6[H_2Mo^{V}_{12}O_{28}(OH)_{12}(Mo^{VI}O_3)_4]\cdot 2H_2O$ (PM-17), where Me = methyl, exhibits similar anti-tumor activity as the Anderson-type POMs which were discussed above.[8]

However, PM-17 shows to be significantly more toxic towards normal cells which is a disadvantage if these inorganic drugs are to be used in clinical trials. Nonetheless, PM-17 shows non-cytotoxicity at lower concentrations which paves the way for dosage-dependent studies of therapeutic anti-tumor research.

Antibacterial properties of POMs are intriguing mainly because POMs are fundamentally different than the currently available antibiotic drugs. Namely, the currently available antibiotics are typically organic molecules featuring a variety of organic functional groups which presumably interact with the biologically-relevant substrates and inhibit the biological processes necessary for bacteria to thrive. In the case of antibacterial activity, antibiotics can inhibit the growth and survival of bacterial cells by 'blocking' the sites or pathways for necessary nutrients to flow and thereby causing the cells to be nutrient deprived and eventually causing cell death. In addition, some organic-based drugs can alter the coding of the intricate cellular processes which can have a negative effect on the overall cell survival. However, due to the current overuse of antibiotics and relatively fast evolution of bacterial generations, the antibiotics are becoming less effective which requires continuous research in development of new antibacterial compounds.[10,11] Several bacteria are known to have developed antibiotic resistance to the currently available medicines causing researchers to try to stay a step ahead in the antibiotic resistance race.

Given their inorganic composition, variety of sizes, structures, and oxidation states, POMs are potential candidates to be used as alternative medicine when the currently available antibiotics fail. Bacteria such as *Staphylococcus* (S.) *aureus* are known to develop resistance to common antibiotics such as methycilin and vancomicin. A number of POMs

have been reported to be effective at killing or suppressing the bacterial growth of several bacteria. Namely, tungstates, molybdates, and vanadates are known to inhibit the growth of methycilin-resistant *Staph. Aureus* (MRSA).[12] Keggin-based polyoxometalates, $(XM_{12}O_{40})^{n-}$, have been reported to be effective in MRSA inhibition. In particular, when combined with oxacilin, a known antibiotic, Keggin-based POMs showed very high antibacterial activity which shows the synergistic effect of POMs and antibiotics to be higher than the sum of the individual effects of the two.[12] However, as is the case with antitumor and anti-viral activity of POMs, only a few reduced POMs have been explored. For that reason, this chapter is of particular interest as it presents the bacterial inhibition, among other structure and property characterizations, of the reduced polyoxometalate (r-POM) species which is of interest to the biomedical and bioinorganic researchers studying the biological properties of POMs.

Potential mechanism of bacterial inhibition by POMs has been proposed by the Yamase group.[13] In their proposed mechanism, the authors argue that the oxidized POMs are reduced physiologically by the electrons in the cellular membranes of the intricate electron transport chain. In doing so, POMs are inhibiting the vital electron transfer inside the cellular membrane which ultimately serves as the pathway for production of ATP. By inhibiting the ATP (cellular energy currency) production, POMs ultimately cause negative effects on the cell survival. The conclusions by Yamase about the mechanism of POM bacterial inhibition are supported by the color change of POMs in the presence of the living bacterial cells *vs*. no color in the presence of dead cells. The color change to dark blue indicates the reduction of POM species by the cellular membrane electron transport chain.

In addition, the authors showed SEM-EDX results illustrating concentration of POMs around the cell membrane. Yamase's results and conclusions are significant because they indicate that the POMs do not necessarily have to enter the cells in order to inhibit the growth and cause cell damage.

In addition to the thorough structural characterization of the title phases, this chapter aims to provide an insight on the effectiveness of reduced POMs in antibacterial and antitumor activity that were revealed in our collaborative studies with Prof. Jeremy Tzeng and his student Yash Raval of the Biological Sciences Department at Clemson. Some data comparing the reduced POMs with the fully oxidized ones will be discussed. Namely, this chapter will present the antibacterial effects of $Cs_6X_2Na(PMo_{12}O_{40})$ (X = Cl (**1**), ICl (**3**), Br (**3**), I (**4**)), a two-electron reduced Keggin-based 'molybdenum blue' species of POMs. Further, a preliminary antitumor study will be presented and discussed. In addition to the biomedical applications of these compounds, this chapter will heavily focus on the discussion about the high temperature, salt-inclusion synthesis of the title compounds. Detailed characterizations including structural characterizations using X-ray diffraction will be presented and the structure-property correlations will be discussed. Finally, a proposed mechanism of antibacterial effect of reduced POMs will be presented along with data supporting the proposed mechanistic claims.

Synthetic Procedure and Discussion

Single Crystal Growth of $Cs_6Cl_2Na(PMo_{12}O_{40})$ (1): The original reaction which produced **1** was targeting a salt-inclusion Keggin-based polyoxometalate, "$Cs_{12}NaCl_8(PMo_{12}O_{40})$", with the $Na@Cl_8@Cs_{12}$ (Figure 4.1), previously reported polynuclear cation.[14] $Cs_2Mo_5O_{16}$, CsCl, Na_2O, MoO_3, MoO_2, and P_4O_{10} reactants were loaded in a nitrogen purged drybox in the following molar ratios: 8:32:2:4:4:1, respectively. The reactants were ground inside the glovebox and were transferred into a silica tube attached to a glass connector to prevent exposure to air while taking the quartz tube outside of the glovebox. The glass connector and the quartz tube were connected to the vacuum line for sealing of the quartz tube under vacuum. The sealed ampoule was placed in a standard box furnace for heating. The reaction temperature was set to 500 ^oC. The heating and cooling rates were set to 2 ^oC per minute. Given that a stoichiometric high-yield of the targeted phase was originally attempted, the reaction cooling rate was set to a relatively fast rate at 2 ^oC per minute in order to synthesize polycrystalline phase. Single crystals were not targeted in this original reaction. However, upon observing the product, crystalline dark blue chunks were the major product. Product: $Cs_6Cl_2Na(PMo^{VI}_{10}Mo^{V}_{2}O_{40})$ (dark blue crystalline chunks). Yield was estimated to be around 80% based on observation of the product under the optical microscope and later confirmed by PXRD. Since the original reaction is relatively stoichiometric with respect to the formation of $Cs_6Cl_2Na(PMo_{12}O_{40})$, it is not surprising that the yield was so high. A potential product distribution could be as follows: $4 \times Cs_6Cl_2Na(PMo_{12}O_{40}) + 24 \times CsCl$ from the four moles of targeted composition "$Cs_{12}NaCl_8(PMo_{12}O_{40})$". Looking at the whole reaction product in

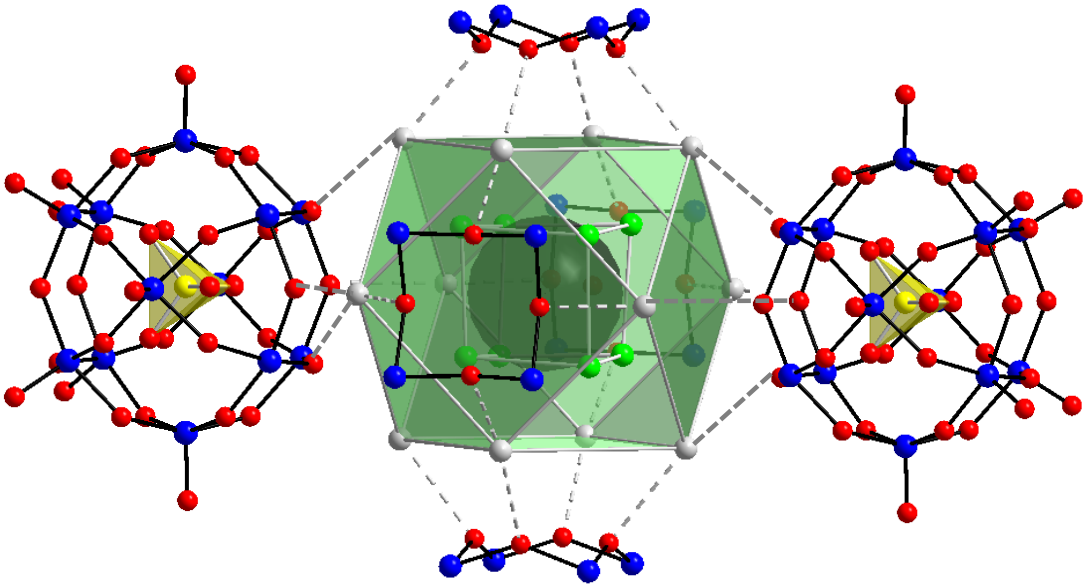

Figure 4.1: Multinuclear cation $Na@Cl_8@Cs_{12}$ (center) shown in light green polyhedral representation. Square Cs windows are shown to illustrate a possible coordination to the apical oxygen atoms on the Keggin-clusters (left and right). Similar coordination of Cs was observed in the original publication where the $Na@Cl_8@Cs_{12}$ cation was coordinated to apical oxygen atoms in the vanadium-based salt inclusion solid.[14]

Figure 4.2, both $Cs_6Cl_2Na(PMo_{12}O_{40})$ and CsCl can be identified which nicely complements the expected phase distribution. As a side note, because a cesium oxide source is unavailable, it is worth mentioning that $Cs_2Mo_5O_{16}$ precursor[15] was prepared using Cs_2CO_3 and MoO_3 in 1:5 molar ration using open air reaction conditions. Reactants were loaded into a crucible and heated to 750 ^oC at 1 ^oC/min, isothermed for 48 hrs and furnace cooled to room temperature. Detailed description of the precursor synthesis along with the PXRD graphs of the product can be found in Chapter 3.

Single Crystal Growth of $Cs_6IClNa(PMo_{12}O_{40})$ (2): Single crystals of $Cs_6IClNa(PMo_{12}O_{40})$ were serendipitously synthesized from an exploratory reaction targeting reduced polyoxomolybdates. The reaction that produced single crystals of **2** was loaded with $Cs_2Mo_5O_{16}$, As_2O_3, MoO_2, and P_4O_{10} in a 8:4:8:1 molar ratio (0.25 g). The reaction was targeting a composition that's similar to the Keggin cluster's composition ($PMo_{12}O_{40}$) with additional As_2O_3 to link the neighboring clusters and to act as a reducing agent to aid in synthesis of reduced POMs. CsCl-NaI eutectic flux (3 times the mass of reactants, 0.75 g) was ground with the oxide reactants inside a nitrogen purged drybox and sealed in a quartz tube under vacuum. The heating program consisted of heating the reactants to 680 ^oC at a rate of 1 ^oC per minute. The reaction was isothermed at 680 ^oC for three days before being cooled to 300 ^oC at a slow rate of 0.1 ^oC per minute to promote crystal growth. From 300 ^oC the reaction was furnace cooled at an approximate rate of 10 ^oC per minute. Half of the product was washed with deionized water and the product was observed under an optical microscope. The product consisted of mainly dark blue crystalline chunks which were solved as **2** using single crystal X-ray diffraction. It should

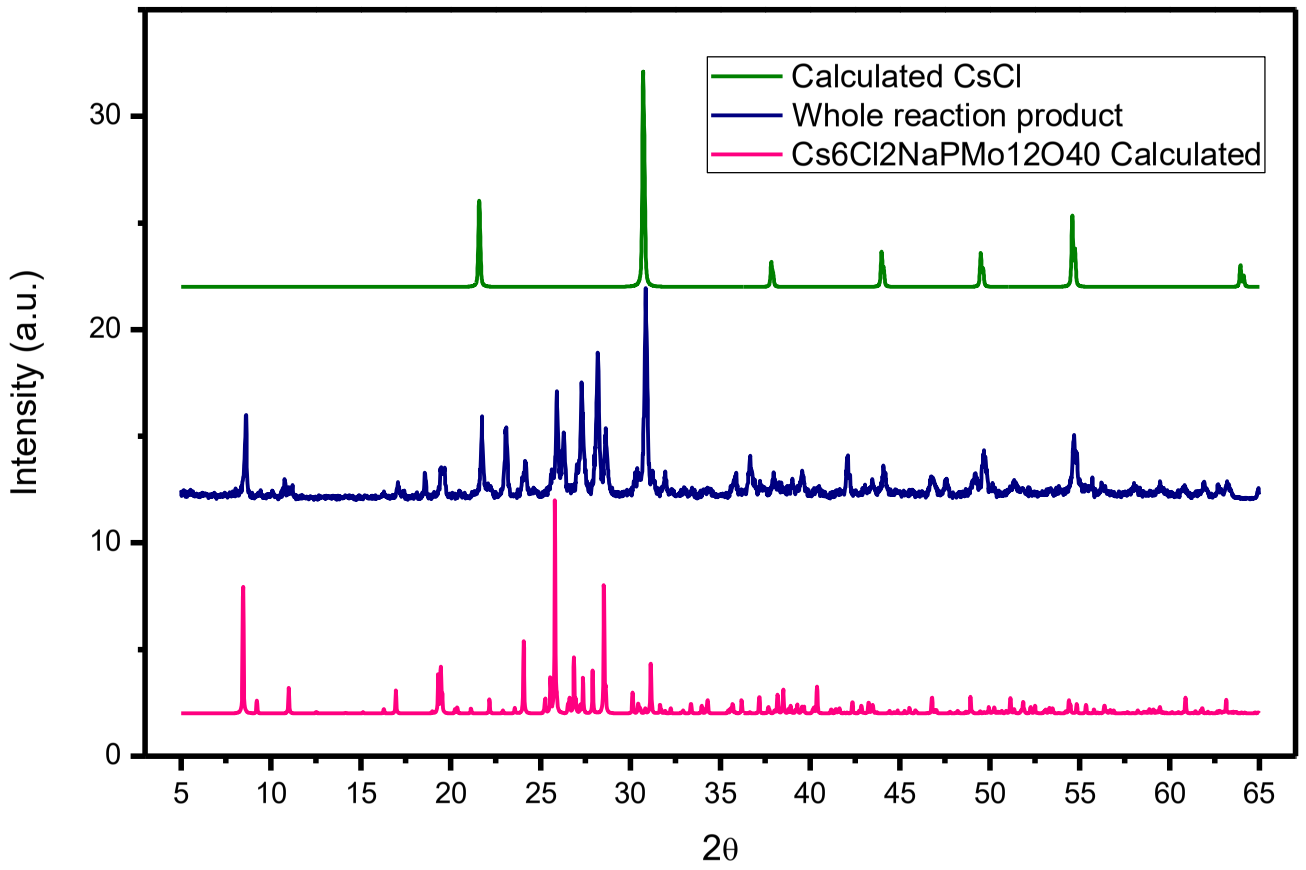

Figure 4.2: PXRD pattern of the whole reaction product which was targeting a $Cs_{12}NaCl_8(PMo_{12}O_{40})$ phase. From the graph, it can be seen that the product contained CsCl which is expected given that $Cs_6Cl_2Na(PMo_{12}O_{40})$ was formed in high yield.

be noted that the title compounds are soluble in water which slightly complicated the isolation and separation of the product from the excess salt flux. However, the title phase is not as soluble in water as the salts (*e.g*. CsCl) used in single crystal synthesis which allowed for quick washing of the product to separate the salt flux from the desired product. When washing the overall reaction, a blue color on the filter paper was able to be seen after washing possibly due to the dissolving of compound **2**. However, blue crystalline chunks were still able to be retrieved for SXRD analysis.

Single Crystal Growth of $Cs_6Br_2Na(PMo_{12}O_{40})$ (3) and $Cs_6I_2Na(PMo_{12}O_{40})$ (4): Single crystal growth of **3** and **4** was attempted by using similar reaction conditions as for **1** and **2** where the salt was replaced by CsBr and NaBr to target the composition of **3** and CsI and NaI for **4**. However, the reactions resulted in dark blue polycrystalline solids which matched the calculated powder X-ray diffraction pattern of **1** (see Figure 4.3).

Stoichiometric Yield Synthesis of 1-4: For the high-yield syntheses, solid state or "shake and bake" method with intermittent grindings was employed. The high yield synthesis of $Cs_6X_2Na(PMo_{12}O_{40})$ (X_2 = Cl_2, ICl, Br_2, I_2) required the use of cesium oxide source in the form of Cs_2MoO_4 to balance the charge since a cesium oxide source was not readily available.[16] This precursor was synthesized using the solid state reaction approach from Cs_2CO_3 and MoO_3 starting materials with the molar ratio of Cs_2CO_3 to MoO_3 being 1:1. Reaction was done in open air according to the reported synthetic procedure at 950 ^oC as discussed in Chapter 3. After the successful synthesis of the Cs-Mo-O precursor, stoichiometric reactions targeting the title compounds were then able to be loaded. As an example, Cs_2MoO_4, CsCl, NaCl, MoO_3, MoO_2, and P_4O_{10} were loaded in molar ratios of

10:4:4:34:4:1, respectively, to target $Cs_6Cl_2Na(PMo_{12}O_{40})$ (**1**). The reaction was ground in a nitrogen-purged drybox and the resulting homogeneous mixture was transferred to a fused silica ampoule. The ampoule was then sealed under vacuum and was heated to 500 ^oC at a rate of 2 ^oC per minute. It was then isothermed at 500 ^oC for 48 hours and cooled back to room temperature at a rate of 2 ^oC per minute. Similar reactions for $Cs_6IClNa(PMo_{12}O_{40})$ (**2**), $Cs_6Br_2Na(PMo_{12}O_{40})$ (**3**) and $Cs_6I_2Na(PMo_{12}O_{40})$ (**4**) were carried out. The only difference between the starting materials of **1**~**4** was the use of corresponding salts, *i.e.* CsCl and NaCl for **1**; CsCl and NaI for **2**; CsBr and NaBr for **3**; and CsI and NaI for **4**. Figure 4.3 shows the calculated powder pattern (pink color) obtained from the single crystal X-ray diffraction solution of **1** along with the observed powder patterns from the stoichiometric high yield reactions targeting **1**~**4** as described above. It is important to note that the observed powder patterns from Figure 4.3 are a result of products that were reground and reheated. As is the case with most solid state reactions, regrinding and reheating allowed for secondary intermixing of particles which can promote the reaction toward completion.

Looking at Figure 4.3, one can see that the observed powder patterns match closely to the calculated powder pattern of **1**. This indicates that the attempted high yield synthesis reactions were successful for **1**~**4**.

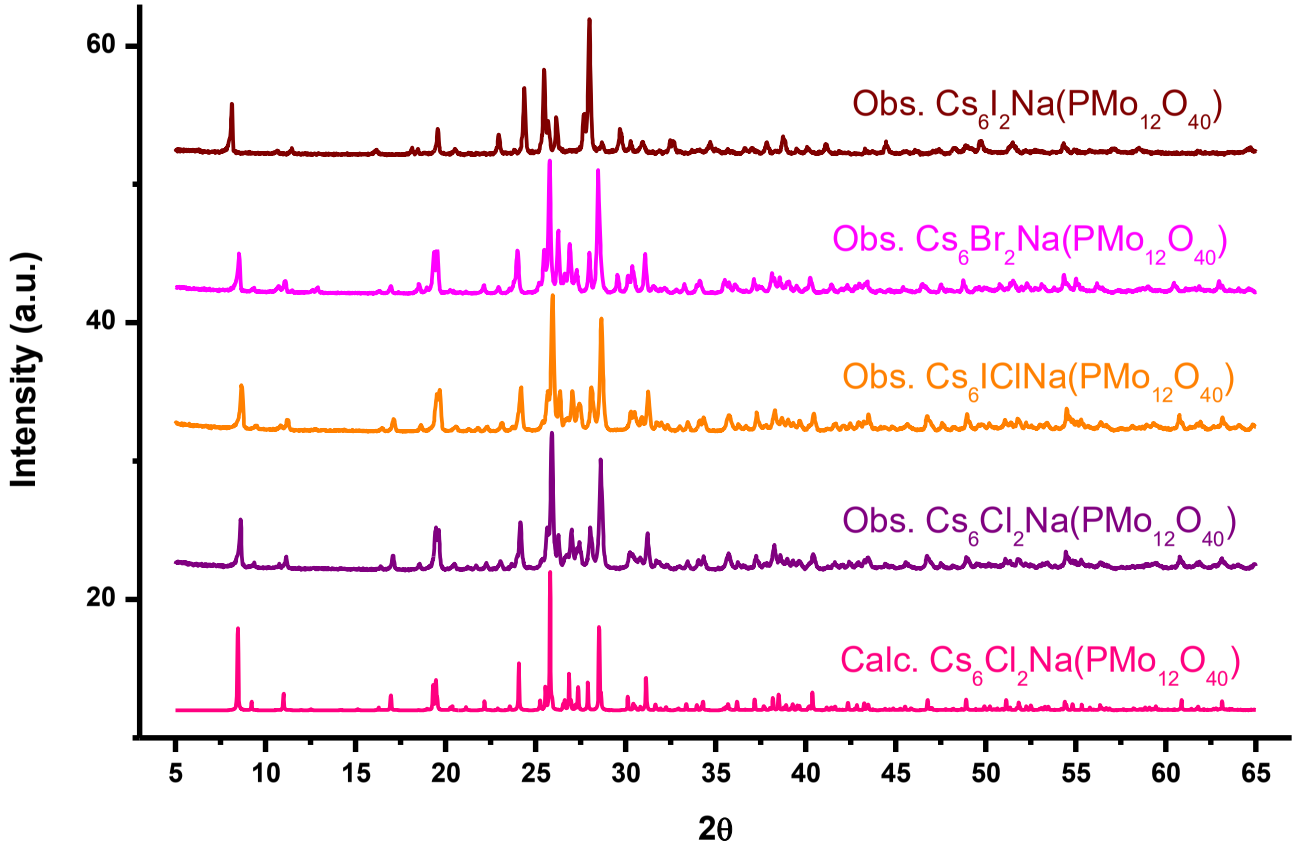

Figure 4.3: PXRD pattern of a high yield synthesis attempt of $Cs_6X_2Na(PMo_{12}O_{40})$ (X_2 = Cl_2, ICl, Br_2, I_2) **1**-**4** showing the successful formation of the three phases. The calculated pattern in red is based on the single crystal solution of $Cs_6Cl_2Na(PMo_{12}O_{40})$ compound.

Characterization

Elemental Analysis (EDS): Energy dispersive spectroscopy EDS was used to qualitatively confirm the presence of elements comprised in the compositions of **1~4**. Elemental analysis was performed on polycrystalline products as well as the single crystals used for the SXRD structure determination of **1~4**.

Powder X–ray Diffraction (PXRD): PXRD was used to confirm the phase formations of **1~4** observed in the various synthetic techniques mentioned in the synthetic procedure section of this chapter. Powder diffraction patterns for a select few synthetic approaches can be seen in Figures 4.2 and 4.3. The powder X–ray diffraction data were collected at room temperature using Cu Kα radiation in the 2θ range of 5–65° with a step size of 0.02° and a scan rate of 0.25°/min.

Single Crystal X–ray Diffraction (SXRD): Dark blue, chunk crystals of **1~2** were selected under an optical microscope equipped with a polarizing light attachment. SXRD data were collected on these single crystals at room temperature using Mo Kα radiation (λ = 0.71073 Å) produced by a graphite monochromator. The crystallographic data can be seen in Table 4.1. The atomic coordinates, selected bond distances, anisotropic thermal parameters and bond valence sums calculations can be seen in Tables 4.2~4.6.

Magnetic Susceptibility: Magnetic susceptibility measurements were performed on $Cs_6Cl_2Na(PMo_{12}O_{40})$ polycrystalline sample using a Quantum Design VSM magnetometer. Temperature–dependent magnetic susceptibility measurements of $Cs_6Cl_2Na(PMo_{12}O_{40})$ were performed on ground powder sample. Quantity of sample used for measurements consisted of 34.0 mg of as-prepared powder for $Cs_6Cl_2Na(PMo_{12}O_{40})$.

Table 4.1: Crystallographic data table for compounds **1~2**.

	1	**2**
empirical formula	$Cs_6Cl_2NaPMo_{12}O_{40}$	$Cs_6IClNaPMo_{12}O_{40}$
formula wt, g/mol	2713.57	2805.02
crystal system	tetragonal	tetragonal
space group	*P* 4/ncc (no. 130)	*P* 4/ncc (no. 130)
a , Å	14.780(2)	15.026(2)
c , Å	19.172(4)	19.145(4)
volume, $Å^3$	4188(12)	4322.57(12)
Z	4	4
D_{calc}, g/cm^3	4.303	4.310
abs coeff	8.489	9.514
crystal size, mm	0.16 x 0.14 x 0.13	0.17 x 0.15 x 0.12
theta range, deg	1.95 - 25.05	2.52 - 25.05
relns collected	32592	34267
indep refIns	1863	1918
R (int)	0.156	0.173
obsd ($I > 2s(I)$)	1802	1675
goodness-of-fit on F^2	1.190	1.118
$R_1[I > 2s(I)]$[a]	0.072	0.061
wR_2 (all data)[b]	0.073	0.067

[a] $R = \Sigma||F_o| - |F_c||/\Sigma|F_o|$. [b] $R_w = [\Sigma w(F_o^2 - F_c^2)^2/\Sigma w(F_o^2)^2]^{1/2}$

Table 4.2: Atomic positions table for **1~2**.

1						**2**					
Atom	Wyckoff	sof	*x*	*y*	*z*	Atom	Wyckoff	sof	x	y	z
Mo(1)	16g	1	0.17826 (11)	0.40507 (10)	0.43921 (8)	Mo(1)	16g	1	0.18362 (7)	0.40588 (6)	0.44020 (5)
Mo(2)	16g	1	0.09461 (11)	0.32140 (11)	0.20278 (7)	Mo(2)	16g	1	0.09450 (6)	0.31554 (7)	0.20378 (5)
Mo(3)	16g	1	0.16694 (11)	0.47470 (11)	0.07056 (8)	Mo(3)	16g	1	0.16143 (7)	0.46891 (7)	0.07155 (5)
P	4c	1	1/4	1/4	0.5714 (4)	P	4c	1	1/4	1/4	0.5723 (2)
Na	4c	1	1/4	1/4	0.3205 (8)	Na	4c	1	1/4	1/4	0.3322 (10)
Cs(1)	8f	1	0.09081 (9)	0.59081 (9)	1/4	Cs(1)	8f	1	0.07887 (6)	0.57887 (6)	1/4
Cs(2)	16g	1	0.36174 (13)	0.61016 (12)	0.39269 (8)	Cs(2)	16g	1	0.36961 (8)	0.61154 (8)	0.39828 (6)
Cl(1)	4a	1	1/4	3/4	1/4	I	4a	1	1/4	3/4	1/4
Cl(2)	4b	1	1/4	3/4	1/2	Cl	4b	1	1/4	3/4	1/2
O(1)	16g	1	0.3538 (11)	0.4787 (9)	0.2626 (7)	O(1)	16g	1	0.3470 (8)	0.4770 (6)	0.2644 (5)
O(2)	16g	1	0.1331 (10)	0.5810 (9)	0.0695 (8)	O(2)	16g	1	0.1228 (7)	0.5706 (7)	0.0720 (6)
O(3)	16g	1	0.1453 (13)	0.4735 (10)	0.3776 (6)	O(3)	16g	1	0.1550 (9)	0.4739 (7)	0.3780 (5)
O(4)	16g	1	0.0944 (11)	0.4220 (14)	0.0019 (8)	O(4)	16g	1	0.0900 (7)	0.4158 (8)	0.0013 (6)
O(5)	16g	1	0.0916 (10)	0.4227 (12)	0.1404 (7)	O(5)	16g	1	0.0892 (6)	0.4134 (8)	0.1412 (6)
O(6)	16g	1	0.2589 (12)	0.4807 (13)	0.1390 (8)	O(6)	16g	1	0.2524 (7)	0.4793 (10)	0.1415 (7)
O(7)	16g	1	0.1305 (13)	0.2917 (10)	0.4049 (8)	O(7)	16g	1	0.1376 (9)	0.2962 (7)	0.4060 (7)
O(8)	16g	1	0.1300 (13)	0.2065 (10)	0.2382 (8)	O(8)	16g	1	0.1359 (8)	0.2021 (7)	0.2382 (7)
O(9)	16g	1	0.2612 (11)	0.4831 (12)	0.0017 (9)	O(9)	16g	1	0.2523 (7)	0.4798 (8)	0.0020 (7)
O(10)	16g	0.5	0.1702 (13)	0.2792 (14)	0.6184 (9)	O(10)	16g	0.5	0.1721 (8)	0.2812 (9)	0.6187 (8)
O(11)	16g	0.5	0.1679 (13)	0.2806 (13)	0.5248 (10)	O(11)	16g	0.5	0.1726 (8)	0.2806 (9)	0.5262 (8)

Table 4.3: Selected bond distances for compounds **1~2**.

		$Cs_6Cl_2Na(PMo_{12}O_{40})$ (1)	$Cs_6IClNa(PMo_{12}O_{40})$ (2)
Mo(1)-O(3)		1.629 (12)	1.628(9)
Mo(1)-O(7)		1.933 (15)	1.904(10)
Mo(1)-O(7)^{i}		1.877 (15)	1.928(10)
Mo(1)-O(4)^{ii}		1.908 (16)	1.898(10)
Mo(1)-O(9)^{iii}		1.888 (15)	1.887(10)
Mo(1)-O(11)^{iii}	x 0.5	2.470(19)	2.495(14)
Mo(1)-O(10)	x 0.5	2.479(19)	2.506(14)
Mo(2)-O(1)^{iv}		1.648 (12)	1.651(8)
Mo(2)-O(6)^{v}		1.894 (16)	1.885(10)
Mo(2)-O(8)		1.901 (15)	1.931(10)
Mo(2)-O(8)^{ii}		1.927 (15)i	1.892(10)
Mo(2)-O(5)		1.917 (15)	1.899(10)
Mo(2)-O(10)^{v}	x 0.5	2.465(19)	2.475(14)
Mo(2)-O(10)^{vi}	x 0.5	2.472(19)	2.485(14)
Mo(3)-O(2)		1.649 (13)	1.634(10)
Mo(3)-O(6)		1.891 (16)	1.920(11)
Mo(3)-O(9)		1.923 (15)	1.914(11)
Mo(3)-O(5)		1.904 (15)	1.911(10)
Mo(3)-O(4)		1.867 (16)	1.897(11)
Mo(3)-O(11)^{vi}	x 0.5	2.411(19)	2.456(13)
Mo(3)-O(10)^{vi}	x 0.5	2.462(19)	2.459(13)

Symmetry codes: i) 0.5-y, x, z; ii)0.5-y, 0.5-x; iii) 0.5-x, y, -0.5+z; iv)y, 0.5-x, z; v)0.5-y, x, z

Table 4.3: Selected bond distances and angles for compounds **1~2** cont…

	1	**2**
Cs(1)-O(3)	3.105(13)	3.131(10)
Cs(1)-O(3)^{xi}	3.105(13)	3.131(10)
Cs(1)-O(5)	3.254(16)	3.247(12)
Cs(1)-O(5)^{xi}	3.254(16)	3.247(12)
Cs(1)-O(2)^{xi}	3.520(15)	3.473(11)
Cs(1)-O(2)	3.520(15)	3.473(11)
Cs(1)-O(1)^{vii}	3.659(16)	3.594(12)
Cs(1)-O(1)^{iv}	3.659(16)	3.594(12)
Cs(1)-X*	3.327(1)	3.637(1)
Cs(1)-O(6)^{xi}	3.654(17)	3.654(12)
Cs(1)-O(6)	3.654(17)	3.654(12)
Cs(1)-O(8)^{xii}	3.691(18)	3.727(12)

*X = Cl(1) for **1** and X = I for **2**

Symmetry codes: (iv) 0.5-y, x, z; (vii) -0.5+x, 1-y, 0.5-z; (xi) -0.5+y, 0.5+x, 0.5-z; (xii) -x, 0.5+y, 0.5-z;

Cs(2)-O(6)^{ix}	3.088(19)	3.149(13)
Cs(2)-O(1)	3.164(13)	3.282(9)
Cs(2)-O(9)^{ii}	3.346(17)	3.349(12)
Cs(2)-O(2)^{ii}	3.418(15)	3.384(12)
Cs(2)-O(5)^{xiii}	3.490(15)	3.406(9)
Cs(2)-O(4)^{ii}	3.541(19)	3.593(12)
Cs(2)-O(9)^{ix}	3.602(17)	3.599(12)
Cs(2)-O(7)^{i}	3.712(19)	3.906(1)
Cs(2)-O(3)	3.794(18)	3.851(12)
Cs(2)-X**	3.351(2)	3.369(1)
Cs(2)-X***	3.806(2)	3.952(1)

** X = Cl(2) for **1** and X = Cl for **2** *** X = Cl(1) for **1** and X = I for **2**

Symmetry codes: (i) 0.5-x, y, 0.5+z; (ii) 0.5-y, 0.5-x, 0.5+z; (iv) 0.5-y, x, z; (xiii) 0.5+x, 1-y, 0.5-z

Na-O(7) x 4	2.473(20)	2.309(18)
Na-O(8) x 4	2.459(20)	2.588(18)

P-O(10) x 4	1.546(19)	1.542(14)
P-O(11) x 4	1.573(20)	1.531(14)

Table 4.4: Anisotropic thermal parameters ($Å^2$) for **1**.

Atom	U11	U22	U33	U12	U13	U23
Mo1	0.0421(9)	0.0311(8)	0.0246(7)	0.0047(6)	-0.0057(6)	0.0017(6)
Mo2	0.0342(8)	0.0417(9)	0.0233(7)	0.0067(7)	0.0054(6)	0.0023(6)
Mo3	0.0400(9)	0.0306(8)	0.0368(9)	0.0061(7)	0.0045(7)	0.0023(7)
P	0.025(2)	0.025(2)	0.019(4)	0.0000	0.0000	0.0000
Na	0.055(6)	0.055(6)	0.045(9)	0.0000	0.0000	0.0000
Cs1	0.0540(7)	0.0540(7)	0.0327(8)	-0.0035(8)	-0.0061(6)	0.0061(6)
Cs2	0.0873(12)	0.0676(10)	0.0491(8)	-0.0249(9)	0.0147(8)	-0.0076(7)
Cl1	0.059(4)	0.059(4)	0.107(10)	-0.018(6)	0.0000	0.0000
Cl2	0.090(7)	0.090(7)	0.117(13)	0.0000	0.0000	0.0000
O1	0.100(12)	0.035(7)	0.031(7)	-0.020(8)	-0.001(7)	-0.019(6)
O2	0.056(9)	0.028(7)	0.079(11)	0.017(6)	0.018(8)	0.007(7)
O3	0.124(15)	0.049(9)	0.021(6)	0.045(9)	-0.003(8)	0.007(6)
O4	0.057(10)	0.123(16)	0.058(9)	-0.017(10)	0.031(8)	-0.051(11)
O5	0.051(9)	0.090(12)	0.052(8)	-0.017(8)	-0.025(8)	0.035(9)
O6	0.063(10)	0.105(14)	0.060(9)	-0.03(1)	-0.016(9)	0.052(10)
O7	0.106(14)	0.049(9)	0.063(10)	-0.030(9)	0.05(1)	-0.022(8)
O8	0.103(13)	0.051(9)	0.050(9)	0.024(9)	-0.040(9)	-0.014(7)
O9	0.046(9)	0.107(14)	0.064(9)	-0.024(9)	0.018(8)	-0.048(10)
O10	0.021(11)	0.031(12)	0.013(9)	-0.002(8)	-0.007(8)	-0.008(8)
O11	0.013(10)	0.022(10)	0.024(10)	0.000(8)	0.006(8)	-0.007(8)

Table 4.5: Anisotropic thermal parameters (Å^2) for **2**.

Atom	U11	U22	U33	U12	U13	U23
Mo1	0.0438(6)	0.0315(6)	0.0250(6)	0.0037(4)	-0.0052(4)	0.0022(3)
Mo2	0.0340(6)	0.0430(6)	0.0236(6)	0.0068(4)	0.0046(4)	0.0004(4)
Mo3	0.0378(6)	0.0311(6)	0.0364(6)	0.0064(4)	0.0041(4)	0.0025(4)
P	0.0233(14)	0.0233(14)	0.015(2)	0.0000	0.0000	0.0000
Na	0.011(2)	0.011(2)	0.24(2)	0.0000	0.0000	0.0000
Cs1	0.0573(5)	0.0573(5)	0.0366(7)	0.0032(5)	-0.0043(3)	0.0043(3)
Cs2	0.0771(7)	0.0753(7)	0.0469(7)	-0.0183(5)	0.0099(5)	0.0040(4)
I	0.0683(9)	0.0683(9)	0.0840(17)	-0.0076(11)	0.0000	0.0000
Cl	0.051(2)	0.051(2)	0.055(4)	0.0000	0.0000	0.0000
O1	0.082(7)	0.039(4)	0.033(5)	-0.016(4)	0.000(4)	-0.016(4)
O2	0.060(6)	0.041(5)	0.075(8)	0.013(5)	0.009(5)	0.000(5)
O3	0.106(8)	0.051(5)	0.027(5)	0.030(5)	-0.002(5)	0.004(4)
O4	0.060(6)	0.095(9)	0.060(7)	-0.024(6)	0.029(5)	-0.037(6)
O5	0.041(5)	0.097(8)	0.069(7)	-0.022(5)	-0.019(5)	0.045(6)
O6	0.051(6)	0.130(11)	0.088(9)	-0.042(7)	-0.023(6)	0.088(9)
O7	0.107(10)	0.042(5)	0.084(9)	-0.023(6)	0.064(8)	-0.024(5)
O8	0.084(8)	0.049(5)	0.069(7)	0.020(6)	-0.044(6)	-0.020(5)
O9	0.043(5)	0.097(8)	0.077(7)	-0.025(6)	0.017(5)	-0.054(7)
O10	0.018(6)	0.037(7)	0.030(7)	0.008(5)	0.002(5)	0.001(6)
O11	0.019(6)	0.033(7)	0.029(7)	0.008(5)	-0.004(5)	-0.002(6)

Table 4.6: Bond valence sums contributions for Mo atoms in compounds **1~2**.

1								
Mo1 -O distances	5+	6+	Mo2 - O distances	5+	6+	Mo3 - O distances	5+	6+
1.629	1.960056	2.119863	1.648	1.861945	2.013753	1.649	1.856919	2.008317
1.933	0.861872	0.932142	1.894	0.957678	1.03576	1.891	0.965475	1.044192
1.877	1.002706	1.084459	1.901	0.93973	1.016348	1.923	0.885483	0.957678
1.908	0.922119	0.997301	1.927	0.875962	0.947381	1.904	0.932142	1.008141
1.888	0.973335	1.052693	1.917	0.89996	0.973335	1.867	1.030176	1.114168
2.486	0.193352	0.209116	2.476	0.198649	0.214845	2.414	0.234887	0.254038
BVS	5.91344	6.395573		5.733925	6.201422		5.905083	6.386535
2								
Mo1 -O distances	5+	6+	Mo2 - O distances	5+	6+	Mo3 - O distances	5+	6+
1.628	1.96536	2.1256	1.651	1.846909	1.997491	1.634	1.933747	2.091409
1.904	0.932142	1.008141	1.885	0.981259	1.061263	1.92	0.892692	0.965475
1.928	0.873598	0.944824	1.931	0.866543	0.937194	1.914	0.907286	0.981259
1.898	0.947381	1.024623	1.892	0.962869	1.041374	1.911	0.914673	0.989247
1.887	0.975969	1.055542	1.899	0.944824	1.021857	1.897	0.949945	1.027396
2.486	0.193352	0.209116	2.476	0.198649	0.214845	2.414	0.234887	0.254038
BVS	5.887802	6.367845		5.801053	6.274024		5.83323	6.308824

The temperature–dependent studies of magnetic susceptibility were measured in applied fields of 1000 Oe at temperatures ranging from 10–300 K.

Thermal Analysis, TGA and DSC: DSC/TGA measurements were done on ground powders (~10 mg) using a SDT Q600 TA Instruments calorimeter. A 110 μL alumina sample and reference pans were used for data collection. The heating profile for the measurement included a heating rate of 20 °C/min from room temperature to 700 °C, followed by a return cooling rate of 20 °C/min in the presence of 75 mL/min nitrogen gas flow.

UV-Vis Spectroscopy of Dissolved Compounds 1~3: UV-Vis spectroscopy was done using a PC-controlled Shimadzu UV-3101 UV-Vis-NIR instrument in the range of 250-800 nm using plastic square cuvettes for data collection. The blank sample containing deionized water was used to collect the baseline before measuring the dissolved title compounds **1**~**3**. The UV-vis study aimed to shed light on the stability of the title compounds in aqueous solutions. Initially, fresh 0.75 mM solutions of **1**~**3** were prepared and attempts to collect data of these concentrated solutions failed due to the high absorbance of the dark blue solutions. By diluting the solutions by a factor of 50, data was able to be collected. UV-vis of the freshly prepared, diluted samples of **1**~**3** were collected and left in the cuvettes with parafilm cover to prevent evaporation of deionized water. Subsequently, data was collected using the following schedule: 1 day old, 2 day old, 3 day old, 7 day old, 14 day old, 17 day old, 21 day old and 28 day old solutions of **1**~**3**. A noticeable change in color of the initial dark blue solution was observed after day 7 after which the solution progressively turned to pale yellow. In addition, a small amount of

yellow precipitate was seen on the bottom of the square plastic cuvettes. The yellow precipitate was identified as the fully oxidized Keggin-based solid $Cs_3(PMo_{12}O_{40})$.

Antibacterial Testing: Antibacterial tests were done in collaboration with professor Tzueng-Rong Tzeng and his PhD student Yash Raval from the Department of Biological Sciences at Clemson University. A quantitative macrobroth dilution tests based on The Clinical Laboratory and Standards Institute (CLSI)[17] standard procedures were used for the determination of minimum inhibitory concentrations (MICs) for compounds **1**~**3**. The bacterial cultures SA1199 (wild strain) and SA1199B (mutant strain overexpressing MDR pump responsible for resistance to antibiotics) were grown in MH-II broth containing nutrients for bacteria to grow. The same broth was used in the two-fold serial dilution assay. The concentration of the highest dilution of compounds **1**~**3** in MH-II broth that inhibits the growth of bacteria is considered as MIC. The final concentration of the bacterial strains after dilution was 5×10^5 CFU/ml in each tube. CFU or colony forming units is a measure of concentration of viable bacterial cells that are able to undergo cell division and aims to distinguish between the colonies formed from, for example, one bacterial cell. The resulting tubes were incubated at 37 ^{o} C for 12-16 hours. It is important to mention that the polycrystalline powders of the title compounds were used to prepare solutions which were filter-sterilized using a 0.22 μm syringe filter. The experiments of MIC evaluations were repeated three times and similar results were obtained as further discussed below. Table 4.7 shows the MIC values for compounds **1**~**3**. Each column in Table 4.7 corresponds to a tube with particular concentration of the title compounds, nutrient broth and the bacterial strains. 5^{th} tube was one of the controls which contained only the nutrients broth and the

Table 4.7: Results of the macrobroth dilution assay showing MIC values for compounds $Cs_6Cl_2Na(PMo_{12}O_{40})$ **(1)**, $Cs_6IClNa(PMo_{12}O_{40})$ **(2)** and $Cs_6Br_2Na(PMo_{12}O_{40})$ **(3)**.

SA1199 Strain

Compound	1st tube concentration	2nd tube concentration	3rd tube concentration	4th tube concentration	5th tube concentration	6th tube concentration
Cs_6Cl_2 (1)	1017.59 ug/ml No pellet seen	508.79 ug/ml No pellet seen	**254.39 ug/ml** **No pellet seen**	127.19 ug/ml Visible pellet	0 ug/ml Visible pellet	Only broth No pellet seen
Cs_6Br_2 (3)	1050.92 ug/ml No pellet seen	**525.46 ug/ml** **No pellet seen**	262.73 ug/ml Visible pellet	131.36 ug/ml Visible pellet	0 ug/ml Visible pellet	Only broth No pellet seen
Cs_6ICl (2)	1051.88 ug/ml No pellet seen	525.94 ug/ml No pellet seen	**262.97 ug/ml** **No pellet seen**	131.48 ug/ml Visible pellet	0 ug/ml Visible pellet	Only broth No pellet seen

SA1199B Strain

Compound	1st tube concentration	2nd tube concentration	3rd tube concentration	4th tube concentration	5th tube concentration	6th tube concentration
Cs_6Cl_2 (1)	1017.59 ug/ml No pellet seen	508.79 ug/ml No pellet seen	**254.39 ug/ml** **No pellet seen**	127.19 ug/ml Visible pellet	0 ug/ml Visible pellet	Only broth No pellet seen
Cs_6Br_2 (3)	1050.92 ug/ml No pellet seen	**525.46 ug/ml** **No pellet seen**	262.73 ug/ml Visible pellet	131.36 ug/ml Visible pellet	0 ug/ml Visible pellet	Only broth No pellet seen
Cs_6ICl (2)	1051.88 ug/ml No pellet seen	525.94 ug/ml No pellet seen	**262.97 ug/ml** **No pellet seen**	131.48 ug/ml Visible pellet	0 ug/ml Visible pellet	Only broth No pellet seen

bacterial strains while the 6th tube contained only the nutrients broth without bacterial strains. Tubes 1 through 4 were the testing tubes which contained the nutrients, bacterial strains and different concentrations of compounds **1**~**3** which were serially diluted from a stock solution. The results were repeated in triplicates and show that the title compounds were equally effective at inhibiting bacterial growth for both the wild strain, SA1199 and the mutant strain overexpressing the MDR pump, 1199B.

ATP Assay Study: SA1199 and SA1199B cells were seeded into each well, allowed to adhere and were lysed, exposed to the ATP substrate solution based on the lucifer/luciferase ATP reaction, known to occur in fireflies, in which the signal was measured using a luminescence counter. Mean and standard deviation were plotted as bar graphs for SA1199 and SA1199B strains being exposed to $Cs_6Cl_2Na(PMo_{12}O_{40})$ (**1**) and $Cs_6IClNa(PMo_{12}O_{40})$ (**2**) compounds.

Cyclic Voltammetry: Measurements were performed using a CH Instruments 660B Electrochemical Workstation. Dimethyl formamide (DMF) was purchased from Alfa Aesar. DMF was purified and deoxygenated using a MBraun solvent purification system. Deionized water was obtained from Millipore purification system (18.25 MΩ.cm-1). All experiments were performed in air-free, nitrogen atmosphere using a standard three-electrode cell with platinum as the working electrode, tungsten being the counter electrode and silver wire as the pseudo-reference. The electrolytes, KCl and hexafluorophosphate (Bu_4NPF_6), were purified by recrystallization and were prepared at the concentration of 0.10 M in H_2O or anhydrous DMF, respectively. Compounds **1** and **2** were prepared at 1.0 mM concentrations in water and the cation-substituted $TBA_4(PMo_{12}O_{40})$ (**4**) (TBA =

tetrabutylammonium) compound was prepared in DMF. All potentials were scanned with a scan rate of 100 mVs^{-1} and were reported relative to Ag/AgCl.

Results and Discussion

A series of new salt-inclusion polyoxometalate compounds has been discovered using molten-salt synthetic approach. The title compounds, $Cs_6X_2Na(PMo_{12}O_{40})$, where X_2 can be Cl_2, ICl, Br_2, and I_2, crystallize in the tetragonal space group, *P* 4/*ncc* (no.130), *Z* = 4. Figure 4.4 shows the perspective view in the ab plane of the cluster surrounded by a salt lattice. In addition, a dark blue solution of 1 is shown in Figure 4.4. This series of compounds is structurally related to the one-electron reduced, $Cs_6I_3Na(PMo_{12}O_{40})$ compound, discussed in Chapter 3. Even though the title compounds **1**~**4** crystallize in the same space group as the one-electron reduced compound described in Chapter 3, the differences in the incorporated salt chains and consequently the oxidation state of the cluster ($PMo_{12}O_{40}$) give these two-electron reduced polyoxomolybdates unique properties which will be discussed in greater detail throughout this chapter. The crystallographic data is presented in Table 4.1 and it includes the unit cell dimensions and other relevant crystallographic information of the refined structure solutions for selected single crystals. Tables 4.2, 4.3, 4.4 and 4.5 provide the atomic positions parameters, selected bond distances and anisotropic displacement parameters for compounds **1** and **2**. Given that the Br and I derivatives, $Cs_6Br_2Na(PMo_{12}O_{40})$ (**3**) and $Cs_6I_2Na(PMo_{12}O_{40})$ (**4**), were unable to be synthesized in the form of single crystals, the single crystal structure of **3** and **4** will not be discussed in detail. However, the observed X-ray powder patterns match up with the calculated pattern of **1** and it should be sufficient data to support the formation of **3** and **4**. In addition, refined cell parameters from the powder X-ray diffraction are shown in Figure 4.5 to show expected unit cell parameters for compounds **1**~**4**.

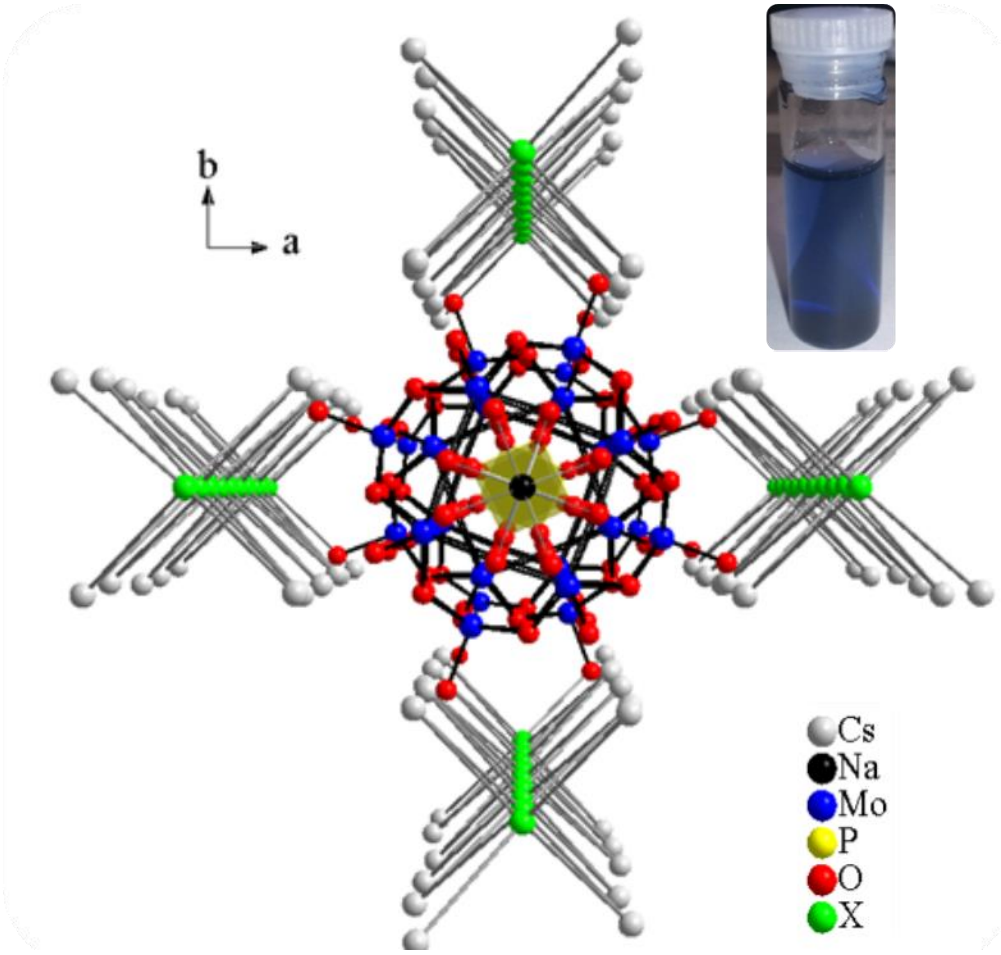

Figure 4.4: Perspective view along the *c*–axis of $Cs_6X_2Na(PMo_{12}O_{40})$ showing the 4–fold symmetry around the Keggin-based cluster, $(PMo_{12}O_{40})^{5-}$. The $[Cs_6X_2]_\infty$ chains extend along the *c*–axis and are templating the pockets for infinite chains comprised of $[-(PMo_{12}O_{40})\text{-}Na\text{-}]_\infty$ in the *ab* plane. The small figure in the right top corner shows a 0.75 mM solution of **1** in water.

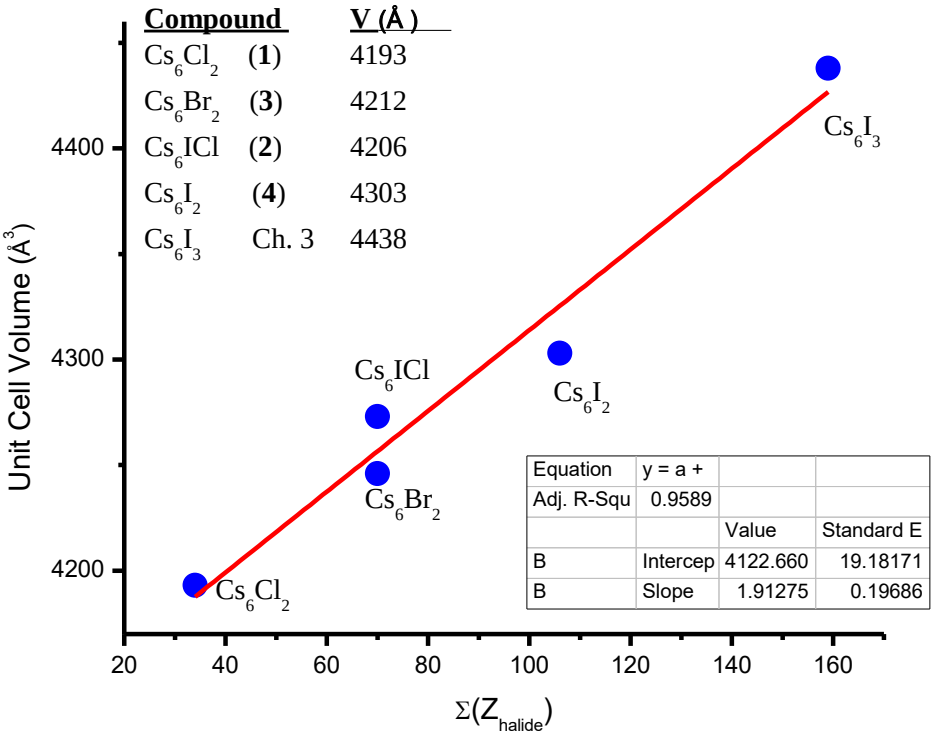

Figure 4.5: Plot of the unit cell volume vs. the sum of atomic numbers for the halide anions (*e.g.* for $Cs_6Cl_2Na(PMo_{12}O_{40})$ (**1**), the sum of the atomic number for two chlorides is 34 (x axis value) and its refined unit cell volume 4193 Å. These volumes were obtained by profile refining the PXRD patterns using *FullProf* (see Chapter 2). The data show expected linear trend with increasing atomic number of the halide elements.

$Cs_6X_2Na(PMo_{12}O_{40})$ compounds, where X_2 = Cl_2, ICl, Br_2, and I_2, consist of the α-Keggin anionic clusters which in general have the formula $(XM_{12}O_{40})^{n-}$, where X is the heteroatom and M is the early transition metal such as Mo. In the case of the title compounds, the Keggin cluster exhibits a pseudo D_4h point group symmetry (as shown for compound in Figure 3.6 in Chapter 3) and is composed of three crystallographically unique molybdenum atoms with a multiplicity of four to give a total number of twelve Mo atoms per formula unit. As is the case with the Keggin cluster described in Chapter 3, the clusters in compounds **1**~**3** can be decomposed into three parts, based on the number of crystallographically unique Mo atoms, as shown in Figure 3.7. Again, it is worth mentioning that the cluster itself is isostructural with the one described in Chapter 3. The main difference arises when different halides and different relative compositions of the halide salts are incorporated which consequently changes the oxidation state of the Mo atoms in the Keggin cluster due to the difference in the number of incorporated halide atoms per formula unit. In order to reduce the amount of redundant information about the structures for otherwise isostructural Keggin clusters in compounds **1**~**4**, the following section will focus the discussion only on the structure of one of the title compounds. The reader is invited to observe the subtle differences in unit cell parameters, atomic positions and selected bond distances for compounds **1** and **2** in Tables 4.1, 4.2 and 4.3, respectively. $Cs_6IClNa(PMo_{12}O_{40})$ (**2**) was chosen to describe the structure in detail. While the salt chain in the title compounds is composed of different halide anions, the overall structure and atomic positions are still very similar to one another. It is expected that from the discussion

of the structure of **2**, the reader should have a clear understanding of the structures as well as the structural differences between the title compounds, **1**~**4**, presented herein.

The three crystallographically unique sites of Mo(1), Mo(2) and Mo(3) along with the oxygen atoms, comprise the metal-oxide framework of the cluster. Looking down the *c*-crystallographic direction, four-fold symmetry can be observed. The Mo(1) atomic sites are located at the C_4 symmetry position at the top of the cluster. The Mo(1) atoms are separated from one another by a distance of 3.600(1) Å and make up the corners of a square as a result of the four-fold symmetry. The local geometry of Mo(1) sites is a distorted octahedral orientation with apical Mo(1)-O(3) bond distance of 1.627(1) Å pointing away from the center of the cluster. The equatorial bonds to oxygen atoms range from 1.887(12) Å for Mo(1)-O(9) to 1.928(11) Å for Mo(1)-O(7). The long oxygen bonds pointing towards the center of the cluster connect the Mo(1) to the disordered phosphate $(PO_4)^{3-}$ unit through two bonds to the half-occupied O(11) atoms with distances of 2.495(14) Å and 2.506(14) Å. Overall, the bond distances between Mo(1) and oxygen atoms, with the exception of O(11), are close to the expected distances for molybdenum atoms with 6^+ oxidation state and are in agreement with the Shannon ionic radius for Mo^{6+}.[18] Bond valence sums calculations were used to provide an indication of the oxidation state of Mo(1). As can be seen in Table 4.6, the bond valence sums for Mo(1) are close to the expected, 6+ oxidation state. Mo(1) atoms connect to the 'belt' of the cluster, Mo(3) sites, through μ-2 oxygen bridges. Mo(3) atoms are in a distorted octahedral geometry with apical Mo(3)-O(2) distances of 1.635(11) Å which point away from the center of the cluster. In the equatorial position of the distorted octahedral geometry, Mo(3) is connected to four

crystallographically unique oxygen atoms O(4), O(5), O(6) and O(9) with distances of 1.897(11) Å, 1.911(11) Å, 1.920(2) Å and 1.914(12) Å, respectively. The long distances to $(PO_4)^{3-}$ in the center of the cluster, Mo(3)-O(10) and Mo(3)-O(11), are 2.459(13) Å and 2.456(13) Å, respectively. The bond valence sums calculation of Mo(3), shown in Table 4.6, is very similar to that of Mo(1) atomic site and is close to the 6+ oxidation state of Mo. Mo(2) atomic sites comprise the bottom square cap of the cluster (with *c* axis being the vertical axis) and are connected to Mo(3) atoms in a similar fashion as Mo(1) is connected to Mo(3). As is the case with Mo(1) and Mo(3), Mo(2) has a local distorted octahedral geometry with short apical oxygen bond of 1.651(10) Å for Mo(2)-O(1). The four equatorial bonds to the oxygen atoms O(5), O(6), O(8) and O(8) are 1.898(11) Å, 1.855(13) Å, 1.930(11) Å and 1.892(11) Å, respectively. Finally, the long oxygen bonds connecting the encapsulated phosphate unit are 2.475(14) Å for Mo(2)-O(10) and 2.485(14) Å for Mo(2)-O(10). The long oxygen bonds for all three Mo sites can be thought of as one single bond given that O(10) and O(11) atoms are half-occupied. As a result of the half-occupied O(10) and O(11) atoms, the $(PO_4)^{3-}$ unit is seemingly connected to eight oxygen atoms in a cubic-like arrangement around the central phosphorous atom. However, the phosphate ion occurs in tetrahedral geometry, with the coordination number of four, and likely changes orientations from one unit cell to another in a disordered fashion which results in the 'average' cubic arrangement of oxygen atoms around the central phosphorous. This crystallographic occurrence has been observed before in similar Keggin-based clusters and was discussed in Chapter 3.[19] Based on the bond valence sums calculations of the three Mo sites, one can observe that all of the sites are close to the 6+ oxidation state of Mo.

However, based on the composition and the results of the physical property studies discussed below, two of the twelve Mo atoms per formula unit should be in their 5^+ oxidation state. These bond valence sums suggest that the charge is not localized on specific Mo sites, but rather the charge is likely delocalized over the three Mo crystallographic sites totaling twelve Mo atoms per formula unit.

An interesting aspect of the structure of the title series of compounds is that different halide atoms can be incorporated which results in slight differences in structure and significant differences in properties (*vide infra*). The difference in structure between **1**~**4**, as mentioned above, is the incorporation of two Cl per formula unit for **1**, one I and one Cl for **2**, two Br for **3** and two I for **4**. The resulting salt chains comprised of $[Cs_6X_2]_\infty$ (see Figure 4.6) seemingly template the pockets where the Keggin–sodium chains, $[–Na–(PMo_{12}O_{40})–]_\infty$, reside, as shown in Figure 4.5. The difference in the salt chains between compounds **1** and **2** are shown in Figure 4.6. As can be seen in this illustration, the $[Cs_6Cl_2]_\infty$ chain in **1** contains Cl atoms in alternating tetrahedral–octahedral coordinations with respect to the coordinated Cs atoms. In **1**, Cl(1) atoms reside in the octahedral environment while the Cl(2) can be found in tetrahedral environment with respect to the Cs atoms. The difference in salt chains of **1** and **2** are shown in Figure 4.6 where the illustration shows the occupancy of octahedral environment by iodide in **2**. This should be expected as iodide is significantly larger than the chloride which resides in the preferential, smaller tetrahedral environment. The distances between Cs(1) and I are 3.637(1) Å (2 x) while the distance between Cs(2) and I is 3.952(1) Å (4 x). The corresponding X site in **1**, Cl(1), is connected to Cs(1) with bond distance of 3.327(1) Å (2 x) and Cs(2)-Cl(1)

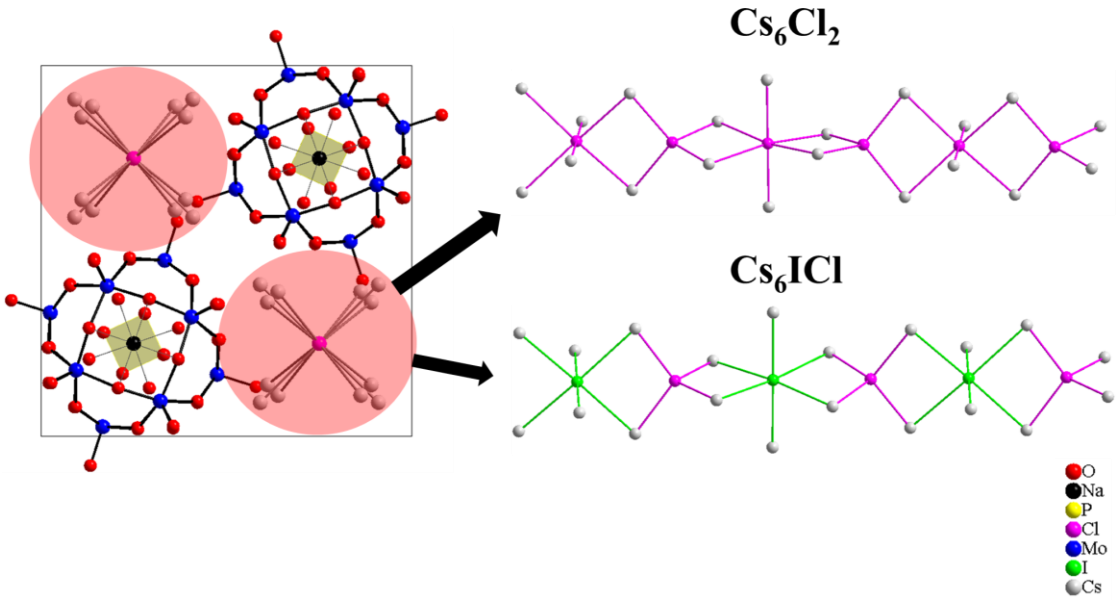

Figure 4.6: (left) Unit cell illustration of $Cs_6X_2Na(PMo_{12}O_{40})$ shown in the *ab* plane with salt lattice highlighted in pink circles. (right top) Partial view of the $[Cs_6Cl_2]_\infty$ chain in $Cs_6Cl_2Na(PMo_{12}O_{40})$ (**1**) extending along the *c*–axis. (right bottom) Partial view of the $[Cs_6ICl]_\infty$ salt chain in $Cs_6IClNa(PMo_{12}O_{40})$ (**2**) extending along the *c*–axis. The two views of the salt chains highlight the differences in composition and coordination in compounds **1** and **2**. In **1**, the two chloride geometries alternate between octahedral and tetrahedral coordination while in **2** the larger iodides are in octahedral coordination and the smaller chloride is in tetrahedral sites with respect to the neighboring Cs atoms.

3.806(2) Å (4 x). These differences in bond lengths between Cs and X atoms are expected for **1** and **2** given the differences in ionic radii of Cl^- and I^- (1.8 vs. 2.2 Å). When comparing the salt chain structure of the one electron reduced, $Cs_6I_3Na(PMo_{12}O_{40})$, and that of in compounds **1** and **2**, it is interesting to notice that halogen bonding interaction does not occur in the latter compounds. The halogen bonding phenomenon is likely governed by the size of the halide atoms used in the synthesis and the number of incorporated halide atoms which is related to the overall charge of the Keggin cluster. In **1** and **2** the charge of the cluster (5^-) allows for only two halide atoms per formula unit whereas in the compound described in Chapter 3, the cluster has a 4^- negative charge which allows for incorporation of an extra negative charge with three iodides per formula unit. This, of course, precludes that the only changed variables are the oxidation state of the cluster and the number of halide atoms incorporated per formula unit with the overall space group and structure being unchanged. The lack of halide interactions between the neighboring X atoms in **1** and **2** is evidenced by the relatively longer halide–halide distances. For **1**, the distance between the neighboring Cl(1) and Cl(2) atoms is 4.793(1) Å and in **2**, the distance between I and Cl is 4.786(1) Å. When these distances are compared to the iodine–iodine distances (~3.2 Å) in the compound described in Chapter 3, one can see that much longer halide–halide distances exist which indicates a lack of halogen bonding for **1** and **2**. It is speculated that this lack of halogen bonding in compounds **1** and **2** is one of the reasons for significant differences in physical properties of the title compounds compared to the physical properties of $Cs_6I_3Na(PMo_{12}O_{40})$.

The most obvious physical difference that can be noticed in the title compounds compared to the one-electron reduced $Cs_6I_3Na(PMo_{12}O_{40})$ is the color. The two-electron reduced compounds, **1**~**4**, are dark blue while the one-electron reduced compound from Chapter 3 is dark brown. In addition, compounds **1**~**4** are soluble in water up to about 1.0 mM at room temperature. The one-electron reduced compound, however, does not dissolve in water; likely due to the presence of halogen bonding in the salt chain which further stabilizes the compound as was discussed in detail in Chapter 3. Figure 4.4 shows a 0.75 mM solution of **1** in deionized water. It should be noted that the highest concentration of compounds **1**~**4** that can be prepared at ambient conditions is about 1.0 mM resulting in a dark blue solution as shown in Figure 4.4. Attempting to prepare higher concentrations results in visible presence of a solid at the bottom of the vial. Initially, the solubility studies were done in order to test the limits of the solubility of these compounds for antibacterial studies. Several solvents including acetonitrile, acetone, dimethyl formamide and ethanol were tested to dissolve compounds **1**~**4**. The highest solubility of **1**~**4** was in water as one would expect due to the ionic nature of the compounds. These compounds are also slightly soluble in ethanol, acetonitrile and dimethyl formamide.

UV-vis solution experiments were done on compounds **1**~**3** in order to see how stable these compounds are in solution. Figure 4.7 shows the UV-vis absorbance plots and the change in absorbance over a period of time. From this figure it can be seen that compound **1** is not very stable in solution. The blue color starts to disappear after day 7 and a yellow precipitate begins to form on the bottom of the cuvette. This yellow

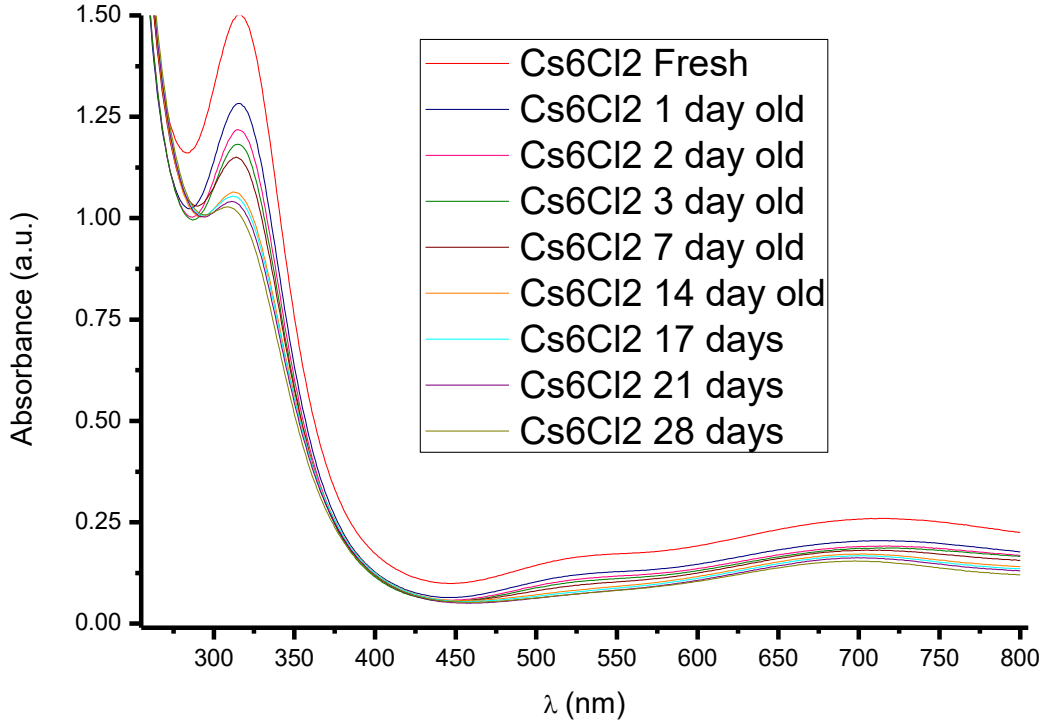

Figure 4.7: Solution UV-vis stability experiment. From this plot, it can be seen that the absorbance at ~310 nm starts to fall off between day zero and day one suggesting that the compound decomposes in solution.

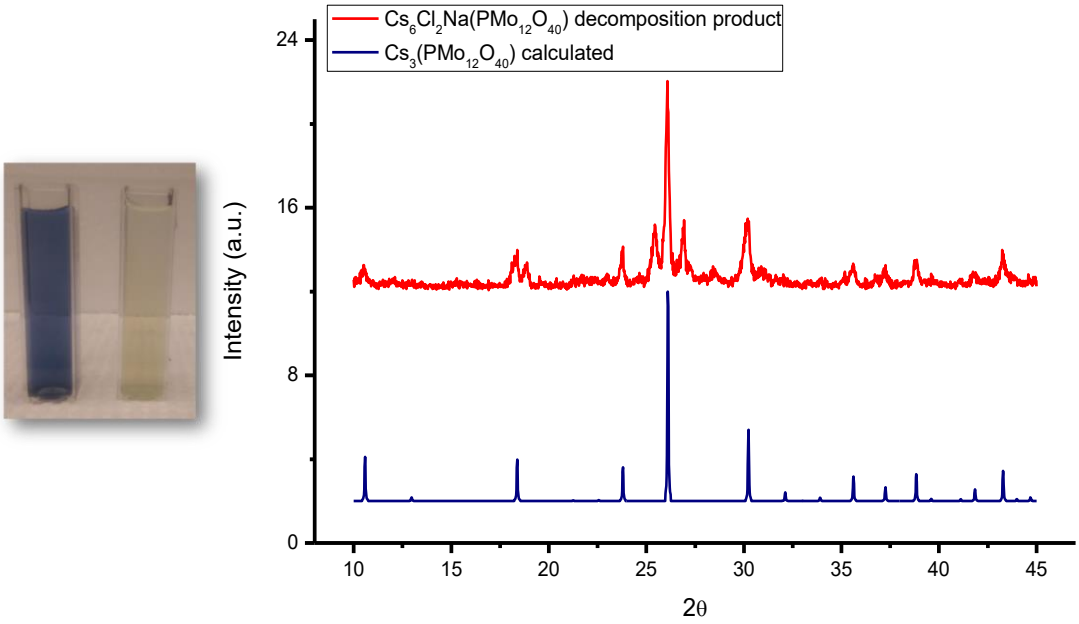

Figure 4.8: Solution UV-vis decomposition product. On the left, a freshly prepared solution (dark blue) and a decomposed product (after 28 days). The powder at the bottom of the yellow cuvette was collected and a PXRD pattern is shown above. The PXRD pattern matches that of the $Cs_3(PMo_{12}O_{40})$ calculated.

precipitate was confirmed by PXRD to be the fully oxidized $Cs_3(PMo_{12}O_{40})$ known compound (as shown in Figure 4.8 above). Almost identical decomposition is seen for compounds **2** and **3**.

Given the reduced state of the clusters in the title compounds, magnetic susceptibility studies were done on **1** in order to reveal any interesting magnetic properties due to the confined electrons within the cluster metal-oxide framework. Figure 4.9 shows the temperature-dependent magnetic susceptibility and inverse susceptibility plots under applied magnetic field of 1000 Oe. As can be seen in the top plot, the negative susceptibility values are indicative of diamagnetic nature of these clusters. When present in a magnetic field, diamagnetic materials repel the field which results in negative magnetic susceptibility values. The results of the magnetic studies indicate that the two electrons in the clusters of **1**~**3** pair up, delocalize over the twelve metal sites, and diamagnetically couple. Based on the literature search, the results of the magnetic susceptibility studies of **1** in which the two *d* electrons pair up are not uncommon among the compounds with Keggin or similar clusters that are reduced by an even number of electrons.[20,21,22] This non-magnetic ground state which exists even at room temperature was first attempted to be explained by Baker in which a multi-route antiferromagnetic exchange was proposed.[23] A few years later, the multi-route antiferromagnetic exchange was questioned by Borshch and co-workers by revealing that the NMR data from Baker's experiment showed that the blue electrons (electron pairs of the two-electron reduced POM species) do not reside on adjacent metal centers.[22] Hence, due to the separation of the two electron spins, it was concluded that a large antiferromagnetic coupling was not the likely cause of the non-magnetic ground state

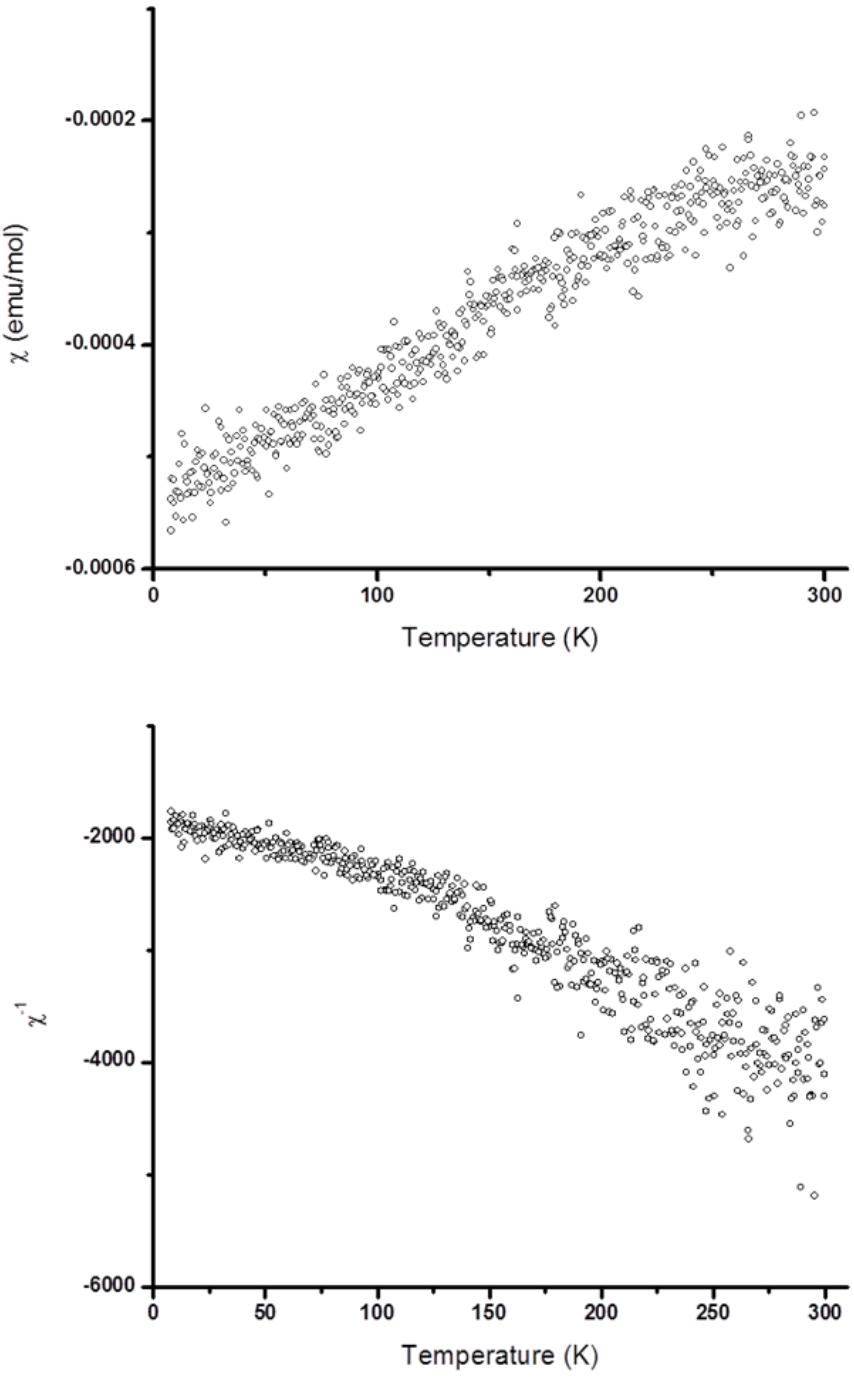

Figure 4.9: Temperature–dependent magnetic susceptibility and inverse susceptibility plots, χ (top graph) and χ^{-1} (bottom graph) versus *T*, of **1** under an applied magnetic field of 1000 Oe.

in the two-electron reduced POMs (and POMs with an even number of electrons, for that matter). Instead, a different mechanism was proposed in which the ground spin singlet state can be stabilized by the electron transfer processes occurring between the twelve metal atoms.[21, 24, 25]

Figure 4.10 shows the thermogravimetric analysis of **1** under nitrogen flow environment. As can be seen from the plot of weight percent (left axis, black line), there is very little loss of mass all the way up to 450 ^{o}C which means that **1** is thermally stable up to that temperature. After 450 ^{o}C, an onset of a weight loss starts and continues all the way up to 700 ^{o}C without an apparent plateau. As a result of this incomplete decomposition, assignment of the decomposed product(s) cannot be done. The right axis (blue line) shows the plot of heat flow, differential scanning calorimetry of **1**. The endothermic peak on heating around 530 ^{o}C is likely the melting peak. An exothermic peak around 430 ^{o}C on cooling is present and is likely a crystallization peak of the incompletely decomposed compound **1**. This exothermic peak is shifted (hysteresis) from the melting peak because of the fast cooling rate. Figure 4.11 shows the TGA and DSC plots for compound **2**. From this plot, it can be seen that 2 is thermally stable up to about 325 ^{o}C. Weight loss starts to occur after this temperature and continues to 700 ^{o} C. As a result of this incomplete decomposition, it is not possible to assign the decomposed products either. Looking at the DSC plot (in blue), one can see an endothermic peak around 530 ^{o}C which likely corresponds to the melting of **2**. The exothermic peak around 430 ^{o}C is also present and is assigned as the crystallization peak for **2**. The DSC plots for **1** and **2** are very similar in that they both have the melting and crystallization peaks around the same temperature which

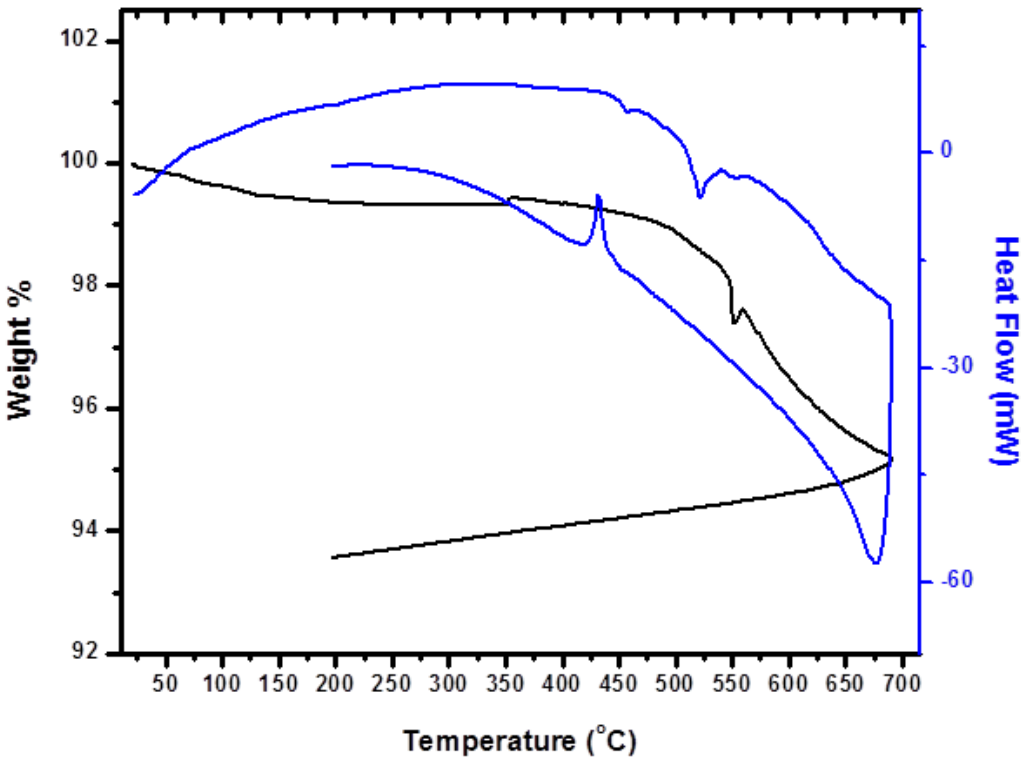

Figure 4.10: TGA and DSC plots for **1**. (right blue) DSC plot, and (left black) TGA. Weight loss in **1** happens from about 450 ºC and extends all the way to 700 ºC. Due to the incomplete decomposition of **1**, assignment of weight loss is inconclusive.

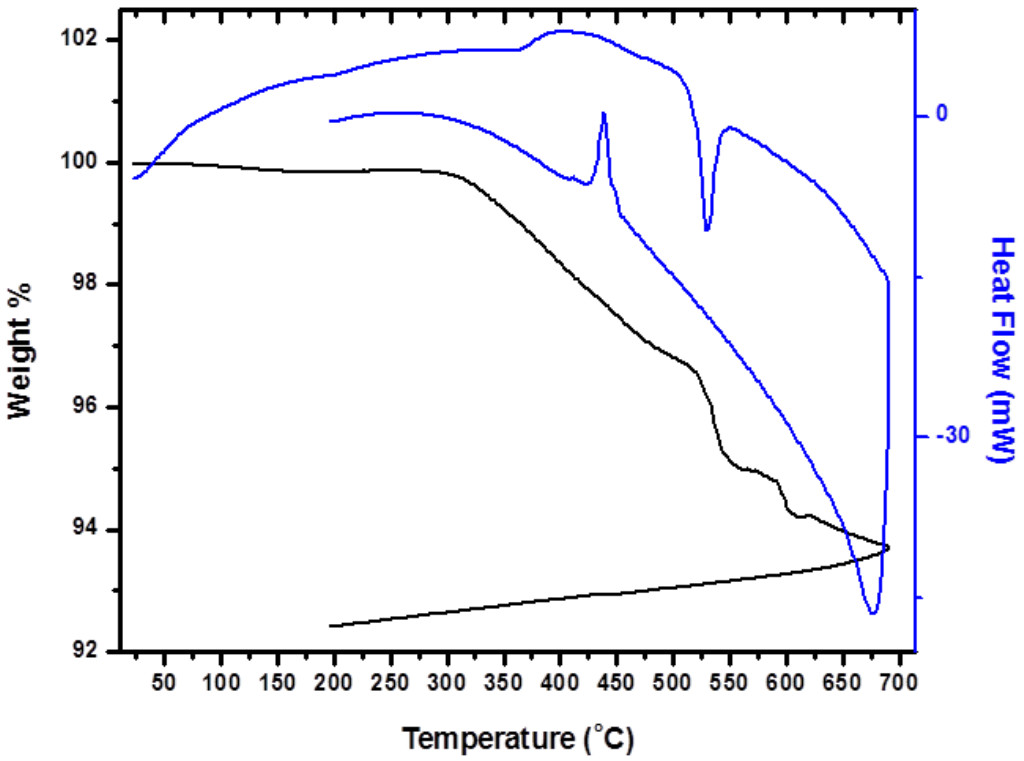

Figure 4.11: TGA (left black) and DSC (right blue) plot for **2**. TGA plot shows that **2** is thermally stable up to about 325 °C.

should be expected given their similar structures. However, the TGA plots show lower thermal stability for **2** compared to that of **1**. This could likely be due to the release of iodine from **2** as was discussed in some detail in Chapter 3 for the decomposition of $Cs_6I_3Na(PMo_{12}O_{40})$.

Reduction-oxidation (redox) properties of compounds **1** and **2** were tested in solution by cyclic voltammetry. Figure 4.12 shows the cyclic voltammograms of **1** (top) and **2** (bottom). The voltammograms were obtained using water as the solvent and KCl as the supporting electrolyte. As can be seen from the two plots, small quazi-reversible waves can be seen. These quazi-reversible waves likely correspond to the oxidation of the two-electron oxidation of Mo ions; Mo^{5+} to Mo^{6+} with anodic potentials (E_{pa}) at 0.0362 V and 0.304 V for **1** and 0.3670 V and 0.6240 V for **2**. The cathodic potentials (E_{pc}) occur at 0.1910 V and 0.0087 V for **1** and at 0.5010 V and 0.1230 V for **2** and are likely due to the quazi-reversible reduction of the Mo^{6+} ions.[26] In the voltammogram of **1**, an extra peak can be seen on the anodic (E_{pa} = 0.4040 V) and cathodic (E_{pc} = 0.3120) sides of the graph. The peaks in both voltammograms are not well defined potentially due to the poor solubility and stability of compounds **1** and **2** in aqueous conditions. As will be discussed later in this chapter, compounds **1**~**3** oxidize in water over time which makes the aqueous conditions for cyclic voltammetry studies non-ideal. In addition, $(PMo_{12}O_{40})^{n-}$ clusters are subject to hydrolysis in aqueous media and as such, poorly defined waves are seen for cyclic voltammetry experiments in such solvents.[26] Given that POMs are subject to hydrolysis in aqueous solvents and due to poor redox waves in such solvents, attempts to dissolve the POMs described herein in organic solvents were made by exchanging the inorganic cations

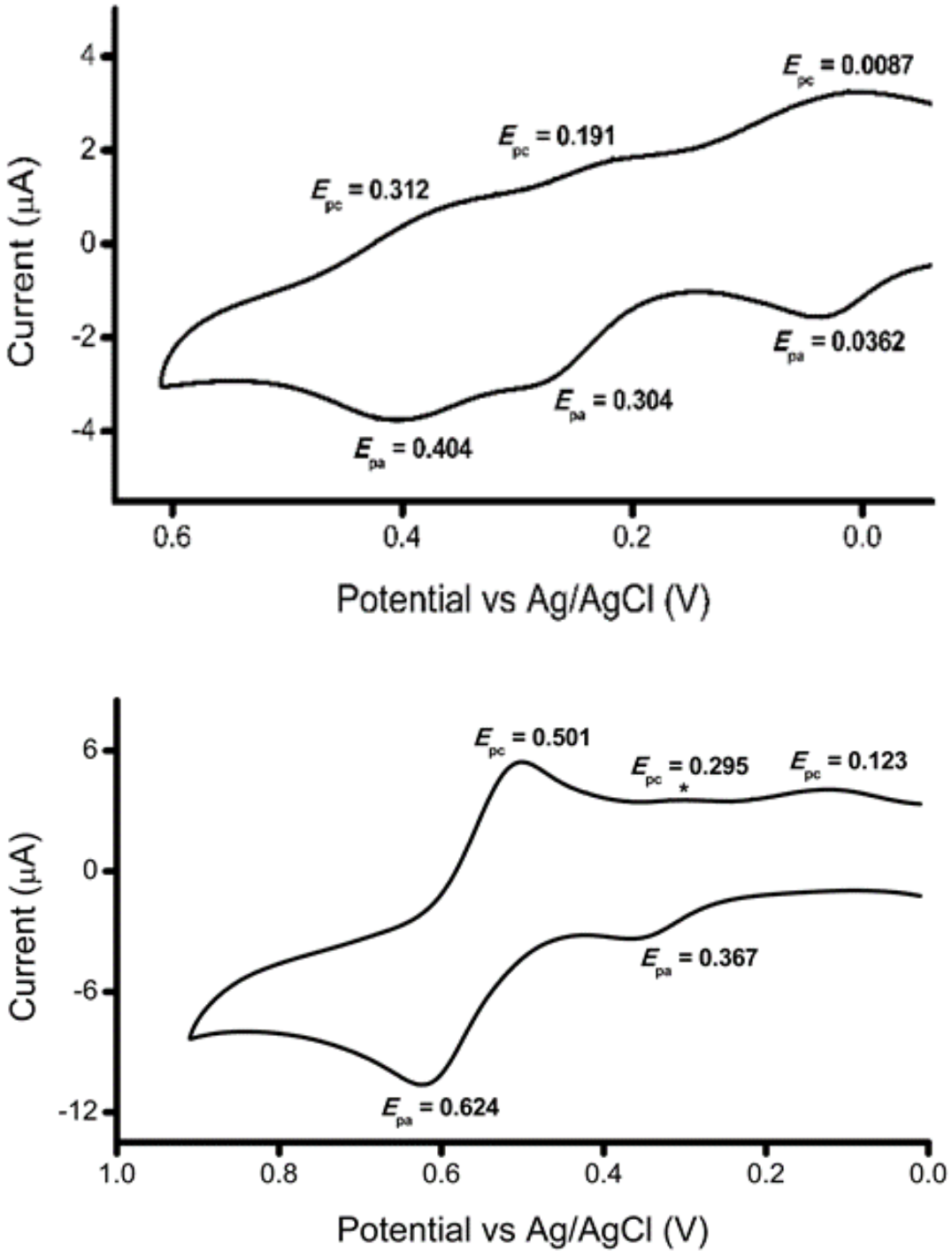

Figure 4.12: (top): Cyclic voltammogram for **1** using water as the solvent. (bottom): Cyclic voltammogram for **2** with water as the solvent. Both voltammograms were obtained in the following conditions: 1.0 mM analyte, 0.10 M KCl, 100 mV s^{-1} scan rate.

by organic quaternary ammonium-based cations. Tetrabutylammonium ($[CH_3(CH_2)_3]_4N^+$, TBA) salt was used to exchange the inorganic cations by dissolving **1** in water and adding (TBA)Cl. After stirring the mixture for two hours a blue precipitate was observed and filtered. The solid was dissolved in dimethylformamide in order to grow single crystals by evaporation of the solvent at room temperature as well as by mild heating (50 ^oC) of the solution. Single crystals of $(TBA)_4(PMo_{12}O_{40})$ (**5**) were isolated and a structure solution was obtained using single crystal X-ray diffraction. Table 4.8 shows the crystallographic information and a *CheckCIF* is included in the appendix. Figure 4.13 shows the partial view of the structure (top) with the calculated and the observed powder patterns on the bottom of Figure 4.13. It should be noted that the observed X-ray powder pattern was obtained from the filtered precipitate from the cation-exchange reaction described above. Based on the formula of **5**, it can be observed that the charge of the POM is 4- which means that the cluster oxidized from the original 5- charge during the cation-exchange reaction.

Magnetic susceptibility was done on this compound and is shown in Figure 4.14. The plot shows a typical paramagnetic response which is indicative of one *d* electron per cluster and thus a 4- charge. In addition, the experimental effective magnetic moment shows a value of around 1.70 B.M. which is close to that of the expected $S = ½$ compound 1.73 B.M. In case of a proton being attached to the cluster, two *d* electrons would be delocalized and diamagnetically coupled resulting in non-magnetic state, as discussed above. Nevertheless, the successful synthesis of **4** resulted in a POM-containing compound that is soluble in common organic solvents that are used in cyclic voltammetry

Table 4.8: Crystallographic data table for compound **5**.

empirical formula	$C_{16}H_{36}N(PMo_{12}O_{40})$
formula wt, g/mol	2064.69
crystal system	tetragonal
space group	*I4*
a , Å	18.726(3)
c , Å	14.571(3)
volume, Å^3	5109.6(14)
Z	2
D_{calc}, g/cm^3	1.34
abs coeff	1.35
crystal size, mm	0.4 x 0.5 x 0.5
theta range, deg	2.18 - 25.05
relns collected	21873
indep reflns	4526
R (int)	0.036
obsd ($I > 2s(I)$)	1508
goodness-of-fit on F^2	1.129
$R_1[I > 2s(I)]$[a]	0.048
wR_2 (all data)[b]	0.130

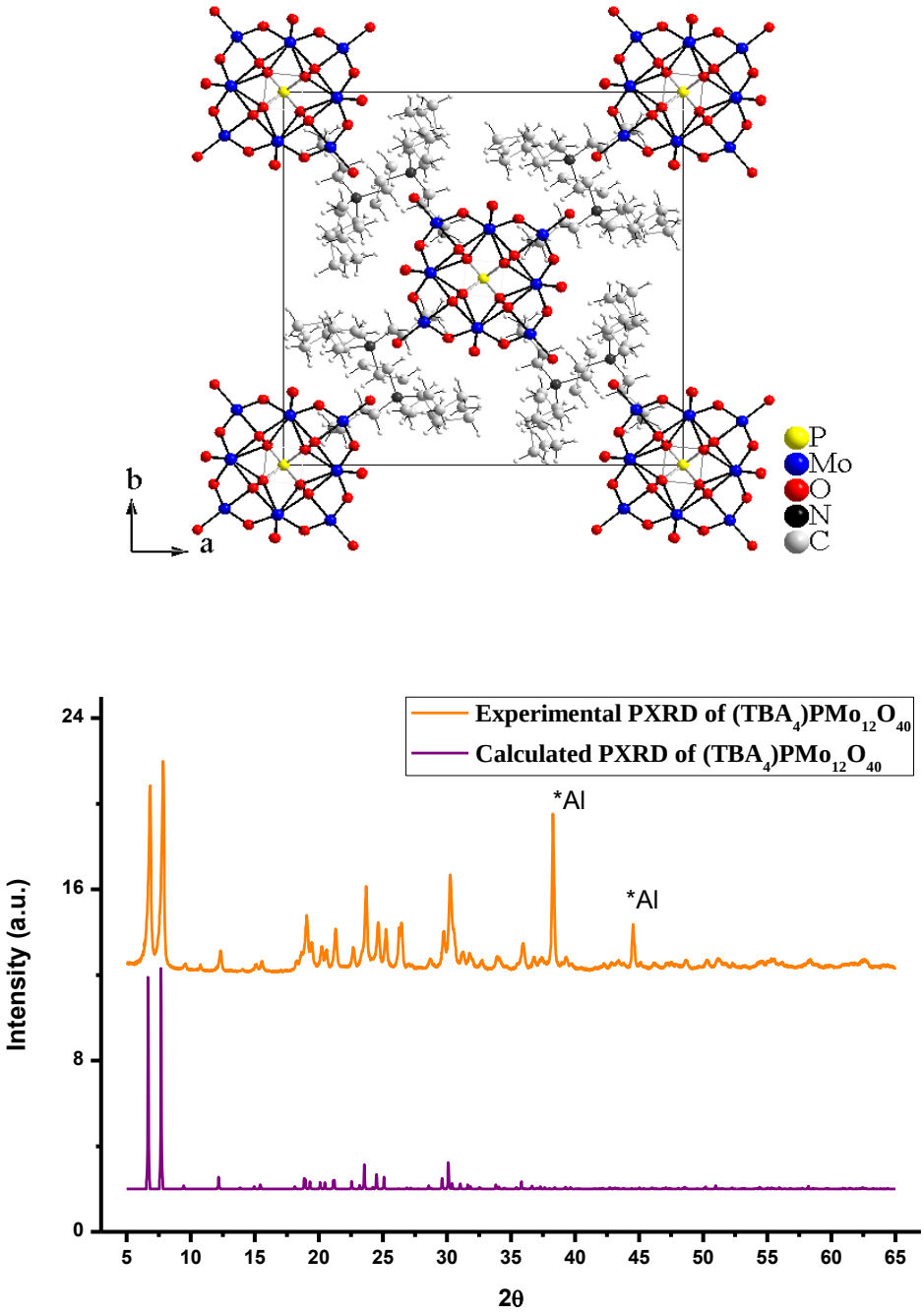

Figure 4.13: (top) View of the structure in the *ab* plane of the ion exchanged product, $TBA_4(PMo_{12}O_{40})$, where TBA stands for tetrabutylammonium. (bottom) Powder X-ray pattern of the obtained product $TBA_4(PMo_{12}O_{40})$ and the calculated pattern. The Al peaks are from the aluminum sample holder.

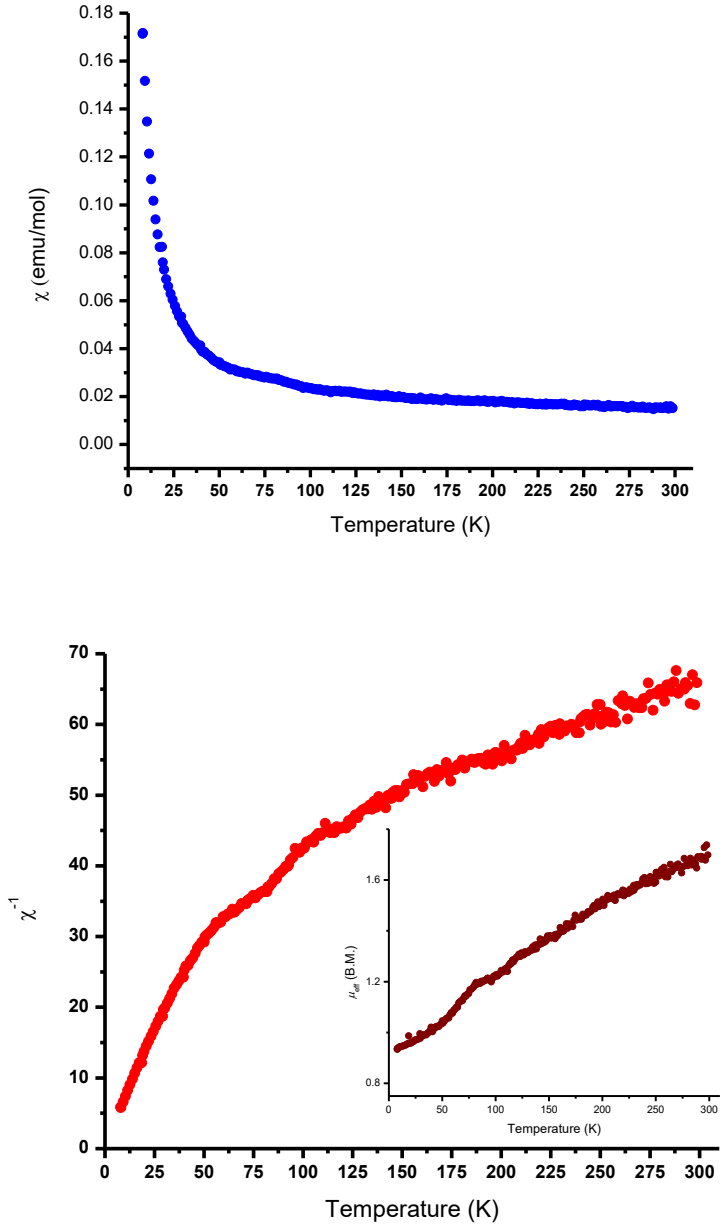

Figure 4.14: (top) Temperature–dependent magnetic susceptibility plot, χ versus *T* in the applied field of 1000 Oe of the one-electron reduced $TBA_4(PMo_{12}O_{40})$ ion exchanged product showing paramagnetic response similar to that of the one electron reduced, $Cs_6I_3Na(PMo_{12}O_{40})$. (bottom) Inverse χ versus *T* with inset showing magnetic moment vs. *T* plot. At room temperature, the magnetic moment is close to the expected, 1.73 B.M.

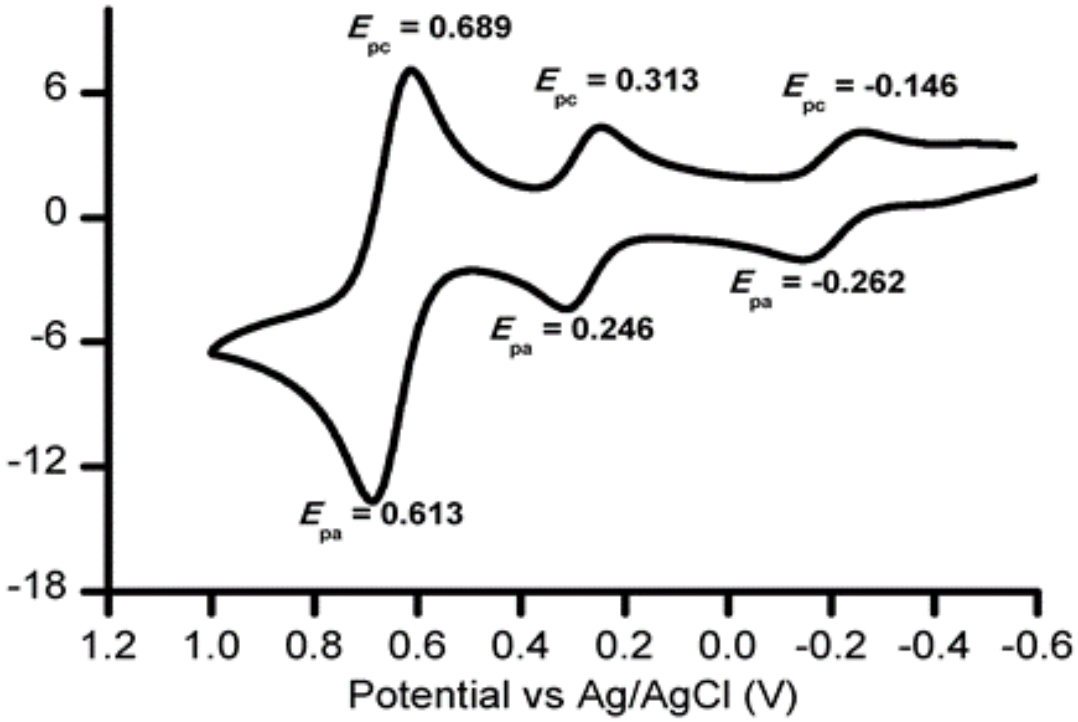

Figure 4.15: Cyclic voltammogram of $TBA_4(PMo_{12}O_{40})$ in anhydrous dimethyl formamide (DMF). 1.0 mM analyte, 0.10 M $[Bu_4N][PF_6]$, $(\eta^5\text{–}C_5H_5)_2Fe$ as internal standard, 100 mV s^{-1} scan rate were used in obtaining the voltammogram.

experiments. Dimethylformamide (DMF) was then used as the solvent to perform the cyclic voltammetry of **4**. Figure 4.15 (above) shows the voltammogram obtained in DMF solution with hexafluorophosphate as the supporting electrolyte. Three distinct quazi-reversible waves are seen and are a result of multi one-electron processes occurring.[26, 27] While the results of electrochemical studies presented in this chapter have been observed before and are not revolutionary, they show that the reduced POMs presented herein are electronically active. These results are useful when discussing the biomedical properties of reduced POMs given that multiple electron transfer processes occur in living cells as will be discussed later in this chapter.

Antibacterial studies were done on *Staphylococcus Aureous* SA1199, wild strain and SA1199B, mutant strain overexpressing the multi-drug resistance pump (MDR) responsible for antibiotic resistance of *Staph. A.* bacterial strains. These studies were done using a quantitative macrobroth dilution assay, based on the Clinical Laboratory and Standards Institute (CLSI) standards,[17] to obtain the minimum inhibitory concentration (MIC) values for the title compounds, **1**~**3**. Two different strains SA1199 and SA1199B were used to evaluate the effect of compounds **1**~**3** on the wild strain, SA1199, as well as the strain overexpressing the MDR pump. Table 4.7 shows the obtained MIC values and the results of the macrobroth dilution study. Figure 4.16 shows the TEM images of the damaged cells in the presence of compounds **1**~**2**. Repeated independent studies on SA1199 and SA1199B strains showed similar results with respect to the MIC values of compounds **1**~**3**. These results are significant because unlike most antibiotics which are ineffective at killing and/or inhibiting the growth of bacterial strains overexpressing the

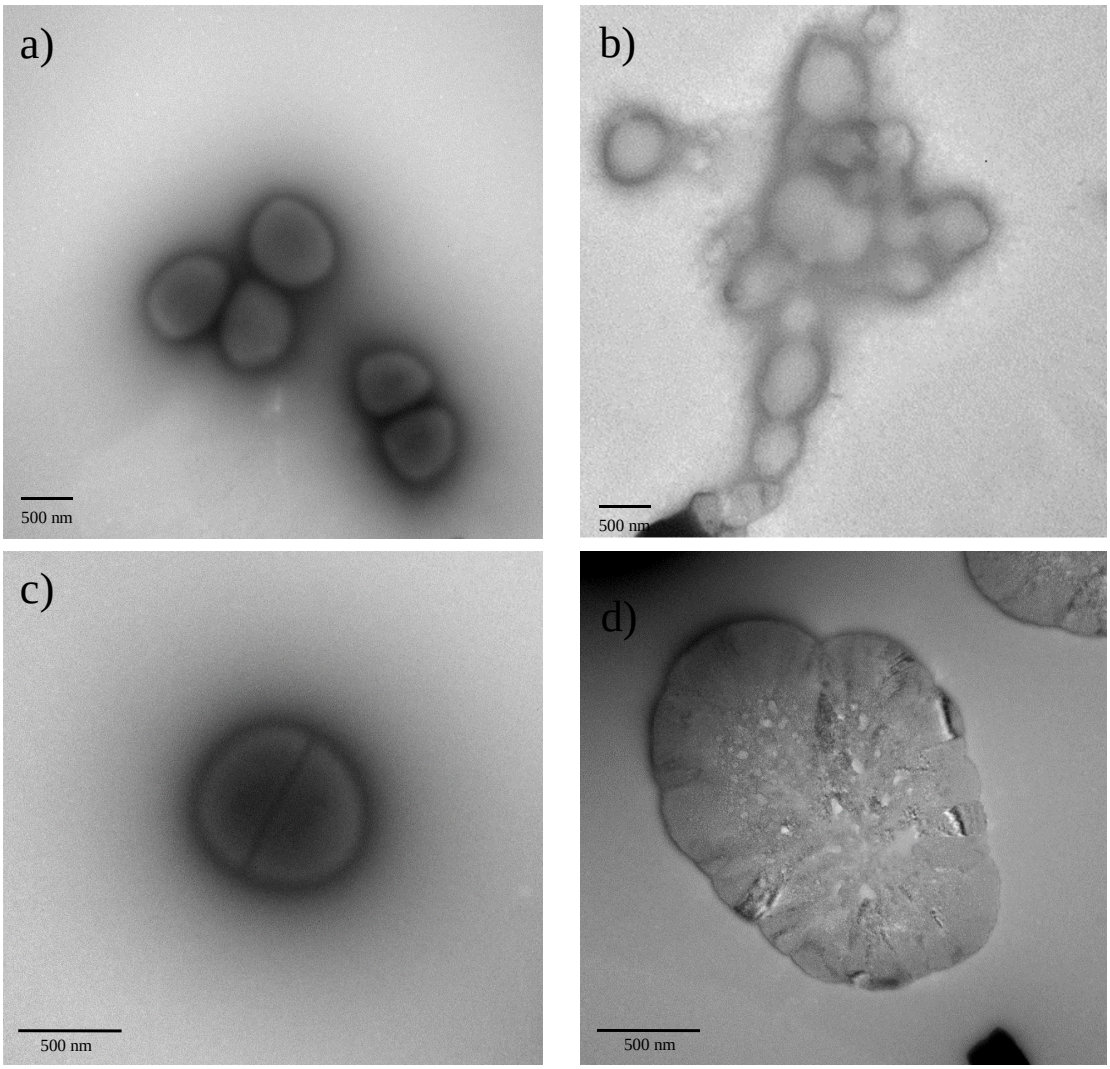

Figure 4.16: (a) A group of SA1199B healthy cells that were not exposed to **1**~**3**. (b) A group of SA1199B cells that were exposed to compound **1** showing cell damage and irregular cell shape. (c) Healthy SA1199B cell undergoing division that was not exposed to compounds **1**~**3**. (d) SA1199B cell showing irregular shape after being exposed to **1**.

*Note: It should be mentioned that not all cells in the samples that were exposed to compounds **1**~**3** showed membrane damage. In fact, many healthy-looking cells were able to be seen. This observation is consistent with the proposed mechanism of bacterial growth inhibition by r-POMs.*

MDR pumps, compounds **1**~**3** seem to show equal inhibition effect on both the wild strain and the problematic mutant strain of *Staph. A.* These results indicate that compounds **1**~**3** are not the substrates of the MDR pump which is considered to be responsible for the ineffectiveness of current antibiotics. As a result, **1**~**3** can be considered as alternative therapeutic antibacterial drugs when current antibiotics fail.

Table 4.9: MIC values of reduced, $Cs_6Cl_2Na(PMo_{12}O_{40})$ (**1**) compared to the oxidized, $Na_3(PMo_{12}O_{40})$ Keggin-based compounds.

Strains	**MICs (μg/ml)**		**MICs (μM)**	
	$Cs_6Cl_2Na(PMo_{12}O_{40})$ (**1**)	$Na_3(PMo_{12}O_{40})$ - oxidized	$Cs_6Cl_2Na(PMo_{12}O_{40})$ (**1**)	$Na_3(PMo_{12}O_{40})$ - oxidized
SA1199B	254.39	1634.6	94	750
SA1199	254.39	817.3	94	375

In addition to the MIC studies, minimum bactericidal concentration (MBC) studies were done on the reduced POM compounds **1**~**3**. MBC is defined as the minimum concentration required to kill 99.9% bacteria. This experiment was performed in order to possibly understand the mechanism by which the r-POMs inhibit the bacterial growth. In all three cases for compounds **1**~**3**, the MBC values were higher than 4 times the MIC values which indicates that the r-POMs do not necessary inhibit the bacterial growth by killing the bacteria. Rather, a different mechanism might be occurring which will be discussed further in this chapter.

Given that the title compounds contain the two-electron reduced Keggin clusters, studies were done to compare the effectiveness of the reduced Keggin POMs, $(PMo_{12}O_{40})^{5-}$ described herein *vs*. the fully oxidized, $(PMo_{12}O_{40})^{3-}$, Keggin cluster in a commercially

available compound $Na_3(PMo_{12}O_{40})$ (Sigma-Aldrich). As can be seen in Table 4.8, the MIC values for the SA1199 and SA1199B strains of the reduced Keggin POM (title compound **1**) are lower compared to the fully oxidized $Na_3(PMo_{12}O_{40})$, commercially available compound. Similar results were also obtained for compound **2**. These results suggest that the reduced polyoxometalates are more effective at inhibiting the growth of bacterial strains SA1199 and SA1199B. From literature reports mainly done by the Yamase group, it can be seen that the fully oxidized POMs have an order of magnitude lower MICs compared to the reduced compounds **1**~**3**. The additional two electrons in the clusters of the title compounds, $(PMo_{12}O_{40})^{5-}$, likely play an important role in bacterial growth inhibition.

The proposed mechanism of inhibition is shown in Figure 4.17. Previously, Yamase and co-workers proposed that the mechanism of inhibition of bacterial growth by POMs involves the electrons in the electron transport chain and the inhibition occurs on the outside of the cell membrane where the fully oxidized POMs accept the electrons from the electron transport chain and thus become reduced.[13] These conclusions are supported by the visible change in color of the solutions containing the cells and POMs. The color was observed to be pale yellow before the addition of bacterial cells. However, after allowing the bacteria to incubate in the presence of POMs, the color changed from pale yellow to dark blue. The blue color is common in the molybdenum species and indicates the reduced state of Mo metals. In addition to the observed color change, SEM-EDX results show that the POMs are present on the surface of bacterial cells. The proximity of POMs to the

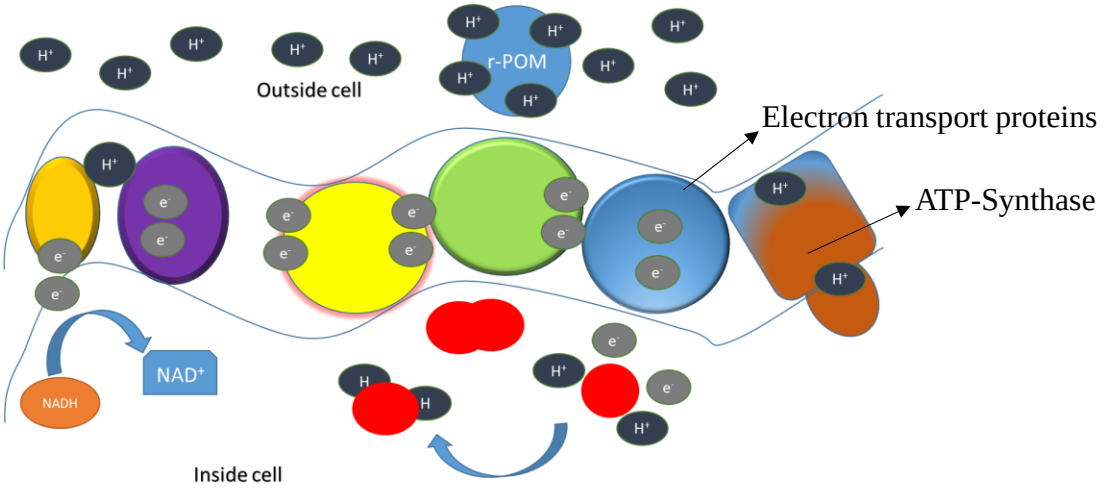

Figure 4.17: Proposed mechanism of bacterial inhibition by the reduced polyoxometalates (r-POMs), **1**~**3**. The highly charged r-POMs weaken the proton-motive force in the electron transport chain by interacting with the protons outside of the cell and thereby slowing down or shutting down the production of ATP.

electron transport proteins in the cellular membrane supports the claim that the POMs are reduced by the electrons in the electron transport chain. However, in the title compounds, **1**~**3**, the POMs are already reduced by two electrons and the cluster carries a higher, 5^-, charge compared to the fully oxidized, 3^- charged, clusters which likely means that a different mechanism for the reduced POMs could exist. Given that the reduced POMs (r-POMs), presented herein, are more effective at inhibiting bacterial growth of SA1199 and SA1199B, new mechanism of bacterial inhibition by POMs is proposed. In Figure 4.17, the illustration shows the electron transport chain inside a cellular membrane with several electron transport proteins embedded within. At the end of the electron transport chain is the illustration of the ATP-Synthase protein which is responsible for production of ATP, the energy currency of all biological cells necessary for various cellular processes. To produce ATP, ATP-Synthase relies on the proton gradient between the outside and the inside of the cell. This proton gradient is also called the proton motive force and is a well-regulated process for production of ATP. In the presence of negatively charged species, the protons are likely drawn to the negatively charged species which slows down or reduces the proton motive force and consequently slows down the production of ATP. It is known, in fact, that reduced polyoxometalate species have higher relative basicity due to the increased negative charge density at the anionic cluster compared to the fully oxidized POMs.[28] Protonation of the reduced POM species has been experimentally observed using cyclic voltammetry as well as through various synthetic methods. The presence of the negatively charged species is analogous to the basic conditions where OH^- would be the

negatively charged ion. For the analogous reasons, basic conditions are detrimental to bacterial cells.[29]

r-POMs described herein, have a negative charge of 5^- and as such would likely draw more protons, due to higher basicity, than the fully oxidized (3^- charged) POMs. This is supported by the results of the MIC studies shown in Table 4.9 showing lower MIC values for the reduced POMs compared to those in the oxidized POMs. The proposed mechanism of inhibition likely means that the compounds **1**~**3** slow down the production of ATP vital for bacterial survival by reducing or weakening the proton motive force which is used by the ATP-Synthase enzyme to make ATP. To test this hypothesis, time-lapsed ATP bioluminescence assay was done to quantify the amount of ATP production over time. The results of this study are shown in Figure 4.18. As can be seen from this figure, the ATP production is significantly reduced in the presence of r-POMs **1** and **2**. Statistical analysis using two-way NOVA test (two variable analysis test) to determine the significance of the reduction in ATP for SA1199 and SA1199B strains in the presence of **1** and **2** shows the probability of the null hypothesis (*i.e.* r-POMs having no effect on ATP production) to be less than 0.1%, or $p < 0.001$. The results of this analysis are highly significant based on the statistics which indicates that the ATP production shown in Figure 4.14 is significantly reduced in the presence of r-POMs **1** and **2** compared to the control in which no POMs were used. The results of the ATP assay studies support the proposed mechanism of bacterial growth inhibition by r-POMs illustrated in Figure 4.17. In addition, electron microscopy work showed that healthy bacterial cells can be found even after being exposed to r-POMs. This indicates that the likely mechanism of inhibition of bacterial growth is not

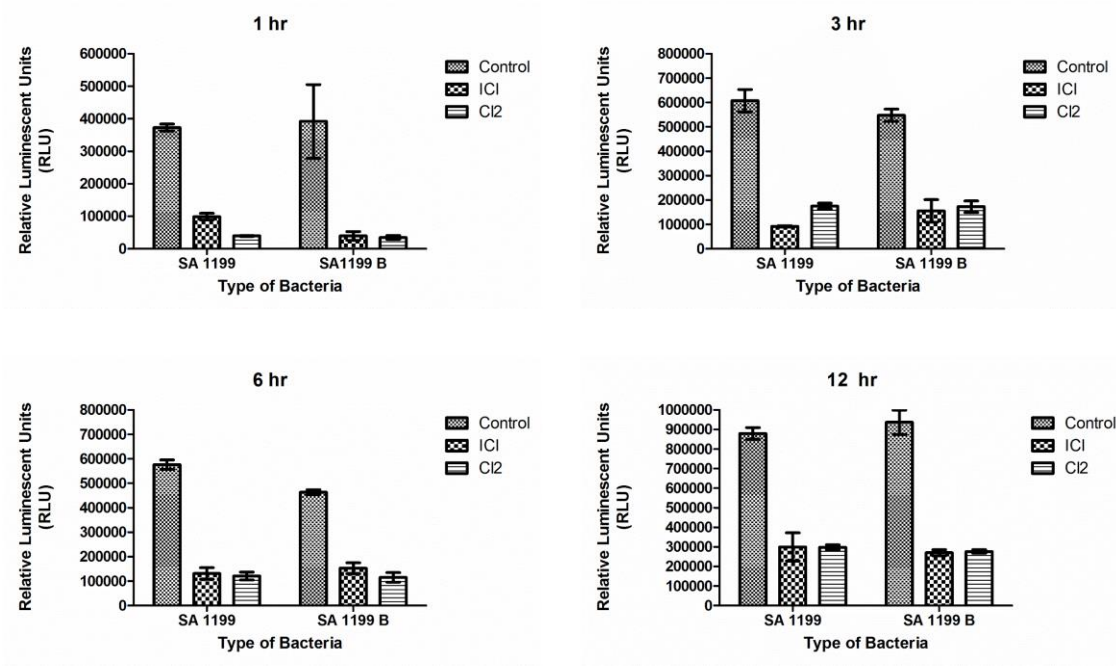

Figure 4.18: Results of the ATP time lapsed assay showing the plots for ATP production (measured in relative luminescence units, RLU) after 1 hour, 3 hour, 6 hour, and 12 hour exposure of SA1199 and SA1199B cells to the POMs $Cs_6Cl_2Na(PMo_{12}O_{40})$ (**1**) (Cl2 in the plots) and $Cs_6IClNa(PMo_{12}O_{40})$ (**2**) (ICl in the plots).

likely occurring through directly killing the cells but rather through the weakening of the proton motive force vital for ATP production.

While it is not possible to make bold conclusions regarding the mechanism of bacterial growth inhibition due to the high complexity of biological cells and their complex processes, the results shown in this chapter indicate that the bacterial growth inhibition is occurring by the interference of r-POMs in the proton motive force required for ATP production. In addition, a possibility of two mechanisms occurring simultaneously cannot be rejected based on the current results. It is possible that two mechanisms are occurring simultaneously where the fully oxidized POMs inhibit the electron transport chain in the ATP production (mechanism proposed by Yamase group) as well as the mechanism proposed herein in which the r-POMs are inhibiting the proton motive force to limit ATP production.

Figure 4.19 shows the preliminary antitumor studies using human colon cancer cells, HT-29, and the cell toxicity toward normal human cells, CCD18-co. The concentrations (and corresponding conversions) used in this experiment are summarized in table below the plot in Figure 4.19. From the cell survival bar plot (top in Figure 4.19) it can be seen that the r-POM **1** is toxic toward both the tumor cells as well as the normal human cells at high concentrations. However, up to 8 μL (29.4 μM concentration of r-POM **1**), normal human cells, CCD18-co show no measurable toxicity (i.e. cell survival 100% within experimental error) while 40% of tumor cells are killed at the same concentration. This result is extremely promising as it paves the way for further research into therapeutic,

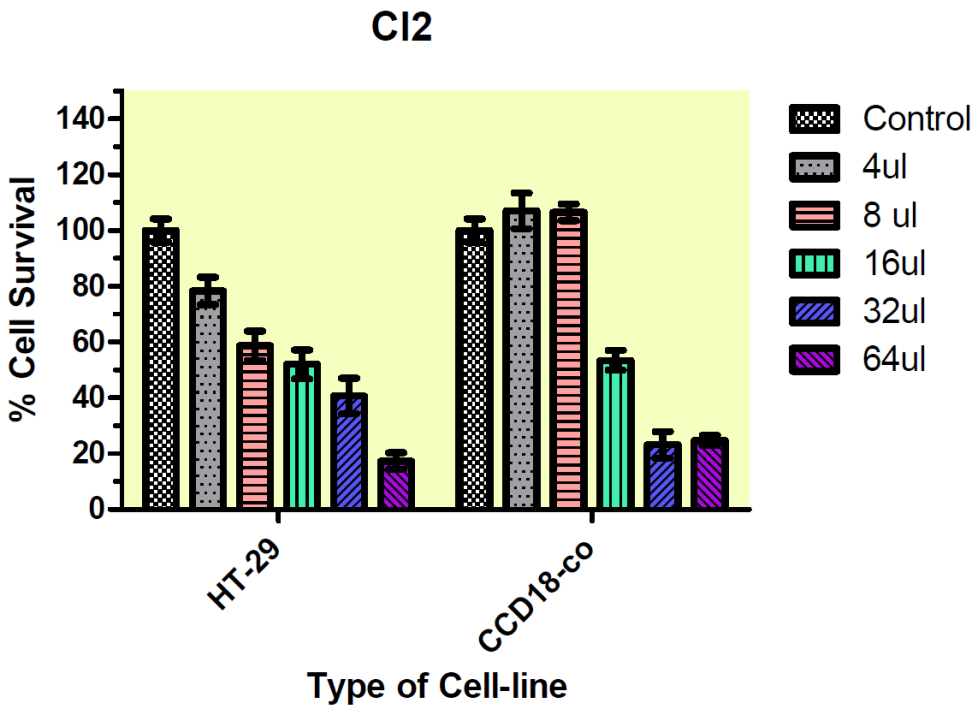

Dosage (µl):	Cs_6Cl_2 (**1**) conc. (µg/ml):	Cs_6Cl_2 (**1**) conc. (µM):
4	39.9	14.7
8	78.3	29.4
16	150.8	56.0
32	280.7	103.0
64	493.4	182.0

Figure 4.19: (top) Plot showing HT-29 and CCD18-co cell survival in the presence of $Cs_6Cl_2Na(PMo_{12}O_{40})$ (**1**) in different concentrations. (bottom table) Table showing dosage volumes in µl, concentrations of **1** in µg/ml and µM.

non-toxic administrations of novel inorganic medicines based on r-POMs for antitumor applications.

Conclusion

A series of new salt inclusion solids containing reduced Keggin polyoxometalate clusters was presented in Chapter 4. These new two-electron reduced polyoxometalates, based on $Cs_6X_2Na(PMo_{12}O_{40})$ (where X can be Cl, Br, and I), are structurally similar to the one-electron reduced, $Cs_6I_3Na(PMo_{12}O_{40})$ compound presented in Chapter 3. Incorporating a slightly different salt lattice, *i.e.* $[Cs_6X_2]_\infty$ salt chains, compared to the $[Cs_6I_3]_\infty$ lattice in compound described in Chapter 3, resulted in Keggin based solids where two of the twelve molybdenum atoms are in their formal 5+ oxidation state. The isolation of Keggin based solids described in this dissertation using high temperature molten salt method is, to the best of our knowledge, the first example of high temperature synthesis of reduced polyoxometalate Keggin clusters. Using the high temperature method for synthesis of polyoxometalates enabled for isolation of reduced species which otherwise are not easily synthesized using conventional methods due to the oxidative conditions in aqueous and other solvents. The structure of the title series of compounds features isolated covalent metal-oxide clusters presumably templated by the $[Cs_6X_2]_\infty$ salt chains running parallel to the cluster chains, $[-(PMo_{12}O_{40})-Na-]_\infty$, where a sodium cation links the neighboring clusters. The salt chain features halide anions in alternating tetrahedral-octahedral environments with respect to the neighboring Cs atoms. In addition to the coordination of Cs to halides, Cs atoms also coordinate to oxygen atoms on the Keggin cluster. The

distance between the neighboring halides in the $[Cs_6X_2]_\infty$ salt chains is much longer compared to that of in the compound described in Chapter 3. This means that the halide…halide interaction does not exist in the title compounds mainly due to the difference in charge on the Keggin cluster (*i.e.* one electron higher (5- vs 4-) for the compounds described in this Chapter) and hence no additional negative charges in the form of halide anions are necessary to balance the positive charge of the polynuclear salt chain. Due to their ionic nature between r-POM and salt lattice, the title compounds are soluble in water up to about 1 mM concentration. The magnetic susceptibility studies revealed that the two electrons, from two Mo^{5+} cations, pair up and interact diamagnetically as was evidenced by the negative magnetic susceptibility values in the χ vs. T plots. As such, these materials may not be particularly interesting to the magnetic communities. Attempts were made to study the electronic properties of the aqueous solutions of the title compounds using cyclic voltammetry but due to the poor solubility in water and the limitations of water as the solvent of choice in cyclic voltammetry, the attempts resulted in broad and undefined waves. For this reason, a reaction targeting cation substitution using organic cations, *i.e.* tetrabutylammonium (TBA), to replace the polynuclear cation, $(Cs_6X_2Na)^{5+}$, in order to dissolve the clusters in organic solvents which are commonly used in voltammetry experiments such as dimethylformamide (DMF). Successful substitution of the inorganic polynuclear cation was achieved and resulted in a DMF soluble solid with the formula of $TBA_4(PMo_{12}O_{40})$. It should be noted that this new solid contains a one-electron reduced polyoxometalate cluster which is different from the starting material being two-electron reduced species. Magnetic susceptibility of the $TBA_4(PMo_{12}O_{40})$ compound shows

paramagnetic behavior which confirms the presence of a one-electron reduced cluster as was also observed in the one-electron reduced, $Cs_6I_3Na(PMo_{12}O_{40})$, described in Chapter 3. Cyclic voltammetry of the 1 mM solution of $TBA_4(PMo_{12}O_{40})$ shows three distinct quazi-reversible waves as a result of three electron redox processes of the molybdenum cations. Because of their solubility in aqueous, physiological conditions, and the previous reports showing biomedical activity (antibacterial, antitumor and antiviral) of POMs, the title compounds were tested for effectiveness in bacterial growth inhibition. Minimum Inhibitory Concentration (MIC) values for several bacterial strains including the SA1199 (wild strain) and SA1199B (mutant strain resistant to antibiotics) of the *Staphylococcus* (S.) *aureus* bacteria were obtained using a serial macrobroth dilution assay based on the Clinical Laboratory and Standards Institute (CLSI). The results of the MIC studies show that the reduced POMs presented herein are not the substrates of the efflux pump which is responsible for the resistance to antibiotics in the mutant strain, SA1199B. Comparing the results of the MIC studies of the reduced polyoxometalates (r-POMs) to the commercially available, fully oxidized Keggin-based POMs, it can easily be observed that the r-POMs are much more effective in the inhibition of bacterial growth with approximately an order of magnitude higher effectiveness. A proposed mechanism of the bacterial inhibition by r-POMs was presented and can be explained by the high surface negative charge of the r-POMs. Previously proposed mechanisms of bacterial growth inhibition of POMs by Yamase and co-workers deals with the reduction of the fully oxidized POMs by the electrons in the electron transport chain in the bacterial cellular membrane and thus slows down a vital cellular process, ATP production. However, given that the r-POMs are already

reduces species, likely mechanism of bacterial growth inhibition deals with the interaction of r-POMs with the proton gradient (or proton motive force) required for synthesis of ATP. Presumably, r-POMs being highly charged, interact with protons outside of the cell and by doing so they weaken the proton motive force which results in decreased production of ATP, the cellular energy currency, and eventually this leads to cellular death. The results of the ATP bioluminescence assay are in line with the expected ATP reduction in the presence of r-POMs which shows a significantly reduced production of ATP compared to the control group. This result provides support that the proposed mechanism is valid, however no bold conclusions can be made due to the complexity of biological systems and intricate cellular processes. It should be noted that the simultaneous action of the two above-described mechanisms of bacterial growth inhibition cannot be rejected based on the available data at hand. It is a perfectly valid hypothesis that the r-POMs can be further reduced by the electrons in the electron transport chain (Yamase proposed mechanism) while simultaneously attracting even more protons and weakening the proton motive force (mechanism proposed herein) and thereby inducing a dual negative effect on the ATP production. While the antibacterial results are exciting and show promise for future studies, the mechanism is still not fully understood. In addition to the antibacterial properties, the r-POMs presented herein also show antitumor effect. Based on the preliminary antitumor studies, r-POMs can be used to inhibit tumor cell growth while having significantly lower relative toxicity on the normal human cells up to certain concentrations. These results are preliminary and further studies, described below, could potentially shed light on the biomedical properties of the r-POMs presented in this chapter. Nevertheless, the results

thus far show the importance and versatility of using new synthetic methods (high temperature molten salt in this case) to produce otherwise inaccessible solids with potentially interesting properties.

Future Work

The solids presented herein have the potential to be used in biomedical applications such as antibacterial, antitumor, and antiviral applications. With the preliminary data showing promising results, mainly for antibacterial and antitumor properties, these solids should be further studied to shed light on their use in biomedical applications. The first obstacle of using r-POMs in biomedical applications is their potential toxicity to humans, animals, and the environment. For that reason, thorough toxicity evaluations of these materials are necessary in order to determine their viability for use in various applications. The second obstacle would be their effectiveness related to the currently available materials. For example, the r-POM usage in antibacterial applications would depend on their effectiveness compared to the currently available antibiotics. In the case of antibiotic resistant bacteria such as the SA1199B strain of *Staph. Aureous*, r-POMs would be potential candidates to be used as antibiotics due to their effectiveness of growth inhibition of SA1199B strain.

In regards to the synthesis of new related compounds similar in composition and structure to the $Cs_6X_2Na(PMo_{12}O_{40})$ series, there are several future directions one can take. For example, reducing the cluster even further than the current two-electron reduced state in order to add another data point in the r-POMs series, could potentially be done by doing aliovalent substitutions of the monovalent cations by divalent and trivalent ones. As an

example, attempts to replace Cs^+ by a similar size, divalent cation, Ba^{2+} can be done according to the targeted composition of $Cs_{6-y}Ba_yX_2Na(PMo_{12}O_{40})$ where each Cs replaced by Ba would further reduce the cluster by one electron. This could potentially produce compounds with even higher negative surface charge on the cluster which would be interesting to test and see if the higher negative charge of the POM has improved antibacterial properties.

Given that only the preliminary data for normal human cell toxicity and colon tumor cell toxicity was done using *in vitro* cell viability tests in the presence of r-POM **1**, it is foreseeable that in-depth studies of antitumor properties of r-POMs presented in this dissertation will be done in the near future.

Literature Cited

1. *Introduction to Polyoxometalate Chemistry: From Topology via Self-Assembly to Applications*; Pope, M.T., Müller, A., Eds.; Kluwer, Dordrecht, 2001.

2. Khan, M.I. *J. Solid State Chem*., **2000**, *152*, 105-112.

3. (a) *Polyoxometalate Chemistry for Nanocomposite Design*; Pope, M.T., Yamase, T., Eds.; Kluwer: Dordrecht, 2002.

   (b) Compain, J.-D.; Mialane, P.; Dolbecq, A.; Mbomekalle, I.M.; Marrot, J.; Secheresse, F. Riviere, E; Rogez G.; Wernsdorfer, W. *Angew. Chem., Int. Ed.*, **2009**, *48*, 3077.

4. (a) Rhule, J.T; Hill, C. L; Judd, D.A., *Chem. Rev*., **1998**, *98*, 327.

   (b) Lv, H.; Geletii, Y.V.; Zhao, C.; Vickers, J.W.; Zhu, G.; Luo, Z.; Song, J.; Lian, T.; Musaev, D. G. and Hill, C.L. *Chem. Soc. Rev*. **2012**, 41, 7572-7589.

   (c) Yamase, T.; Fujita H.; Fukushima K. *Inorg Chim Acta*. **1988**, *151*, L15–L18.

5. Inoue, M.; Suzuki, T.; Fujita, Y.; Oda, M.; Matsumoto, N. and Yamase, T. *J. Inorg. Biochem*. **2006**, *100*, 1225-1233.

6. Jasmin C.; Raybaud N.; Chermann J.C.; Haapala D.; Sinoussi F.; Boy Loustau C.; Bonissol C.; Kona P.; Raynaud M. *Biomedicine*. **1973**, *18*, 319–327.

7. Jasmin C.; Chermann J.C.; Herve G.; Teze A.; Souchay P.; Boy Loustau C.; Raybaud N.; Sinoussi F.; Raynaud M. *J. Natl. Cancer Inst*. **1974**, *53*, 463–474.

8. Yamase T.; Fujita H.; Fukushima K. *Inorg. Chim. Acta*. **1988**, *151*, L15–L18.

9. *Antitumor and antiviral activities of certain polyoxometalates.* Yamase T.; Tomita K.; Seto Y.; Fujita H. Technomic Publishing Company Inc., 1992.

10. Spellberg, B.; Shlaes, D. *Clin. Pharmacol. Ther*. **2014**, *96*, 151-153.

11. Bush, K. Courvalin, P.; Dantas, G.; Davies, J.; Eisenstein, B.; Huovinen, P.; Jacoby, G.A.; Kishony, R.; Kreiswirth, B.N.; Kutter, E.; Lerner, S.A.; Levy, S.; Lewis, K.; Lomosvskaya, O.; Miller, J.H.; Mobashery, S.; Piddock, L.J.; Projan, S.; Thomas, C.M.; Tomasz, A.; Tulkens, P.M.; Walsh, T.R.; Watson, J.D.;

Witkowski, J.; Witte, W.; Wright, G.; Yeh, P.; Zgurskaya, H.I. *Nat. Rev. Microbiol*. **2011**, *9*, 894-896.

12. Yamase, T.; Fukuda, N.; and Tajima, Y. *Biol. Pharm. Bull*. **1996**, *19*, 459-465.

13. Yamase, T. *Prog. Mol. Subcell. Biol.*, **2013**, *54*, 65.

14. Queen, W. L.; Hwu, S.-J.; and Reighard, S. *Inorg. Chem*. **2011**, 49, 1316-1318.

15. Gatehouse, B.M.; Miskin, B.K. *Acta Cryst*. **1975**, *B31*, 1293.

16. Kool, F. X. N. M.; Koster, A. S.; and Rieck, G. D. *Acta Cryst.* **1970**, *B26*, 1974.

17. CLSI. *Methods for Dilution Antimicrobial Susceptibility Tests f or Bacteria That Grow Aerobically*; Approved Standard—Ninth Edition. CLSI document M07-A9. Wayne, PA: Clinical and Laboratory Standards Institute; 2012.

18. Shannon, R.D. *Acta Cryst*. **1976**, *A32*, 751-767.

19. (a) Evans, H. T. Jr.; Pope, M. T. *Inorg. Chem*. **1984**, *23*, 501-504.

(b) Niu, J-Y.; Shan, B-Z.; and You, X-Z. *Transition Met. Chem*. **1999**, *24*, 108-114.

20. Duncan, D.C.; Hill, C.L. *Inorg. Chem*. **1996**, *35*, 5828-5835.

21. Borras-Almenar, J. J.; Clemente, J. M.; Coronado, E.; Tsukerblat, B. S. *Chem. Phys*. **1995**, *195*, 1-15.

22. Duclusaud, H.; Borshch, S. *J. Am. Chem. Soc*. **2001**, *123*, 2825-2829.

23. (a) Kozik, M.; Casan-Pastor, N.; Hammer, C. F.; Baker, L. C. W. *J. Am. Chem. Soc*. **1988**, *110*, 7697.

(b) Acerete, R.; Casan-Pastor, N.; BasSerra, J.; Baker, L. C. W. *J. Am. Chem. Soc*. **1989**, **111**, 6049.

(c) Casan- Pastor, N.; Bas-Serra, J.; Coronado, E.; Pourroy, G.; Baker, L. C. W. *J. Am. Chem. Soc.* **1991**, *113*, 5658.

(d) Casan-Pastor, N.; Baker, L. C. W. *J. Am. Chem. Soc*. **1992**, *114*, 10384.

(e) Casan-Pastor, N.; Baker, L. C. W. In *Polyoxometalates: From Platonic Solids to Anti-Retroviral Activity*; Pope, M. T., Müller, A., Eds.; Kluwer Academic Publishers: Dordrecht, 1994; p 203.
(f) Kozik, M.; Baker, L. C. W. In *Polyoxometalates: From Platonic Solids to Anti-Retroviral Activity*; Pope, M. T., Müller, A., Eds.; Kluwer Academic Publishers: Dordrecht, 1994; p 191.

24. (a) Borshch, S. A.; Bigot, B. *Chem. Phys. Lett*. **1993**, *212*, 398.

(b) Borshch, S. A. *Inorg. Chem*. **1998**, *37*, 3116.

25. Borras-Almenar, J. J.; Clemente, J. M.; Coronado, E.; Tsukerblat, B. S. *Chem. Phys*. **1995**, **195**, 17.

26. Maeda, K.; Katano, H.; Osakai, T.; Himeno, S.; Saito, A. *J. Electroanal. Chem*. **1995**, *389*, 167.

27. Maeda, K.; Himeno, S.; Osakai, T.; Saito, A.; Hori, T. *J. Electroanal. Chem.* **1994**, *364*, 149.

28. Sadakane, M.; Steckhan, E. *Chem. Rev*. **1998**, *98*, 219−237.

29. Krulwich, T.A.; Sachs, G.; Padan, Etana. *Nature Rev. Microbiol.* **2011**, *9*, 330-343.

CHAPTER FIVE

SYNTHESIS AND CHARACTERIZATION OF THE TRANSITION-METAL-LINKED REDUCED POLYOXOMETALATE PSEUDO-ONE-DIMENSIONAL NANOSTRUCTURES, $Cs_6X_2M(PMo_{12}O_{40})$ (X = Cl, Br, I and M = Ti, V, Mn, Fe)

Introduction

Early transition metal oxides in their highest oxidation states (*i.e.* V^{5+}, Mo^{6+}, W^{6+}) are known to be electronic insulators with theoretical band gaps between 3 and 4 eV.[1] The molecular orbital theory of these oxides shows that the n*d* (e_g) orbitals of the MO_6 octahedra overlap with six *sp* hybrid orbitals of the oxygen atom to give a set of six σ-bonding and σ^*-antibonding orbitals. The metal *d* (t_{2g}) orbitals overlap with the three surrounding *p* (π) orbitals of the oxygen ligands to form the π bonding and π^* antibonding molecular orbitals. In a bulk material, these newly formed discrete molecular orbitals will broaden into bands which is predicted by the band theory of solids.[2] The newly formed σ and π bands are filled and make up the valence band. The next level in energy is constituted by the π^* band which is called the conduction band. For the fully oxidized early transition metal oxides, their conduction band is empty and therefore these oxides are electronic insulators. The separation between the π and the π^* bands is referred to as the band gap. For oxides such as MoO_3 and WO_3, this gap is between 3 and 4 eV in energy which makes these materials less interesting in terms of their electronic properties. However, in the ternary oxides of the type A_xMO_3 (M = Mo, W; X is typically ~0.3) where A can be alkali, alkali-earth, rare earth elements or hydrogen, interesting electronic properties arise from

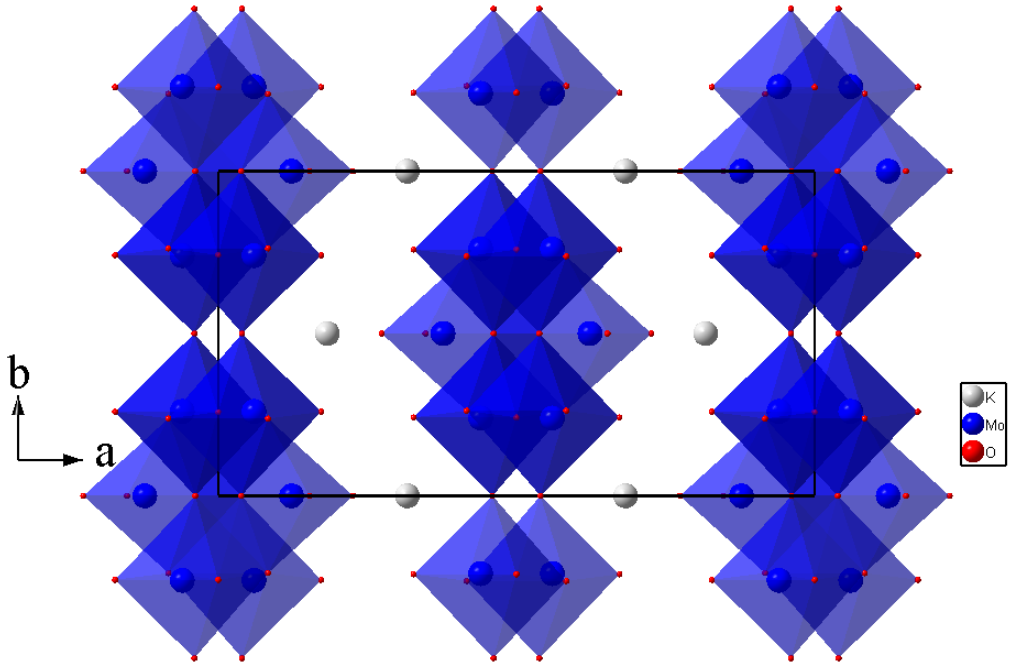

Figure 5.1. The crystal structure of the molybdenum blue bronze[3]

the introduction of valence *d* electrons. These electronically reduced ternary molybdenum and tungsten species were originally called bronzes for their bright colors, obvious metallic appearance, and luster and have attracted interest mainly due to their metallic, semiconducting and, later, superconducting properties. The molybdenum species of the type $A_{0.3}MoO_3$ are also known as 'blue bronzes' for their deep blue color.

The electronic conductivity of A_xMO_3 solids can be explained by the molecular orbital theory and the one-dimensional (1D) metal-oxygen connectivity in their crystal structures.[2] Comparing the molecular orbitals of the fully oxidized MO_3 and the ternary A_xMO_3 solids, the additional electrons, donated by the A-site cations, in the latter occupy the π^* or the conduction band. As such, the π^* electrons in the conduction band can

delocalize along the metal-oxygen-metal pathways, along the *b* monoclinic direction in A_xMoO_3, resulting in electron conductance in the bulk material. Considering the framework dimensionality, these ternary early transition metal bronzes are generally low dimensional solids with 1-dimensional (1D) chains or 2-dimensional (2D) sheets of metal oxygen connectivity.[1]

For example, Figure 5.1 shows the crystal structure of the $K_{0.3}MoO_3$ molybdenum blue bronze.[3,4] $K_{0.3}MoO_3$ crystallizes in the monoclinic space group *C*2/*m* and features rigid molybdenum oxide octahedral, MoO_6, which form clusters of octahedra connected through corner sharing of oxygen and propagate along the monoclinic, *b* crystallographic direction. $K_{0.3}MoO_3$ shows metallic behavior above 180 K.[5, 6] This metallic behavior is due to the electrons donated by the potassium to the empty 4*d* (Mo) conduction band. Low dimensionality or anisotropy in the metal-oxide framework, has shown to be an important feature of many technologically important materials. For example, the success of the microelectronics industry has mostly relied on the development of low dimensional semiconductors. However, in regards to the topic of this dissertation, apart from the hybrid materials, semiconducting or conducting polyoxometalates as standalone materials are not found in literature. This is likely due to the difficulty of obtaining greater than zero-dimensional (0D) polyoxometalate metal-oxide frameworks which contain electron conducting pathways. In addition, given that the majority of polyoxometalates feature early transition metals that are in their fully oxidized states (*i.e.* d^0 configuration), their conduction band, as discussed for MoO_3 and WO_3, is empty resulting in electronically insulating properties of these materials.

Interestingly, the metal-oxygen 1D connectivity in the compounds $Cs_6X_2Na(PMo_{12}O_{40})$, presented in Chapter 4, and the compound discussed in Chapter 3, can easily be envisaged if the insulating sodium ions are to be replaced by a transition metal element to potentially facilitate the delocalization of electrons throughout the metal-oxide chain which features reduced Keggin polyoxometalate clusters. In such a case, the Keggin polyoxometalate clusters would be linked in a one-dimensional chain arrangement along the *c* crystallographic direction resulting in a similar connectivity (with respect to metal-oxygen connectivity) as the one shown for $K_{0.3}MoO_3$ in Figure 5.1.

However, given that the sodium ion in compounds $Cs_6X_2Na(PMo_{12}O_{40})$ and $Cs_6I_3Na(PMo_{12}O_{40})$ is coordinated to eight oxygen atoms, and the fact that the preferred coordination numbers for transition metals are six and four for octahedral and tetrahedral geometries, respectively, it is not immediately intuitive to replace Na^+ ion by a transition metal ion in an eight coordination environment. Inorganic textbooks demonstrate that low coordination numbers (four, five and six) are most common among first-row transition-metals.[7] Less common coordination numbers such as coordination number of eight is rarely observed. In fact, a search of the Cambridge Structural Database (CSD), shows that the eight-coordination geometry of transition metals accounts for less than 1% of all transition metal complexes reported.[8] In addition, square-antiprismatic (D_{4d}) eight-coordination of the transition-metal-containing compounds with structurally rigid, all-inorganic, ligands are not known in literature. It is very exciting and interesting that the first example of such a compound was isolated using molten-salt synthesis approach presented in this chapter. An exploratory reaction targeting the expanded Keggin cluster, $(PV_2Mo_{12}O_{42})^{4-}$, with

vanadium square pyramid caps on opposite ends, resulted in serendipitous isolation of an eight-coordinate, D_{4d}, vanadium cation residing between the neighboring Keggin polyoxometalate clusters.

Literature search for the eight-coordinate transition-metal complexes resulted in a limited number of eight-coordinate first-row transition-metal (TM) compounds.[9, 10, 11] Most examples of the eight-coordinate TM compounds had non-oxo ligands, usually sulfur, nitrogen or phosphorous.[12] Recent paper published by Kortz group identifies several first row TM ions with oxo eight-coordination in a cubic-type arrangement.[13] Interestingly, the authors were able to isolate first-row TM polyoxopalladates ($[M^{II}Pd^{II}_{12}P_8O_{40}H_z]^{(16-n-z)-}$, where M is Mn^{II}, Fe^{III}, Co^{II}, Cu^{II} and Zn^{II}) with eight-coordinate TMs being trapped inside the palladium-oxide framework in a cubic-type arrangement. The TM-oxygen bond distances in these unusually coordinated complexes range from 2.078 Å to 2.369 Å. Recently, Chen and coworkers published a Co^{II} eight-coordinate oxo D_{4d}, complex showing interesting magnetic properties with slow magnetic relaxation and stepped-magnetization.[14] The authors argue that the Co^{II} single ion magnet (SIM) is due to anisotropy reminiscent of that in single molecule magnets (SMMs).

What can be seen from the examples above and the fundamental knowledge from inorganic chemistry textbooks is that an important aspect of a metal in regards to its ability to form eight-coordinate geometry is its size. Intuitively, the larger the ionic radius of a metal, the more likely it is to accommodate eight ligands in order to form eight-coordinate geometry. This is expected as larger metals are more likely to reduce the anion-anion electrostatic repulsion of the donor ligand atoms. Pauling suggested that for common eight-

coordinate geometries (square-antiprism and dodecahedron), a cation-anion ratio of at least 0.67 is necessary for stabilizing an eight-coordinate compound.[15] In addition to its size, the formal charge of the metal is also significant. Based on the literature search, a general trend can be noticed in regards to the formal charge of the metal in an eight-coordinate environment. Namely, eight-coordination mainly occurs in complexes where it is possible for metal atoms to be in a d^0, d^1, d^2 electronic configuration as is the case for Zr(IV) or Mo(IV, V).[16, 17] It has also been predicted that the chelate effect of the ligand tends to stabilize the unusual eight-coordinate complexes.[18] Given that the Keggin polyoxometalate can be thought of being as a polydentate ligand due to its large number of oxygen atoms, it is expected that a transition metal will be stabilized by being trapped by the chelate effect of the multi-dentate oxygen sites on the Keggin polyoxometalate.

Based on the single crystal structure of $Cs_6Cl_{1.56}V(PV_{2.18}Mo_{9.82}O_{40})$ (**1**), **1** features a vanadium cation in its eight-coordinate, VO_8, square-antiprismatic environment between the neighboring Keggin polyoxometalate clusters. This arrangement of the vanadium cation and the Keggin clusters results in infinite 1-dimensional (1D) chains of metal-oxide connectivity. The discussion in this chapter will largely focus on the synthesis of related derivative compounds based on $Cs_6X_2M(PMo_{12}O_{40})$, where X = Cl, Br, I and M = Ti, V, Mn and Fe. The structure of these compounds will be discussed in detail especially as it pertains to the 1D metal-oxide chain and the unusual square-antiprismatic eight-coordination of the transition-metal. Several derivatives were able to be synthesized in high yield including, $Cs_6Cl_2V(PMo_{12}O_{40})$ (**2**), $Cs_6Cl_2Ti(PMo_{12}O_{40})$ (**3**), $Cs_6Cl_2V(PVMo_{11}O_{40})$ (**4**), $Cs_6I_2V(PMo_{12}O_{40})$ (**8**), $Cs_6I_2V(PVMo_{11}O_{40})$ (**9**), $Cs_6Cl_2Mn(PMo_{12}O_{40})$ (**10**), and

$Cs_6Cl_2Fe(PMo_{12}O_{40})$ (**11**). The synthesis of different derivatives, especially pertaining to the identity of M, provides a unique possibility to study the properties of these compounds as a function of the change of M and the *d* valence electron count (*e.g.* d^4 vs d^5 for Mn^{3+} and Fe^{3+}, respectively). In addition to the synthesis and structure description, some property measurements including magnetic susceptibility on compounds **2** , **3**, **10** and **11** were performed.

Synthetic Procedure and Discussion

Single Crystal Growth of $Cs_6Cl_{1.56}V(PV_{2.18}Mo_{9.82}O_{40})$ (1): The original reaction which produced the $Cs_6Cl_{1.56}V(PV_{2.18}Mo_{9.82}O_{40})$ single crystals was targeting a slightly modified structure of the compound presented in Chapter 4, $Cs_6Cl_2Na(PMo_{12}O_{40})$. Namely, attempts were made to synthesize the vanadium-capped expanded Keggin cluster with the formulation of $(PV_2Mo_{12}O_{42})^{4-}$. The two vanadium (IV) atoms were targeted to be at the opposite ends of the cluster that would potentially occupy the square oxygen windows of the Keggin cluster. However, it was initially thought that even though the $[Cs_6Cl_2]_\infty$ salt lattice was targeted, the same structure as the one in Chapter 4 compounds (*i.e.* $Cs_6Cl_2Na(PMo_{12}O_{40})$) may not be possible because of the lack of sodium ions to make a link for the infinite chain between Keggin clusters. Rather, for this particular exploratory reaction, a similar system was explored with small modifications to the starting materials in hopes of synthesizing a new polyoxometalate compound that does not necessarily resemble the structure of those described in Chapter 4. Though the $[Cs_6Cl_2]_\infty$ salt lattice in the targeted phase resembles that in compounds in Chapter 4, the $[Cs_6Cl_2]_\infty$ salt was merely used to balance the 4- charge of the expanded Keggin. A stoichiometric reaction targeting $Cs_6Cl_2(PV_2Mo_{12}O_{42})$ was loaded with Cs_2MoO_4, CsCl, VO_2, MoO_3, MoO_2, P_4O_{10} in a 2:2:2:7.5:2.5:0.25 molar ratios, respectively. The total mass of the reactants was 0.3 grams. It should be noted that in this reaction, a stoichiometric product was targeted and no excess salt flux was used. From previous experience targeting similar systems, it could be observed that single crystals formed without the presence of excess flux which likely suggests that the temperature used in such reactions was sufficiently high enough for

melting of the reaction mixture and formation of single crystals. The above mentioned reactants were weighed and ground inside a nitrogen-purged glovebox. As a side note, MoO_3 oxide being a fine powder was difficult to measure accurately due to it sticking to the weighing boat. However, extra careful approach was taken when weighing while making sure to transfer all of MoO_3 to the mortar with gentle shaking of the weighing boat.

In regards to the starting materials, the Cs_2MoO_4 precursor was synthesized using a solid state approach with Cs_2CO_3 and MoO_3 as the reactants. This procedure is described in greater detail in Chapter 3. The grinding of the reactants for the synthesis of **1** took place for approximately five minutes or until the entire mixture looked homogeneous to the observer. Next, the reactants were scraped off and transferred into fused-silica tubes and a glass connector was connected to seal the reactants from the outside environment while taking the reaction mixture out of the glovebox and attaching the tubes to the vacuum line. While the tubes were connected to the vacuum line, they were flame sealed using a flame torch. The sizes of the sealed ampoules were approximately 10 cm in length. Then, the sealed ampoules were wrapped in heating blankets and were placed inside a standard box furnace for the heating step. The reaction mixture was heated to 500 ^oC in four hours and was allowed to isotherm at 500 ^oC for 48 hours. After the isotherm step, the reaction was cooled to 350 ^oC at a slow rate (72 hours cooling) in order to promote single crystal growth. The reaction was then cooled to 150 ^oC in 24 hours and was allowed to furnace cool to room temperature. After the heating, the reaction ampoule was broken and placed in a petri dish for product analysis and observation. Given that no salt flux was used in this reaction, the product was not washed with DI water. Instead, the entire product was placed under an

optical microscope to observe the reaction product(s). Small (~0.2 mm in longest dimension) black columns/needles were able to be seen growing on the side of the glass at the bottom of the tube. The largest portion of the product remained towards the bottom of the tube and obvious melt occurred based on the observation of the shiny faces and the single homogeneous chunk. The color of the product was the same for both the columns/needles as well as for the large chunk both being black in color. Several single crystals were separated and mounted for single crystal X-ray diffraction analysis. The remaining product, including the large black chunk, was ground and subjected to X-ray powder diffraction. Looking at the powder X-ray diffraction pattern in Figure 5.2, it can be observed that the overall product powder pattern largely resembles that of the synthesized single crystals of $Cs_6Cl_{1.56}V(PV_{2.18}Mo_{9.82}O_{40})$ based on the calculated powder pattern using the single crystal X-ray structure solution. This suggests that the bulk of the product is compound **1** which should be expected as the reaction stoichiometry was not far off from the composition of compound **1**. Intensity mismatch is evident when comparing the calculated of **1** and the observed pattern possibly due to the preferred orientation given that column/needle shaped crystals were present in the reaction product. In the figure, calculated diffraction patterns for CsCl and $Cs_6Cl_2Na(PMo_{12}O_{40})$ are also included for comparison.

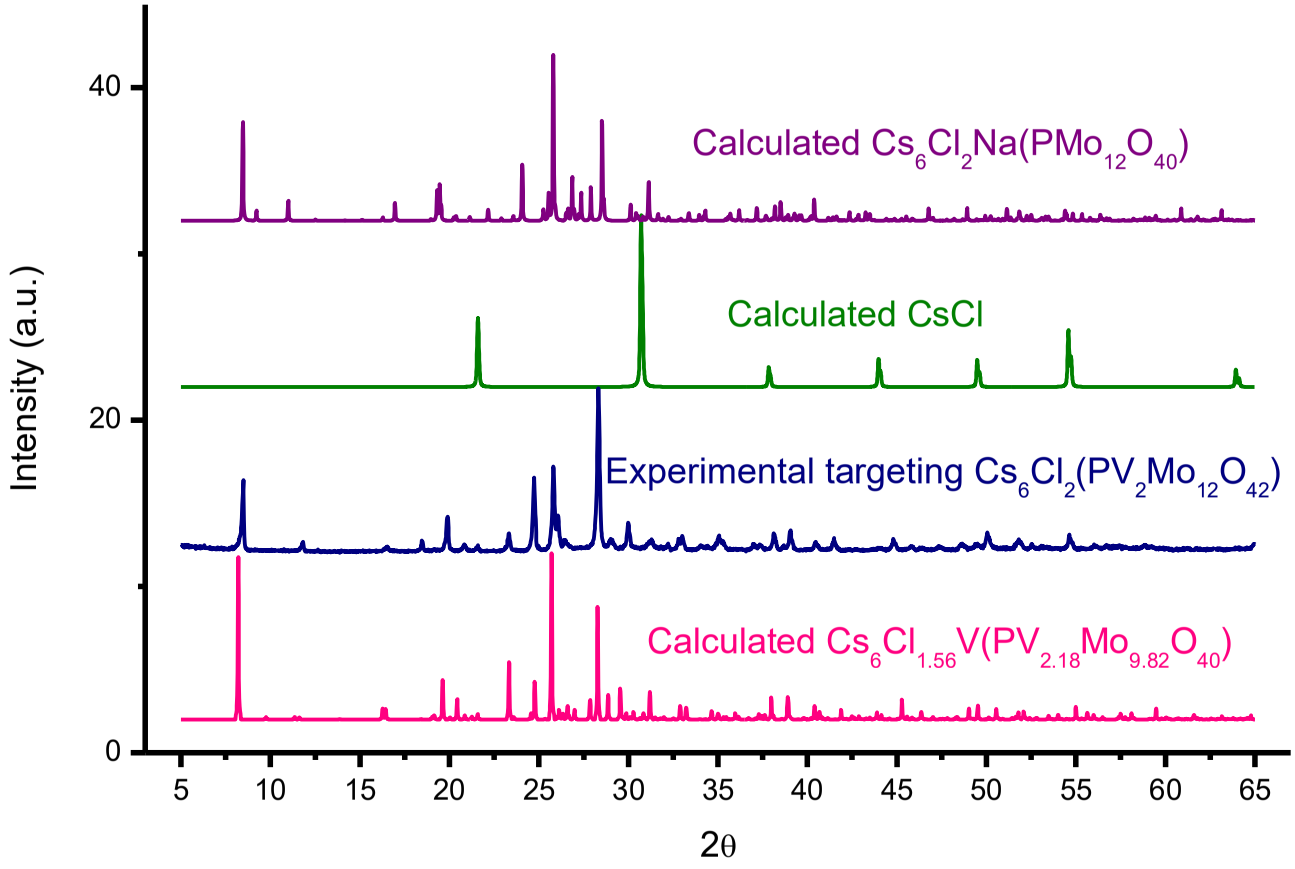

Figure 5.2: PXRD of the overall product of the single crystal growth reaction where $Cs_6Cl_{1.56}V(PV_{2.18}Mo_{9.82}O_{40})$ (**1**) was synthesized.

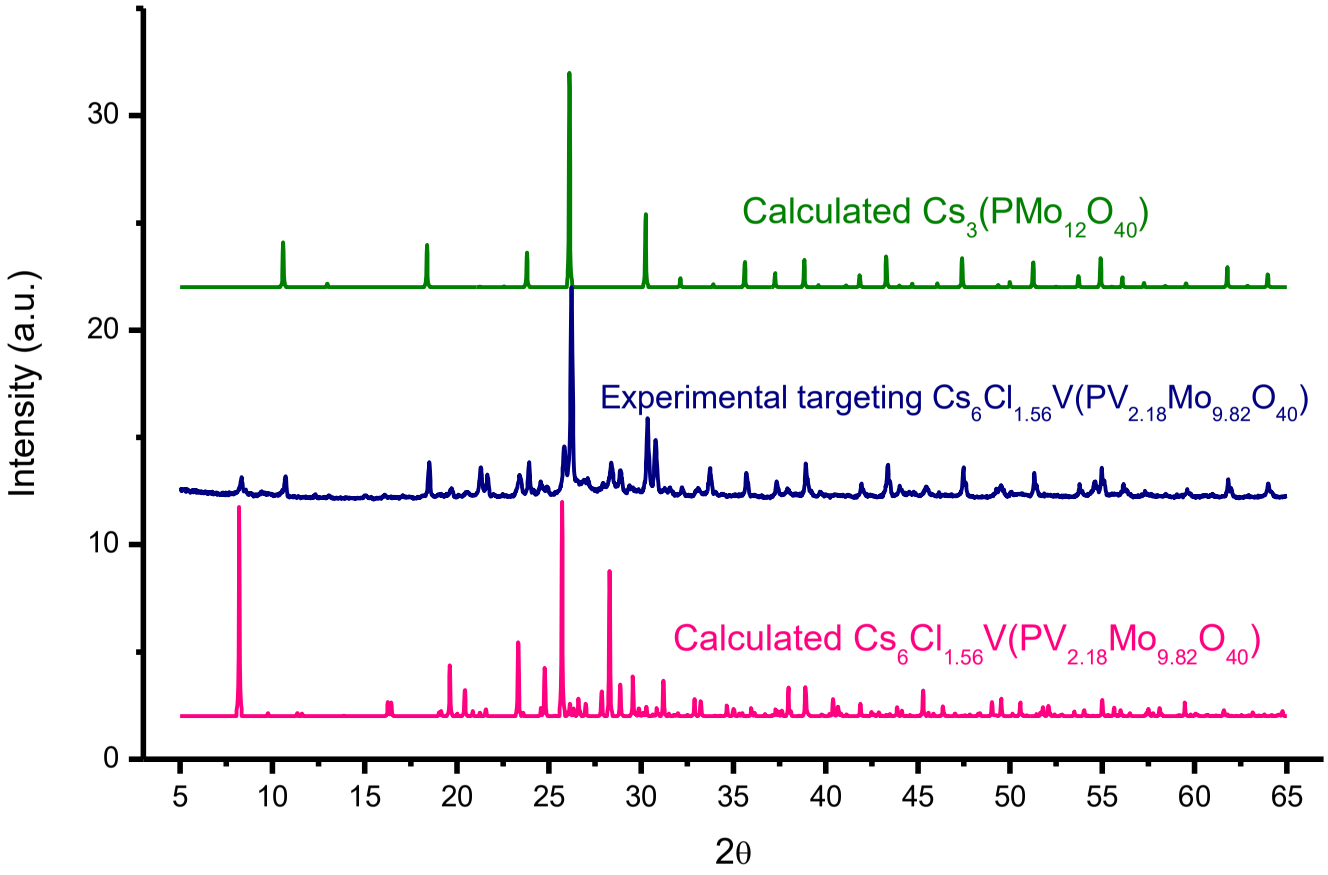

Figure 5.3: PXRD of the attempted stoichiometric high yield synthesis of the disordered, $Cs_6Cl_{1.56}V(PV_{2.18}Mo_{9.82}O_{40})$, composition based on the single crystal X-ray solution.

High Yield Synthesis of $Cs_6Cl_{1.56}V(PV_{2.18}Mo_{9.82}O_{40})$ (1): Stoichiometric synthesis of the disordered compound **1,** was attempted using Cs_2MoO_4, CsCl, VO_2, MoO_3, MoO_2 and P_4O_{10} in the following molar ratios 2.22:1.56:3.18:7.06:0.54:0.25, respectively. Looking at the starting materials, several redox active species are present which complicates things when specific oxidation states are targeted for certain transition metal sites. For example, controlling the reaction conditions to target a specific oxidation state of V, exclusively, in ($PV_{2.18}Mo_{9.82}O_{40}$) may not be possible due to potentially competing redox chemistry occurring between V and Mo. Rather, controlling the overall (average) oxidation states of both V and Mo in ($PV_{2.18}Mo_{9.82}O_{40}$) is more conceivable. As such, the above reaction relied on the assumption that the lattice energy of a stoichiometric composition (*i.e.* no side products/impurity phases) of the targeted product, would aid in the 'averaging' of the competing redox chemistries and the formation of **1**. Given that **1** is largely disordered with respect to the occupancy of several atomic sites, initial stoichiometric reaction targeting the disordered phase, **1**, was loaded. The reactants were weighed and ground inside a nitrogen-purged glovebox and were transferred into an agate mortar. The reactants were then ground until a visible homogeneous mixture was obtained. Usually, the grinding process took place between five and ten minutes. The ground mixture of reactants was then transferred into fused silica tubes and a glass connector was attached to the tubes to prevent exposure to air while bringing the reaction outside the glovebox. The silica tube with attached glass connector was connected to the vacuum line and was flame sealed and cut using a flame torch. Next, the sealed ampoule was placed inside a standard box furnace for the heating step. The reaction was heated to 500 ^oC in five hours

and was allowed to isotherm at this temperature for 48 hours. Cooling of the reaction took place in 5 hours from 500 ^{o}C to 25 ^{o}C. Given that a stoichiometric polycrystalline powder was targeted, the cooling of the reaction was relatively fast as single crystals were not targeted in this reaction. Figure 5.3 shows the powder X-ray diffraction pattern of the attempted stoichiometric reaction for **1** (shown in blue color, middle line). The bottom, pink colored, powder pattern is the calculated pattern based on the single crystal structure solution of **1**. The top powder pattern in this figure is the calculated pattern for the $Cs_3(PMo_{12}O_{40})$ which was commonly synthesized as a by-product in some previous reactions including those targeting compounds in Chapters 3 and 4. This Keggin-based compound contains the fully oxidized Mo^{6+} sites and can be considered as a thermodynamic 'sink' phase in the reaction systems where molybdenum is preferentially oxidized to its formal 6+ oxidation state. Based on the comparison of the powder patterns in Figure 5.3, it can be concluded that $Cs_3(PMo_{12}O_{40})$ is the main product of the above reaction. In addition, low intensity peaks matching the calculated powder pattern of compound **1** can also be seen in the experimental powder pattern. This is especially evident when looking at the low angle peak, around eight 2θ. Based on the results of the powder X-ray analysis of the targeted stoichiometric reaction, the title compound did not form or formed in a very small yield. The reason for this might be because under the conditions employed for this particular reaction, a thermodynamic 'sink' phase in the form of $Cs_3(PMo_{12}O_{40})$ is preferentially synthesized. This is somewhat different compared to the single crystal synthesis where slower cooling might have helped with the formation of single crystals of **1**. Because the majority of the formed product ($Cs_3(PMo_{12}O_{40})$) contains

the fully oxidized Mo^{6+} cations, a significant amount of the reduced species should also be present. One source of the reduced metal centers likely is part of the small amount of the synthesized $Cs_6Cl_{1.56}V(PV_{2.18}Mo_{9.82}O_{40})$ or related phases. However, definite answer of the product distribution and the redox reactions occurring is complicated by a large number of variables particularly the presence of multiple redox active species in vanadium and molybdenum metals. Based on the failed attempt of the stoichiometric synthesis of the disordered, $Cs_6Cl_{1.56}V(PV_{2.18}Mo_{9.82}O_{40})$ phase, new reactions targeting non-disordered phase were targeted with $Cs_6Cl_2V(PMo_{12}O_{40})$ composition. Note that this composition is identical to the one described in Chapter 4 except that a sodium cation is replaced by a vanadium cation.

High Yield Synthesis of $Cs_6Cl_2V(PMo_{12}O_{40})$ (2): Stoichiometric high yield synthesis of **2**, was attempted using a similar procedure as the one for compound **1**. However, in the case of **2**, the synthesis was targeting a non-disordered phase. Cs_2MoO_4, CsCl, VO_2, MoO_3, MoO_2 and P_4O_{10} were loaded in 2:2:1:7.5:2.5:0.25 molar ratios with the total amount of reactants being 0.5 g. The reactants were weighed and ground inside a nitrogen-purged glovebox before being transferred into fused silica tube with the glass connector being subsequently attached to the tube. The reaction was then brought out of the glovebox and attached to the vacuum line. The tube was evacuated and was flame sealed using a torch flame. Next, the reaction was placed inside a standard box furnace and the same heating program was used as for the attempted stoichiometric synthesis of **1**. A homogenous black polycrystalline chunk was found at the bottom of the tube. This solid chunk was ground using an agate mortar and pestle and was used for powder X-ray

diffraction. Looking at the Figure 5.4, it can be seen that a high yield stoichiometric synthesis reaction was successful based on a close match with the calculated powder pattern. It should be noted that the calculated powder pattern was obtained from the single crystal structure solution of **1**. However, the occupancy of the disordered atomic sites was changed to 100% occupancy and no disorder in the molybdenum sites was used in the simulation of the powder pattern. In addition to the qualitative comparison of the observed and calculated powder patterns, profile refinement was used to show a close match between the calculated and experimental powder patterns as well as to extract the unit cell parameters from the powder pattern. Figure 5.5 shows the refined powder pattern with observed intensities shown using crosses, the red line represents the calculated and blue is the difference. Vertical orange ticks represent the Bragg reflections. Above this graph is a table which shows the unit cell parameters of the single crystal structure solution of the disordered phase, **1**, as well as the profile refined parameters of the high yield synthesis of the non-disordered phase, **2**. Looking at the numbers of the SXRD vs. PXRD unit cell parameters, it can be seen that there is a very close match in the unit cell dimensions of the two. One might expect slight differences due to the disordered state of compound **1** vs. the ordered state of compound **2**. For example, in compound **1**, partial occupancy of the Cl sites as well as the shared occupancy of the Mo sites, may lead to shorter unit cell dimension(s) in one or more directions as can be seen by comparing *a*, *c* axes lengths and the volume. However, based on the numbers shown in the table, these differences are likely insignificant.

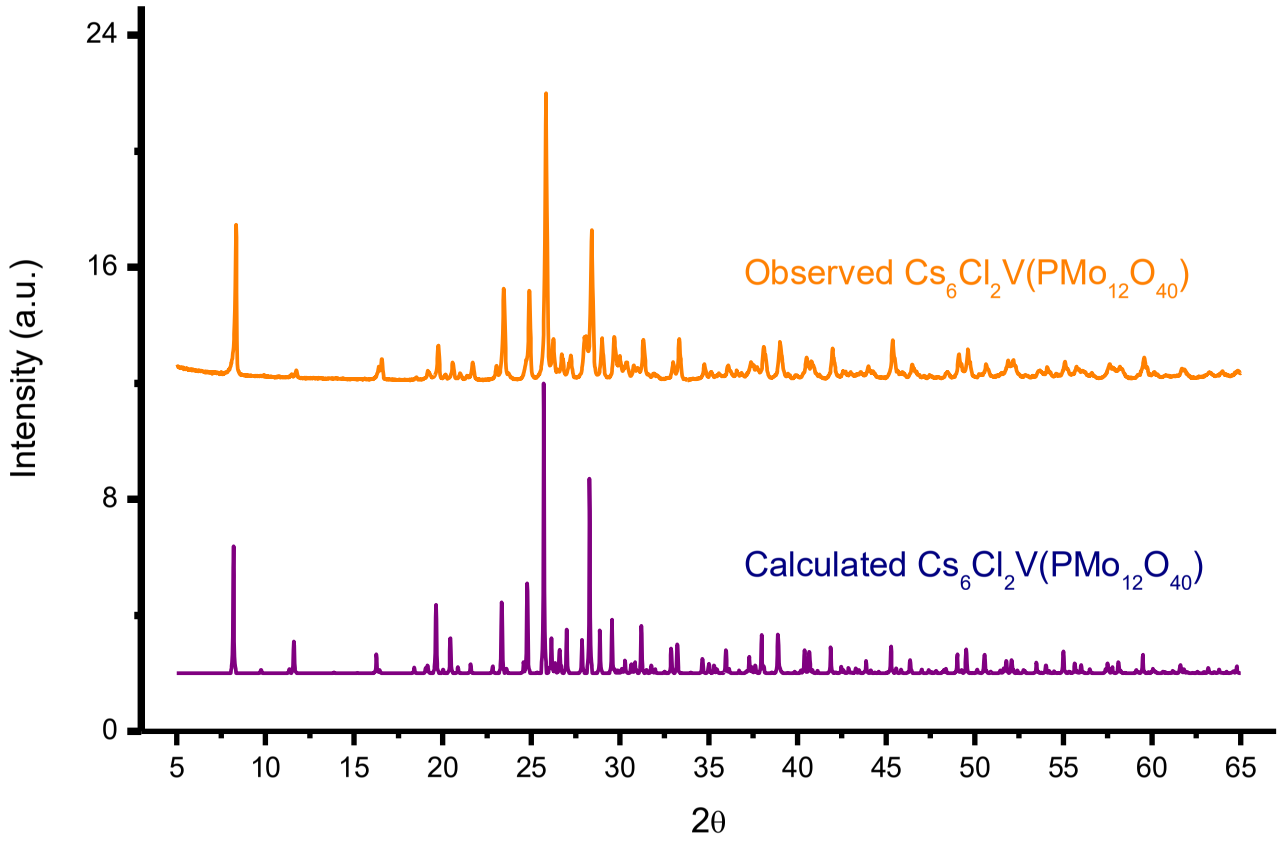

Figure 5.4: PXRD pattern of a high yield synthesis attempt of $Cs_6Cl_2V(PMo_{12}O_{40})$. The calculated pattern is based on the single crystal structure solution of **1**. However, the powder pattern represents the non-disordered phase with full occupancy of the atomic sites.

			SXRD			
a (Å)	*b* (Å)	*c* (Å)	α (deg.)	β (deg.)	γ (deg.)	*V* (Å^3)
15.2395(1)	15.2395(1)	18.1251(2)	90	90	90	4209.42(53)
			PXRD			
a (Å)	*b* (Å)	*c* (Å)	α (deg.)	β (deg.)	γ (deg.)	*V* (Å^3)
15.2524(4)	15.2524(4)	18.1318(6)	90	90	90	4218.09(60)

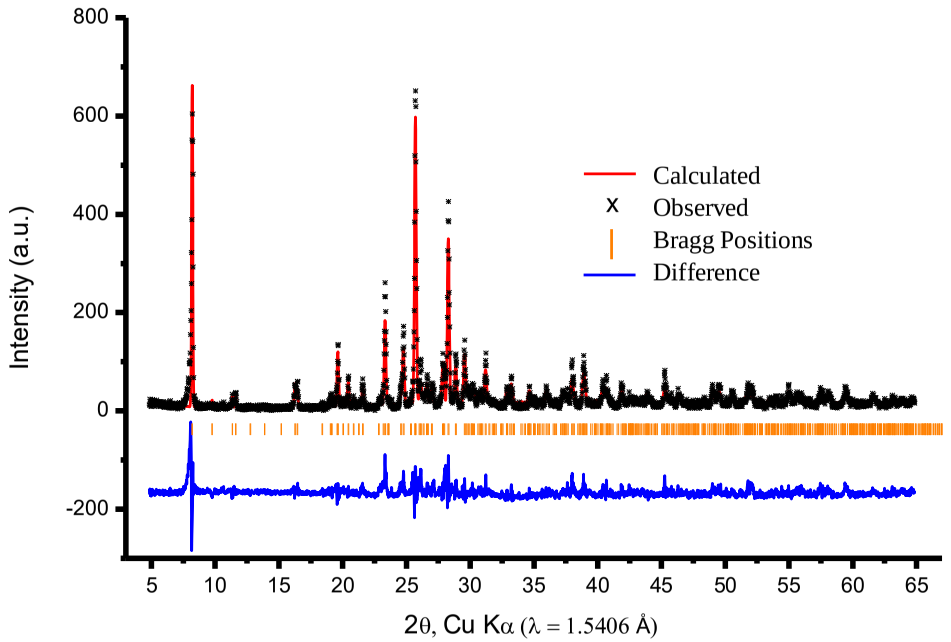

Figure 5.5: Profile refinement of the PXRD pattern of the synthesized $Cs_6Cl_2V(PMo_{12}O_{40})$, **2**, compound with the unit cell dimensions comparison shown in the table above. The SXRD data is based on the disordered compound, **1**.

High Yield Synthesis of $Cs_6Cl_2Ti(PMo_{12}O_{40})$ (3): Stoichiometric yield synthesis of **3** was attempted, where the attempts to replace the V^{4+} starting material was replaced by the d^0 cation, Ti^{4+}. As mentioned above, it was originally believed that the M in $Cs_6Cl_2M(PMo_{12}O_{40})$ was tetravalent (see discussion section below). In this reaction, Cs_2MoO_4, CsCl, TiO_2, MoO_3, MoO_2 and P_4O_{10} were used in 2:2:1:7.5:2.5:0.25 molar ratios, respectively. The total amount of reactants was 0.5 grams and the reaction conditions including the heating/cooling program was the same as for the synthesis of **2**. The product of this reaction was a very dark blue polycrystalline chunk which was ground and a powder X-ray diffraction analysis was done for phase identification/confirmation. Looking at the powder pattern in Figure 5.6, a close match between the calculated and the observed can be seen which indicates a successful stoichiometric synthesis of **3**.

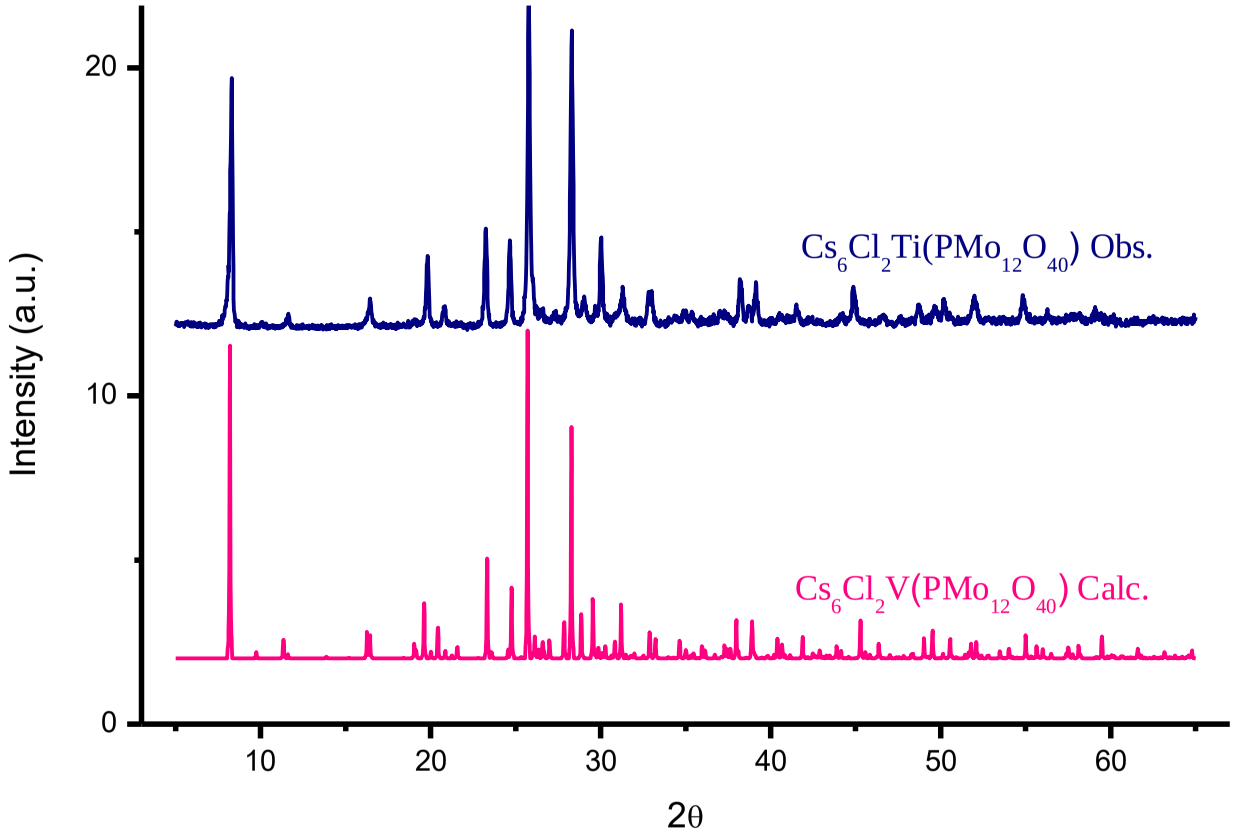

Figure 5.6: PXRD pattern of a high yield synthesis attempt of $Cs_6Cl_2Ti(PMo_{12}O_{40})$. The calculated pattern is based on the single crystal structure solution of **1**. However, the powder pattern represents the non-disordered phase with full occupancy of the atomic sites.

Stoichiometric Attempt Syntheses of $Cs_6Cl_2V(PV_xMo_{12-x}O_{40})$, where x = 1 (4); x = 2 (5); x = 3 (6); x = 4 (7): Attempts to synthesize high yield stoichiometric powders of compounds **4**~**7** were made. Because the original single crystal growth reaction produced disordered Keggin cluster with Mo sites being shared with vanadium, attempts to synthesize a solid solution series of the Keggin cluster with the formulation of $(PV_xMo_{12-x}O_{40})^{8-}$ were made. In these reactions, the $[Cs_6Cl_2]$ salt lattice and the linking vanadium cation were kept constant for compounds **4**~**7**. It should be noted that in the synthesis of **4**~**7**, the vanadium atoms that are part of the Keggin cluster framework were targeted to be in the V^{5+} oxidation state. The reduced sites were the Mo atoms with four Mo^{5+} for **4**, three Mo^{5+} for **5**, two Mo^{5+} for **6** and one Mo^{5+} for **7**. Due to the complexity of the chemical system and the presence of multiple redox active transition metal species such as Mo^{6+}, Mo^{5+}, V^{5+} and V^{4+}, it is difficult to know which species will be oxidized and which ones will be reduced. Compound **4** was synthesized using Cs_2MoO_4, CsCl, VO_2, MoO_3, MoO_2, V_2O_5 and P_4O_{10} in the following molar ratios 2:2:1:7:2:0.5:0.25, respectively. The reactants were weighed and ground inside a nitrogen-purged glovebox and were loaded into fused silica tubes. The remaining synthesis procedures including the heating and cooling programs were followed exactly as for compounds **2** and **3**. Compounds **5**~**7** were synthesized using the same procedure as for **4** except that different amounts of V_2O_5, MoO_3 and MoO_2 were used to target stoichiometric compositions. Powder X-ray diffraction was used for phase identification and phase confirmation of the targeted compositions of compounds **4**~**7**. The color of compounds **4**~**7** was black for **4**, grey for **5** and yellow/green for **5**, **6** and **7**. Figure 5.7 shows the PXRD patterns of the as-prepared products for

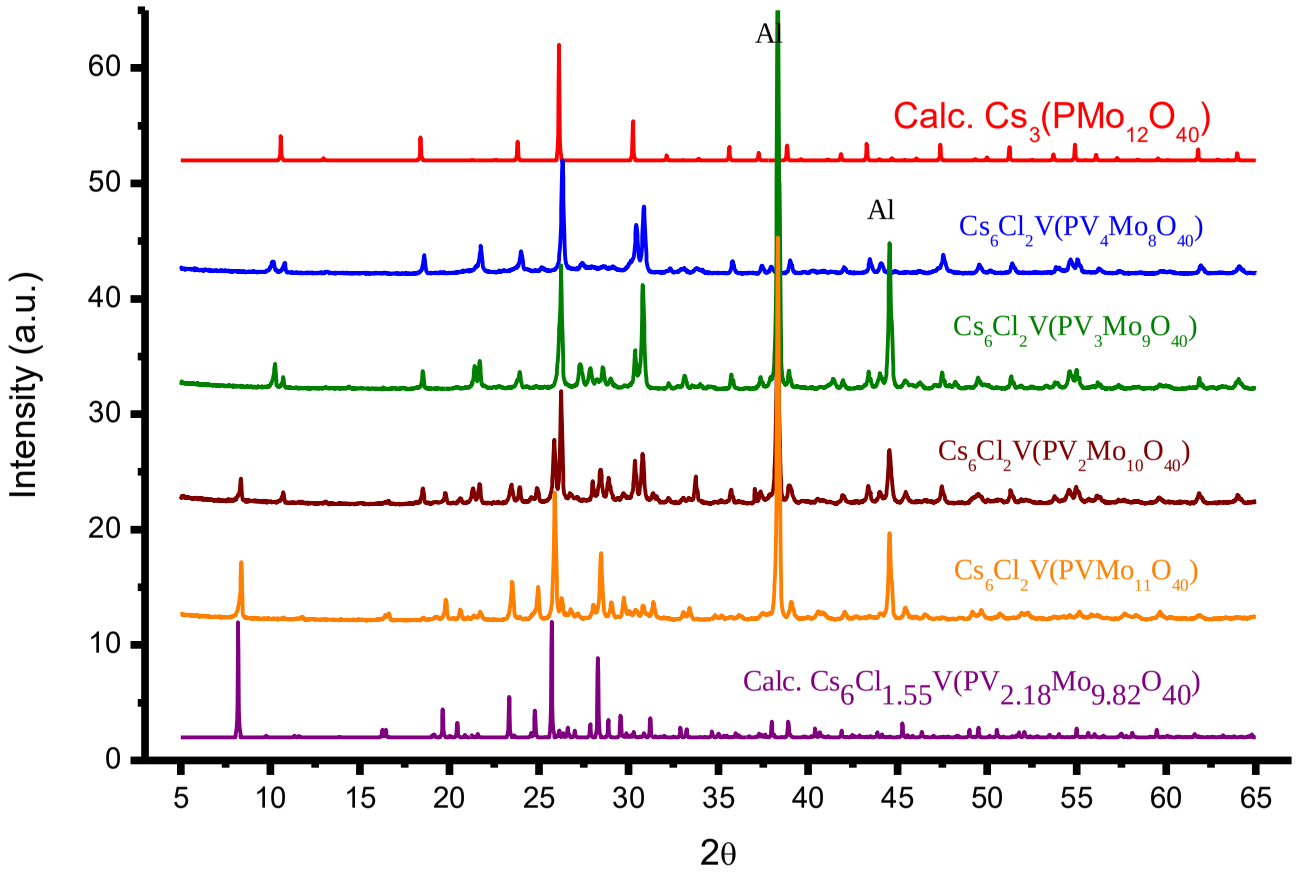

Figure 5.7: PXRD pattern of a stoichiometric yield synthesis attempt reactions for compounds **4**~**7**. The peaks around 37 and 44 2θ correspond to the aluminum peaks from the sample holder.

compounds **4**~**7**. Based on the obtained PXRD patterns, it can be observed that compound **4**, with x = 1, formed with few impurity peaks present. The large peaks around 38 and 44 2θ are due to the aluminum sample holder diffracting as a result of a small sample size used for PXRD. Moving on to x = 2 composition, some impurity peaks start to show up. In addition, the intensity of the first peak corresponding to the targeted phase decreases which could be an indication of the decrease in the amount of the targeted phase. Careful analysis of the powder patterns resulted in identification of the impurity peaks. These impurity peaks correspond to the fully oxidized Keggin-based polyoxometalate compound, $Cs_3(PMo_{12}O_{40})$ which is considered a thermodynamic sink and has been a common occurrence in many reactions as discussed so far in this dissertation. With increasing x from 2 to 4, this impurity phase tends to increasingly dominate while the formation of the targeted phases is completely suppressed with x = 3 and x = 4. The reason for this preferential formation of the fully oxidized, $Cs_3(PMo_{12}O_{40})$ compound, can be rationalized by the relatively easy reducibility of V_2O_5 by MoO_2 and the preference of molybdenum to be in its highest oxidation state. The oxidation of MoO_2 to MoO_3 and the progressive increase of MoO_3 in **4**~**7** likely is the key factor contributing to the formation of the fully oxidized $Cs_3(PMo_{12}O_{40})$ compound. This point will be further discussed below. Overall, the attempted synthesis reactions of **4**~**7** were partially successful with only the compound **4**, with x = 1, formed.

Stoichiometric Attempt Syntheses of $Cs_6I_2V(PMo_{12}O_{40})$ (8) and $Cs_6I_2V(PVMo_{11}O_{40})$ (9): To show the versatility of the title series of compounds with respect to the salt lattice replacement, stoichiometric reactions targeting $[Cs_6I_2]$ salt lattice

were attempted. Reactions using similar reactants as for compounds **1**~**7** were loaded with stoichiometric compositions targeting compounds **8** and **9**. CsI was used for **8** and **9** in place of CsCl reactant. The remaining reaction conditions were the same as for the stoichiometric synthesis of compounds **2**~**7**. Based on the analysis of powder patterns from Figure 5.8, it can be seen that a close match exists between the calculated "$Cs_6I_2V(PMo_{12}O_{40})$" and the observed powder patterns for **8** and **9**. It should be mentioned that the calculated powder pattern for "$Cs_6I_2V(PMo_{12}O_{40})$" in Figure 5.8 was obtained from the single crystal structure solution of **1**, where chlorine was replaced by iodine and the occupancy of the molybdenum sites was set to 100% without vanadium sharing the same sites. The original calculated powder pattern of the disordered phase **1** is shown for comparison (top line) in Figure 5.8. Even though a very close match of the peak positions can be observed, some intensity mismatch is evident. This intensity mismatch could be due to the preferred orientation or a disorder in the composition of atomic sites. However, given that a stoichiometric reaction was targeted and no extra impurity peaks can be identified, it is more likely that the mismatch in intensities between observed and calculated patterns is due to preferred orientation.

Stoichiometric Attempt Syntheses of $Cs_6Cl_2Mn(PMo_{12}O_{40})$ (10) and $Cs_6Cl_2Fe(PMo_{12}O_{40})$ (11): Reactions targeting Mn and Fe derivatives were attempted. Stoichiometric reactions with respect to the composition as well as the oxidation states of the metals in the targeted phase were loaded using the following reactants: Cs_2MoO_4, CsCl, M_2O_3 (M = Mn, Fe), MoO_3, MoO_2, and P_4O_{10} using the molar ratios 2:2:0.5:8:2:0.25, respectively. The reactants were weighed and ground inside a nitrogen-purged glovebox

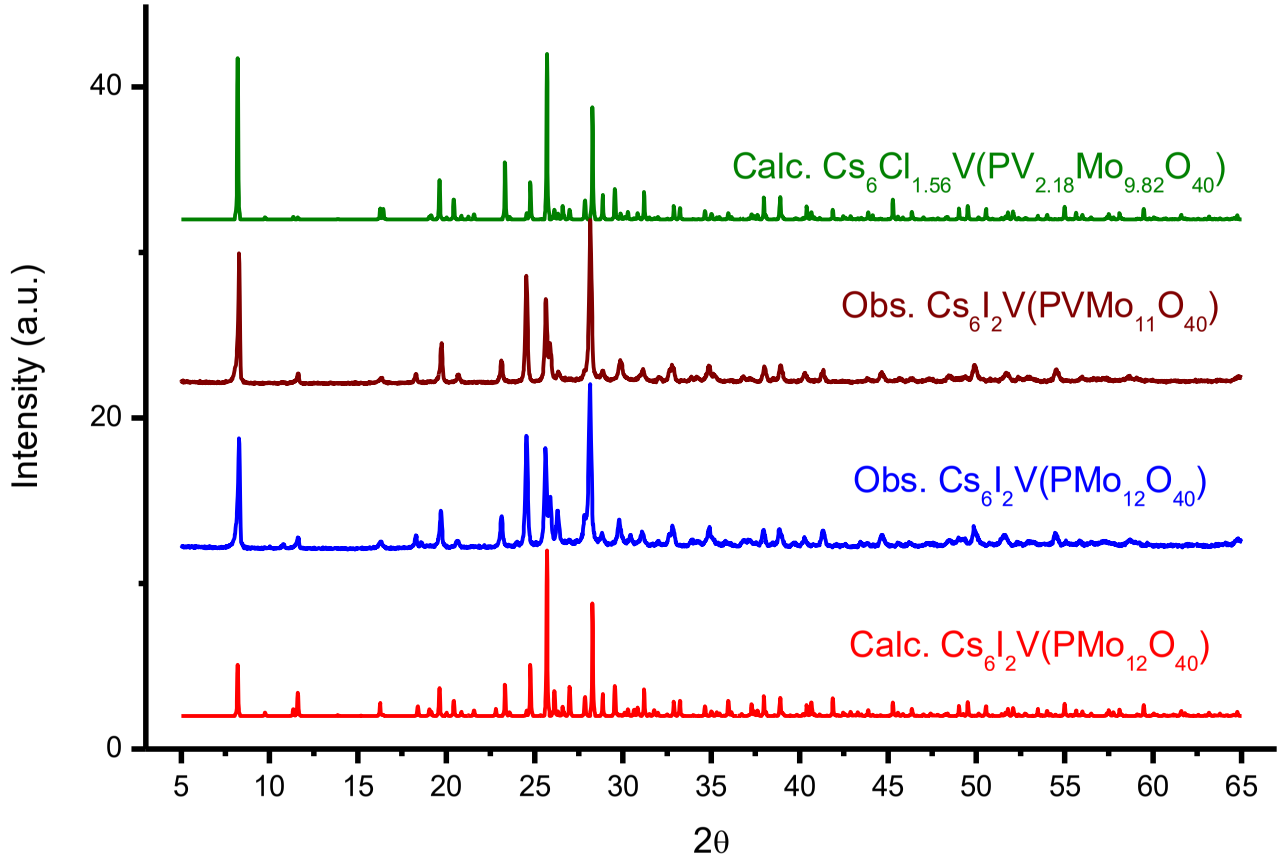

Figure 5.8: PXRD pattern of a stoichiometric yield synthesis attempt reactions for compounds **8**~**9**. The calculated powder pattern shown in red for $Cs_6I_2V(PMo_{12}O_{40})$ was obtained from the single crystal structure solution of **1**.

and were transferred into fused silica tubes before being evacuated and sealed using a torch flame. The heating program consisted of heating the reactions to 480 ^{o}C at a rate of 1 ^{o}C per minute and dwelling at 480 ^{o}C for two days. The cooling process was set to 25 ^{o}C at a rate of 1 ^{o}C per minute. Black polycrystalline powders were retrieved by breaking the silica ampoules and grinding the products. Powder X-ray analysis of compounds **10** and **11** shown in Figure 5.9 reveals that a close match exists with the calculated powder pattern based on $Cs_6Cl_2V(PMo_{12}O_{40})$ (**2**). It is interesting to point out that compounds **10** and **11** formed with, presumably, Mn and Fe atoms adopting the unusual square antiprismatic geometry between the Keggin clusters. However, another option is that the Mn and Fe atoms are part of the Keggin framework, replacing one of the Mo atoms. It is possible that the Mo atom is occupying the square antiprismatic geometry between the neighboring Keggin clusters. Based on the literature search, it seems more likely that the larger Mo^{4+} would adopt the square antiprismatic geometry compared to the smaller Mn^{3+} and Fe^{3+} ions. Single crystal structures of these compounds would be able to show whether the Mn^{3+} and Fe^{3+} atoms adopt the unusual square antiprismatic eight-coordination.

Stoichiometric Attempt Synthesis of $Cs_6Cl_2V(PMo_{12}O_{40})$ Using a V^{3+} source: It was originally believed that the vanadium site linking the neighboring clusters was formally V^{4+} and for that reason, VO_2 was used as the starting material in the original synthesis of **2**. However, the bond valence sums calculations, as discussed below, indicate that the vanadium is formally V^{3+}. Attempts to synthesize **2** using V_2O_3 as the V^{3+} source were done. Cs_2MoO_4, CsCl, V_2O_3, MoO_3, MoO_2 and P_4O_{10} were loaded in a 2:2:0.5:8:2:0.25 molar ratios, respectively, with the total amount of reactants being 0.3 g.

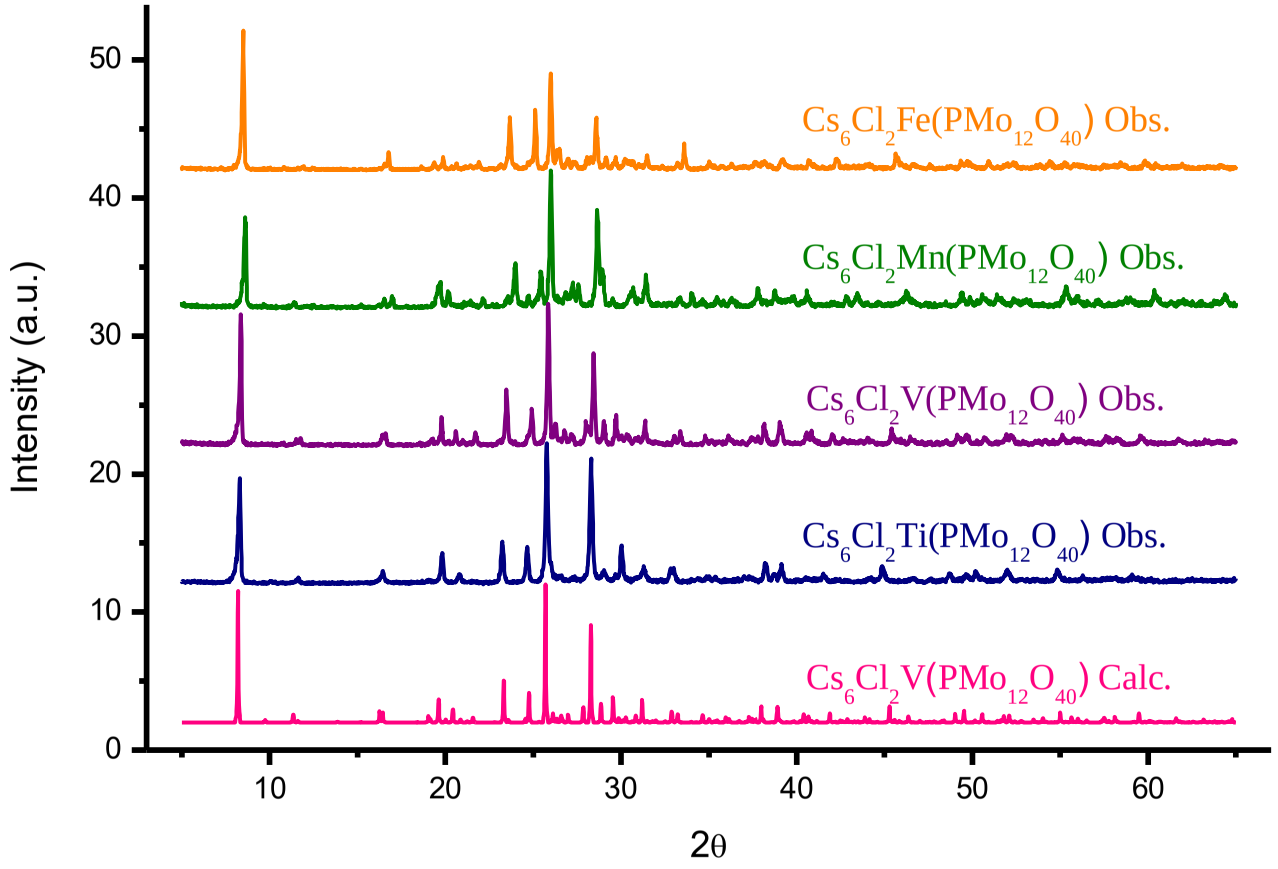

Figure 5.9: PXRD pattern of a stoichiometric yield synthesis attempt reactions for compounds **10**~**11**. For comparison, the PXRD of vanadium (**2**) and titanium (**3**) derivatives were also included.

The remaining synthetic procedures including the weighing, transferring, sealing and heating of the reactants were the same as those for the original synthesis of **2** as described above. Figure 5.10 shows the PXRD pattern of the stoichiometric reaction where V_2O_3 was used as the V^{3+} source. From this powder pattern it can be seen that the observed pattern matches with that of the calculated for phase **2**. The results of the stoichiometric synthesis using V_2O_3, indicate that compound **2** forms with V_2O_3 as the source of the linking vanadium cation. This also supports the fact that the system is flexible with respect to the oxidation state of vanadium as long as the overall stoichiometry for formation of **2** is satisfied.

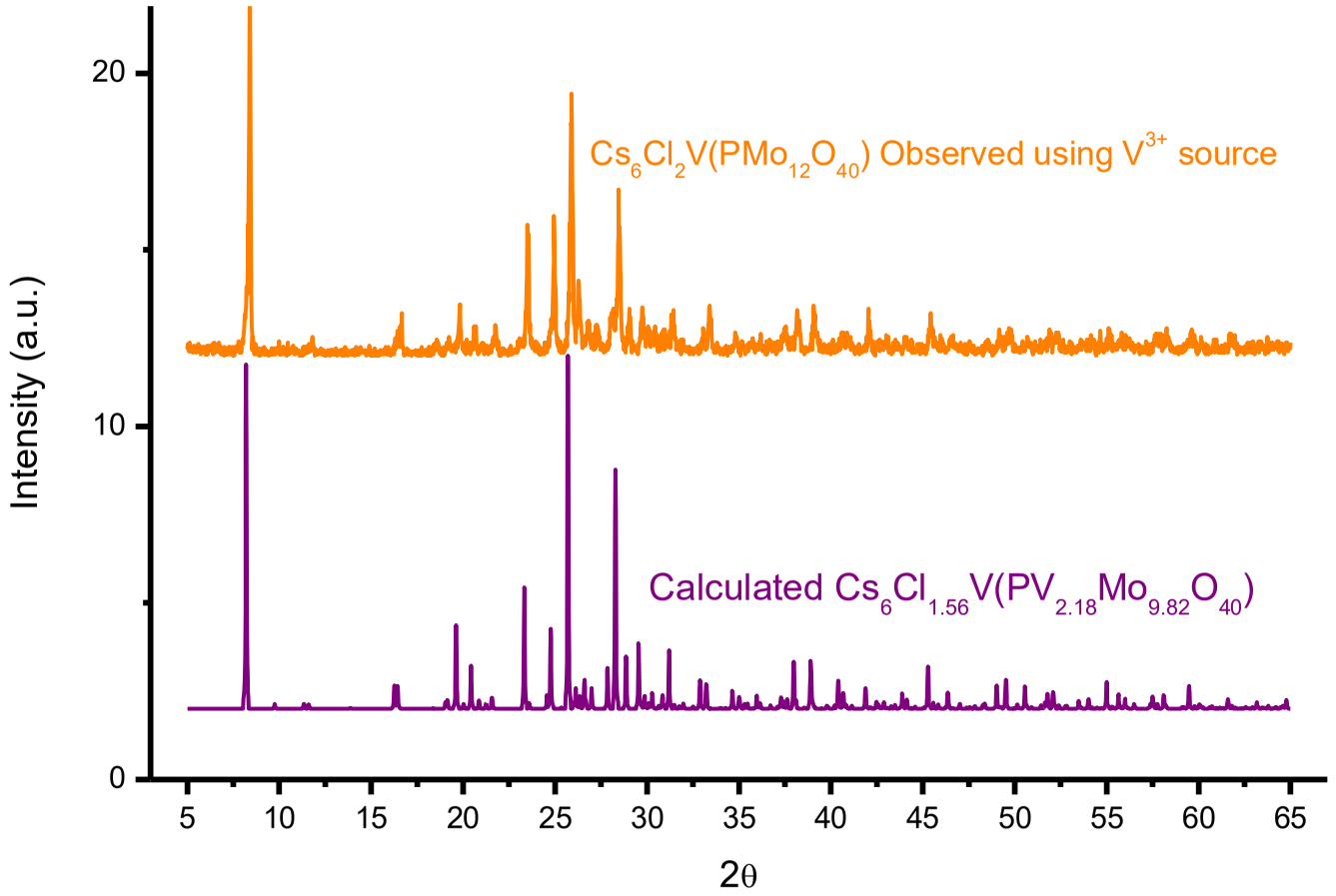

Figure 5.10: PXRD pattern of a stoichiometric yield synthesis attempt reaction for compound **2** using V_2O_3 as the V^{3+} source.

Characterization

Elemental Analysis (EDX): EDX was used to qualitatively confirm the presence of elements comprised in the compositions of **1**, **2**, **3**, **10**, and **11**. Elemental analysis was performed on polycrystalline products of **2**, **3**, **10**, and **11** as well as the single crystals used for the SXRD structure determination of **1**. SEM images for the polycrystalline products for **2**, **3**, **10** and **11** are shown in Figure 5.15 below.

Powder X–ray Diffraction (PXRD): PXRD was used to confirm the phase formations of the compounds observed in the various synthetic techniques mentioned in the synthetic procedure section of this chapter. Powder diffraction patterns for a select few synthetic approaches can be seen in Figures 5.2 through 5.10. The powder X–ray diffraction data were collected at room temperature using Cu Kα radiation in the 2θ range of 5–65° with a step size of 0.02° and a scan rate of 0.25°/min. Typical powder collection time was about two hours except in the profile refinement cases, where the powder pattern collection time was about four hours.

Profile refinement of PXRD patterns: Polycrystalline powder synthesized using high-yield stoichiometric reaction was used for profile refinement to provide the unit cell parameters for comparison to the SXRD unit cell constants. Fullprof software package was used for profile refinements.[19]

Single Crystal X–ray Diffraction (SXRD): Black column/needle crystals of **1** were selected under an optical microscope equipped with a polarizing light attachment. SXRD data were collected on these single crystals at room temperature using Mo Kα radiation (λ = 0.71073 Å) produced by a graphite monochromator. The crystallographic

data can be seen in Table 5.1. The atomic coordinates, selected bond distances, anisotropic thermal parameters and bond valence sums calculations can be seen in Tables 5.2~5.6, *CheckCif* is in Appendix.

Magnetic Studies: Magnetic susceptibility measurements were performed on $Cs_6Cl_2V(PMo_{12}O_{40})$ (**2**), $Cs_6Cl_2Ti(PMo_{12}O_{40})$ (**3**), $Cs_6Cl_2Mn(PMo_{12}O_{40})$ (**10**), and $Cs_6Cl_2Fe(PMo_{12}O_{40})$ (**11**) polycrystalline samples using a Quantum Design VSM magnetometer (Clemson Physics Department). Temperature–dependent magnetic susceptibility measurements on **2**, **3**, **10**, and **11** were performed on ground powder samples. Quantity of samples used for measurements consisted of 94, 139, 263, and 272 mg for **2**, **3**, **10**, and **11**, respectively. The temperature–dependent studies were measured in applied fields of 200 Oe at temperatures ranging from 10–300 K.

Table 5.1: Crystallographic data table for compound **1**.

empirical formula	$Cs_6Cl_{1.56}V(PV_{2.18}Mo_{9.82}O_{40})$
formula wt, g/mol	2628.01
crystal system	tetragonal
space group	*P* 4/*ncc* (no. 130)
a, Å	15.240(2)
c, Å	18.125(4)
volume, $Å^3$	4209.4(12)
Z	4
D_{calc}, g/cm^3	4.147
abs coeff	4.46
crystal size, mm	0.11 x 0.05 x 0.04
theta range, deg	2.38 - 25.04
reflections collected	32251
independent reflections	1873
R(int)	0.098
obsd ($I > 2s(I)$)	1508
goodness-of-fit on F^2	1.120
$R_1[I > 2s(I)]^a$	0.088
wR_2 (all data)^b	0.098

aR = Σ||Fo| − |Fc||/Σ|Fo|. bRw = [Σw(Fo2 − Fc2)2/Σw(Fo2)2]1/2, w = 1/[σ2(Fo2) + (0.1522P)2 + 96.2005P]

where P = (Fo2 + 2Fc2)/3

Table 5.2: Atomic parameters for compound **1**.

Atom	Wyckoff notation	sof	x	y	z
Cs(1)	16g	0.63	0.3875(5)	0.6102(6)	0.4042(4)
Cs(1A)	16g	0.37	0.3625(8)	0.6226(8)	0.3912(6)
Cs(2)	8f	0.36	0.105(2)	0.605(2)	1/4
Cs(2A)	8f	0.64	0.0920(14)	0.5920(14)	1/4
Cl(1)	4b	0.74	1/4	3/4	1/2
Cl(2)	4a	0.82	1/4	3/4	1/4
P	4c	1.00	1/4	1/4	0.5739(4)
Mo(1)	16g	1.00	0.18392(10)	0.40606(9)	0.43689(8)
Mo(2)	16g	0.85	0.31591(10)	0.40551(9)	0.21076(7)
V(2)	16g	0.15	0.31591(10)	0.40551(9)	0.21076(7)
Mo(3)	16g	0.60	0.03368(12)	0.33856(13)	0.57342(10)
V(3)	16g	0.40	0.03368(12)	0.33856(13)	0.57342(10)
V	4c	1.00	1/4	1/4	0.3260(3)
O(1)	16g	1.00	0.0265(8)	0.3464(8)	0.2743(7)
O(2)	16g	1.00	-0.0638(11)	0.3765(11)	0.5735(8)
O(3)	16g	1.00	0.3510(14)	0.2901(10)	0.2537(9)
O(4)	16g	1.00	0.1465(10)	0.2908(8)	0.3943(8)
O(5)	16g	1.00	0.0884(14)	0.4072(10)	0.4978(8)
O(6)	16g	1.00	0.2505(10)	0.4768(13)	0.4980(9)
O(7)	16g	1.00	0.2485(11)	0.4734(15)	0.1495(10)
O(8)	16g	1.00	0.1557(16)	0.4747(9)	0.3699(8)
O(9)	16g	1.00	0.4116(13)	0.4099(11)	0.1487(10)
O(10)	16g	0.50	0.1711(13)	0.2826(14)	0.5248(12)
O(11)	16g	0.50	0.2226(14)	0.3300(14)	0.1233(13)

Table 5.3: Anisotropic thermal parameters (Å^2) for compound **1**.

Atom	U_{11}	U_{22}	U_{33}	U_{12}	U_{13}	U_{23}
Atom	U11	U22	U33	U12	U13	U23
Cs1	0.099(5)	0.114(5)	0.045(3)	-0.053(4)	0.016(2)	-0.006(2)
Cs1A	0.084(5)	0.060(3)	0.032(3)	-0.007(3)	0.004(3)	-0.006(2)
Cs2	0.069(12)	0.069(12)	0.032(6)	0.011(10)	0.007(4)	-0.007(4)
Cs2A	0.063(5)	0.063(5)	0.025(3)	0.011(5)	-0.006(2)	0.006(2)
Cl1	0.075(6)	0.075(6)	0.084(11)	0.0000	0.0000	0.0000
Cl2	0.104(8)	0.104(8)	0.101(14)	-0.020(12)	0.0000	0.0000
P	0.033(2)	0.033(2)	0.019(4)	0.0000	0.0000	0.0000
Mo1	0.0442(9)	0.0350(9)	0.0224(8)	0.0059(6)	-0.0026(5)	-0.0008(5)
Mo2	0.0472(10)	0.0341(9)	0.0149(9)	-0.0059(6)	0.0001(5)	-0.0019(5)
V2	0.0472(10)	0.0341(9)	0.0149(9)	-0.0059(6)	0.0001(5)	-0.0019(5)
Mo3	0.0326(11)	0.0436(13)	0.0341(12)	0.0063(7)	0.0000(7)	-0.0018(7)
V3	0.0326(11)	0.0436(13)	0.0341(12)	0.0063(7)	0.0000(7)	-0.0018(7)
V	0.0315(16)	0.0315(16)	0.026(3)	0.0000	0.0000	0.0000
O1	0.031(6)	0.049(7)	0.038(6)	0.012(5)	0.002(5)	0.003(5)
O2	0.065(9)	0.068(9)	0.052(9)	0.025(8)	0.011(6)	-0.011(7)
O3	0.132(15)	0.052(8)	0.045(8)	0.017(9)	0.037(9)	0.016(6)
O4	0.074(9)	0.039(7)	0.058(8)	-0.012(6)	0.031(7)	-0.018(6)
O5	0.144(16)	0.064(9)	0.060(9)	-0.042(9)	0.077(10)	-0.030(7)
O6	0.057(9)	0.125(14)	0.065(10)	0.022(9)	-0.017(8)	-0.053(10)
O7	0.066(10)	0.167(19)	0.069(11)	-0.040(11)	-0.021(8)	0.084(12)
O8	0.181(19)	0.036(7)	0.036(8)	0.042(9)	-0.002(9)	0.002(6)
O9	0.108(14)	0.078(11)	0.071(10)	0.044(10)	0.055(10)	0.031(9)
O10	0.028(10)	0.039(11)	0.032(11)	0.009(8)	-0.003(8)	-0.012(9)
O11	0.028(10)	0.035(11)	0.045(13)	0.004(8)	-0.003(9)	-0.005(9)

Table 5.4: Selected bond distances for compound **1** in Angstroms.

Mo(1)O$_7$		**[Mo(2)V(2)]O$_7$**		**[Mo(3)V(3)]O$_7$**	
Mo1—O8	1.661(15)	Mo2—O1i	1.621(12)	Mo3—O2	1.598(17)
Mo1—O5	1.823(18)	Mo2—O7	1.834(19)	Mo3—O5	1.918(16)
Mo1—O6	1.849(17)	Mo2—O9	1.847(18)	Mo3—O7xiv	1.921(18)
Mo1—O4i	1.973(13)	Mo2—O3vii	1.978(16)	Mo3—O6vii	1.922(16)
Mo1—O4	1.996(13)	Mo2—O3	1.997(16)	Mo3—O9xi	1.935(17)
Mo1—O10	2.473(21)	Mo2—O11	2.492(22)	Mo3—O10	2.442(22)
Mo1—O10i	2.490(2)			Mo3—O11x	2.417(14)

PO$_8$ ≡ PO$_4$		**Cs(1)O$_8$Cl**		**Cs(2)O$_8$Cl$_3$**	
P—O11xi	1.571(22)	Cs1—O2i	3.139(15)	Cs2—O8iv	3.041(35)
P—O11xii	1.571(22)	Cs1—O7ii	3.175(21)	Cs2—O8iv	3.041(35)
P—O11xiii	1.571(22)	Cs1—O1i	3.203(14)	Cs2—O2v	3.277(16)
P—O11xiv	1.571(22)	Cs1—O9ii	3.245(18)	Cs2—O2vi	3.277(16)
P—O10vii	1.572(20)	Cs1—O6	3.375(19)	Cs2—O9vii	3.471(43)
P—O10xv	1.572(20)	Cs1—O6iii	3.358(10)	Cs2—O9viii	3.471(43)
P—O10	1.572(20)	Cs1—O5i	3.477(21)	Cs2—O7iv	3.473(44)
P—O10i	1.572(20)	Cs1—O5iii	3.602(17)	Cs2—O7	3.473(44)
		Cs1—Cl1	3.462(8)	Cs2—Cl2	3.125(46)
VO$_8$				Cs2—Cl3	3.886(48)
V—O4i	2.106(15)			Cs2—Cl3iv	3.886(48)
V—O4xv	2.106(15)				
V—O4vii	2.106(15)				
V—O4	2.106(15)				
V—O3xv	2.113(18)				
V—O3i	2.113(18)				
V—O3	2.113(18)				
V—O3vii	2.113(18)				

Table 5.5: Selected bond angles for compound **1.**

∠O-Mo(1)-O		∠O-Mo(2)-O		∠O-Mo(3)-O	
O6—Mo2—O8	102.60(76)	O1—Mo2—O3	102.47(64)	O2—Mo3—O6	99.99(48)
O8—Mo2—O4	100.61(77)	O1—Mo2—O3	101.82(58)	O2—Mo3—O5	102.17(78
O8—Mo2—O5	103.43(75)	O1—Mo2—O9	100.60(68)	O2—Mo3—O7	101.20(82
O1—Mo2—O8	103.89(40)	O6—Mo2—O7	103.05(73)	O2—Mo3—O9	101.43(75
O6—Mo2—O4	90.92(64)	O3—Mo2—O3	72.54(71)	O6—Mo3—O5	84.87(67)
O4—Mo2—O4	74.55(74)	O3—Mo2—O7	90.97(73)	O9—Mo3—O5	90.68(68)
O4—Mo2—O5	90.71(65)	O7—Mo2—O9	93.35(76)	O9—Mo3—O7	84.44(74)
O5—Mo2—O6	93.75(70)	O9—Mo2—O3	93.20(72)	O7—Mo3—O6	91.38(71)

∠O-V-O	
O4—V—O4	107.64(56)
O4—V—O4	69.60(52)
O4—V—O3	143.11(57)
O4—V—O3	145.75(62)
O4—V—O3	85.90(55)
O4—V—O3	84.36(62)
O3—V—O3	67.64(58)
O3—V—O3	103.83(68)

Table 5.6: Bond valence sums calculations for compound **1**.[20]

	r_0 Mo^{5+}	r_0 Mo^{6+}		r_0 Mo^{5+}	r_0 Mo^{6+}		r_0 Mo^{5+}	r_0 Mo^{6+}
$Mo(1)O_7$			**$Mo(2)O_7$**			**$Mo(3)O_7$**		
Mo1—O8	1.80	1.94	Mo2—O1	2.00	2.17	Mo3—O2	2.13	2.31
Mo1—O5	1.16	1.25	Mo2—O7	1.13	1.22	Mo3—O5	0.90	0.97
Mo1—O6	1.08	1.17	Mo2—O9	1.09	1.18	Mo3—O7xi	0.89	0.96
Mo1—O4i	0.77	0.84	Mo2—O3vii	0.76	0.83	Mo3—O6vi	0.89	0.96
Mo1—O4	0.73	0.79	Mo2—O3	0.72	0.78	Mo3—O9xi	0.86	0.93
Mo1—O10 x 1/2	0.10	0.11	Mo2—O11 x 1/2	0.10	0.10	Mo3—O10 x 1/2	0.11	0.12
Mo1—O10i x 1/2	0.10	0.10				Mo3—O11 x 1/2	0.12	0.13
$\sum (Mo^{5,6+})$	**5.74**	**6.20**		**5.80**	**6.27**		**5.89**	**6.37**

	r_0 P^{5+}		r_0 V^{3+}	r_0 V^{4+}	r_0 V^{5+}
$PO_8 \equiv PO_4$		**VO_8**			
P—O11 x 4 x 1/2	2.26	V—O3 x 4	1.47	1.64	1.73
P—O10 x 4 x 1/2	2.26	V—O4 x 4	1.50	1.68	1.76
$\sum (P^{5+})$	**4.52**	$\sum (V^{3+,4+,5+})$	**2.97**	**3.32**	**3.49**

	r_0 Cs^+		
$Cs(1)O_{10}$		**$Cs(2)O_{10}$**	
Cs1—O2i	0.14	Cs2—O8iv	0.19
Cs1—O7ii	0.13	Cs2—O8iv	0.19
Cs1—O1i	0.12	Cs2—O2v	0.10
Cs1—O9ii	0.11	Cs2—O2vi	0.10
Cs1—O6	0.08	Cs2—O9vii	0.06
Cs1—O6iii	0.08	Cs2—O9viii	0.06
Cs1—O5i	0.06	Cs2—O7iv	0.06
Cs1—O5iii	0.04	Cs2—O7iv	0.06
$\sum (Cs^+)$	**0.75**	**0.80**	

Results and Discussion

A series of new salt-inclusion solids based on the Keggin cluster were synthesized using the molten salt high temperature method. The series of compounds presented herein, including compound **1**, $Cs_6Cl_{1.56}V(PV_{2.18}Mo_{9.82}O_{40})$, and its derivatives are structurally related to the compounds presented in Chapter 3 and Chapter 4. The main difference between these compounds is the oxidation state of the transition metal cation (molybdenum and vanadium) that are incorporated into the Keggin framework. In addition, some variations between the salt chains and the cation linker between clusters in these related solids results in a change of oxidation state as was the case with $Cs_6I_3Na(PMo_{12}O_{40})$ and the $Cs_6X_2Na(PMo_{12}O_{40})$ series presented in Chapters 3 and 4, respectively. The most interesting aspect of all of the Keggin-based solids presented in this dissertation is that they seem to be reasonably flexible with respect to the modification of the cations between the neighboring Keggin clusters (and hence the modification of charge on the cluster), halide anion incorporation and even the modification of the type of framework connectivity (*i.e.* ionic vs. covalent). Along those same lines, serendipitous synthesis of the current compound, **1**, using molten-salt high temperature method, showed that the linking cation (Na^+) between the neighboring Keggin clusters running along *c*–axis can be replaced by vanadium and other transition metal cations. In doing so, the oxidation state of the cluster becomes further reduced as a result of charge balance. In the original reaction that produced single crystals of **1**, attempts were made to synthesize a vanadium-capped expanded Keggin cluster with two vanadium cations occupying and coordinating the square oxygen windows on opposite ends of the Keggin cluster in hopes of synthesizing a new salt

inclusion solid (*SIS*) to be used in comparative antibacterial studies as a result of the 'expanded' $(PV_2Mo_{12}O_{42})^{4-}$ Keggin cluster. The idea was to try to make a larger Keggin cluster with vanadium square pyramid caps on opposite ends of the cluster to study the antibacterial properties as a function of small change of the cluster shape. In addition, given the proposed mechanism of bacterial inhibition by Yamase and the one proposed herein in Chapter 4, having two vanadium sites would likely change the redox properties of the cluster itself which would be interesting to study in the bacterial inhibition experiments.

The square oxygen windows are close to having a perfect separation from each oxygen site to the center of the square (distance of ~1.8 Å) for coordinating a transition metal in a square pyramidal or octahedral environment. Given that vanadium is known to adopt square pyramidal geometry, the two vanadium cations capping the Keggin cluster were predicted to be in their square pyramidal geometry with the short apical vanadium oxygen double bond pointing away from the cluster as is the case with the molybdenum atoms and other similar vanadium-capped Keggin clusters. In addition to the comparative antibacterial studies on the basis of larger expanded Keggin cluster compared to that in the compounds used in Chapter 4, the exploratory reaction targeting **1** was also loaded in hopes of synthesizing new isolated polyoxometalate-containing solids with a higher number of *d* valence electrons. This was done in order to probe the potentially interesting magnetic and/or electronic properties. The targeted composition of $Cs_6Cl_2(PV_2Mo_{12}O_{42})$ was chosen featuring the previously synthesized salt chain of $[Cs_6Cl_2]_\infty$ with the assumption that such a compound would form mainly due to potentially favorable lattice energy. However, given that no sodium cations were present in the synthesis of **1**, it was predicted that the structure

of the targeted compound, $Cs_6Cl_2(PV_2Mo_{12}O_{42})$, would not have the exact same framework as that in solids presented in Chapters 3 and 4. Rather, a different structure was expected. Interestingly, the reaction targeting $Cs_6Cl_2(PV_2Mo_{12}O_{42})$ produced a compound with the structure that is very similar to the structures presented in Chapters 3 and 4. From a reaction using Cs_2MoO_4, CsCl, VO_2, MoO_3, MoO_2 and P_4O_{10} in 2:2:2:7.5:2.5:0.25 molar ratios, respectively, black columns/needles were formed on the side of the glass at the bottom of the fused silica ampoule. In addition to single crystals, a homogeneous black polycrystalline chunk was also found on the bottom of the tube. The single crystals were analyzed using single crystal X-ray diffraction and a full data collection was done on the crystals that produced the best preliminary X-ray diffraction results.

X-ray structure solution reveals that **1** crystallizes in a tetragonal crystal system, *P*4/*ncc* (no.130) space group, $Z = 4$. For illustration of the structure of **1**, see Figures 5.11~5.13. Table 5.1 presents the crystallographic data which includes the unit cell constants and refinement parameters. It should be noted that **1** also crystallizes in the same space group as the compounds presented in Chapters 3 and 4. Comparing the structure of **1** to those of the related solids presented in this dissertation, it can be observed that **1** has a very similar structure as that in the $Cs_6Cl_2Na(PMo_{12}O_{40})$ compound from Chapter 4. Apart from the crystallographic disorder in **1**, its structure is largely the same as that of $Cs_6Cl_2Na(PMo_{12}O_{40})$ with a major difference being the replacement of Na^+ for presumably a V^{3+} cation (based on bond valence sums calculations, see below). The salt chain structure, $[Cs_6Cl_{1.56}]_\infty$, though disordered, is the same as for the Chapter 4 compound, with two

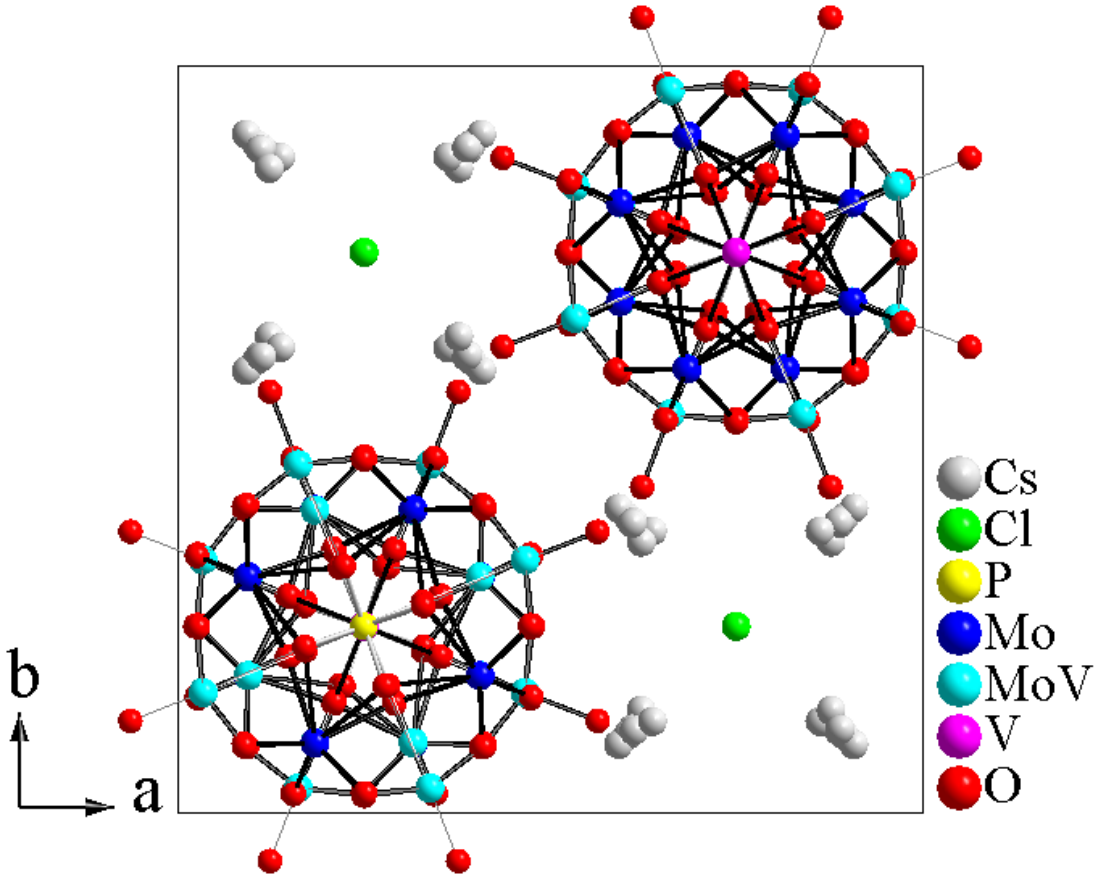

Figure 5.11: Perspective view along the *c*–axis of $Cs_6Cl_{1.56}V(PV_{2.18}Mo_{9.82}O_{40})$ showing the 4–fold symmetry around the one–dimensional chains of $[V\text{-}(PV_{2.18}Mo_{9.82}O_{40})\text{-}V]_\infty$ chains. This chain extends along the *c*–axis and runs parallel to the $[Cs_6Cl_{1.56}]$ salt lattice.

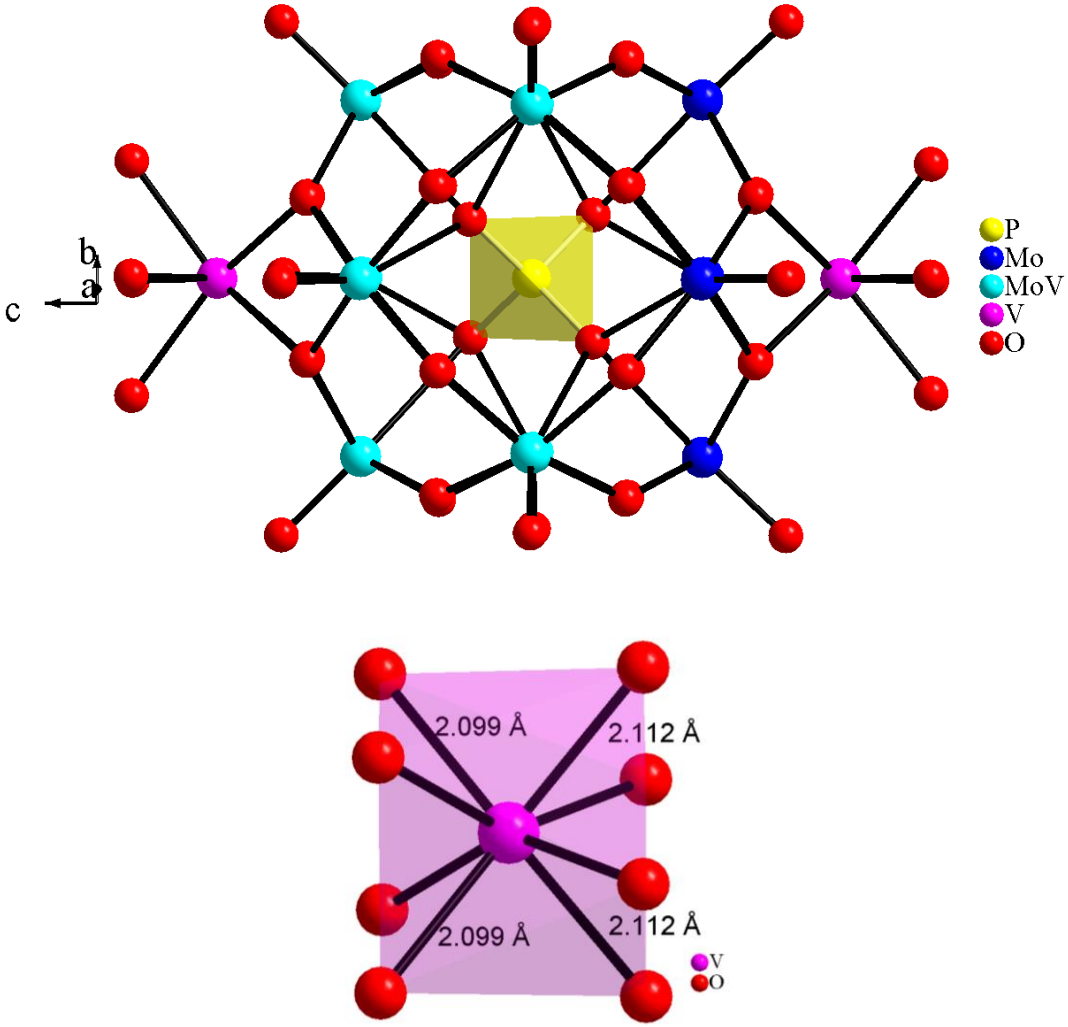

Figure 5.12: (top) Disordered cluster of $Cs_6Cl_{1.56}V(PV_{2.18}Mo_{9.82}O_{40})$ (1) showing mixed atomic sites where Mo and V share common sites for two of the three crystallographically unique metal sites of the Keggin framework. Linking vanadium cation is shown in purple and occupies a square antiprismatic geometry with respect to the neighboring oxygen. The vanadium cation links the neighboring clusters and extends the chain along the *c*–axis. (bottom) VO_8 square antiprismatic coordination.

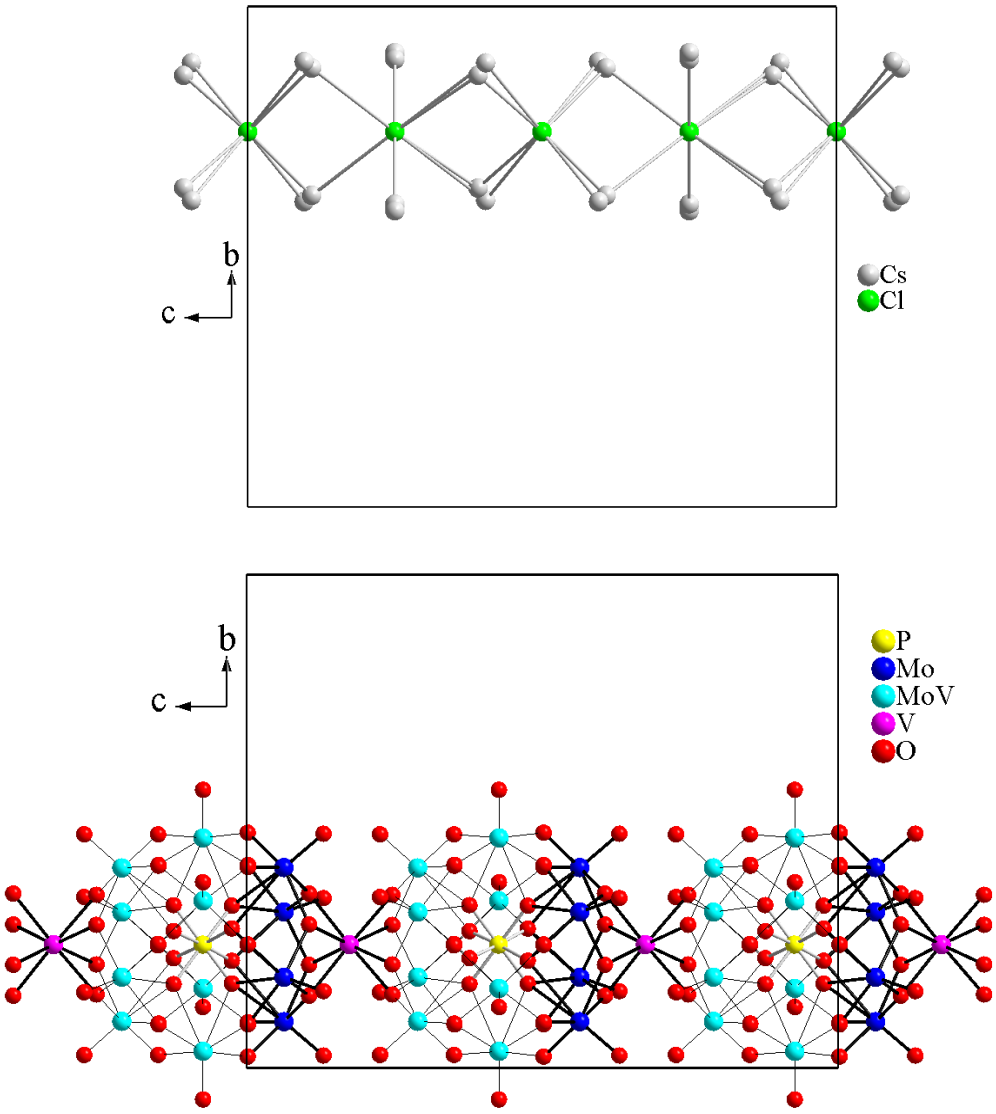

Figure 5.13: (top) $[Cs_6Cl_{1.56}]$ infinite salt chain running along the *c*–axis. Apart from the positional disorder of Cs atoms and the occupancy disorder of Cl, this salt chain is identical to the one discussed in Chapter 4. (bottom) Metal oxide connectivity in $Cs_6Cl_{1.56}V(PV_{2.18}Mo_{9.82}O_{40})$ (**1**) showing the infinite chain along the *c*–axis.

distinct coordinations of the Cl anion being tetrahedral and octahedral with respect to the neighboring Cs cations. The differences in structures of the current compound and those in the previous chapters will be discussed in more detail latter the Results and Discussion section of this chapter.

The α-Keggin cluster in **1** exhibits a pseudo-D_{4h} point group symmetry and is composed of $(PV_{2.18}Mo_{9.82}O_{40})^{7.44-}$. Based on this composition, it indicates that a disorder in occupancy of molybdenum (and vanadium) atoms is present. The initial structure solution was done with full occupancy of the molybdenum sites without vanadium atoms sharing the same sites. However, initially large thermal parameters of the Mo sites as well as the overall *R* factor (being around 14%) revealed that a lighter atom is likely to be in those sites. Refining only vanadium in the molybdenum sites resulted in unreasonably mall thermal parameters, on the other hand, which indicated that a shared site between molybdenum and vanadium exists for the atomic positions of Mo(2) and Mo(3) and hence the Mo(2)V(2) and Mo(3)V(3) sites were created. The non-integer composition in compound **1** was arrived at by first refining the occupancy of molybdenum in the individual Mo-sites, which resulted in significantly lower than 100% occupancy for Mo(2) and Mo(3). The molybdenum occupancy in Mo(1) atomic site after refining the composition of molybdenum, was 98% which indicated that this site is likely fully occupied by molybdenum. Then, the shared Mo(2)V(2) and Mo(3)V(3) sites were created and the sums of the occupancy of the shared sites were constrained to 100%. Refining the occupancy of each of the three transition metal sites resulted in 98% occupancy of Mo for Mo(1), 85% occupancy for Mo(2), 15% occupancy for V(2); 60% occupancy for Mo(3) and 40%

occupancy of V(3) sites. While these occupancies in atomic positions seem random, the results of the single crystal structure refinement of four different single crystals showed a relatively uniform distribution with the largest variation of occupancy being 7% for the Mo(3)V(3) and 5% for the Mo(2)V(2) sites. In addition to the X-ray structure solutions, selected crystals including the data crystal were analyzed by scanning electron microscopy with an energy dispersive X-ray attachment for elemental analysis. Figure 5.14 shows the results of the SEM EDS analysis of the SXRD data crystal. The crystal was analyzed using EDS elemental analysis at four different regions along the column for improved statistics. The average atomic weight % of the four obtained regions along the crystal will be used in the discussion herein. The results of EDX analysis show that the composition of the data crystal largely resembles that obtained from single crystal X-ray diffraction. The composition ratios of Mo/V and Mo/P are close to the expected values based on the SXRD composition of **1**.

Looking at the structure of the cluster itself, the major difference compared to the clusters from Chapters 3 and 4, as pointed above, is the disorder in the molybdenum sites. Mo(1), the only non-disordered site, is coordinated to seven oxygen atoms with two of the seven oxygen atoms being half-occupied. These half occupied oxygen atoms are part of the phosphate $(PO_4)^{3-}$ anion encaged inside the cluster framework. The phosphate anion is spatially disordered with respect to the alternating of oxygen atoms and as such it shows a PO_8 unit that is in a cubic arrangement with respect to the oxygen atoms. However, given that the oxygen atoms are 50% occupied, this results in the average expected PO_4^{3-} composition. The Mo(1) site, for that reason, shows a coordination to seven rather than six

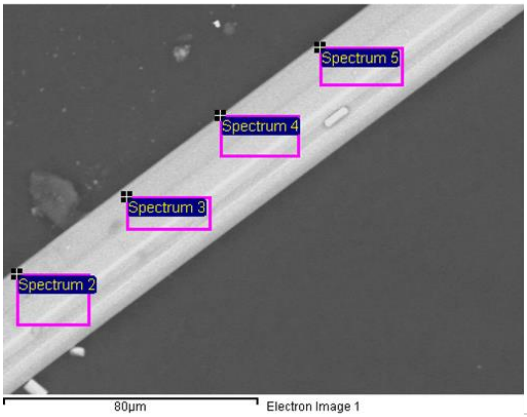

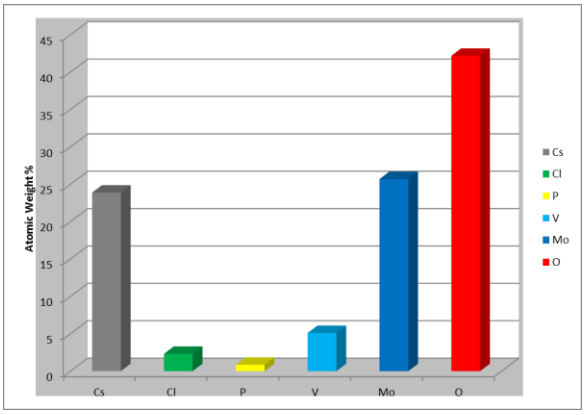

Processing option : All elements analysed (Normalised)

Atomic Weight %

Spectrum	In stats.	O	P	Cl	V	Mo	Cs	Total
Avg. Spectrum	Yes	42.1765	0.85	2.3085	5.099	25.686	23.88	100
Spectrum 2	Yes	39.3465	0.87	1.9885	4.799	27.256	25.74	100
Spectrum 3	Yes	40.6765	0.84	2.4385	5.529	24.366	26.15	100
Spectrum 4	Yes	44.2465	0.94	2.4585	4.999	25.906	21.45	100
Spectrum 5	Yes	44.4265	0.8	2.3285	5.079	25.196	22.17	100

	Cs	Cl	V	P	Mo	O
EDS Mol %	5.48	1.99	3.06	0.84	8.1	80.53
Expected Mol %	9.75	2.53	5.17	1.62	15.95	64.98

	Mo/V	Cs/Cl	Mo/P	V/P
EDS Mol % Ratios	2.65	2.75	9.64	3.64
Expected Mol % Ratio	3.09	3.85	9.85	3.19

Figure 5.14: (top left) SEM image of the SXRD data crystal of **1**. (top right) Atomic weight % plot of the elemental composition of **1**. (middle table) Atomic weight % of different areas corresponding to spectrums 2~5 on the data crystal. (bottom left table) Experimental and expected molar %. (bottom right table) Molar % ratios of the experimental and expected compositions.

oxygen atoms with two of the seven oxygen atoms pointing towards the center of the cluster. The metal oxygen bond length to the phosphate oxygen atoms is 2.473(21) and 2.490(2) Å for Mo(1)–O(10) and Mo(1)–O(10)^{i}, respectively. The equatorial metal oxygen bonds range from 1.823(18) Å to 1.996(13) Å and are close to the expected molybdenum-oxygen bonds for a Mo(V) and Mo(VI) ion. The short apical Mo(1)–O(8) bond pointing away from the center of the cluster is 1.661(15) Å long and is similar to the expected apical molybdenum-oxygen bond in polyoxometalates. The Mo(2)V(2) disordered site has similar metal to oxygen bonding as Mo(1). The equatorial metal-oxygen bond distances range from 1.834(19) Å to 1.997(16) Å. The apical bond is somewhat shorter than that in Mo(1) with the bond length being 1.621(12) Å. This shorter bond distance is expected given that smaller vanadium is sharing the same site. This is especially evident with the Mo(3)V(3) atomic site which has a larger percent of vanadium and thus the apical Mo(3)V(3)–O(2) bond distance is 1.598(17) Å and is much shorter than those in the Mo(1) and Mo(2)V(2) sites. The equatorial Mo(3)V(3)–O distances range from 1.918(16) Å to 1.935(17) Å.

Looking at the angles of the above three metal sites in Table 5.5, it can be observed that the apical-Mo-equatorial bond angles are greater than 90^{o} which is expected given the curvature of the cluster itself. Transition metal oxides with d^0 and mixed d^0–d^1 electronic configuration are known to have out-of-center distortion of the octahedra along *z* axis.[20] The above three crystallographically unique metal sites along with the oxygen atoms, comprise the metal-oxide framework of the α-Keggin cluster. The metal-oxide framework

encapsulates a phosphate anion in which the oxygen atoms are disordered as discussed above.

The bond valence sums calculations[21] for Mo(1), Mo(2)V(2), and Mo(3)V(3) from Table 5.6, show similar bond valence sums with 5.74, 5.80, and 5.89, respectively. Initially, because a V^{4+} oxide source was used in the original synthesis, it was thought that the vanadium site between the neighboring Keggin clusters should be in its V^{4+} oxidation state as well. As such, based on the cation charge (*i.e.* $[Cs_6Cl_{1.56}V^{4+}]^{8.44+}$) and the expected charges of the three metal sites in the Keggin cluster from the overall composition, it should be expected that the average oxidation state of the three sites would be approximately 5.55. However, bond valence sums calculations show that the linking vanadium site is formally V^{3+} charge. In this case the charge of the polynuclear cation would have to be 7.44+. Consequently, the charge on the cluster would have to be 7.44- for charge balance. This would result in the average expected oxidation state of the three metallic sites to be approximately 5.63+ which falls short of the observed averaged BVS of 5.81 for the three sites. A more sensible approach to calculate the BVS parameters was to not only use the contribution of molybdenum but also to take the contribution of vanadium into account. This was done by calculating the BVS of all three sites as if they were fully occupied with molybdenum or vanadium. Then, the percent occupancy of each element in a particular site was multiplied by their respective BVS parameters. Finally, the values obtained for Mo-calculated BVS and V-calculated BVS were added together. As an example, Mo(2)V(2) site contains 85% molybdenum and 15% vanadium. The BVS of the Mo(2)V(2) site, based on full occupancy of Mo is shown in Table 5.6. This value was multiplied by 0.85 to yield

4.93. Then the vanadium BVS was obtained with vanadium fully occupying the Mo(2)V(2) site. Similarly, the obtained V-calculated BVS, 4.81, was multiplied by the vanadium occupancy, 0.15, to give 0.72. Adding the Mo- and V- calculated BVS parameters together resulted in 5.65 as the revised BVS parameter for the Mo(2)V(2) site. Calculating the BVS parameters for all three metallic sites using the above described approach resulted in revised BVS parameters of 5.74, 5.65, and 5.53 for Mo(1), Mo(2)V(2), and Mo(3)V(3), respectively. Average of the three values, 5.63, is exactly the same as the expected BVS (also 5.63) based on the overall composition. Though the BVS results are never an ultimate proof of the oxidation state of a metal, the results obtained from these calculations suggest that the oxidation states were assigned correctly. In addition, the BVS results suggest that a charge delocalized state exists within the cluster between the three metal sites of the Keggin cluster as was the case with the clusters presented in Chapters 3 and 4.

Synthesis of single crystals of the remaining derivatives of compound **1** were attempted using the same reaction procedure as that used for synthesis of single crystals of **1**. In all cases for compounds **2**~**4** and **8**~**11** single crystals were unable to be formed in large enough size suitable for SXRD analysis (*i.e.* larger than 0.1 mm in smallest dimension). Figure 5.15 shows the Scanning Electron Microscopy (SEM) images of the reaction products in which single crystals of $Cs_6Cl_2V(PMo_{12}O_{40})$ (**2**), $Cs_6Cl_2Ti(PMo_{12}O_{40})$ (**3**), $Cs_6Cl_2Mn(PMo_{12}O_{40})$ (**10**) and $Cs_6Cl_2Fe(PMo_{12}O_{40})$ (**11**) were attempted to be synthesized. From this figure, it can be seen that the sizes of the single crystals are fairly small. For compounds **10** and **11**, comparatively larger crystals are seen. This is possibly due to the fact that in the attempted syntheses of **10** and **11**, a trivalent M^{III} (M = Mn and

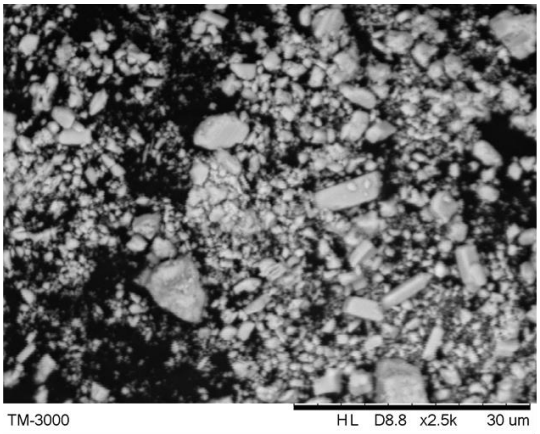

$Cs_6Cl_2V(PMo_{12}O_{40})$ (**2**)

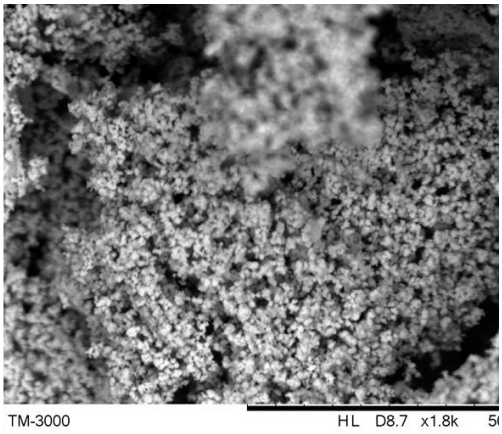

$Cs_6Cl_2Ti(PMo_{12}O_{40})$ (**3**)

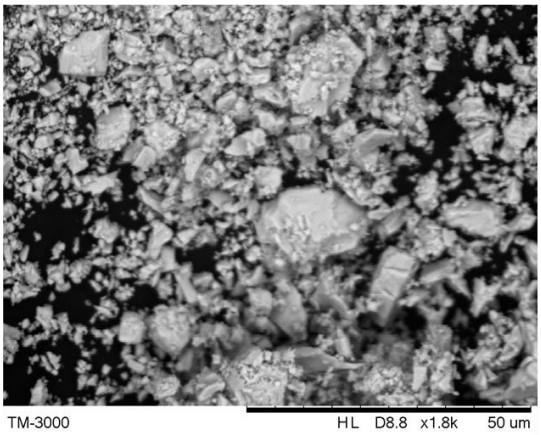

$Cs_6Cl_2Mn(PMo_{12}O_{40})$ (**10**)

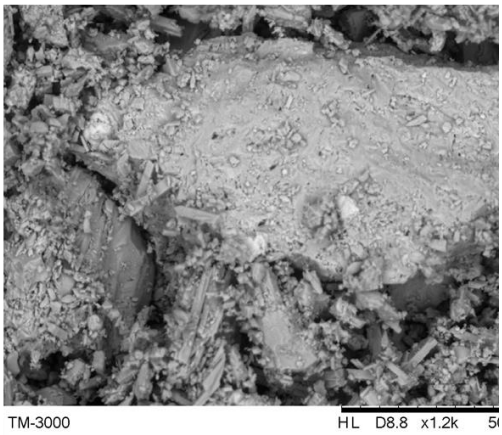

$Cs_6Cl_2Fe(PMo_{12}O_{40})$ (**11**)

Figure 5.15: SEM images of reaction products targeting sizeable single crystals for SXRD of compounds **2**, **3**, **10**, and **11**. Energy Dispersive Spectroscopy (EDS) of these crystals shows expected distribution of elements.

Fe, respectively) was used as opposed to the tetravalent M^{IV} for **2** and **3** (M = V and Ti, respectively). As was discussed above, it was originally thought that the linking transition-metal cation (M) between the Keggin clusters, was tetravalent. However, bond valence sums calculation (discussed below) of the vanadium site clearly indicates that the vanadium site between the Keggin clusters is trivalent. Based on single crystal structure of **1**, the transition-metal sites for the remaining derivatives should also be trivalent. So in the reactions targeting single crystals of **10** and **11**, redox chemistry to convert to trivalent M was not needed which may have played a role in growth of larger crystals. In any event, the single crystals produced for reactions targeting single crystals of **10** and **11** were still not large enough for SXRD analysis. Future directions section will discuss proposed reactions in order to grow sizeable single crystals of the compounds presented in this chapter.

To further attempt the growth of sizeable single crystals, in the case of compound **2**, the reaction temperature was increased by 20 ^{o}C to several set temperatures ranging from 480 ^{o}C and all the way up to 600 ^{o}C. In addition, the cooling rate was slowed down to 0.05 ^{o}C/min in hopes of allowing for longer diffusion of reactants beneficial for growth of larger crystals. All of the attempted single crystal growth reactions for compounds **2**, **3**, **4**, **8**~**13** resulted in homogeneous polycrystalline chunks. In the case of higher temperatures (*i.e.* greater than 480 ^{o}C) and slower cooling rates (shown in Figure 5.15 above), small needles/columns were observed under an optical microscope on the side of the polycrystalline chunks suggesting that the single crystals are indeed growing with the changed heating program parameters. However, the single crystals were still too small and

diffracted poorly on the single crystal diffractometer. To show that the above mentioned compounds were able to be synthesized in high yield, PXRD patterns are shown for each (see synthesis procedure and PXRDs above). In addition, unit cell parameters were extracted from each PXRD pattern by refining the profile parameters for each synthesized compound. Table 5.7 shows the refined parameters for each successful synthesis of several derivatives described above. The changes in the unit cell parameters (*e.g*. unit cell volume) are indicative of the respective incorporation of different sized atoms. Figure 5.16 is a combined plot of the unit cell volumes as a function of the sum of atomic numbers (Z) of the halide atoms in different salt lattices of compounds with similar structures presented in this dissertation. As expected, based on Vegard's Law, an approximation predicting the increase in unit cell parameters as a result of change in composition, the size of the unit cell increases linearly as the atomic number (Z) of the halide anion increases.[22] Figure 5.17 shows the refinement plots of the PXRD patterns for compounds **3**, **4**, **8**, **9**, **10**, **11**. In each plot, the red dots represent the experimental powder patterns, black line represents the calculated patterns based on the single crystal structure solution of **1**, and the blue line represents the difference between the experimental and calculated patterns. It should be noted that the calculated pattern for targeted composition was adapted to represent the targeted phase in each case. For example for compound **3**, in the calculation of the expected PXRD based on **1**, the linking vanadium in PXRD of **1** was replaced by titanium, the chlorine was set to be fully occupied and the disorder in molybdenum sites was removed with full occupancy of Mo sites. Similar calculation of PXRD powders was done for the remaining refined powder patterns. Based on the refined profile parameters, no impurity

Table 5.7 Comparison of the unit cell constants for compounds **1~4, 8~11**.

Compound	*a* (Å)	*c* (Å)	*V* (Å^3)	Source
$Cs_6Cl_{1.56}V(PV_{2.18}Mo_{9.82}O_{40})$, **1**	15.240(2)	18.125(4)	4209.4(12)	Single Crystal
$Cs_6Cl_2V(PMo_{12}O_{40})$, **2**	15.254(2)	18.120(8)	4216.2(20)	Powder
$Cs_6Cl_2Ti(PMo_{12}O_{40})$, **3**	15.317(1)	17.961(3)	4213.84(8)	Powder
$Cs_6Cl_2V(PVMo_{11}O_{40})$, **4**	15.252(1)	18.120(4)	4215.14(10)	Powder
$Cs_6I_2V(PMo_{12}O_{40})$, **8**	15.522(3)	18.100(9)	4360.89(25)	Powder
$Cs_6I_2V(PVMo_{11}O_{40})$, **9**	15.518(2)	18.070(7)	4351.41(19)	Powder
$Cs_6Cl_2Mn(PMo_{12}O_{40})$, **10**	15.009(8)	18.701(5)	4212.78(34)	Powder
$Cs_6Cl_2Fe(PMo_{12}O_{40})$, **11**	15.199(1)	18.202(2)	4204.84(6)	Powder

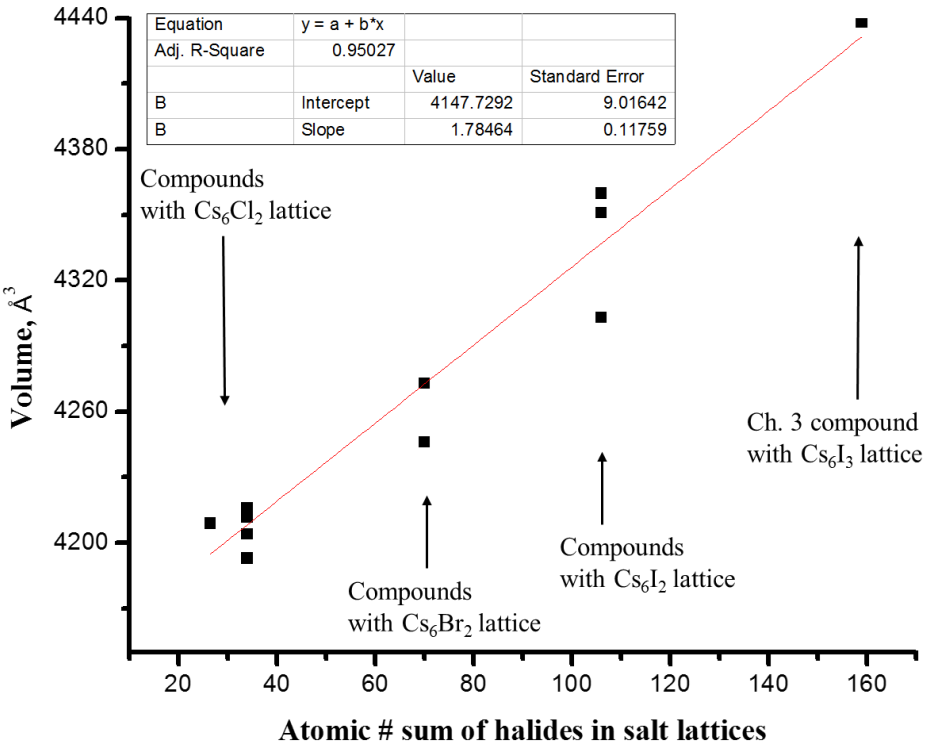

Figure 5.16: Combined plot of the unit cell volume (from PXRD profile refinement) as a function of the sum of halide atomic numbers in the salt lattice for compounds in chapters 3, 4, and 5.

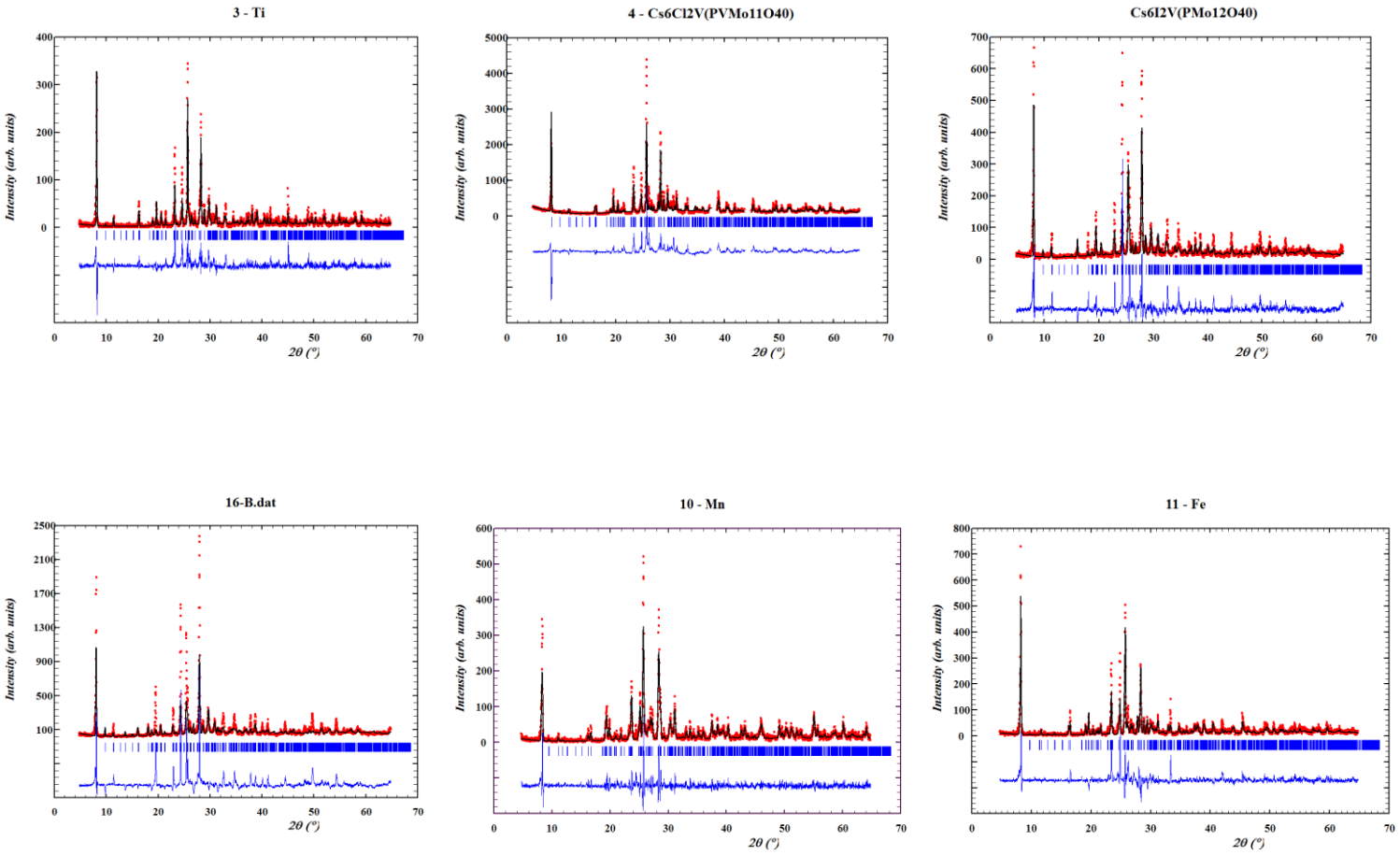

Figure 5.17: PXRD patterns showing refined profile parameters of stoichiometric yield synthesis reactions for compounds **3, 4, 8, 9, 10, 11.** Unit cell dimensions were obtained from these refinements to show a trend in the unit cell constants for different derivatives.

peaks were observed for compounds **2**, **3**, **4**, **8, 9**, **10**, **11** (see Table 5.7 above). However, intensity differences in the calculated vs. observed patterns are evident, see blue lines. The difference in intensities of PXRD patterns vs. the expected intensities can be due to preferred orientation of crystallites giving rise to certain *hkl* planes being overrepresented and others being underrepresented. For example, in the case of plate-like or column like crystals, crystals 'prefer' to lay flat with the long axis parallel with the sample holder. Crystals of compounds presented herein are indeed column/needle-like. However, some of the PXRD patterns show much larger intensity mismatch compared to others. For example PXRD pattern of $Cs_6I_2V(PMo_{12}O_{40})$ (**8**) shows large intensity mismatch with the calculated powder pattern compared to compound $Cs_6Cl_2V(PMo_{12}O_{40})$ (**2**), for example, showing close to expected intensities between observed and calculated patterns. The intensity mismatch in some compounds may not only be due to preferred orientation and should not be overlooked. It is possible that in the case of compound **8**, larger iodine atoms influence certain Cs sites (in the spatially disordered Cs atomic sites) to be less occupied compared to the chlorine atoms in compound **2** which can result in large differences in intensities due to large *hkl* shifts.[23] These *hkl* shifts are more pronounced in compounds with large differences in unit cell dimensions and, as a result may show a mismatch in calculated vs. observed intensities. The shifts in *hkl*s are easily refined for compounds with similar unit cell dimensions such as the case in compound **2** which is expected to have similar unit cell parameters as those observed in compound **1** from SXRD. However, for compounds with larger unit cell parameters such as in compound **8**, due to the larger iodine atoms (crystal radii for I^- = 2.06 Å vs. 1.67 Å for Cl^-),[24] the cell dimensions are expected to be larger

resulting in more pronounced *hkl* shifts. Another possibility for the large intensity mismatch in PXRDs of compounds **8** and **9** is possibly due to disorder in certain atomic sites. For example, in the SXRD structure of **1**, Cs atoms are spatially disordered (see Table 5.2, atomic coordinates of the Cs sites). This could also be the case for compounds **8** and **9**. Atomic positions refinements were attempted on powder patterns for compounds **2**~**4** and **8**~**11.** However, likely due to poor quality of data, the atomic positions refinements resulted in unreasonable change in atomic position coordinates even if only the heavy elements (Cs and Mo) were refined. In order to unambiguously solve the crystal structures of all of the compounds presented herein, growing sizable (approximately larger than 0.1 mm in the smallest dimension) single crystals would be invaluable to understand the slight changes in structures of compounds presented in this chapter.

Structurally, the most interesting aspect of the solids presented in this chapter compared to those presented in Chapters 3 and 4, is that the covalent metal oxide connectivity propagates along the *c*–axis. The individual Keggin clusters are linked together through a vanadium ion in an unusual eight-coordinate square antiprismatic environment. Vanadium (V) is coordinated to two crystallographically unique oxygen atoms with the multiplicity of four to yield a VO_8 polyhedron. The vanadium-oxygen distances range from 2.106(15) Å for V–O(4) and 2.113(18) Å for V–O(3). Based on the bond valence sums calculations from Table 5.6, this linking vanadium is formally in its trivalent state. Originally, this was not expected due to the fact that a V^{4+} oxide source was used in the synthesis. However, given that several metal oxide starting materials were used, likely some redox chemistry occurred *in situ* which converted V^{4+} to V^{3+}. Looking at the

reactants, the only other reduced species that was present in the synthesis of **1** besides VO_2, was MoO_2 which most likely oxidized to MoO_3 and in turn reduced V^{4+} according to the reaction below.

$$VO_2 + MoO_2 \longrightarrow \tfrac{1}{2}\, V_2O_3 + \tfrac{1}{2}\, MoO_3 + \tfrac{1}{2}\, MoO_2$$

In order to show that the title compounds can be synthesized using a V^{3+} source, a reaction targeting the same composition as that for **2** in which V_2O_3 was used as the starting reactant instead of VO_2, was attempted. In such a case, the relative amount of MoO_2 would have to be decreased as a result of a lower counter cation charge ($\{Cs_6Cl_2V^{3+}\}^{7+}$) while the overall stoichiometric composition was held constant. The negative charge on the Keggin cluster in this case would be 7- which results in four *d* valence electrons per one cluster. The PXRD of the reaction targeting $Cs_6Cl_2V^{3+}(PMo_{12}O_{40})$ (**2**) in which V_2O_3 was used as the V^{3+} source is shown in Figure 5.10. As can be seen from this powder pattern, the targeted compound was successfully synthesized. This shows that the synthesis of the title compounds is flexible with respect to the choice between V_2O_3 and VO_2 as the bridging vanadium source as long as the overall stoichiometry, including charge balance, is satisfied.

Given that the original compound, **1**, contains a disorder in the composition of molybdenum, reactions targeting several derivatives where molybdenum was replaced by vanadium with the representative formula $Cs_6Cl_2V(PV_xMo_{12-x}O_{40})$. The values of x were varied in my attempts from x = 1 ($Cs_6Cl_2V(PVMo_{11}O_{40})$ (**4**)), x = 2 ($Cs_6Cl_2V(PV_2Mo_{10}O_{40})$ (**5**)), x = 3 ($Cs_6Cl_2V(PV_3Mo_9O_{40})$ (**6**)) and x = 4 ($Cs_6Cl_2V(PV_4Mo_8O_{40})$ (**7**)). In these targeted compositions, the vanadium atoms that are a part of the Keggin clusters (inside

the parentheses), were targeted to be in their fully oxidized state in order to see how flexible the system is with respect to the mixed metal compositions. With regards to the catalytic performance of polyoxometalates in organic synthesis reactions, mixed metal polyoxometalates could potentially show to be superior in performance compared to those with only a single transition metal as part of the framework.[25, 26]

Looking at the results of the above described reactions targeting compositions of **4**~**7**, it can be concluded that the synthesis of these compounds was only partially successful. Compound **4**, where only one molybdenum (6^+) was replaced by a vanadium (5^+), was successfully synthesized based on the results of powder X-ray diffraction (see Figure 5.7). Only a partial match can be observed between **5** and the calculated powder pattern which indicates that, under the reaction conditions employed, **5** was unable to be synthesized in high yield. Impurity phase in the form of $Cs_3(PMo_{12}O_{40})$ shows up as the main product for reactions targeting **5**~**7**. One potential problem with the reactions where **4**~**7** were targeted was that VO_2 was used as the source of the linking vanadium (V^{4+}) between clusters due to the original belief that the linking vanadium was tetravalent. Based on bond valence sums calculations, the linking vanadium should be formally trivalent. However, a reaction where VO_2 was used to synthesize $Cs_6Cl_2V(PMo_{12}O_{40})$ (**2**), was successful which indicates that the system is fairly flexible with respect to the reduction of V^{4+} to V^{3+} in reactions where MoO_2, a reduced species, was present. In the case of the unsuccessful reactions targeting **5**~**7**, the amount of the reduced species, MoO_2, progressively was decreased going from reactions targeting compounds **5** to **7** which likely lowered the chance of V^{4+} being reduced to V^{3+} by MoO_2 *in situ*. This is consistent with

the results of the observed powder patterns for reactions targeting compositions of **4**~**7** illustrated in Figure 5.7. Reaction targeting **4** (highest amount of MoO_2) was successful while reaction targeting **5** (lesser amount of MoO_2) was only partially successful. The remaining two reactions targeting compositions of **6** and **7** (lowest amount of MoO_2) were unsuccessful. Based on the new knowledge and the bond valence sums results, a more obvious approach to synthesize compounds **4**~**7** would be to use V_2O_3 starting material as the V^{3+} source of the linking vanadium to bypass the need for *in situ* reduction of V^{4+} to V^{3+}. For example, a reaction targeting $Cs_6Cl_2V^{3+}(PV_4Mo_8O_{40})$ (**7**) would have Cs_2MoO_4, CsCl, V_2O_3, MoO_3, V_2O_5, P_4O_{10} reactants in molar ratios of 2:2:0.5:6:2:0.25, respectively. Using these reactants the oxidation state of the metals in the targeted product would be satisfied with no additional *in situ* redox chemistry needing to occur.

Given that the title compounds feature reduced transition-metal ions, magnetic susceptibility measurements were carried out on polycrystalline samples of $Cs_6Cl_2V(PMo_{12}O_{40})$ (**2**), $Cs_6Cl_2Ti(PMo_{12}O_{40})$ (**3**), $Cs_6Cl_2Mn(PMo_{12}O_{40})$ (**10**) and $Cs_6Cl_2Fe(PMo_{12}O_{40})$ (**11**). Figure 5.18 shows the magnetic susceptibility, χ_M, and inverse magnetic susceptibility, χ_M^{-1}, as a function of temperature, *T*, for compound **2**. From this plot it can be seen that, based on χ_M^{-1} vs. *T*, compound **2** seemingly deviates from paramagnetic behavior and potentially exhibits ferromagnetic interactions. However, extrapolating the linear region of the χ_M^{-1} vs. *T* plot (*i.e.* 50-300 K), clearly results in a negative Weiss constant of -1116, obtained from the plot of $\chi = C/(T-\theta)$, where θ is the Weiss constant. The negative Weiss constant indicates antiferromagnetic interactions above 50 K. Looking at the Figure 5.19, showing χT vs. *T* plot, a small inflection at low

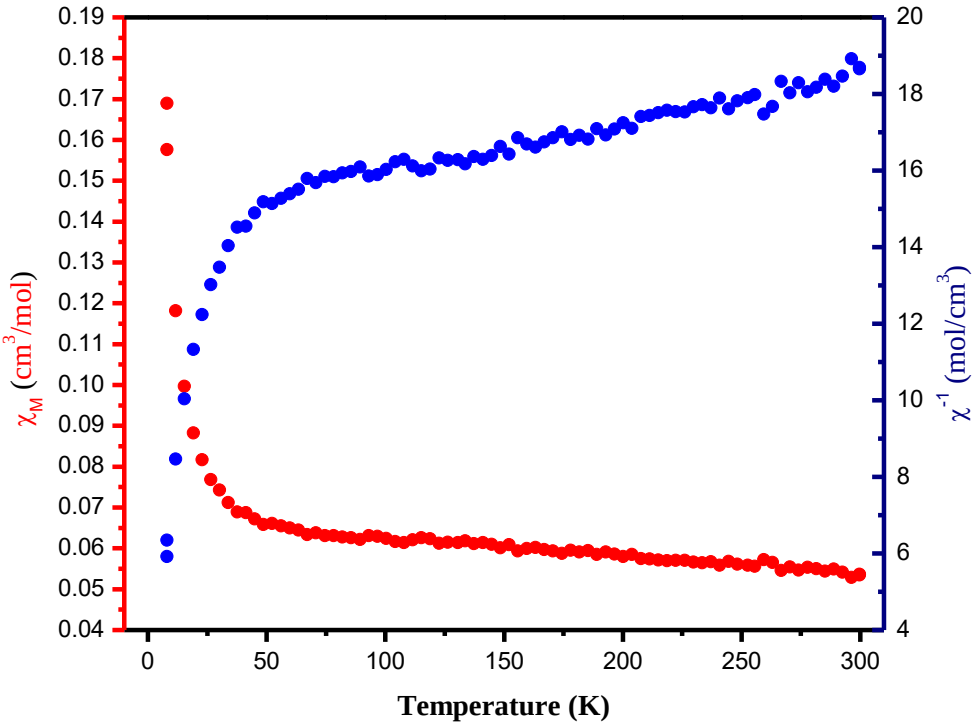

Figure 5.18: Temperature–dependent magnetic susceptibility and inverse susceptibility plots, χ_M (red) and χ^{-1} (blue) versus *T*, of **2** under an applied magnetic field of 200 Oe.

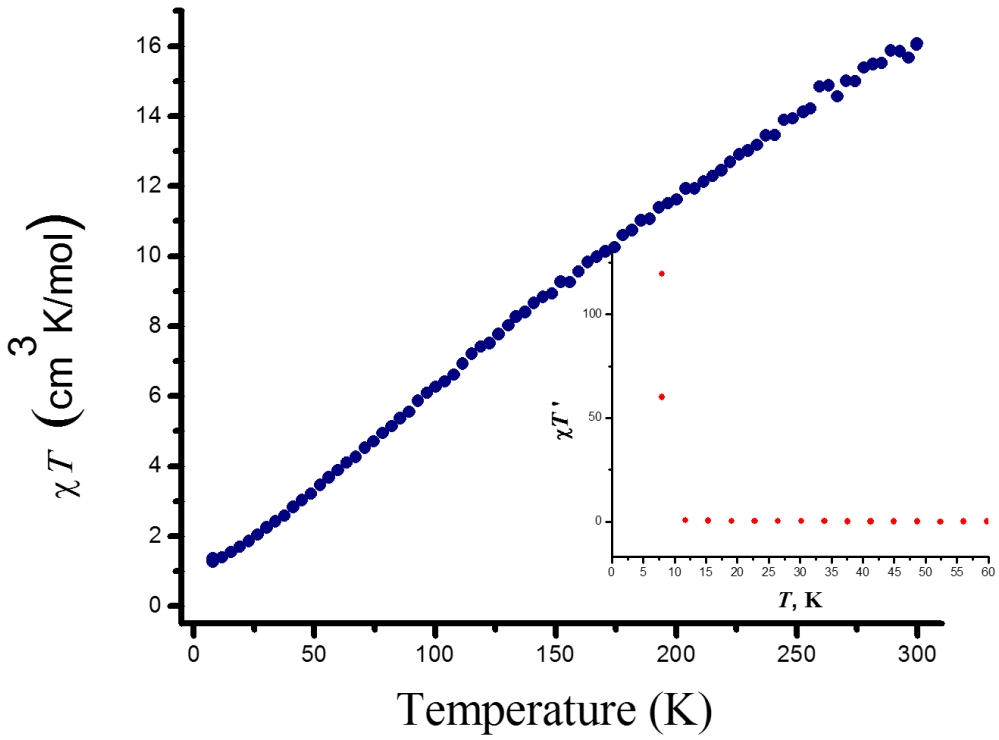

Figure 5.19: χT vs. T plot of **2** showing temperature dependence as a result of non-paramagnetic behavior. Derivative of the χT vs. T plot, $\chi T'$, is shown in the inset. The region of the inset plot is zoomed in to point out the change around 12 K.

temperature (~12 K) can be seen potentially indicating a ferrimagnetic transition. Indeed, by plotting a derivative curve of the χT vs. T, $\chi T'$ vs. T inset plot, inflection is seen around 12 K. However, above this temperature, antiferromagnetic interactions seem to be occurring. In addition to the type of interaction observed, magnetic susceptibility measurements were also used to obtain the experimental magnetic moment which can potentially reveal the spin state of the magnetic ions in **2**. Experimental magnetic moment, μ_{exp} = 3.19 BM (Bohr Magnetons), was obtained. The expected magnetic moment of $Cs_6Cl_2V(PMo_{12}O_{40})$ (**2**), based on S = 3 (S = 1 for V^{3+} and S = 2 for Mo^{5+} (x 4)) would be 6.93 BM. The much smaller μ_{exp} suggests that not all valence *d* electrons in **2** are unpaired potentially due to antiferromagnetic coupling or diamagnetic coupling of even spins of Mo^{5+} in the Keggin cluster. In fact, as is the case with molybdenum blue species and polyoxomolybdates that are reduced by an even number of electrons, the even electrons tend to pair up resulting in diamagnetic pairing between the neighboring Mo^{5+} sites. A new calculation of the expected magnetic moment based on only the number of *d* electrons in the vanadium site was done. For the high spin case in a square-antiprismatic crystal field, see Figure 5.20, the expected magnetic moment (based on spin only), μ_{eff}, should be 2.83 BM. This is much closer to the experimentally observed 3.19 BM, however, the larger experimental value likely indicates some spin-orbit coupling or a possible small contribution from unpaired S = ½ Mo^{5+} spins.

Looking at the magnetic susceptibility plots for compound **3**, from the χ_M^{-1} vs. T plot in Figure 5.21, a similar magnetic behavior is seen in compound **3** compared to that in **2**. Initially looking at the χ_M^{-1} vs. T plot, it appears that ferromagnetic interactions are

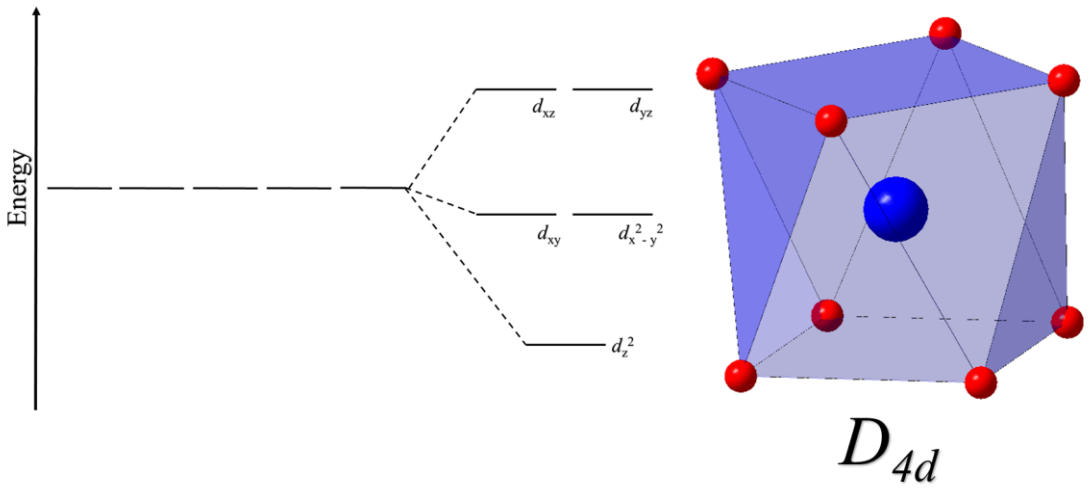

Figure 5.20: Expected crystal field splitting in a square-antiprismatic ligand field.

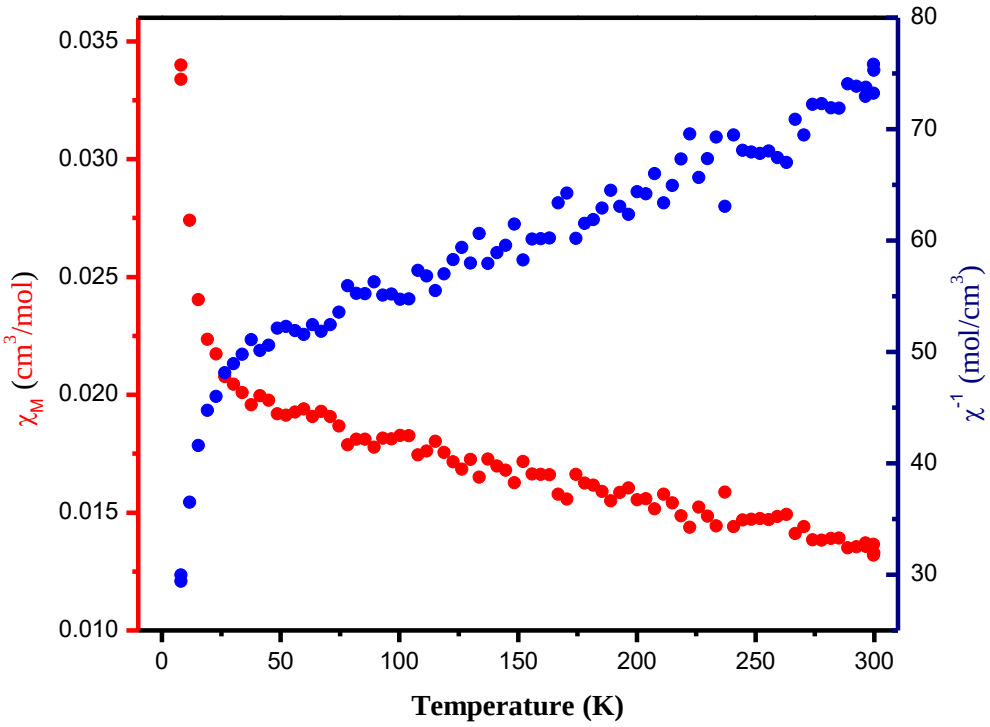

Figure 5.21: Temperature–dependent magnetic susceptibility and inverse susceptibility plots, χ (red) and χ^{-1} (blue) versus *T*, of **3** under an applied magnetic field of 200 Oe.

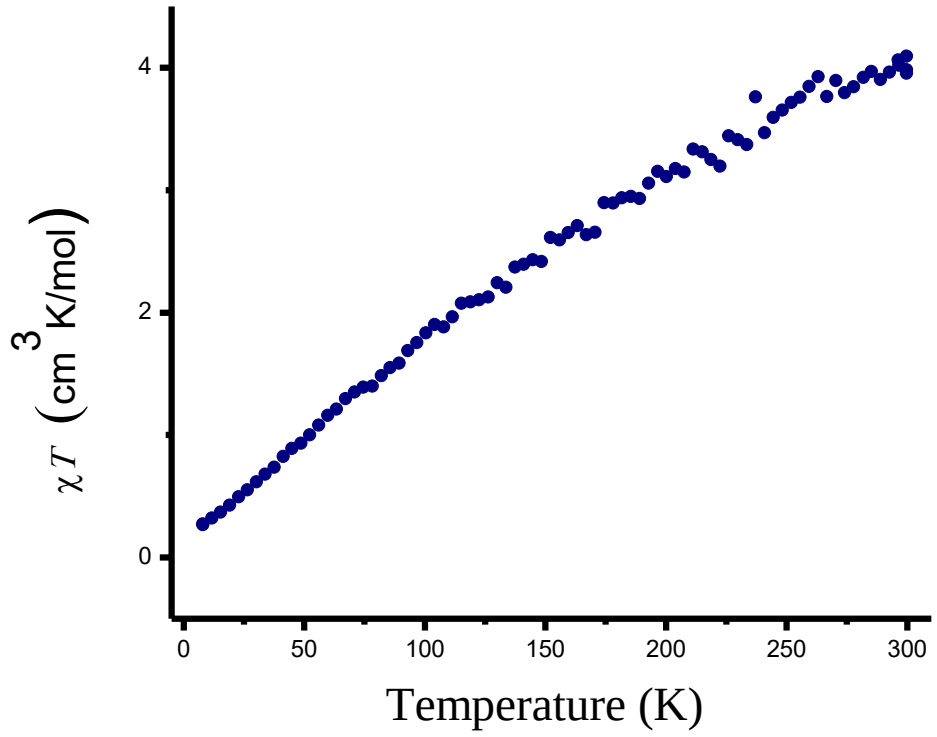

Figure 5.22: χT vs. T plot of **3** showing temperature dependence and deviation from paramagnetic behavior.

present. However, extrapolating the linear region above 40 K results in a Weiss constant of -533 K. As was the case for compound **2**, the negative Weiss constant indicates antiferromagnetic interactions. Assuming diamagnetic interactions between the four electrons in the four Mo^{5+} ions, expected magnetic moment based on spin only of the Ti^{3+}, S = ½, in **3**, was calculated to be 1.73 BM using the $\mu_{s.o.} = (n(n+2))^{1/2}$ equation. The experimental μ_{exp} moment was 1.59 BM for compound **3**. This is close to the expected moment and indicates that diamagnetic pairing of the Mo^{5+} electrons likely exists. Smaller than 1.73 BM value could possibly be due to some antiferromagnetic interactions occurring which would result in lower observed magnetic moment.

Magnetic susceptibility plots for compound **10** are shown in Figures 5.23 and 5.24. Interestingly, magnetic susceptibility temperature product, χT vs. T, plot for compound **10** in Figure 5.24 shows an increase in χT response as result of a decrease in temperature. This is indicative of ferromagnetic interactions. Linear fitting of the χ_M^{-1} vs. T plot (Figure 5.23) above 50 K shows a positive Weiss constant of 15.9 which is another indication of ferromagnetic interactions. Experimental magnetic moment of 1.82 BM was obtained indicating a low spin case for Mn^{3+}. Based on a high spin Mn^{3+}, d^4, ion, the magnetic moment should be 4.90 BM. In case of a low spin (*i.e*. two spins unpaired), d^4 ion, in a D_{4d} field (see Figure 5.20), the expected magnetic moment should be 2.83 BM. The low experimentally obtained magnetic moment for **10**, could possibly be due to some coupling between neighboring spins of Mn^{3+} and Mo^{5+}. In addition, it is a possibility that Mn^{3+} was reduced to Mn^{2+} by one of the Mo^{5+} sites. In such a case, the total d valence electron count in the Mo sites of the Keggin cluster should be three electrons, two of which presumably

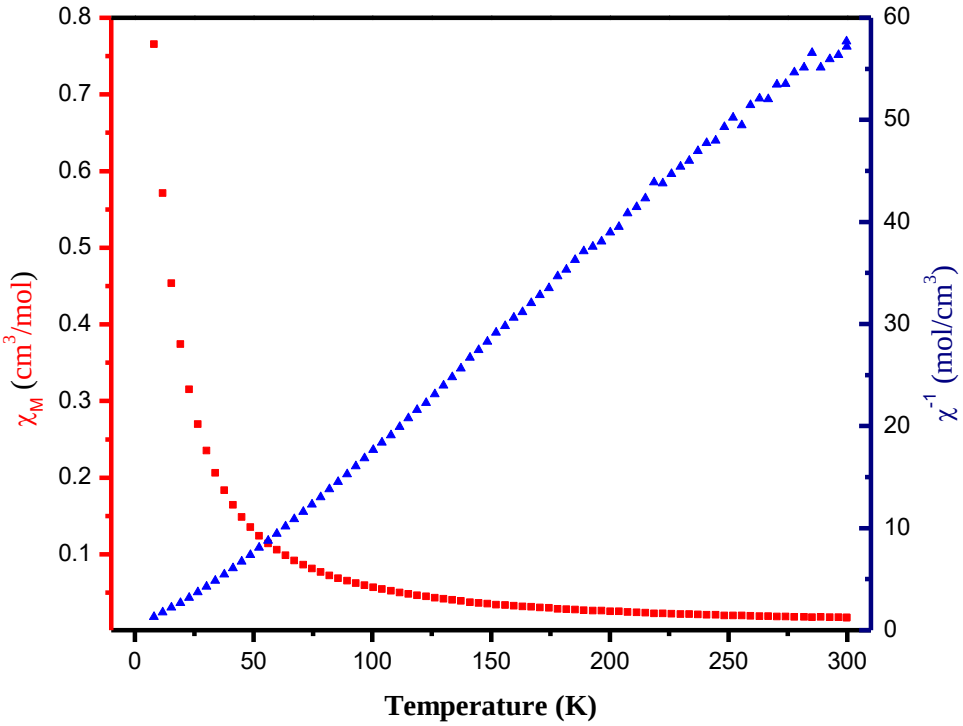

Figure 5.23: Temperature–dependent magnetic susceptibility and inverse susceptibility plots, χ (red) and χ^{-1} (blue) versus *T*, of **10 (Mn)** under an applied magnetic field of 200 Oe.

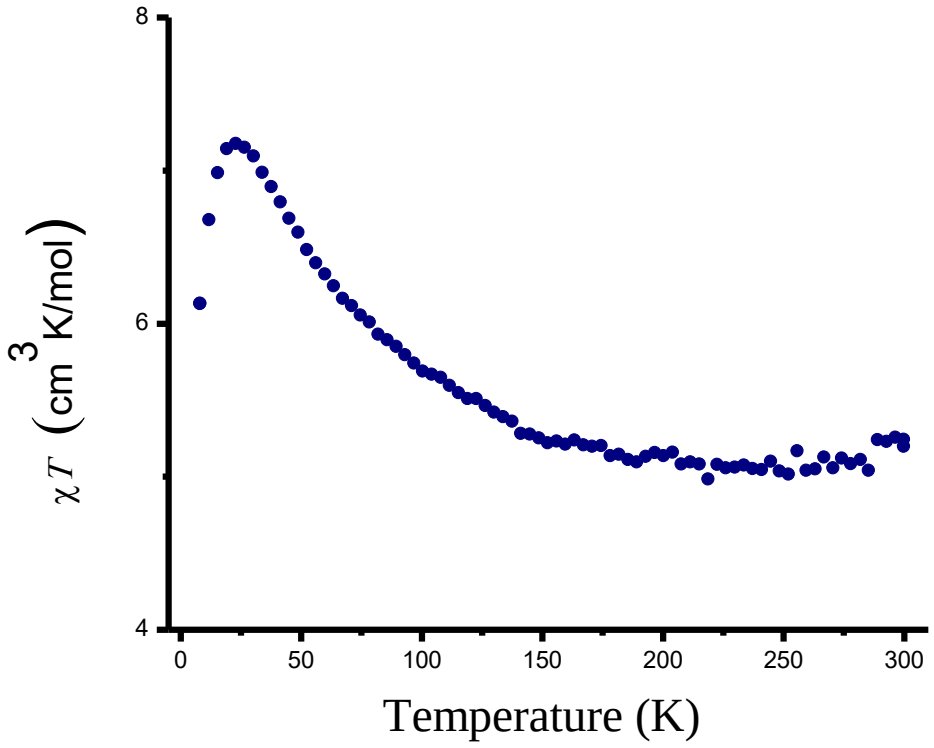

Figure 5.24: χT vs. T plot of **10 (Mn)** showing temperature dependence as a result of non-paramagnetic behavior.

would couple diamagnetically leaving one electron to couple with the Mn^{2+} (d^5) low spin case (one unpaired electron). From the magnetic susceptibility plots, it is evident that some ferromagnetic interactions are likely occurring so the possibility of a low spin Mn^{2+} case is a valid one.

Finally, looking at the magnetic susceptibility plots of d^5, Fe^{3+} ion derivative, compound **11,** in Figures 5.25 and 5.26, possible antiferromagnetic interactions are indicated by the gradual drop in χT values as temperature decreases in the χT vs. T plot. However, a characteristic cusp at T_N (Neel temperature) indicative of antiferromagnetic behavior is not seen in the χ_M^{-1} vs. T plot down to the experimental temperature of about 10 K. Extrapolating the linear portion of the χ_M^{-1} vs. T plot results in the Curie-Weiss fitted plot with a negative Weiss constant of -99.5 which likely confirms the antiferromagnetic interactions. Experimental magnetic moment from the high temperature linear fit of the χ_M^{-1} vs. T plot resulted in 1.99 BM. The expected magnetic moment for d^5 spin only, high spin case is 5.92 BM and for the low spin case of Fe^{3+} ion a magnetic moment of 1.73 BM would be expected. Given that the 1.73 BM expected magnetic moment is closer to the experimental value, this likely indicates that the Fe^{3+} site in **11** is a low spin case.

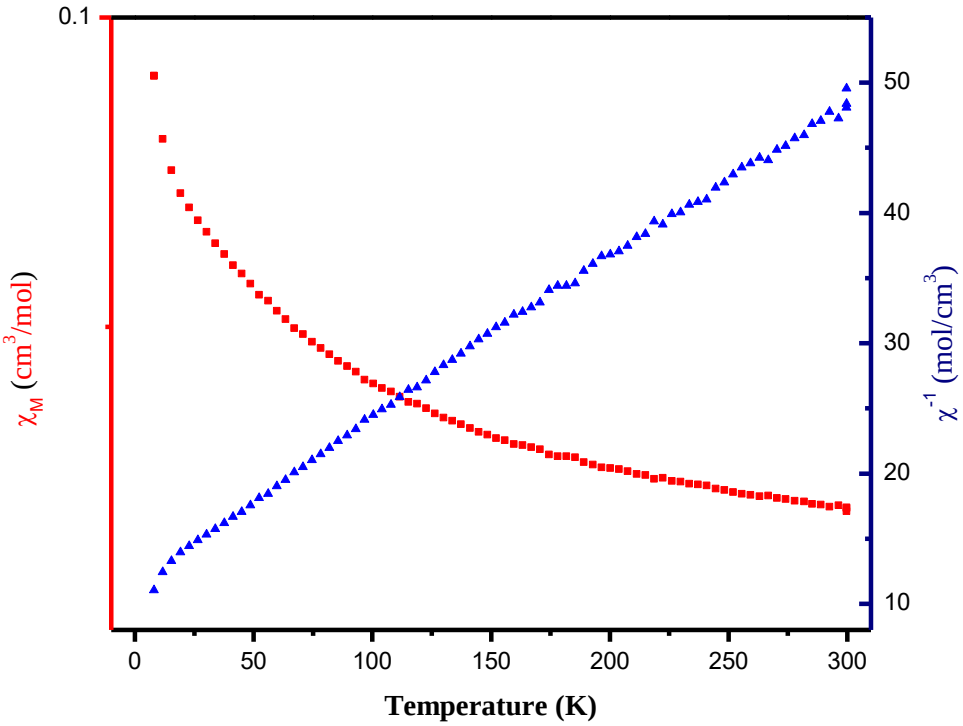

Figure 5.25: Temperature–dependent magnetic susceptibility and inverse susceptibility plots, χ (red) and χ^{-1} (blue) versus *T*, of **11 (Fe)** under an applied magnetic field of 200 Oe.

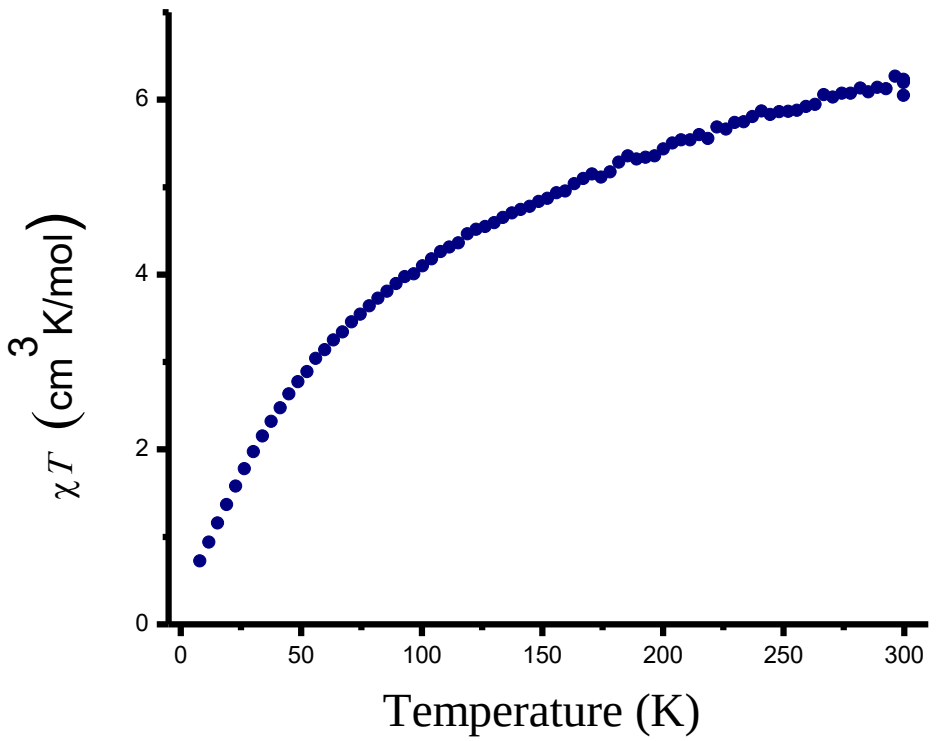

Figure 5.26: χT vs. T plot of **11 (Fe)** showing temperature dependence and deviation from paramagnetic behavior.

Conclusions

In this chapter, several new salt-inclusion solid nanostructures containing discrete polyoxometalate clusters were presented. The general composition of the solids discussed in Chapter 5 is $Cs_6X_2M(PMo_{12}O_{40})$, where X can be Cl, Br, and I and M can be Ti, V, Mn, and Fe. As was the case for compounds in Chapters 3 and 4, compounds presented herein feature a series of Keggin cluster compounds synthesized for the first time, hitherto, using high temperature molten-salt method. In addition, compounds presented in Chapter 5 feature an unusual square-antiprismatic (D_{4d}) eight-coordination of the first-row transition-metal (M in the general formula above). To the best of my knowledge, this is the first example of an all-inorganic, rigid compound with the square-antiprismatic coordination of a first-row transition-metal complex. Oxo complexes of first-row transition metals with eight-coordination environment are rare due to unfavorable small size of the metals. However, in compounds presented herein, the Keggin cluster with multiple oxygen (four per cluster in the case of compounds presented herein) donors acts as a multidentate ligand seemingly resulting in chelate effect stabilization of the eight-coordinate first-row transition metals. Originally, because a tetravalent vanadium oxide source (VO_2) was used in the original synthesis of **1**, it was believed that the eight coordinate metal site was tetravalent. However, bond valence sums calculations clearly indicate a trivalent state. Subsequent reactions in which trivalent first-row transition metals (V^{III}, Mn^{III}, Fe^{III}) were used in synthesis showed the formation of targeted compounds which is another indication that the M site is trivalent. In addition to the replacement of M, halide anion Cl^- in the salt lattice seems to be easily replaced by other halide anions, i.e. Br^- and I^-. To further show

the flexibility of the compounds presented in Chapter 5, vanadium was attempted to be doped in the metal centers of the Keggin cluster (*i.e.* molybdenum sites). It was shown that up to only one molybdenum per twelve in the Keggin cluster can be replaced by a vanadium in both the Cl^- and I^- compounds and further doping of the vanadium into Mo sites was proven to be unsuccessful. Successful high yield synthesis of $Cs_6Cl_2V(PMo_{12}O_{40})$ (**2**), $Cs_6Cl_2Ti(PMo_{12}O_{40})$ (**3**), $Cs_6ClV(PVMo_{11}O_{40})$ (**4**), $Cs_6I_2V(PMo_{12}O_{40})$ (**8**), $Cs_6I_2V(PVMo_{11}O_{40})$ (**9**), $Cs_6Cl_2Mn(PMo_{12}O_{40})$ (**10**), $Cs_6Cl_2Fe(PMo_{12}O_{40})$ (**11**), $Cs_6Br_2V(PMo_{12}O_{40})$ (**12**), and $Cs_6Br_2Ti(PMo_{12}O_{40})$ (**13**) were able to be carried out. Profile refinement of the powder X-ray patterns for these compounds showed expected linear trend with the increased size of halide anion. Magnetic susceptibility measurements of compounds **2**, **3**, **10**, and **11** showed that the even number of Mo^{5+} spins in the Keggin cluster tend to pair up which is a common occurrence in similar clusters reduced by an even number of electrons. Based on these preliminary magnetic susceptibility measurements, it seems that the magnetic contributions arise solely from the trivalent first-row transition-metals. Compounds **2**, **3**, and **11** show deviation from paramagnetic behavior with indications of antiferromagnetic interactions. Interestingly, compound **10** (Mn derivative) shows ferromagnetic interactions based on the positive Weiss constant and shape of the χT vs. T curve. In the case of **2** high spin (in D_{4d} field) seems to be favored while in the case of **10** and **11**, low spins are favored. It should be said that having single crystal structures of all of the derivatives studied using magnetic susceptibility measurements would make it easier to predict the interactions between spins and their spin states (*e.g.* d^4 vs. d^5 in **10**, Mn site).

Given that several transition metal derivatives with different *d* valence electron counts were able to be isolated, this family of compounds presents a platform to study their magnetic properties as a function of first-row transition-metal ion.

Future Work

Concerning the synthesis of single crystals, it would be invaluable to have single crystal structures of all of the derivatives described herein. This would facilitate the study of their properties such as magnetic and or electronic. To try to grow larger single crystals of these compounds, higher temperatures could possibly prove to be successful as was the case for growth of larger crystals for compounds 10 and 11 (see SEM images). In addition, longer cooling times (*e.g.* slower than 0.05 ^{o}C per minute rate) would aid in growth of larger crystals. Finally, the use of eutectic salt flux with the high yield products could possibly increase the chance of growing larger crystals due to increased diffusion of reactants as a result of using a high temperature 'solvent'.

More in depth magnetic studies are needed to reveal any interesting properties of these materials. For example, field-dependent magnetic susceptibility measurements are in line for all of the compounds synthesized especially compound **10** showing ferromagnetic interactions. In addition, due to potential diamagnetic contribution of the Keggin cluster with an even number of electrons in these compounds, the diamagnetic contribution should be subtracted in all. In order to do this, the diamagnetic contribution of the Keggin cluster with even number of electrons should be measured and subtracted from the magnetic susceptibility measurements. By synthesizing a compound with d^0 electron count in the M site of $Cs_6Cl_2M(PMo_{12}O_{40})$, where there are four Mo^{5+} sites, would be an ideal candidate

to measure its diamagnetic contribution due to paired spins of Mo^{5+} ions. Given that the M site in the title compounds is trivalent, it would be intuitive to use Sc^{3+} ion as the d^0 ion to replace the paramagnetic ions in the title compounds and measure the magnetic contribution of only the Mo ions in the Keggin cluster.

Finally, because of the 1D metal-oxide connectivity running along the *c* crystallographic direction, possible interesting electronic properties may arise from existence of electron delocalization pathways along *c*. As is the case with the reduced molybdenum blue 1D $K_{0.3}MoO_3$ compounds featuring corner shared clusters of octahedra, title compounds may also show interesting electronic properties such as metal-like electronic behavior. Resistivity measurements and heat capacity measurements are in line for all of the derivatives presented herein to reveal any electronic transport phenomena. As mentioned above, due to the flexibility of the structure with respect to the incorporation of different transition metal ions and halide ion replacement, this series of compounds presents an interesting platform to study their properties as a function of different chemical compositions.

Literature Cited

1. Greenblatt, M. *Chem. Rev*. **1988**, *88*, 31.

2. Kittel, C. *Introduction to solid state physics*. John Wiley and Sons, Inc., USA, **1953**.

3. Graham, J.; Wadsley, A. D. *Acta Cryst*. **1966**, *20*, 93.

4. Travaglini, G.; Watcher, P. *Sol. St. Comm*. **1981**, *37*, 599.Wang, S.; Hwu, S.–J. *J. Am. Chem. Soc.* **1992**, *114*, 6920.

5. Wold, A.; Kunnmann, W.; Arnott, R. J.; Ferretti, A. *Inorg. Chem*. **1964**, *3*, 545.

6. Couchard, G. H.; Perstein, J.; Sienko, M. J. *Inorg. Chem*. **1967**, *6*, 1682.

7. Cotton, F.A.; Wilkinson, G.; Murillo, C.A.; Cochmann, M. *Advanced Inorganic Chemistry*, 6th ed.; Wiley: New York, 1999.

8. Cambridge Structural Database (CSD), *Version 5.30*.

9. Lippard, S. J. *Prog. Inorg. Chem*. **1967**, *8*, 109.

10. Wang, S.; Westmoreland, T.D. *Inorg. Chem*. **2009**, *48*, 719.

11. Muetterties, E. L. *Inorg. Chem.* **1973**, *12*, 1963.

12. Conradie, J.; Patra, A.K.; Harrop, C.; Ghosh, A. *Inorg. Chem*, **2015**, *54*, 1375.

13. Barsukova-Stuckart, M.; Izarova, N. V.; Barrett, R.; Wang, Z.; Tol, J.v.; Kroto, H.W.; Dalal, N.S.; Keita, B.; Heller, D.; Kortz, U. *Chem. Eur. J.* **2012**, *18*, 6167.

14. Chen, L.; Wang, J.; Wei, J-M.; Wernsdorfer, W.; Chen, X-T.; Zhang, Y-Q.; Song, Y.; Xue, Z-L. *J. Am. Chem. Soc*. **2014**, *136*, 12213.

15. Mackay, R.A.; Henderson, W. *Introduction to Modern Inorganic Chemistry*, 6th ed. 2002.

16. Archer, R.D.; Day, R.O.; Illingsworth, M.L. *Inorg. Chem*. **1979**, *18*, 2908.

17. Hoard, J.L.; Hamor, T.A.; Glick, M.D. *J. Amer. Chem. Soc*., **1968**, *90*, 3177. Pribush, R.A.; Archer, R.D. Inorg. Chem., 1974, 13, 2556.

18. Tong, W.; Zhang, R.; Zhang, T.; Yang, L. *RSC Adv*., **2015**, *5*, 22031.

19. Carjaval, J. R. *Physica B*, **1993**, *192*, 55.

20. Bhuvanesh, N.S.P.; Gopalakrishnan, J. *J. Mater. Chem*., **1997**, *7*, 2297.

21. Brown, I.D.; Altermatt, D. *Acta Cryst*. **1985**, *B41*, 244.

22. Vegard, L. *Zeitschrift fur Physik*, **1921**, *5*, 17.

23. McCusker, L. B.; Von Dreele, R. B.; Cox, D. E.; Louer, D.; Scardi, P. *J. Appl. Cryst*. **1999**, *32*, 36.

24. Shannon, R.D.; *Acta Cryst.* **1976**, *A32*, 751.

25. Palermo, V.; Villabrille, P. I.; Vazquez, P. G.; Caceres, C. V.; Tundo, P.; Romanelli, G. P. *J. Chem. Sci*. **2013**, *125*, 1375.

26. Rao, P. S. N.; Venkateswara Rao, K. T.; Sai Prasad, P. S.; Lingaiah, N. *Catal. Commun.* **2010**, *11*, 547.

CHAPTER SIX

EXPLORATORY SYNTHESIS AND CHARACTERIZATION OF RELATED POLYOXOMETALATE (POM)-CONTAINING ORGANIC-INORGANIC HYBRID SOLIDS FEATURING NON-COVALENT INTERACTIONS BETWEEN POMs AND ORGANIC LIGANDS

Introduction

Over the last few decades, polyoxometalates have attracted large interest due to their promising applications in catalysis, biology, optics, magnetism, and material science.[1] Their nano size, discrete geometry, electronic properties and excellent reactivity, make polyoxometalates unique molecular metal oxide materials which can be used as standalone functional materials or as part of hybrid multifunctional nanostructures. The latter materials find more interest among researchers due to the ability of attaining unique and novel properties that otherwise would not be possible with polyoxometalates as standalone materials. For example, the use of polyoxometalates for light harvesting in photocatalytic and photoelectronic applications is well established.[2] However, as standalone materials they are unable to efficiently absorb light in the visible region due to large band gaps and insulating nature of the fully oxidized polyoxometalates. Because the POM ions feature transition metals that are generally fully oxidized with d^0 electronic configuration, their light absorption is mainly attributed to the ligand-to-metal charge transfer (LMCT) in the 200-500 nm region which results in the excitation of an electron from the filled bonding orbital (HOMO) to the unoccupied anti-bonding orbital (LUMO). The resulting

photoexcited POM is highly reactive which can lead to both substrate oxidation and reduction depending on the conditions.[3] On the other hand, the ability of polyoxometalates to accept and donate electrons is an advantage which makes these materials intriguing for photoelectronic applications. Given their structural and electronic versatility, POMs can become very attractive materials for photocatalysis. They possess structural features of some well-known photocatalysts, such as M-O-M (M = transition metal) connectivity, and are very robust with respect to oxidation as they generally have d^0 electronic configurations. For several decades POMs have been known to exhibit photoactivity and it was in the 1980s when the photoactivity of POMs was demonstrated by the research groups of Hill, Papaconstantinou, Yamase and others.[3]

In addition to their photocatalytic properties, POMs also show promise in the formation of metal-organic frameworks (MOFs) or the so-called POMOFs. Over the years, metal organic frameworks (MOFs) have attracted scientists for their unusual structural features pertinent to advanced applications in gas storage, heterogeneous catalysis, separations and molecular recognition.[4] MOFs are defined as extended solids constructed of metal ion or metal cluster centers as building blocks that are interconnected by organic bridging units.[5] MOFs are interesting particularly with respect to their facile synthesis utilizing secondary building units made of organic ligands and metal centers to target porous structures with desired size and shape through the so-called reticular synthesis.[6] Because of their porous nature, special emphasis in MOFs has been placed on gas storage for energy applications[7] and heterogeneous catalysis.[8] MOFs in general, have large surface areas allowing for maximal reversible sorption of the guest species required for gas storage

and/or access to available active sites for heterogeneous catalysis.[7,8] Recently, inorganic polyoxometalates (POMs) have been successfully incorporated as the inorganic units in MOF frameworks resulting in composite polyoxometalate-organic frameworks or so-called POMOFs.[9] Literature reports describing the incorporation of POMs in MOF materials certainly provided initial motivation for the synthesis and characterization of compounds presented in this chapter.

The main idea behind the research efforts described in this chapter was the potential for synthesis of POMOFs for applications in gas storage and catalysis, including solar-driven catalysis. The main idea was that POMs, being much larger than the metal centers in conventional MOFs, would be used to replace the metal centers in MOFs and create larger pores compared to the conventional MOFs as they occupy relatively more space. Further, the presence of multiple metal redox centers is intriguing for the potential study of catalytic activity of these materials. The organic ligands in POMOFs were targeted to serve as spacers to help create 3D porous frameworks in which substrate reactions can be catalyzed by POM redox centers. Essentially, the POM can be thought of as occupying the corners of a cube while the organic ligands would be the edges and the created void space of a cube can be thought of as a micro vessel for gas storage and a micro beaker for catalytic reactions of substrates. The typical hybrid frameworks that were explored in this research contained, as illustrated in Figure 6.1, POM−M−POM, POM−L−POM, POM−M−L−M−POM and POM−L−M−L−POM linkages where M is a

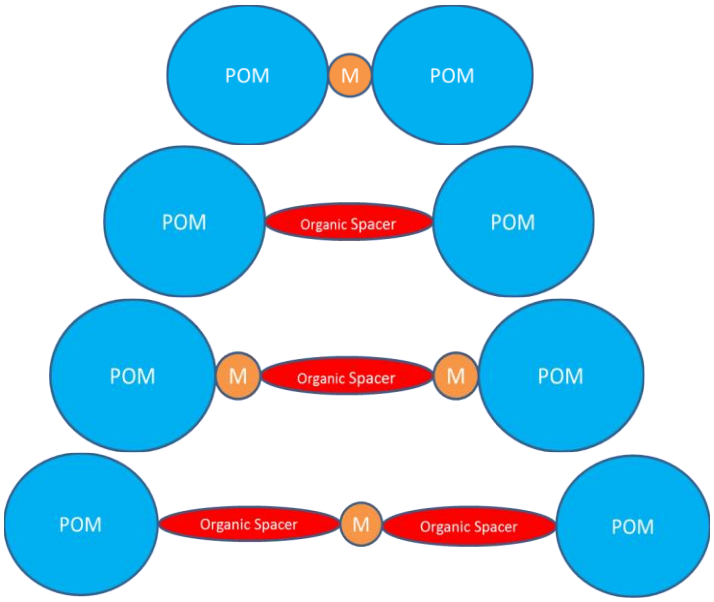

Figure 6.1: Possible POM-POM bridges that were explored in the synthetic efforts described in this chapter.

metal linker and L is an organic spacer. Due to the relatively low thermal stability of the organic spacers, the reactions targeting POMOFs were done using mild-temperature (< 200 ^{o}C) under hydro/solvothermal conditions where specific parameters including selection of solvent media, establishment of reactant stoichiometry and adjustment of pH of the starting solutions were carefully considered. To ensure homogeneity of the reaction mixture, solvent medium selection was particularly important given that the starting reactants have different solubilities in solvents because of the dissimilar bonding nature of the starting materials (*i.e*. ionic vs. covalent vs. van der Waals). In most cases, organic ligands such as 4,4'-bipyridine require organic solvents to be completely dissolved while the precursors

(*e.g.* POM salt) require aqueous/polar solvents due to largely ionic bonding nature of these materials. For this reason, a selection of mutually miscible aqueous and organic solvents (*e.g.*, water/alcohols) was used.

Synthesis of POMOFs is conceivably difficult using *bottom-up, one-pot* synthetic routes due to the formation of undesirable non-POM containing phases. Moreover, it is difficult to control the *in situ* formation of POMs and in turn designed synthesis of final POMOF products is almost impossible. In order to target desired materials and gain more control over the formation of the final products, a more sensible approach was to use pre-synthesized soluble POMs which serve as building blocks to facilitate self-assembly of hybrid POMOF materials. This idea of using pre-synthesized POMs can easily be understood from the organic synthesis perspective where several step-wise reactions need to occur in order to arrive at the final product formation. Having a pure starting material (in this case pre-synthesized POMs) for each step-wise reaction ensures that the products will form in higher yields. In the case of using simple metal oxides in *bottom-up* synthesis, several side reactions can occur which would make it difficult for the *in situ* formation of POMs. Similar to organic synthesis, these side reactions can be thought of as impurity phases that limit the formation of desired product(s). This is especially evident in multi-step reactions as impurities do not generally scale linearly with each step.

In this research, the existing water-soluble POM-containing salts were used for the potential synthesis of POMOFs, including the ones that were newly discovered *via* salt-inclusion chemistry in our laboratory. Namely, $Cs_5(V_{14}As_8O_{42}Cl)$[10] (**V14**) and $Cs_{11}Na_3Cl_5(V_{15}O_{36}Cl)$[11] (**V15**), both water-soluble salt-inclusion solids, were used as the

source of the building block polyoxometalate anions. Several exploratory hydrothermal reactions using **V14** and **V15** as the pre-synthesized POMs produced new hybrid POM-organic solids including, $[Cu_3(bpy)_2(Hbpy)_2]\bullet[V_{14}As_8O_{42}Cl]_2$ (**1**), $[Cu(bpy)]_2\bullet[H_3V_{14}As_8O_{42}Cl]$ (**2**), $[(H_2bpy)]_2\bullet[V_{14}As_8O_{42}Cl]$ (**3**), and $[(bpy)_2(H_2bpy)_3(Hbpy)_2]\bullet[V_{15}O_{36}Cl]_2\bullet 4H_2O$ (**4**) where bpy = 4,4'-bipyridine. Chapter 6 will mainly focus on the synthesis and structure description of compounds **1**~**4**. Special emphasis on bonding interactions between the POM and the organic ligand, 4,4'-bipyridine, will be placed when discussing the structures of **1**~**4**. Given that compounds **1**~**4** have different overall structures, discussions about each compound will be presented separately throughout the chapter. Similarities, as well as the differences, in these four structures as they relate to the bonding nature between the POM, bpy (and copper where applicable) will be discussed for all four compounds. For compounds **1**~**3**, the polyoxometalate in all three has the same composition, $(V_{14}As_8O_{42}Cl)^{n-}$. Interestingly, there are some obvious differences between the POM cluster symmetries in **1**~**3** compared to the published $Cs_5(V_{14}As_8O_{42}Cl)$ solid. Given that **V14** was originally used in the synthesis of **1**~**3**, it is conceivable that the transformations in symmetry of the cluster in **1**~**3** had to occur by breaking bonds and re-formation of the same resulting in overall symmetry change of the cluster. These transformations may have some mechanistic relevance in terms of POM formations as well as their (in)stability in solution and will be discussed in detail below.

Synthetic Procedure and Discussion

The compounds presented in this chapter are a result of exploratory reactions in which polyoxometalate (POM)-based metal-organic-frameworks (MOFs) were targeted (also known as POMOFs). The nature of exploratory synthetic research is such that not many paramaters are known under which the targeted compounds form. Soluble polyoxovanadates (POVs) were used in hydrothermal reaction conditions for the self-assembly of the targeted compounds. In order to counterbalance the negative charge of POMs, transition metal ions such as Cu^{2+} and Zn^{2+} were used with 4,4'-bipyridine (bpy) ligand to form -POM-M-bpy- frameworks. The reaction parameters such as pH, the ratios of POMs, bpy and M were varied to reveal under which conditions the targeted compounds would form. Though the targeted POMOFs were unable to be synthesized (if POMOFs are defined by large porous structures) under the employed conditions, the isolated hybrid inorganic-organic compounds presented in this chapter helped to better understand the nature of bonding interactions between the negatively charged POVs, the transition metal cation, M, and the organic ligand, bpy.

Synthesis of $Cs_5(V_{14}As_8O_{42}Cl)$ (V14), polyoxovanadate-containing precursor: High yield synthesis of $Cs_5V_{14}As_8O_{42}Cl$ (**V14**) precursor was done by loading a slightly modified stoichiometric reaction compared to the reported synthetic route.[10] CsCl, Cs_3VO_4, As_2O_3, V_2O_3 and VO_2 were loaded in 3:4:12:2:34 molar ratios (0.75 g total reactants), respectively. The reaction mixture was ground and loaded into a carbon-coated fused silica tube inside a nitrogen-purged drybox and was flame-sealed under vacuum. It should be

noted that the carbon coating prevents the deterioration of the ampoule caused by a potential reaction between the fused silica and the reactants, mainly molten chloride salt, at high temperature. The mixture of the reactants was heated to 600 ^{o}C at a rate of 2 ^{o}C per minute and was isothermed for 72 hours before being cooled to room temperature at 2 ^{o}C per minute. The dark brown polycrystalline powder was ground and was subjected to powder X-ray diffraction for confirmation of phase formation as shown in Figure 6.2 below. The figure shows the calculated powder pattern (bottom) and the as-prepared patterns from two different batches. From this figure, it can be seen that the calculated powder pattern for $Cs_5(V_{14}As_8O_{42}Cl)$ matches closely that of the as-prepared precursor.

Synthesis of $Cs_{11}Na_3Cl_5(V_{15}O_{36}Cl)$ (V15), polyoxovanadate-containing precursor: Stoichiometric synthesis of $Cs_{11}Na_3Cl_5(V_{15}O_{36}Cl)$ (**V15**) precursor was done using a similar procedure as the published synthetic approach.[11] CsCl, NaCl, Cs_3VO_4, V_2O_5, VO_2 were loaded in molar ratios of 9:9:8:2:33, respectively. The reactants were weighed, ground, and loaded into carbon-coated fused silica tubes inside a nitrogen-purged glovebox. Then, the mixture was sealed under vacuum using a flame torch. The fused silica ampoules containing the reactants were loaded into a standard box furnace for the heating step. The reactions were heated to 600 ^{o}C at a rate of 2 ^{o}C per minute and were allowed to isotherm at 600 ^{o}C for three days before being cooled back down to room temperature at 2 ^{o}C per minute. The dark green powder was ground and subjected to powder X-ray diffraction for phase confirmation. Figure 6.3 shows the powder X-ray diffraction patterns for two separate batches along with the calculated pattern based on the published single

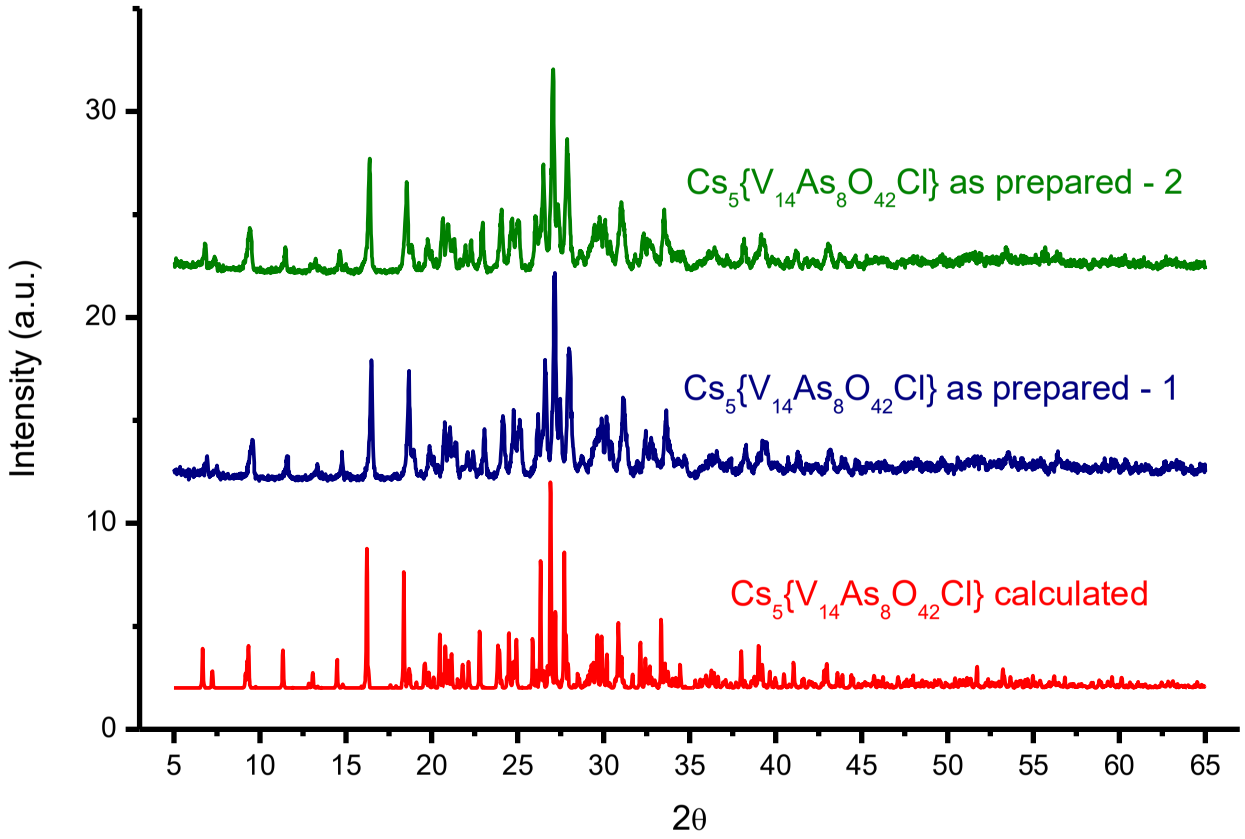

Figure 6.2: PXRD pattern of the $Cs_5(V_{14}As_8O_{42}Cl)$ precursor synthesis. The bottom (red) line is the calculated based on the published single crystal X-ray structure solution. Middle (blue) and top (green) are patterns for two different batches of as-prepared precursors.

crystal structure solution of **V15**. A close match between the calculated and observed powder patterns is evident which confirms the successful synthesis of **V15** precursor.

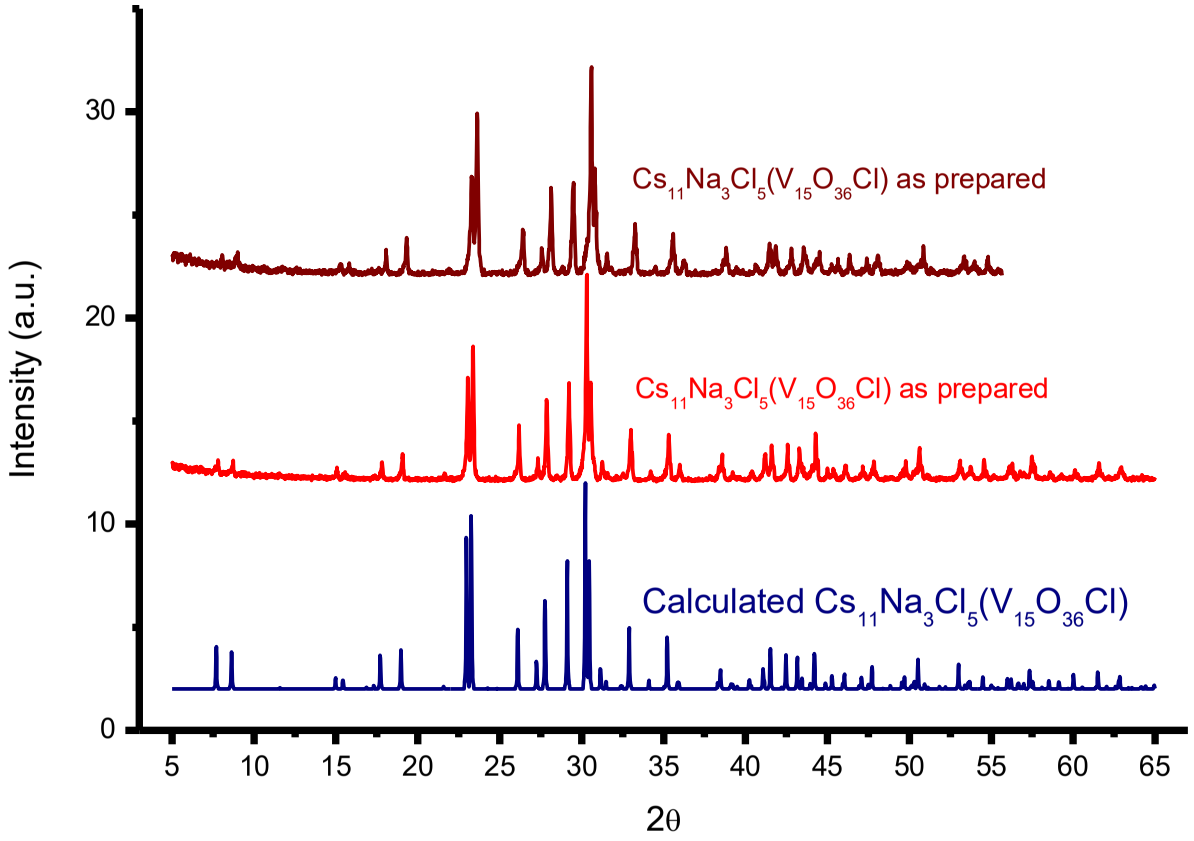

Figure 6.3: PXRD pattern of the $Cs_{11}Na_3Cl_5(V_{15}O_{36}Cl)$ precursor synthesis. The bottom (blue) line is the calculated based on the published single crystal X-ray structure solution. Middle (red) and top (brown) are patterns for two different batches of as-prepared precursors.

Single Crystal Synthesis of $[Cu_3(bpy)_2(Hbpy)_2]\bullet[V_{14}As_8O_{42}Cl]_2$ (1): Single crystals of **1** were grown using hydrothermal reaction conditions. $Cu(OAc)_2$ (OAc = acetate, CH_3COO^-), 4,4'-bipyridine (bpy, $C_{10}H_8N_2$), $Cs_5(V_{14}As_8O_{42}Cl)$ were weighed and loaded in 1:10:1 molar ratios, respectively with the total amount of reactants being 0.125 g. 10 mL of deionized water was used as the solvent for the original synthesis of **1**. This reaction produced about 12 mg of single crystals or ~8% overall yield (based on $Cs_5(V_{14}As_8O_{42}Cl)$ starting material) of **1** while the remaining product was the army green powder (see the discussion below about the identity of this powder). The yield of this reaction was improved by using a mixed solvent system which allowed for better solubility of starting materials. The solvent used in the synthesis of **1** was a mixture of 5 ml H_2O and 5 ml ethanol. The reason for this 'cocktail' mixture of solvents was to ensure that both the POM precursor and the organic ligand (bpy), which have different solubility in water, were dissolved in the mixed solvent system. Though the increase in temperature (and pressure for that matter) in hydrothermal reaction conditions would likely entice the reactants to dissolve at elevated temperatures anyway, ensuring that the reactants are soluble at lower temperatures (*e.g.* room temperature) would be beneficial in case the crystal growth of targeted phases occurs upon cooling at lower temperatures (and pressures). **V14** precursor and $Cu(OAc)_2$ were dissolved in 5 ml of water while bpy was dissolved in 5 ml of ethanol. The pH of the two solutions was tested and recorded. The **V14** / $Cu(OAc)_2$ solution was slightly acidic with a pH of 6.3. The ethanol solution was also acidic with pH being approximately 5. Each solution was stirred for five minutes before combining the two solutions in a Teflon-lined stainless steel hydrothermal reaction vessel. The pH of the

combined solutions was measured to be close to 6. Then, the pH of the mixture was adjusted to pH of 3 with a dropwise addition of 1M HCl solution. The Teflon-lined hydrothermal reaction vessel was closed and was placed in a standard box furnace for the heating step. The reaction was heated to 160 ^{o}C at a rate of 1 ^{o}C per minute and was allowed to isotherm at 160 ^{o}C for 48 hours. To promote the formation of single crystals, slow cooling at a rate of 0.1 ^{o}C per minute was programed to occur from 160 ^{o}C to 25 ^{o}C. Upon opening the reaction vessel, army green powder was able to be seen at the bottom of the Teflon container. Filtering the solution and isolating the solids revealed the dark green (almost black) columns mixed in with the army green powder. The dark green columns, with a yield of about 40 % based on visual observation under an optical microscope, were mounted and were identified as compound **1** using single crystal X-ray diffraction studies. The remaining portion of the product was ground and powder X-ray diffraction was done in order to identify the army green powder along with any additional impurities. Further, powder X-ray diffraction was also used to confirm the presence of compound **1**. Figure 6.4 shows the powder pattern of the above described reaction in which single crystals of **1** were formed. Looking at this figure, compound **1** can easily be identified by observing a close match between the calculated pattern of **1** and that of the observed powder of the overall reaction. In addition to the identification of **1**, no other impurity peaks can be seen except the broad hump between 15 and 35 2θ which is likely caused by the formation of amorphous products. It should be noted that the quality of this powder pattern is relatively poor possibly due to the small sample size as well as the presence of amorphous phases (note the amorphous broad hump). Given that no other crystalline phases appear in the

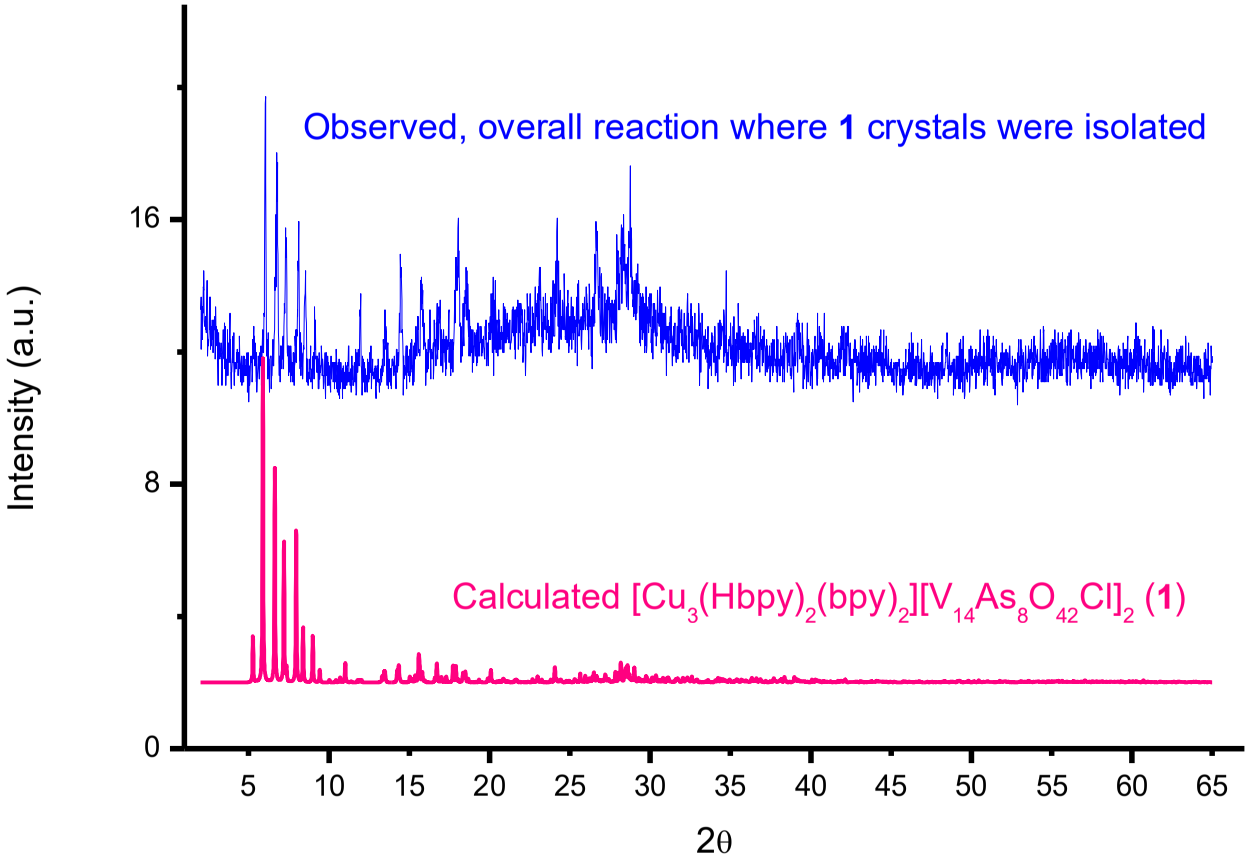

Figure 6.4: PXRD pattern of the overall reaction product (blue, top) where single crystals of **1** were synthesized. The bottom (pink) pattern is the calculated based on the single crystal X-ray structure solution of **1**.

powder pattern shown in Figure 6.4, the army green powder is most likely the amorphous impurity phase causing the broad hump in the powder pattern.

Single Crystal Synthesis of $[Cu(bpy)]_2$•$[H_3V_{14}As_8O_{42}Cl]$ (2): Single crystals of **2** were grown using similar reaction conditions as those used in the synthesis of single crystals of **1**. One modification that was made in synthesis of **2** was the relative ratios of bpy to $Cu(OAc)_2$ and **V14**. Namely, the amount of bpy was reduced resulting in the overall molar ratios of 1:2:1 for $Cu(OAc)_2$, bpy, **V14**, respectively. The total mass of reactants, 0.125 g, were weighed and dissolved in ethanol for bpy and water for $Cu(OAc)_2$, **V14** before being combined together in a Teflon container. The pH was adjusted to approximately 1.5 by a dropwise addition of 1M HCl solution. The heating program for this reaction was the same as that for the synthesis of single crystals of **1**. Short dark green columns were able to be isolated with a yield of less than 10% based on the observation of the overall product under an optical microscope. Army green powder was the major product as was the case for the reaction which produced single crystals of **1**. Figure 6.5 shows the PXRD pattern of the overall solid product of the reaction that produced crystals of **2**.

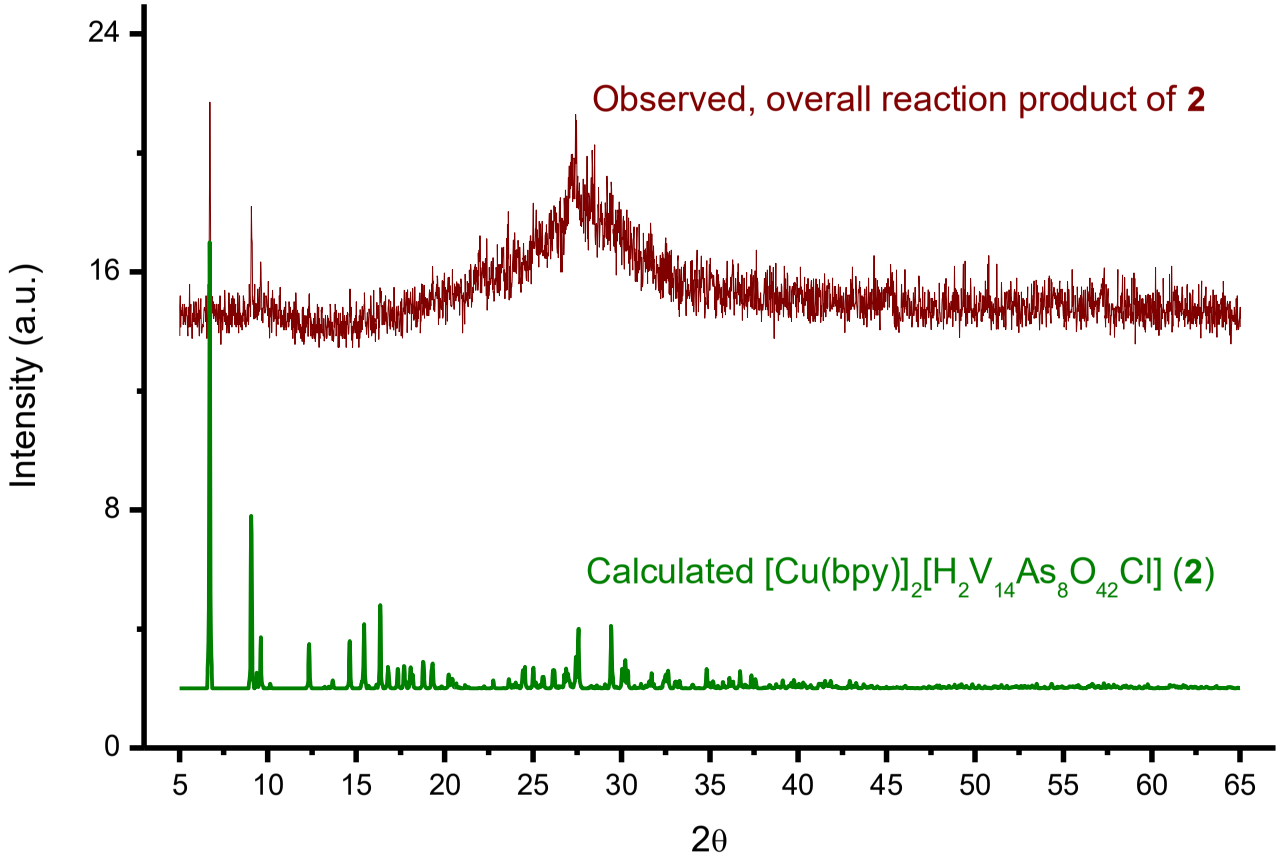

Figure 6.5: PXRD pattern of the overall reaction product (brown, top) where single crystals of **2** were synthesized. The bottom (green) pattern is the calculated based on the single crystal X-ray structure solution of **2**.

Single Crystal Synthesis of $[H_2(bpy)]_2$•$[V_{14}As_8O_{42}Cl]$ (3): Single crystals of $[H_2(bpy)]_2$•$[V_{14}As_8O_{42}Cl]$ (**3**) were synthesized using hydrothermal reaction conditions. In the reaction that produced **3**, $ZnCl_2$ was used in place of $Cu(OAc)_2$ as the potential source of linking transition metal cation. The reactants were loaded using the molar ratios of 1:10:1 for $ZnCl_2$, bpy, and **V14**, respectively with the total amount of reactants being 0.125 g. The water soluble reactants were first dissolved in water while bpy was dissolved in ethanol. The pH of the combined reaction mixtures was adjusted to pH 4 by dropwise addition of 1M HCl. The reaction was then loaded into a Teflon-lined autoclave and was heated to 160 ^oC at 1 ^oC per minute. Subsequently, the reaction was isothermed at 160 ^oC for 48 hours before being cooled back to 25 ^oC at a rate of 0.1 ^oC per minute. The product was filtered and washed using vacuum filtration and single crystals of **3** were isolated under an optical microscope and were mounted for single crystal X-ray diffraction. The yield of the single crystals was qualitatively estimated based on the observation of the products under an optical microscope with the single crystal yield being about 60% of the overall filtered product. Figure 6.6 shows the PXRD pattern of the overall solid product of the reaction that produced a relatively high yield of single crystals of compound **3**.

Single Crystal Synthesis of $[(bpy)_2(H_2bpy)_3(Hbpy)_2]$•$[V_{15}O_{36}Cl]_2$•$4H_2O$ (4): Single crystals of **4** were grown from a reaction analogous to that in which single crystals of **1** were synthesized. In the case of the reaction where **4** was synthesized, **V15** was used as the source of the POM starting material. $Cu(OAc)_2$, bpy, **V15** were weighed in 1:10:1 molar ratios, respectively with the total mass of the starting materials being 0.125 g. The inorganic starting materials were dissolved in 5 ml of water and bpy was dissolved in 5 ml

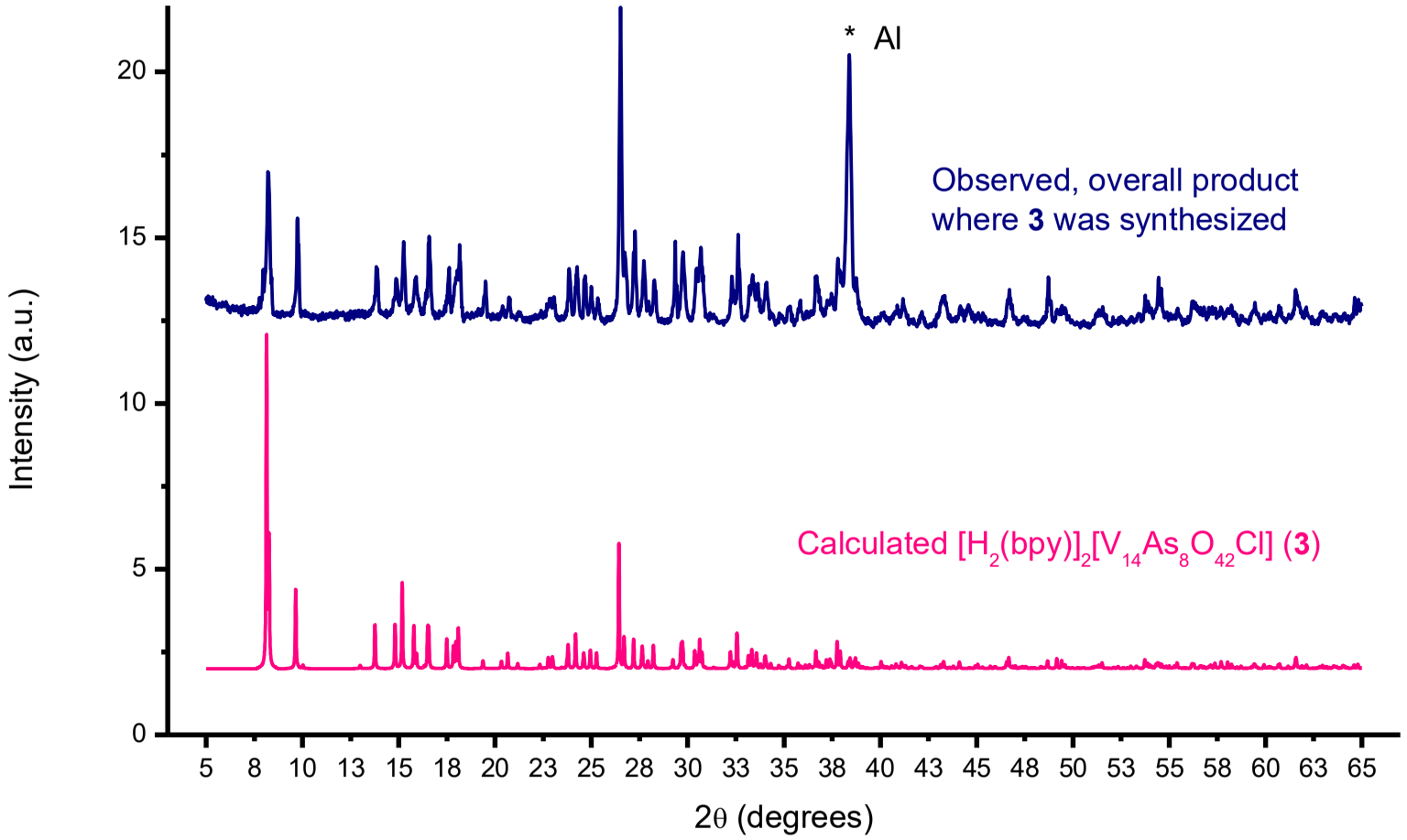

Figure 6.6: PXRD pattern of the overall product of the reaction where **3** was synthesized. The bottom (pink) pattern is the calculated based on the single crystal structure solution of **3**. Top (blue) pattern is the observed. Because a small amount of product was used in the PXRD experiment, aluminum peak appears due to the sample pan diffracting.

of ethanol. The two mixtures were combined and the final pH was adjusted to approximately 5 with a dropwise addition of 1M HCl. The heating program was the same as that for the synthesis of **1**. Upon opening the hydrothermal reaction vessel, a dark green powder was observed at the bottom of the Teflon cup. This powder was filtered using standard vacuum filtration and was washed using DI water. The dispersion of powder on the filter paper allowed for isolation of single crystals of **4** in a very low yield (< 5%, based on qualitative observation). The crystals of **4** were column-like and the color appeared black initially. However, upon smearing these crystals on a white sheet of paper, a dark green color was seen. Several crystals were mounted for single crystal X-ray diffraction analysis. The remaining product was ground and subjected to powder X-ray diffraction in order to identify the dark green powder and any additional impurities present. Figure 6.7 shows the powder X-ray diffraction pattern for the overall reaction where **4** was synthesized. The observed powder pattern was compared to that of the calculated based on the single crystal structure solution of **4**. A broad hump spanning from 15 to 30 2θ can again be seen which is due to the amorphous phase(s) being present in the final product of the reaction. Even though a small yield of crystals of **4** was observed, the most intense peaks matching the calculated powder pattern of **4** can still be identified, especially in the 5-10 2θ range.

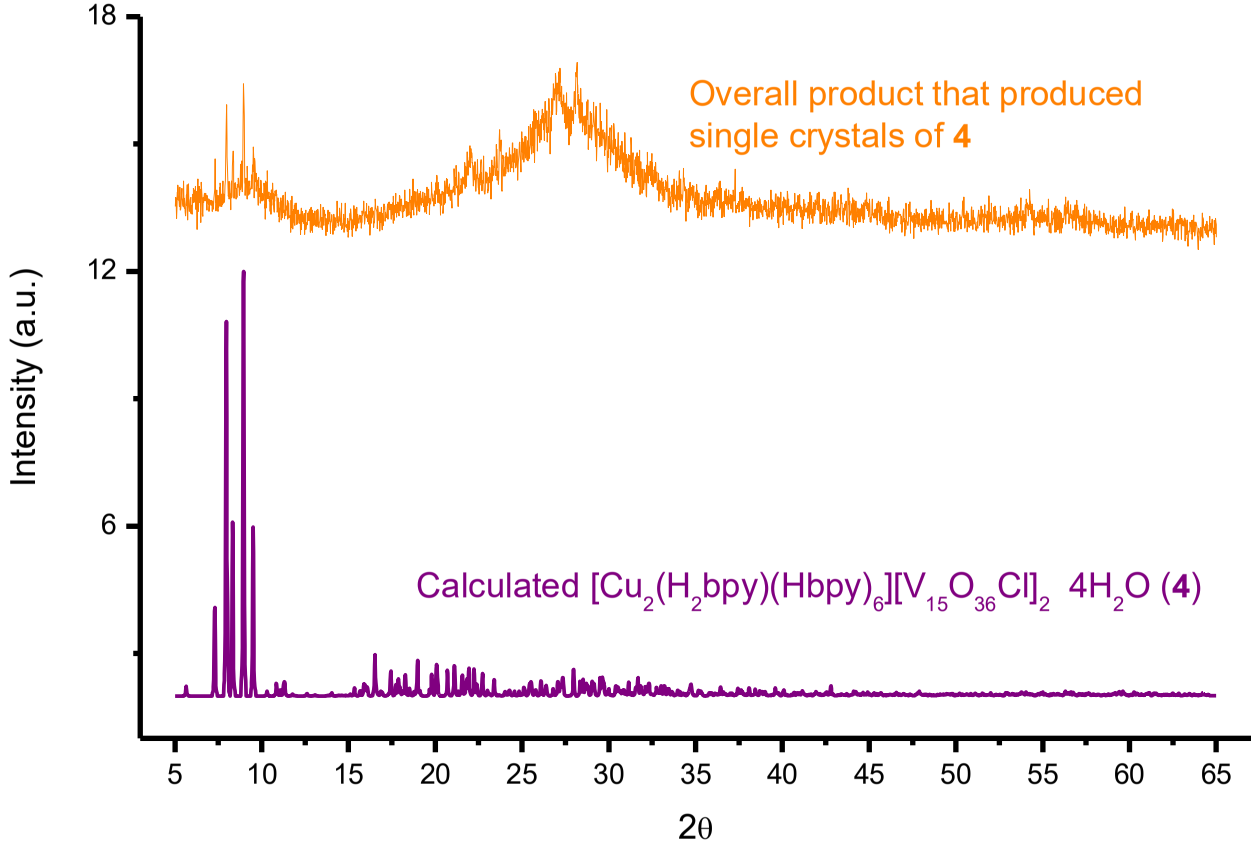

Figure 6.7: PXRD pattern of the overall product of the reaction where **4** single crystals were synthesized. The bottom pattern is the calculated based on the single crystal structure solution. Top (orange) is the observed pattern.

Characterization

Elemental Analysis, Energy Dispersive Spectroscopy (EDS): EDS was used to qualitatively confirm the presence of heavier elements comprised in the compositions of **1~3**. In most cases, elemental analysis was performed on the single crystals used for the SXRD structure determination of **1~3**.

Elemental Analysis, C H N: Elemental analysis using C H N analyzer was used to confirm the presence of carbon, hydrogen and nitrogen comprised in the compositions of **1** and **3**. It should be noted that compounds **2** and **4** were not analyzed due to the poor reaction yields and the inability to collect ~10 mg of single crystals. From the C H N data of **1** and **3**, relative ratios of these elements were obtained and used in conjunction with the single crystal X-ray diffraction data in order to arrive at the final compositions of compounds **1** and **3**, especially regarding the presence of hydrogen (protonated vs. non-protonated 4,4'-bipyridine molecules). In both cases, elemental analysis was performed on single crystals of **1** and **3**. 10 mg of ground single crystals of **1** and **3** were weighed in tared tin capsules. The tin capsules were then folded and flattened before being placed in an autosampler of the PerkinElmer 2400 Series II CHNS/O analyzer. The samples, along with the tin blank sample, were then combusted and the content of analytically important by-product gases (CO_2, H_2O and N_2) were analyzed. From the content of these by-product gases, the instrument calculated the weight percent of carbon, hydrogen and nitrogen which was the raw data obtained for samples **1** and **3**. Finally, the weight percent amounts of each element were converted to mole percent and were compared to the expected relative molar

ratios of C:H:N in 4,4'-bipyridine and the protonated, $[H(4,4'\text{-bipyridine})]^{+}$ and $[H_2(4,4'\text{-bipyridine})]^{2+}$. Table 6.4 and Table 6.5 shows the experimental elemental analysis of single crystals of **1** and **3**, respectively, including the comparison to the expected values.

Powder X–ray Diffraction (PXRD): PXRD was used to confirm the phase formations of **1~4** observed in the original synthetic procedures that produced these compounds. In addition, PXRD was used to confirm the successful synthesis of **V14** and **V15** precursors. Powder patterns for these reactions are shown in Figures 6.2~6.7. The powder X–ray diffraction data were collected at room temperature using Cu Kα radiation in the 2θ range of 5–65 ° with a step size of 0.02 ° and a scan rate of 0.25 °/min.

Single Crystal X–ray Diffraction (SXRD): Single crystals of **1~4** were selected under an optical microscope equipped with a polarizing light attachment. SXRD data were collected on these single crystals at low temperature (at about -80 ^{o}C) using Mo Kα radiation (λ = 0.71073 Å) produced by a graphite monochromator. The reason for low temperature data collection was primarily due to the presence of light atoms (*i.e.* C, H, N). The low temperature employed in SXRD data collection reduced the thermal motion of atoms allowing for relatively easier structure solutions. The crystallographic data can be seen in Table 6.1 and 6.2. The atomic coordinates, anisotropic thermal parameters, selected bond distances and angles and bond valence sums calculations can be seen in Tables 6.3, 6.6~6.17.

Fourier Transform Infra-red (FTIR): FTIR was done in order to possibly identify unique vibrations present in the 4,4'-bipyridine molecule. It was especially of importance to attempt to identify the N-H stretch (around 3300-3000 cm^{-1}) of the

protonated 4,4'-bipyridine. However, this band is quite weak and oftentimes it is not easily identified. The FTIR data were collected on a NICOLET Magna IR Spectrometer 550. Initial sample preparation procedures were done by isolating and weighing approximately 10 mg of single crystals of **1** and **3**. Each sample was then mixed in with dry KBr salt. The amount of KBr salt used was approximately 100 mg. The single crystals, along with KBr, were ground in an agate mortar until the mixture appeared homogenous. Then, the ground mixtures were pressed into disk-like pellets using a standard hydraulic pellet press dye. The obtained pellets were translucent and approximately 2 mm thick. The pellets were attached to the sample holder using scotch tape with only a small portion of the pellet being attached to the tape to hold the sample in place during the measurements. The samples, including the KBr blank, were measured in the frequency range of 400 cm^{-1} to 4000 cm^{-1}.

Table 6.1: Crystallographic data for compounds **1** and **2**.

empirical formula	$[Cu_3(bpy)_2(Hbpy)_2]\bullet[V_{14}As_8O_{42}Cl]_2$, **1**	$[Cu(bpy)]_2\bullet[H_2V_{14}As_8O_{42}Cl]$, **2**
formula wt, g/mol	4855.34	2461.46
crystal system	Monoclinic	Monoclinic
space group	*C* 2/*c* (no. 15)	*P* $2_1/n$ (no. 14)
a , Å	31.431(6)	14.233(3)
b , Å	13.442(3)	11.490(2)
c , Å	35.131(7)	19.568(4)
α , deg.	90	90
β, deg.	107.30(3)	109.83(3)
γ, deg.	90	90
volume, $Å^3$	14171(5)	3010.5(10)
Z	4	2
D_{calc}, g/cm^3	2.28	2.72
abs coeff	6.02	7.26
crystal size, mm	0.20 x 0.10 x 0.10	0.15 x 0.08 x 0.08
theta range, deg	1.36 - 25.05	2.09 - 25.05
relns collected	29875	23159
indep reflns	12222	5323
R(int)	0.139	0.184
obsd ($I > 2s(I)$)	817	416
goodness-of-fit on F^2	1.771	0.995
$R_1[I > 2s(I)]$[a]	0.090	0.107
wR_2 (all data)[b]	0.187	0.248

bpy = 4,4'-bipyridine = C10H8N2

Table 6.2: Crystallographic data for compounds **3** and **4**.

empirical formula	$[H_2(bpy)]_2$•$[V_{14}As_8O_{42}Cl]$, **3**	$[(bpy)_2(H_2bpy)_3(Hbpy)_2]$•$[V_{15}O_{36}Cl]_2$•$4H_2O$, **4**
formula wt, g/mol	2336.38	3908.41
crystal system	Orthorhombic	Monoclinic
space group	*F ddd* (no. 70)	*P* $2_1/n$ (no. 14)
a , Å	13.481(3)	12.161(2)
b , Å	20.265(4)	22.021(4)
c , Å	42.808(9)	22.298(5)
α , deg.	90	90
β, deg.	90	95.09(3)
γ, deg.	90	90
volume, $Å^3$	11695(4)	5947.8(20)
Z	8	2
D_{calc}, g/cm^3	2.65	2.18
abs coeff	5.35	2.39
crystal size, mm	0.18 x 0.10 x 0.10	0.12 x 0.08 x 0.08
theta range, deg	2.22 - 25.05	1.85 - 25.05
relns collected	24101	50793
indep reflns	2599	10504
R(int)	0.100	0.182
obsd ($I > 2s(I)$)	208	865
goodness-of-fit on F^2	1.068	0.956
$R_1[I > 2s(I)]$[a]	0.059	0.0795
wR_2 (all data)[b]	0.153	0.186

bpy = 4,4'-bipyridine = C10H8N2

Results and Discussion

*Assignment of hydrogen atoms and balance of overall charge in compounds **1~4***

It is a well-known fact that due to the low electron density (*i.e.* one electron per atom), hydrogen atoms cannot be easily detected by X-ray diffraction. For this reason, the assignment of hydrogen atoms on respective carbon sites was done by adding 'dummy' or calculated hydrogen atom positions on the carbon sites that are already expected to have a hydrogen atom. For example, a benzene carbon atom is sp^2 hybridized and as such should have one hydrogen attached in which the hydrogen atom bisects the angle between the carbon atom bonded to hydrogen and the two vicinal carbon atoms. The ideal angle between the hydrogen atom, carbon atom and the next neighbor carbon atom is 120^o for benzene or any sp^2 hybridized carbon for that matter. Therefore the calculated positions of 'dummy' hydrogen atoms in crystallography are always in the same plane as the carbon atoms. The assignment of hydrogen atoms in this fashion is commonly done (where appropriate) in X-ray diffraction experiments. However, in some cases, it is not possible to assign these 'dummy' hydrogen atoms due to complete or neutral coordination around certain elements. For example, each nitrogen site on the bpy ligand has a lone pair which can easily attract protons (or Cu atoms in the case of compound **1)**. However, given that bpy nitrogen can exist in neutral form, *i.e.* unprotonated, as well as protonated, it is impossible to know and assign hydrogen atoms using X-ray diffraction data without knowing the local environments around elements (such as nitrogen with sp^2 hybridization)

Table 6.3: Bond Valence Sums Calculations for Compounds **1**~**4**.

$[Cu_3(bpy)_2(Hbpy)_2]\bullet[V_{14}As_8O_{42}Cl]_2$, **1**								
Atom	Calculated BVS	Assigned Oxidation	Atom	Calculated BVS	Assigned Oxidation	Atom	Calculated BVS	Assigned Oxidation
V(1)	4.14, 4.35	4+	V(2)	4.10, 4.32	4+	V(3)	3.76, 3.96	4+
V(4)	4.24, 4.46	4+	V(5)	4.00, 4.21	4+	V(6)	4.01, 4.22	4+
V(7)	4.30, 4.53	4+	V(8)	4.68, 4.93	5+	V(9)	4.50, 4.74	5+
V(10)	4.34, 4.56	4+	V(11)	4.02, 4.23	4+	V(12)	3.99, 4.20	4+
V(13)	4.49, 4.72	4+	V(14)	4.01, 4.23	4+	Cu(1)	0.75, 0.80	1+
Cu(2)	1.85, 1.99	2+						

$[Cu(bpy)]_2\bullet[H_2V_{14}As_8O_{42}Cl]$, **2**								
Atom	Calculated BVS	Assigned Oxidation	Atom	Calculated BVS	Assigned Oxidation	Atom	Calculated BVS	Assigned Oxidation
V(1)	4.01, 4.22	4+	V(2)	4.30, 4.53	4+	V(3)	4.28, 4.50	4+
V(4)	4.36, 4.58	4+	V(5)	4.00, 4.21	4+	V(6)	4.23, 4.45	4+
V(7)	4.28, 4.50	4+	Cu(1)	0.51, 0.57	1+			

$[H_2(bpy)]_2\bullet[V_{14}As_8O_{42}Cl]$, **3**								
Atom	Calculated BVS	Assigned Oxidation	Atom	Calculated BVS	Assigned Oxidation	Atom	Calculated BVS	Assigned Oxidation
V(1)	4.22, 4.44	4+	V(2)	4.24, 4.46	4+	V(3)	4.12, 4.33	4+
V(4)	4.23, 4.46	4+	V(5)	4.18, 4.40	4+			

$[(bpy)_2(H_2bpy)_3(Hbpy)_2]\bullet[V_{15}O_{36}Cl]_2\bullet 4H_2O$, **4**								
Atom	Calculated BVS	Assigned Oxidation	Atom	Calculated BVS	Assigned Oxidation	Atom	Calculated BVS	Assigned Oxidation
V(1)	4.10, 4.32	4+	V(2)	4.76, 5.01	5+	V(3)	4.50, 4.75	5+
V(4)	4.70, 4.96	5+	V(5)	4.38, 4.60	4+	V(6)	4.08, 4.29	4+
V(7)	4.67, 4.91	5+	V(8)	4.66, 4.90	5+	V(9)	3.99, 4.20	4+
V(10)	4.46, 4.69	5+	V(11)	4.57, 4.81	5+	V(12)	4.58, 4.82	5+
V(13)	4.39, 4.62	4+	V(14)	4.61, 4.85	5+	V(15)	4.29, 4.52	4+

and the presence of relatively close hydrogen bond donors and acceptors. For this reason, a careful analysis of the structure around each electronegative anion, such as nitrogen as well as oxygen atoms on the polyoxometalate cluster, was done. Initially, the environments of the nitrogen sites on the bpy ligands were carefully examined to see if any possible hydrogen bonding can possibly occur.

Given that typical donor-acceptor X-Z distances in X–H···Z (where both X and Z are electronegative atoms and X is the donor and Z is the hydrogen bond acceptor) range from 2.2 to 2.5 Å for potential hydrogen bonds,[12] the nitrogen environments in compound **1** were extended to search for nearby atoms that would be in the range of 2.2 and 2.5 Å. For compound **1**, this resulted in finding of a suitable donor-acceptor hydrogen bond connectivity between the neighboring N(4)-N(4) sites being 2.36 Å long. Figure 6.8 shows the connectivity between the neighboring N(4) atoms. The distance of 2.36 Å falls in the range of strong hydrogen bond category where the acceptor to donor distance is between 2.2 and 2.5 Å. When looking at the electron density map in the X-ray diffraction data, hydrogen atoms were unable to be found near N(4) atomic site. However, this is most likely due to the limitation of X-ray diffraction technique with respect to the scattering factor of hydrogen being low, as previously mentioned. Nonetheless, due to the close proximity of the two neighboring nitrogen sites, it is conceivable that a proton is present on the N(4) atomic site and is likely being shared by the neighboring nitrogen atom due to the relative close proximity of the two nitrogen sites. Similar approach was taken when looking at the remaining nitrogen atomic sites. However, N(1), N(2) and N(3) atoms are connected to copper which likely eliminates these three sites from participating in hydrogen bonding. In

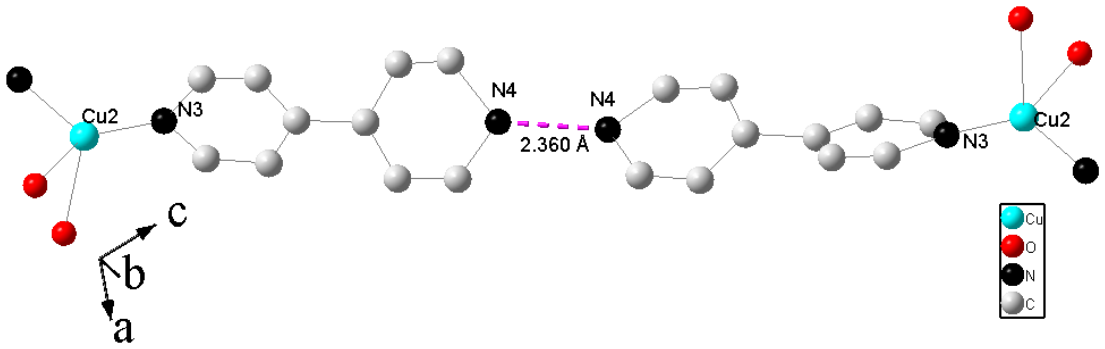

Figure 6.8: The connectivity between the two neighboring 4,4'-bipyridine units in **1** highlighting the close distance between the N(4) atomic sites and indicating the existence of hydrogen bond between the two nitrogen atoms.

fact, by extending the connectivity of the neighboring nitrogen atoms, N(1), N(2), and N(3) atomic sites in **1**, it can be observed that these three nitrogen atoms do not have suitable hydrogen donor or acceptor distances and hence these three atomic sites were ruled out as participants in hydrogen bonding.

Based on the results of X-ray diffraction studies, elemental analysis (EDS and CHN) bond valence sum calculations, and a careful analysis of the potential atomic sites where protons might be attached, the composition (especially as it relates to the number of protonated atomic sites, *i.e*. on nitrogen atoms) in compound **1**, $[Cu_3(bpy)_2(Hbpy)_2]\bullet[V_{14}As_8O_{42}Cl]_2$, was able to be derived. Looking at the bond valence sums calculations in Table 6.3, one can see that the cluster is likely mixed-valent with twelve of the fourteen vanadium sites being formally 4+ oxidation state while the remaining two vanadium atoms are fully oxidized, 5+ oxidation state. Comparing this to the original cluster in **V14** where all fourteen vanadium atoms are in their formal tetravalent state, two of the fourteen vanadium atoms in **1** were oxidized in solution during the reaction. This is not uncommon occurrence in polyoxometalates as solution-based synthesis generally leads to fully oxidized early transition metals unless reducing agents are used. The resulting overall negative charge on the cluster, based on the bond valence sum calculations (Table 6.3), is 3- which results in overall 6- charge (3- times two clusters) per formula unit. To counter-balance this anionic charge of 6-, two copper sites, namely Cu(1) (x 2) and Cu(2) (x 1) are monovalent and divalent, respectively. The two copper sites result in the cationic charge of 4+ which does not satisfy the overall 6- charge on the cluster. However, given that a relatively short distance occurs between the neighboring

nitrogen atoms (as discussed above), N(4) (x 2 per formula unit), one hydrogen atom (overall two per formula unit) per two N(4) sites are connected resulting in the additional two positive charges per formula unit.

With the four positive charges from the two copper sites and two positive charges from the protonated nitrogen atoms, the charge balance of the overall formula is now satisfied. Experimentally, relative number of hydrogen atoms can be quantified by using combustion CHN elemental analyzer. Table 6.4 shows the elemental analysis results for compound **1**. From this data, one can easily observe that the experimental amount of C, N, and H is close to the theoretical based on the overall formula. Of particular interest is the amount of hydrogen atoms observed in the experimental data compared to the expected

Table 6.4 Elemental Analysis Results for $[Cu_3(bpy)_2(Hbpy)_2]\bullet[V_{14}As_8O_{42}Cl]_2$, **1**. What is the standard deviation of wt %? The Experimental g/formula unit is not necessary.

Elements	Experimental (wt. %)	Experimental (g / formula unit)	Experimental (mol / formula unit)
C	9.79	475.34	39.6
N	2.02	98.08	7
H	0.76	36.9	36.9
	Theoretical (wt. %)	**Theoretical (g / formula unit)**	**Theoretical (mol/formula unit)**
C	9.88	480	40
N	2.31	112	8
H	0.70	34	34

hydrogen content. Looking at the last column (Experimental and Theoretical mol/formula unit), we can see that the moles of hydrogen atoms are 36.9 from the experimental results compared to theoretically expected 34 moles of hydrogen per formula unit. It should be noted that the 34 moles of hydrogen number includes the assigned protons on N(4) site. In case each of the bpy molecules is not protonated, the number of hydrogen atoms would be 32. Given that the experimental number of moles of hydrogen per formula unit is higher than 32, it likely suggests that extra hydrogen atoms should be present in the overall

formula. However, based on the experimental data at hand (CHN analysis), there should be about five (4.9, to be exact) extra protons rather than only two extra protons which was assigned based on the combination of bond valence sums results and the analysis of local environments with respect to possible hydrogen bond donor-acceptor distances. Two possible reasons for the higher than expected number of hydrogen atoms in the elemental analysis experiment are 1) the elemental analysis technique may not be sensitive enough to distinguish between small number of protons. This is especially the case when metals are present as part of the sample. 2) Another possibility is that surface water on the sample was present which increased the amount of hydrogen content in the CHN experiment. One way to check whether these compounds absorb water on the surface is by collecting FTIR vibrational spectra. A distinctive broad water peak should be seen in the 3000-3500 cm^{-1} region. Looking at the FTIR spectrum of compound **1** in Figure 6.9, one can see a small broad peak in the above-mentioned region that is possibly due to surface water. In addition, this region is also assigned to the aromatic C-H stretching vibrations. However, the latter vibration should not be as broad as the O-H stretch. It is possible that the extra protons showing up in the CHN elemental analysis experiment are due to the small amount of surface water.

Composition of compound $[Cu(bpy)]_2 \bullet [H_3V_{14}As_8O_{42}Cl]$, (**2**), as it relates to the extent of protonation, was finalized using a similar approach as that for compound **1**. Looking at the bond valence sums calculations for compound **2**, as is the case with the original salt-inclusion solid, **V14**, all of the vanadium sites are formally tetravalent. This means that the overall charge on the ($V_{14}As_8O_{42}Cl$) cluster is 5-. With two monovalent

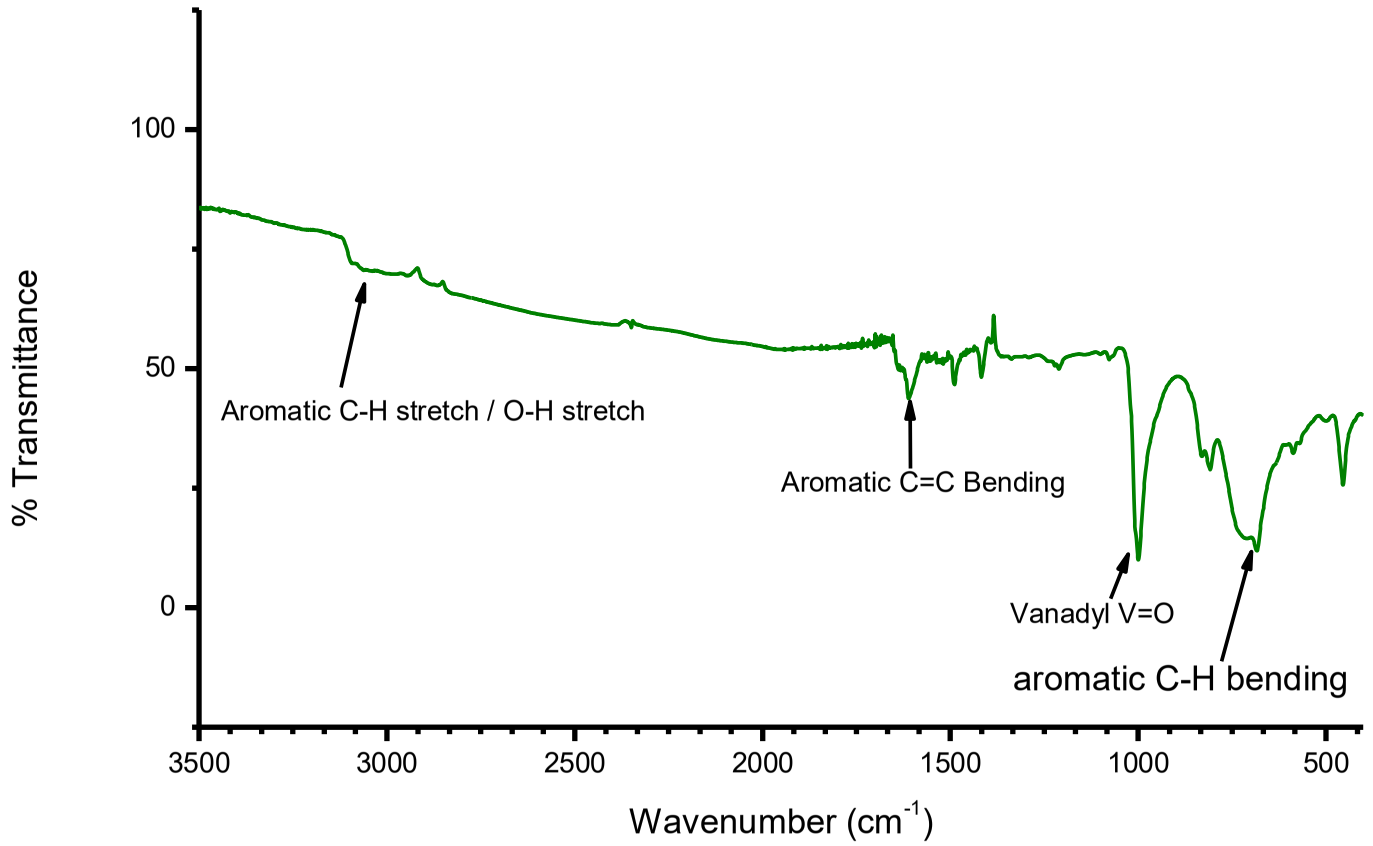

Figure 6.9: FTIR of collected single crystals of **1** with assigned vibrations showing aromatic vibrations in the 4,4'-bipyridine molecule as well as vanadyl V=O vibration. Possible O-H stretch vibration can be seen around 3300 cm^{-1} indicating the presence of surface water.

copper sites per formula unit, there still need to be three positive charges to balance the overall negative charge of the 5- cluster. Initially, the nitrogen site environments were analyzed for potential presence of hydrogen bond donor-acceptors as was done for compound **1**. However, given that both N(1) and N(2) atomic sites are coordinated to copper, this likely means that the nitrogen sites are not protonated. Instead, the protonation may have occurred on the vanadyl oxygen atoms on the ($V_{14}As_8O_{42}Cl$) cluster. Extending the distance to search for nearby hydrogen bond donor-acceptor pairs such as N···O (where N is the acceptor and O is the donor, N···H-O) resulted in suitable hydrogen bond donor-acceptor distances of 3.274 Å for N(2)···O(23), 3.063 Å for N(2)···O(22), and 2.918 Å for N(1)···O(19), as seen in Figure 6.10. All three of these oxygen atoms are the vanadyl oxygen atoms pointing away from the center of the cluster. These distances between hydrogen bond donors and acceptors fall in the range of moderate to weak hydrogen bonds. Based on these three suitable hydrogen bond donor-acceptor distances, the assignment of protons on the vanadyl oxygen atoms was able to be done. With three protons on the cluster and two monovalent copper atoms per formula unit, the overall 5- charge on the cluster is now satisfied. Ideally, having experimental data such as C, H, N elemental analysis to confirm the content of three extra protons per formula unit would be desired. However, due to small crystal size and the initial small overall yield of **2**, C, H, N elemental analysis was unable to be done for compound **2**.

Unlike in compounds **1** and **2**, in compound **3** there are no copper atoms present so the balance of negative charge on the cluster inevitably had to come from protonated species such as 4,4-bipyridine. Upon analysis of the local environments of potential

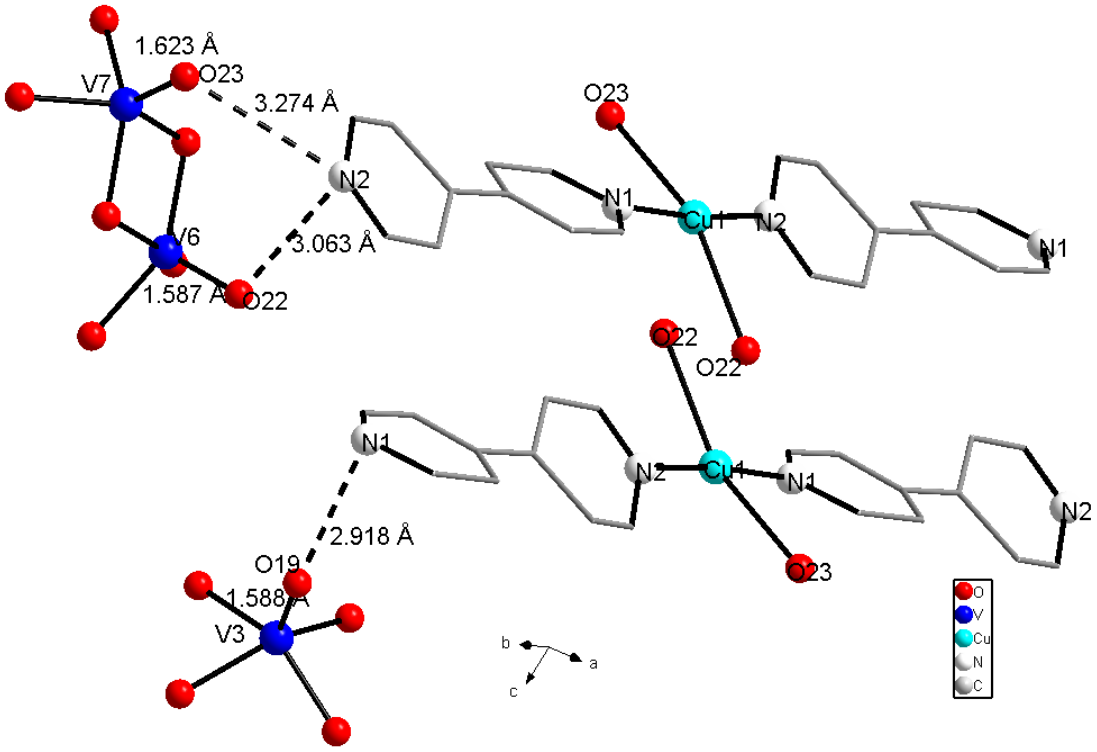

Figure 6.10: Connectivity between the potential hydrogen bond donor-acceptor pairs highlighting the distances between the neighboring oxygen atoms on the cluster (partial drawing) and the nitrogen sites on the 4,4'-bipyridine molecules in compound **2**. It is believed that the oxygen sites O(23), O(22) and O(19) are protonated.

hydrogen bond donor-acceptor pairs, one can see that there is a suitable hydrogen bond donor-acceptor distance between the neighboring nitrogen and oxygen atoms. This distance is 2.729(1) Å between N(1) and O(6) sites and falls in the moderate range of hydrogen bond strength. Though in most cases hydrogen atoms are unable to be located from the electron density maps of single crystal X-ray data, in compound **3**, protons on the N(1) site were located by looking at the electron density maps and observing a potential hydrogen atom (H(1)) with a distance to N(1) of 0.86 Å. This H(1) proton is hydrogen-bonded to the oxygen (O(6)) on the ($V_{14}As_8O_{42}Cl$) cluster with a distance of 1.880 Å. Figure 6.11 illustrates the connectivity through hydrogen bonding between the nitrogen atoms on the 4,4'-bipyridine molecules and the neighboring oxygen atoms on clusters in **3**. Given that the 4,4'-bipyridine molecule in **3** is crystalographically symmetric, there are two N(1) sites per molecule of 4,4'bipyridine and hence there are four N(1) atomic sites per formula unit. This likely means that there are also four hydrogen atoms on N(1) atoms per formula unit. From the bond valence sums calculations, given the symmetry of the cluster and the multiplicity of the five vanadium sites, it is not very easy to assign the oxidation state of each vanadium site. For example, V(3) and V(4) sites have a multiplicity of four (per formula unit) and in case of mixed oxidation states (*i.e.* 1 x V^{5+} and 3 x V^{4+}) in each, the bond valence sums calculations are not going to be straightforward. Ideally in sites with mixed oxidation state such as the one above, it should be expected that the bond valence sums show an oxidation state proportional to the number of V^{5+} and V^{4+} states in one site. In case of a site with multiplicity of 4 and mixed oxidation state site having 1 x V^{5+} and 3 x V^{4+}, it should be expected that the bond valence sum is about 4.25. However,

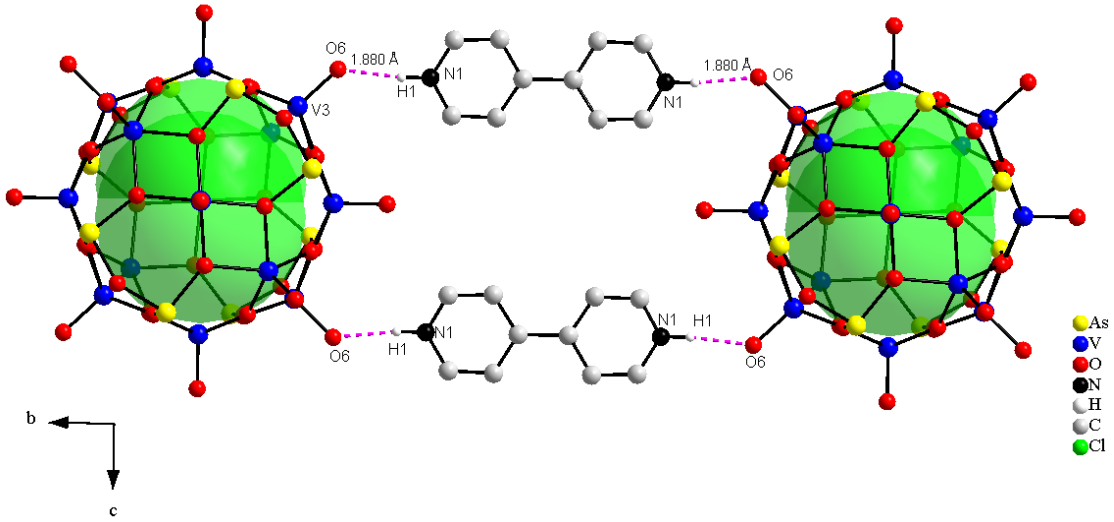

Figure 6.11: Hydrogen bonding between the protonated 4,4'-bipyridine molecules and the vanadyl oxygens on the cluster in compound **3**. The hydrogen bonding between the cluster and 4,4'-bipyridine units make an infinite non-covalent chain running along *b* direction. Surprisingly, in compound **3** the hydrogen atoms were able to be found and assigned by looking at the electron density map around N(1) atomic site.

to complicate things even more, delocalization of electrons within the cluster between the neighboring metal sites likely means that the assignment of oxidation states using such approach may not be completely valid. For this reason, having experimental data to confirm

Table 6.5 CHN Elemental Analysis of $[(H_2bpy)]_2$•$[V_{14}As_8O_{42}Cl]$ (**3**) single crystals

Elements	Experimental (wt. %)	Experimental (g / formula unit)	Experimental (mol / formula unit)
C	10.96	256.07	21.34
N	2.08	48.60	3.47
H	1.05	24.53	24.53
	Theoretical (wt. %)	**Theoretical (g / formula unit)**	**Theoretical (mol/formula unit)**
C	10.27	240	20
N	2.40	56	4
H	0.86	20	20

the overall oxidation state would help. Provided that enough single crystals of compound **3** were able to be obtained, CHN elemental analysis was performed in order to find out the composition of hydrogen atoms and hence the degree of protonation of the compound can be inferred. Looking at the results of CHN elemental analysis in Table 6.5, one can observe that the number of hydrogen atoms is higher than expected by four hydrogen per formula unit. This could potentially be due to surface water as discussed for compound **1**. Another possibility is that, since there are four positive charges per formula unit from the protonated bpy molecules and the anionic charge on the cluster is 5- (based on bond valence sums calculations), the extra positive charge could be accounted for if one of the oxygen sites on the cluster is protonated. However, CHN elemental analysis shows, not one, but four extra hydrogen atoms per formula unit, three of which would still need to be accounted. In order to possibly explain the presence of extra hydrogen atoms, FTIR was done to see if any surface water might be present on the sample that was used for CHN analysis. Though the CHN elemental analysis was done on dried samples that were kept in the desiccator,

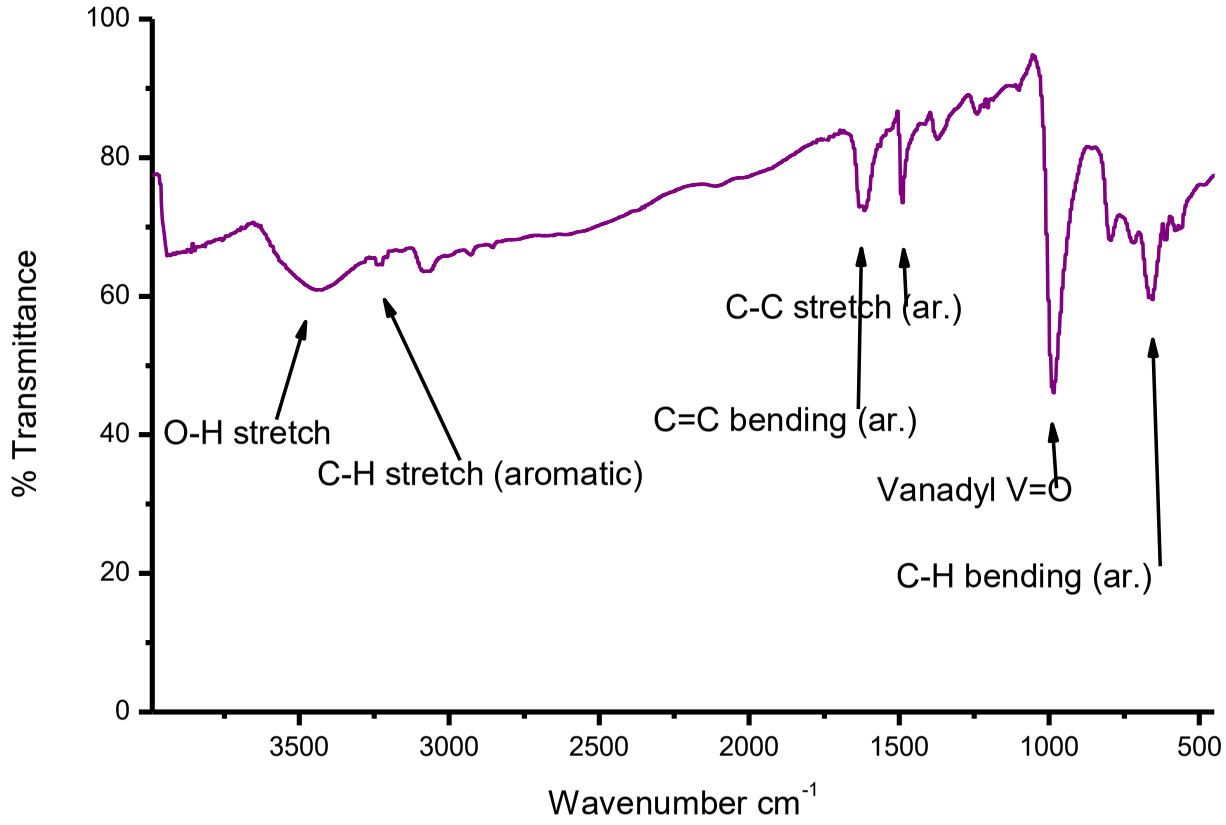

Figure 6.12: FTIR of the collected single crystals of **3** with assigned peaks showing aromatic vibrations in the 4,4'-bipyridine molecule as well as vanadyl V=O vibration. Noticable O-H stretch vibration can be seen around 3300-3500 cm^{-1} indicating the presence of surface water.

transferring the samples during preparation steps may have caused the absorption of water on the surface. Looking at the Figure 6.12, the presence of the broad O-H stretching vibration between 3300 and 3500 cm^{-1} can easily be observed. This is likely due to the surface water and is causing the count of hydrogen atoms to be higher than expected in the CHN elemental analysis. The anionic cluster charge of 5- in compound **3**, $[H_2(bpy)]_2$•$[V_{14}As_8O_{42}Cl]$, can be counter balanced by four protons that are on the nitrogen atoms on the 4,4'-bipyridine molecules. Because of the lack of additional suitable distances in hydrogen bond donor-acceptor pairs, the remaining positive charge likely comes from one of the vanadium atoms (per cluster) being fully oxidized. This would, of course, reduce the negative charge on the cluster to 4-. Because of the high symmetry of the cluster (*i.e.* multiplicity of vanadium sites being greater than one) and the nature of delocalization between the vanadium sites within the cluster, using bond valence sums calculations to determine which one of the vanadium sites contains a V^{5+} cation was unable to be done unambiguously. However, the overall charge balance is satisfied with four protonated nitrogen atoms (per formula unit) in case the ($V_{14}As_8O_{42}Cl$) cluster carries four negative charges.

Compound $[(bpy)_2(H_2bpy)_3(Hbpy)_2]$•$[V_{15}O_{36}Cl]_2$•$4H_2O$, **4,** the second POV–org–POV type (Fig. 6.1), its composition was finalized using similar approaches as described above. Bond valence sums calculations (see Table 6.3) for the $(V_{15}O_{36}Cl)^{7-}$ cluster in **4** show mixed-valent vanadium sites with six V^{4+} and nine V^{5+} cations. This results in anionic charge on the cluster of 4- per cluster or 8- per formula unit. The anionic charge, 8-, is counterbalanced by eight protons on the 4,4'-bipyridine nitrogen atoms. These protons

were indirectly found by extending the connectivity between potential hydrogen bond donor and acceptor pairs. By extending the connectivity between oxygen and nitrogen atoms, four suitable hydrogen bond donor-acceptor distances were able to be found, see Figure 6.13 for illustration. These four short distances are between nitrogen and oxygen sites that each have a multiplicity of two resulting in eight (per formula unit) potential hydrogen bond donor-acceptor pairs. These four nitrogen-oxygen pairs are N(2)-O(22), N(5)-O(16), N(6)-O(28), and N(7)-O(24) with separations of 2.766 Å, 2.810 Å, 2.701 Å, and 2.746 Å, respectively. All of these distances fall in the moderate strength range of hydrogen bonds describing the donor-acceptor pairs. With four protons on the N(2), N(5), N(6), and N(7) sites, each having a multiplicity of two per formula unit, the overall anionic charge on the cluster (8- per formula unit) is satisfied.

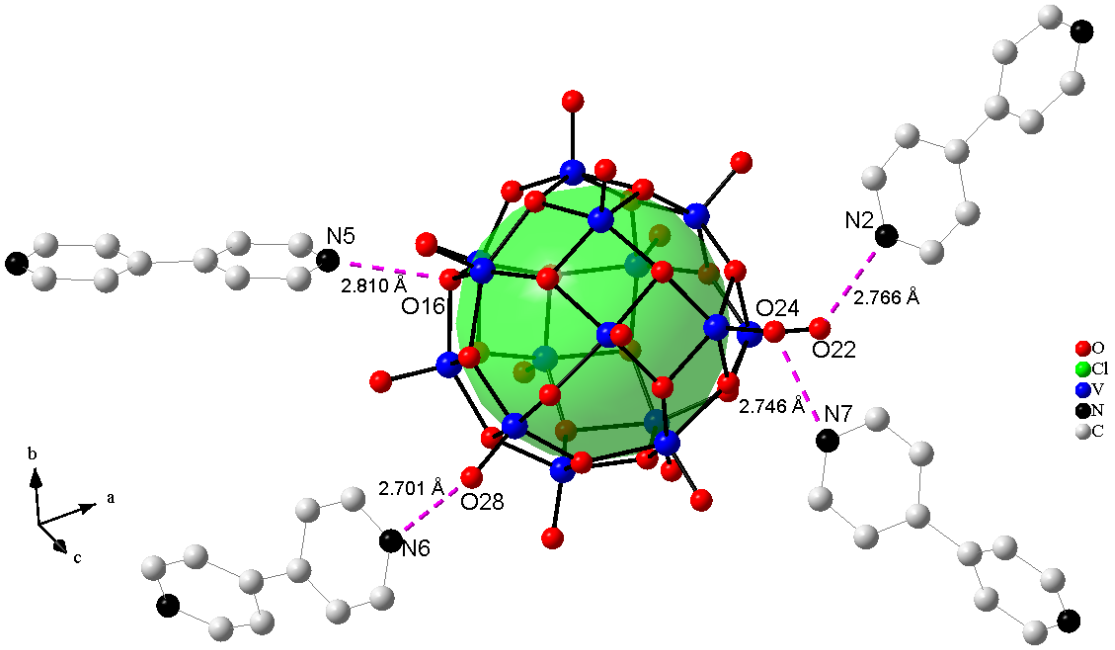

Figure 6.13: $(V_{15}O_{36})^{7-}$ cluster surrounded by 4,4'-bipyridine units illustrating potential hydrogen bond donor-acceptor pairs in compound **4**.

Structure of $[Cu_3(bpy)_2(Hbpy)_2]\bullet[V_{14}As_8O_{42}Cl]_2$ (**1**)

Compound **1** crystallizes in the monoclinic crystal system, *C* 2/*c* (no. 15) space group, $Z = 4$, with the unit cell dimensions of $a = 31.431(6)$ Å, $b = 13.442(3)$ Å, $c = 35.131(7)$ Å, $\beta = 107.30(3)^{o}$. The remaining constants and crystallographic information is presented in Table 6.1. A perspective view of the structure of 1 in the ac plane is shown in Figure 6.14. As is the case with the original cluster in $Cs_5(V_{14}As_8O_{42}Cl)$ (**V14**) compound, the $[V_{14}As_8O_{42}Cl]^{3-}$ cluster in **1** features a variety of bonding modes between the neighboring oxygen and vanadium atoms. These bridging modes, also referred to as μ_2 and μ_3, are based on vanadium atoms sharing two and three oxygen atoms, respectively. As is the case with the cluster in the original **V14** compound, the cluster in **1** contains 8 x μ_3 and 20 x μ_2 oxygen atoms. However, the structure and symmetry of the cluster in **1** vs that in **V14** is significantly different. The difference in orientation and symmetry of clusters in compounds **1**~**3** compared to the original cluster in **V14** will be discussed later in this chapter after some general discussions about the structures in **1**~**3**.

$[V_{14}As_8O_{42}Cl]^{3-}$ cluster in **1** is composed of fourteen crystallographically unique vanadium atoms, eight unique arsenic sites, 42 independent oxygen atoms and a central (enclosed) chloride anion. Atomic coordinates and thermal paramaters can be seen in Table 6.6 and Table 6.7, respectively. Each vanadium is coordinated to five oxygen atoms with four equatorial μ_2 and μ_3 oxygen sites. A short vanadyl, apical V = O bond is pointing away from the center of the cluster on each vanadium site. These apical V = O bond distances range from 1.552(14) Å for V(13) to 1.622(13) Å for V(5) and are close to the vanadyl bond distances observed in similar clusters.[10,11] The equatorial vanadium to oxygen bond

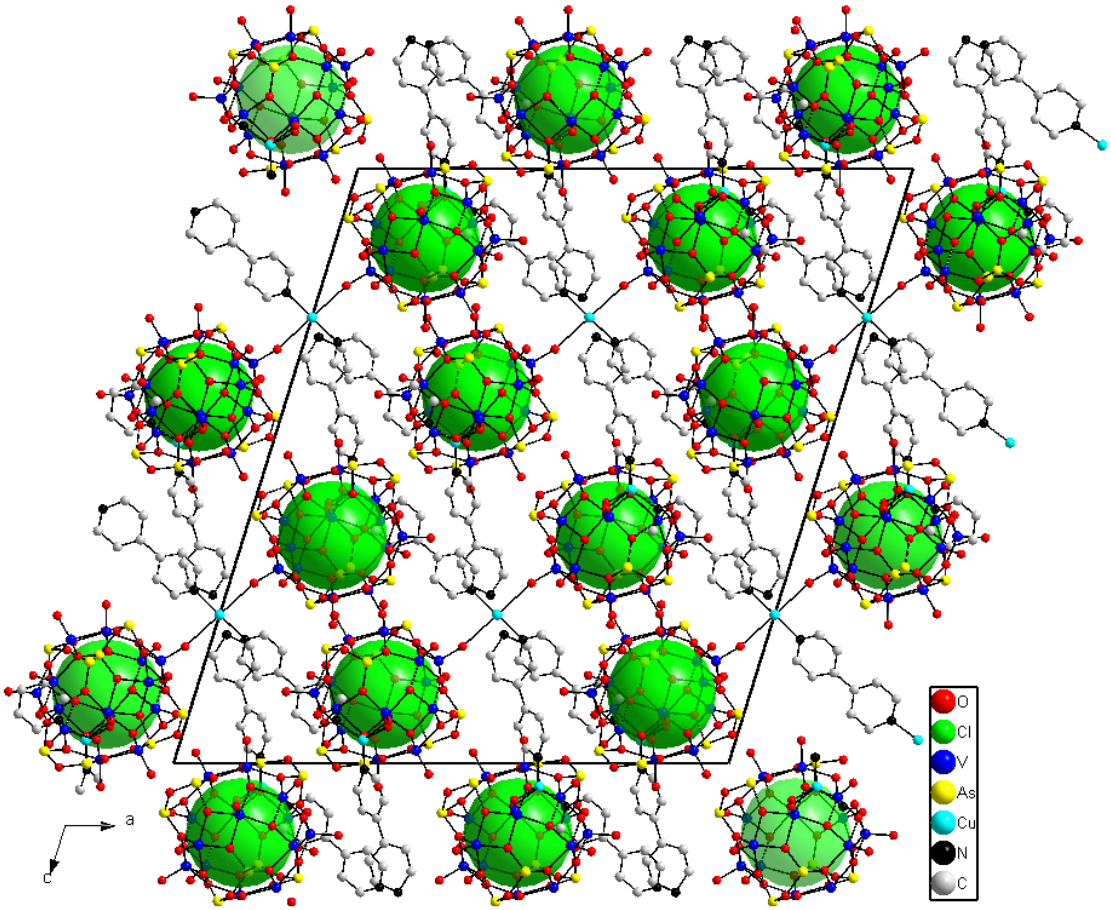

Figure 6.14: Perspective view of the structure of **1** in the *ac* plane.

Table 6.6: Atomic coordinates (x 10^4 Å) and parameters for compound **1**.

Atom	Wyckoff notation	sof	x	y	z
As(1)	8*f*	1.00	110(1)	9169(2)	831(1)
As(2)	8*f*	1.00	514(1)	10743(2)	326(1)
As(3)	8*f*	1.00	1571(1)	10251(2)	2320(1)
As(4)	8*f*	1.00	2400(1)	8755(2)	208(1)
As(5)	8*f*	1.00	1948(1)	11906(2)	1823(1)
As(6)	8*f*	1.00	2917(1)	10814(2)	3294(1)
As(7)	8*f*	1.00	1564(1)	7260(2)	-6(1)
As(8)	8*f*	1.00	2116(1)	12403(2)	3076(1)
V(1)	8*f*	1.00	705(1)	8221(3)	220(1)
V(2)	8*f*	1.00	904(1)	10864(3)	1366(1)
V(3)	8*f*	1.00	2370(1)	6966(3)	918(1)
V(4)	8*f*	1.00	801(1)	8828(3)	1726(1)
V(5)	8*f*	1.00	1474(1)	11666(3)	860(1)
V(6)	8*f*	1.00	1342(1)	9793(3)	63(1)
V(7)	8*f*	1.00	3582(1)	11196(3)	4203(1)
V(8)	8*f*	1.00	2620(1)	10869(3)	1376(1)
V(9)	8*f*	1.00	633(1)	6997(3)	923(1)
V(10)	8*f*	1.00	2157(1)	10895(3)	569(1)
V(11)	8*f*	1.00	1945(1)	7990(3)	2214(1)
V(12)	8*f*	1.00	2540(1)	9671(3)	2084(1)
V(13)	8*f*	1.00	3857(1)	11851(3)	3278(1)
V(14)	8*f*	1.00	2857(1)	8916(3)	1183(1)
Cu(1)	8*f*	1.00	0	8833(5)	2500
Cu(2)	8*f*	1.00	1720(3)	13744(6)	395(2)
Cl	8*f*	1.00	1593(4)	8827(11)	1167(3)
O(1)	8*f*	1.00	400(4)	8264(9)	640(3)
O(2)	8*f*	1.00	1514(4)	10966(10)	395(4)
O(3)	8*f*	1.00	903(4)	7002(10)	505(3)
O(4)	8*f*	1.00	2680(4)	6138(10)	819(4)
O(5)	8*f*	1.00	797(4)	9687(10)	244(4)
O(6)	8*f*	1.00	3195(5)	11772(10)	3119(4)
O(7)	8*f*	1.00	2328(4)	10931(10)	1801(4)
O(8)	8*f*	1.00	881(4)	11045(11)	811(3)
O(9)	8*f*	1.00	1492(4)	11509(10)	1424(4)
O(10)	8*f*	1.00	550(4)	9647(9)	1232(3)

Table 6.6: Atomic coordinates (x 10^4 Å) and parameters for compound **1** (continued).

Atom	Wyckoff notation	sof	x	y	z
O(11)	8*f*	1.00	2011(4)	9653(10)	238(4)
O(12)	8*f*	1.00	1185(5)	10151(10)	-387(4)
O(13)	8*f*	1.00	2127(4)	11497(9)	1051(3)
O(14)	8*f*	1.00	2804(4)	9617(10)	1655(4)
O(15)	8*f*	1.00	1763(5)	11435(11)	2225(4)
O(16)	8*f*	1.00	2298(5)	12642(11)	3590(4)
O(17)	8*f*	1.00	340(4)	7923(9)	-182(4)
O(18)	8*f*	1.00	1301(4)	8061(11)	2030(4)
O(19)	8*f*	1.00	1270(4)	8327(10)	79(3)
O(20)	8*f*	1.00	95(4)	10154(10)	486(4)
O(21)	8*f*	1.00	1364(4)	12809(10)	717(4)
O(22)	8*f*	1.00	3020(4)	11621(11)	1482(4)
O(23)	8*f*	1.00	583(5)	11666(11)	1466(5)
O(24)	8*f*	1.00	3000(5)	11278(12)	3786(4)
O(25)	8*f*	1.00	2642(4)	10189(10)	915(4)
O(26)	8*f*	1.00	445(4)	8877(11)	1965(4)
O(27)	8*f*	1.00	2514(4)	13179(12)	2950(4)
O(28)	8*f*	1.00	2101(5)	7646(13)	2670(4)
O(29)	8*f*	1.00	3843(5)	11257(11)	3764(4)
O(30)	8*f*	1.00	230(5)	6256(11)	827(4)
O(31)	8*f*	1.00	2444(7)	11245(10)	3093(4)
O(32)	8*f*	1.00	649(4)	7627(10)	1403(4)
O(33)	8*f*	1.00	4044(5)	11094(11)	3034(4)
O(34)	8*f*	1.00	1979(4)	9489(11)	2226(4)
O(35)	8*f*	1.00	1148(4)	10057(11)	1861(4)
O(36)	8*f*	1.00	1721(7)	6950(14)	466(5)
O(37)	8*f*	1.00	2043(5)	7871(11)	-61(5)
O(38)	8*f*	1.00	2350(5)	11684(11)	325(4)
O(39)	8*f*	1.00	3373(6)	8865(13)	1207(5)
O(40)	8*f*	1.00	2925(5)	9941(15)	2489(4)
O(41)	8*f*	1.00	2503(5)	8280(14)	689(4)
O(42)	8*f*	1.00	3653(5)	10128(14)	4383(6)

Table 6.6: Atomic coordinates (x 10^4 Å) and parameters for compound **1** (continued).

Atom	Wyckoff notation	sof	x	y	z
N(1)	8*f*	1.00	2304(6)	13830(13)	723(6)
N(2)	8*f*	1.00	-598(7)	8770(20)	2085(7)
N(3)	8*f*	1.00	1525(10)	13680(20)	-106(6)
N(4)	8*f*	1.00	-232(9)	6200(20)	2167(11)
C(1)	8*f*	1.00	3148(6)	13873(18)	1238(7)
C(2)	8*f*	1.00	3606(7)	13837(18)	1527(7)
C(3)	8*f*	1.00	2780(8)	13855(18)	1357(8)
C(4)	8*f*	1.00	3069(9)	13855(18)	833(8)
C(5)	8*f*	1.00	2337(7)	13872(17)	1089(6)
C(6)	8*f*	1.00	-920(8)	8373(19)	2162(7)
C(7)	8*f*	1.00	3671(7)	13430(20)	1900(6)
C(8)	8*f*	1.00	2658(9)	13849(18)	578(7)
C(9)	8*f*	1.00	-651(9)	9170(30)	1733(10)
C(10)	8*f*	1.00	1021(8)	10780(30)	-1460(9)
C(11)	8*f*	1.00	-757(10)	6330(20)	1339(9)
C(12)	8*f*	1.00	3963(12)	11380(20)	914(14)
C(13)	8*f*	1.00	3667(14)	10760(50)	782(12)
C(14)	8*f*	1.00	-335(13)	6610(30)	1447(13)
C(15)	8*f*	1.00	4068(10)	11000(30)	1638(11)
C(16)	8*f*	1.00	1536(14)	14260(30)	-440(20)
C(17)	8*f*	1.00	5114(11)	11660(30)	3188(15)
C(18)	8*f*	1.00	-714(11)	5770(30)	1983(11)
C(19)	8*f*	1.00	1268(17)	12930(30)	-250(12)
C(20)	8*f*	1.00	-996(16)	7040(30)	633(12)

lengths range from 1.834(13) Å for V(8)-O(13) to 2.18(2) Å for V(3)-O(36). These distances are expected for vanadium to oxygen bond distance based on the Shannon radii of V^{4+}, V^{5+} cations and O^{2-}.[14] Table 6.5 shows the selected bond distances for **1**. In addition to the vanadium-oxygen connectivity, three coordinate arsenic also connects to oxygen atoms. Each of the eight crystallographically independent arsenic sites are in trigonal pyramidal geometry with a lone-pair of electrons presumably pointing away from the cluster. Bond distances between the arsenic and oxygen atoms in **1** are of typical length for the trivalent, As^{3+}-oxygen connectivity in trigonal pyramidal geometry. These bond distances range from 1.556(18) Å to 1.858(15) Å for As(6)-O(31) and As(8)-O(31), respectively.

POM clusters in **1** feature copper-oxide inter-cluster connectivity. Two independent copper sites, Cu(1) and Cu(2) are connected to the vanadyl oxygen atoms with bond distances of 2.654(13) Å (x 2) for Cu(1)-O(26) and 2.205(15) Å and 2.448(14) Å for Cu(2)-O(21) and Cu(2)-O(42), respectively. Figure 6.15 shows the connectivity between the copper Cu(1) atoms (while Fig. 6.8 shows the coordination to Cu(2)) and the oxygen atoms on the cluster. In addition to the oxide connectivity, these copper atoms coordinate to the nitrogen atoms on the 4,4'-bipyridine ligands. The bond distance between Cu(1) and N(2) is 2.01(2) Å (x 2). This completes the coordination around Cu(1) resulting in a square planar geometry. Based on the bond valence sums (BVS) calculations, Cu(1) site is formally monovalent, see bond valence sums in Table 6.3.

Unlike the Cu(1) site, Cu(2) is in a tetrahedral coordination with respect to the neighboring oxygen and nitrogen atoms. The bond distances between Cu(2) and nitrogen

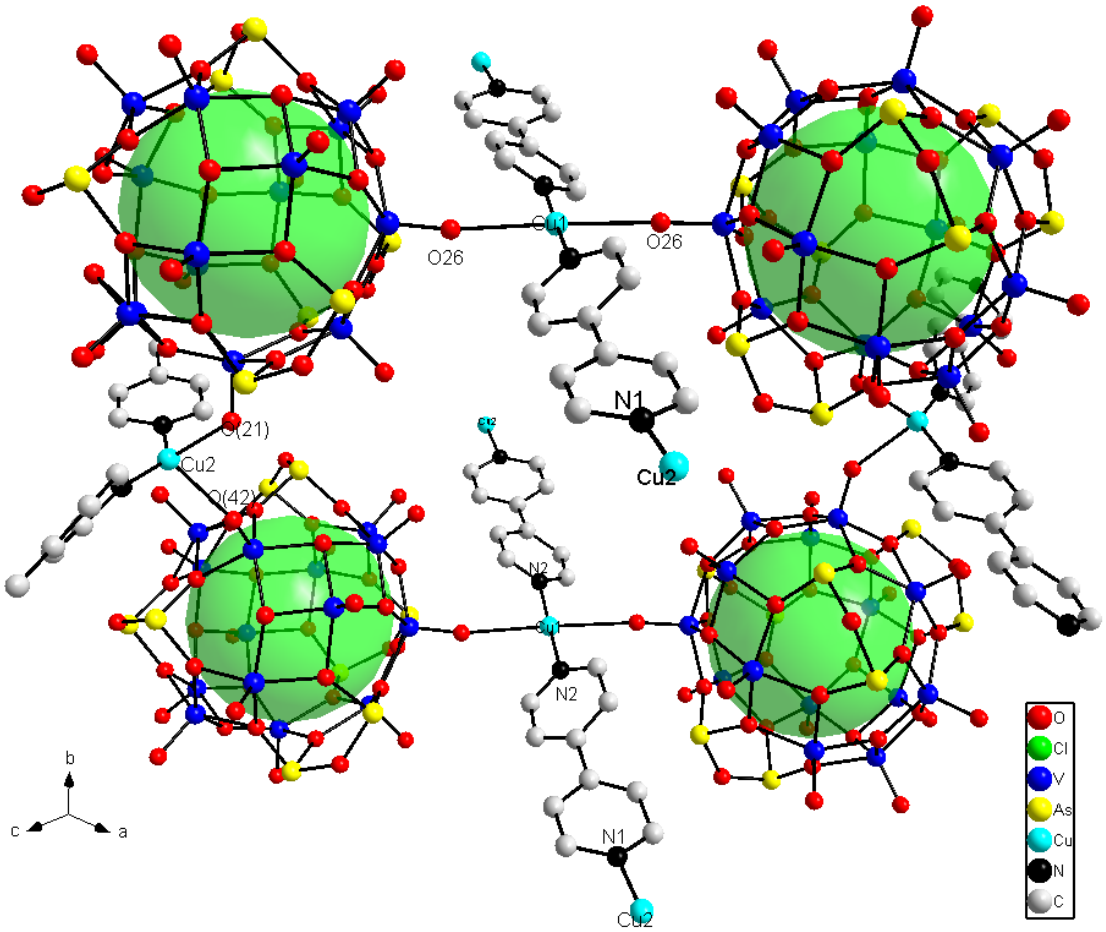

Figure 6.15: Connectivity between copper and oxygen in compound **1**.

Table 6.7: Anisotropic thermal parameters ($Å^2$ x 10^3) for compound **1**.

Atom	U11	U22	U33	U23	U13	U12
As(1)	36(1)	42(1)	49(1)	-1(1)	11(1)	-1(1)
As(2)	37(1)	38(1)	43(1)	0(1)	5(1)	2(1)
As(3)	50(1)	51(2)	41(1)	-4(1)	10(1)	3(1)
As(4)	71(2)	46(2)	62(2)	3(1)	33(1)	6(1)
As(5)	48(1)	40(1)	48(1)	-7(1)	6(1)	-1(1)
As(6)	74(2)	53(2)	69(2)	-12(1)	23(1)	-11(1)
As(7)	64(2)	52(2)	62(2)	-10(1)	15(1)	2(1)
As(8)	59(2)	67(2)	65(2)	-3(1)	12(1)	-9(1)
V(1)	36(2)	35(2)	41(2)	-3(1)	6(1)	1(2)
V(2)	37(2)	39(2)	44(2)	-3(2)	9(2)	3(2)
V(3)	40(2)	32(2)	51(2)	0(2)	15(2)	4(2)
V(4)	38(2)	44(2)	43(2)	1(2)	14(2)	-1(2)
V(5)	44(2)	29(2)	45(2)	-3(2)	10(2)	-3(2)
V(6)	42(2)	35(2)	44(2)	-3(2)	12(2)	-2(2)
V(7)	58(2)	46(3)	70(3)	9(2)	16(2)	1(2)
V(8)	43(2)	37(2)	51(2)	-4(2)	10(2)	-5(2)
V(9)	45(2)	38(2)	44(2)	0(2)	10(2)	-3(2)
V(10)	47(2)	33(2)	52(2)	0(2)	21(2)	-3(2)
V(11)	47(2)	45(2)	44(2)	7(2)	12(2)	7(2)
V(12)	40(2)	50(2)	44(2)	0(2)	2(2)	6(2)
V(13)	63(2)	45(2)	55(2)	-8(2)	22(2)	-2(2)
V(14)	57(2)	55(3)	68(3)	-1(2)	9(2)	2(2)
Cu(1)	64(3)	139(6)	91(4)	0	-11(3)	0
Cu(2)	205(7)	205(8)	174(6)	20(5)	12(5)	-40(6)
Cl	191(11)	236(16)	97(7)	-23(8)	-12(7)	134(11)
O(1)	43(7)	27(7)	35(6)	8(5)	16(6)	-2(6)
O(2)	49(8)	34(8)	58(8)	-2(6)	28(7)	-7(7)
O(3)	62(9)	46(9)	24(6)	2(6)	8(6)	15(7)
O(4)	53(8)	34(8)	65(9)	11(7)	19(7)	21(7)
O(5)	39(7)	39(8)	49(8)	5(6)	21(6)	5(6)
O(6)	65(9)	39(9)	46(8)	-8(6)	21(7)	-14(7)
O(7)	42(7)	37(8)	48(8)	-11(6)	11(6)	2(6)
O(8)	45(7)	64(10)	26(7)	-9(6)	16(6)	-9(7)
O(9)	30(6)	41(8)	49(8)	-7(6)	5(6)	1(6)
O(10)	44(7)	31(8)	36(7)	-11(6)	-5(6)	-2(6)
O(11)	37(7)	41(9)	51(8)	-10(6)	10(6)	4(6)
O(12)	78(10)	31(8)	56(9)	0(7)	32(8)	-11(8)
O(13)	40(7)	28(7)	46(7)	-6(6)	12(6)	-9(6)
O(14)	43(7)	37(8)	47(8)	6(6)	8(6)	-3(7)
O(15)	68(9)	43(9)	45(8)	-9(7)	-6(7)	-12(8)

Table 6.7: Anisotropic thermal parameters ($Å^2$ x 10^3) for compound **1** (continued).

Atom	U11	U22	U33	U23	U13	U12
O(16)	58(9)	39(9)	66(9)	-7(7)	16(7)	5(7)
O(17)	50(8)	20(7)	47(8)	-2(6)	-2(6)	-1(6)
O(18)	44(7)	51(9)	40(7)	12(6)	11(6)	-2(7)
O(19)	29(6)	38(8)	46(7)	2(6)	7(6)	10(6)
O(20)	41(7)	37(8)	51(8)	7(6)	8(6)	8(7)
O(21)	43(7)	39(8)	49(8)	10(6)	16(6)	3(7)
O(22)	34(7)	53(10)	69(9)	-25(8)	8(7)	-9(7)
O(23)	59(9)	39(9)	91(11)	-9(8)	38(9)	15(8)
O(24)	64(10)	70(12)	40(8)	10(7)	0(7)	-14(9)
O(25)	45(8)	32(8)	61(9)	5(7)	13(7)	4(7)
O(26)	52(8)	62(11)	42(8)	-8(7)	6(7)	3(8)
O(27)	33(7)	76(12)	43(8)	-17(7)	14(6)	-5(7)
O(28)	72(10)	73(12)	62(10)	34(9)	26(8)	36(9)
O(29)	64(9)	44(9)	50(8)	4(7)	14(7)	8(8)
O(30)	56(9)	52(10)	66(9)	-9(8)	18(8)	-19(8)
O(31)	167(18)	23(8)	34(8)	11(6)	44(10)	17(10)
O(32)	40(7)	45(9)	47(8)	-2(7)	9(6)	2(7)
O(33)	73(10)	51(10)	60(9)	-11(8)	30(8)	6(8)
O(34)	49(8)	39(9)	76(10)	19(7)	24(7)	16(7)
O(35)	51(8)	48(9)	40(7)	0(6)	14(6)	-4(7)
O(36)	190(20)	73(13)	97(13)	-52(11)	115(14)	-72(14)
O(37)	51(9)	41(10)	92(11)	2(8)	14(8)	-7(8)
O(38)	88(11)	36(9)	76(10)	-8(8)	44(9)	-21(9)
O(39)	89(13)	72(13)	68(11)	0(9)	23(9)	-8(10)
O(40)	58(10)	119(18)	50(9)	6(10)	1(8)	1(10)
O(41)	63(10)	94(15)	56(9)	-17(9)	23(8)	-14(10)
O(42)	56(10)	58(12)	135(15)	13(11)	30(10)	-8(9)
N(1)	46(11)	30(10)	80(15)	-15(9)	-11(10)	-9(9)
N(2)	73(15)	110(20)	69(15)	-9(14)	42(13)	1(15)
N(3)	180(30)	90(20)	47(13)	-39(13)	50(15)	-50(20)
N(4)	68(17)	90(20)	200(30)	50(20)	12(19)	23(15)
C(1)	30(10)	70(17)	57(14)	6(11)	16(10)	2(11)
C(2)	54(14)	64(17)	72(16)	15(12)	41(12)	7(12)
C(3)	65(15)	52(16)	79(17)	-22(13)	28(13)	-15(13)
C(4)	70(16)	42(15)	89(19)	6(13)	24(15)	7(13)
C(5)	47(12)	61(16)	37(12)	-6(10)	5(10)	-12(11)
C(6)	53(14)	71(18)	47(13)	-15(12)	-4(11)	-5(13)
C(7)	51(14)	150(30)	27(12)	-6(14)	11(10)	10(16)
C(8)	83(19)	44(15)	65(16)	13(12)	16(14)	0(14)
C(9)	51(16)	120(30)	100(20)	20(20)	3(16)	-5(17)
C(10)	47(15)	160(40)	90(20)	-50(20)	23(15)	-23(18)
C(11)	80(20)	61(19)	71(18)	3(14)	21(16)	14(16)
C(12)	100(20)	50(20)	210(40)	20(20)	110(30)	-5(17)
C(13)	90(30)	420(100)	100(30)	140(40)	20(20)	-50(40)
C(14)	120(30)	150(40)	180(40)	-110(30)	110(30)	-70(30)
C(15)	57(17)	140(30)	120(30)	60(20)	3(19)	-14(19)
C(16)	120(40)	60(30)	330(70)	50(40)	60(40)	-50(20)
C(17)	70(20)	150(40)	190(40)	100(40)	50(30)	30(20)
C(18)	80(20)	170(40)	130(30)	80(30)	30(20)	40(20)
C(19)	290(60)	80(30)	110(30)	-30(20)	120(40)	-60(30)
C(20)	220(50)	100(30)	120(30)	20(30)	90(30)	-40(30)

Table 6.8: Selected bond distances (Å) for compounds **1**.

AsO_3							
As(1)-O(1)	1.768(12)	As(2)-O(5)	1.742(13)	As(3)-O(34)	1.746(13)	As(4)-O(37)	1.714(15)
As(1)-O(10)	1.776(11)	As(2)-O(20)	1.769(13)	As(3)-O(15)	1.768(15)	As(4)-O(41)	1.742(15)
As(1)-O(20)	1.784(13)	As(2)-O(8)	1.798(12)	As(3)-O(35)	1.777(12)	As(4)-O(11)	1.743(13)
As(5)-O(9)	1.763(12)	As(6)-O(31)	1.556(18)	As(7)-O(36)	1.640(19)	As(8)-O(16)	1.754(14)
As(5)-O(7)	1.791(13)	As(6)-O(6)	1.765(13)	As(7)-O(37)	1.776(14)	As(8)-O(27)	1.784(14)
As(5)-O(15)	1.794(15)	As(6)-O(24)	1.783(14)	As(7)-O(19)	1.778(12)	As(8)-O(31)	1.858(15)
VO_5							
V(1)-O(17)	1.583(12)	V(2)-O(23)	1.585(13)	V(3)-O(4)	1.584(13)	V(4)-O(26)	1.587(14)
V(1)-O(3)	1.926(13)	V(2)-O(8)	1.946(11)	V(3)-O(16)#1	1.959(14)	V(4)-O(18)	1.918(13)
V(1)-O(19)	1.984(12)	V(2)-O(10)	1.955(13)	V(3)-O(24)#1	2.002(16)	V(4)-O(32)	1.950(14)
V(1)-O(1)	1.987(11)	V(2)-O(9)	1.996(13)	V(3)-O(41)	2.035(18)	V(4)-O(35)	1.959(14)
V(1)-O(5)	1.989(14)	V(2)-O(35)	1.997(13)	V(3)-O(36)	2.18(2)	V(4)-O(10)	2.008(13)
V(5)-O(21)	1.622(13)	V(6)-O(12)	1.587(14)	V(7)-O(42)	1.558(18)	V(8)-O(22)	1.568(13)
V(5)-O(2)	1.923(13)	V(6)-O(2)	1.938(13)	V(7)-O(29)	1.951(14)	V(8)-O(13)	1.834(13)
V(5)-O(13)	1.974(12)	V(6)-O(19)	1.985(14)	V(7)-O(3)#2	1.964(13)	V(8)-O(25)	1.880(14)
V(5)-O(9)	1.978(13)	V(6)-O(5)	2.002(12)	V(7)-O(24)	1.978(14)	V(8)-O(14)	1.948(13)
V(5)-O(8)	2.002(13)	V(6)-O(11)	2.017(12)	V(7)-O(36)#2	1.986(15)	V(8)-O(7)	1.973(13)
V(9)-O(30)	1.566(14)	V(10)-O(38)	1.592(14)	V(11)-O(28)	1.599(14)	V(12)-O(40)	1.608(15)
V(9)-O(32)	1.874(13)	V(10)-O(25)	1.899(13)	V(11)-O(18)	1.934(13)	V(12)-O(14)	1.926(13)
V(9)-O(3)	1.901(12)	V(10)-O(13)	1.906(12)	V(11)-O(27)#1	1.968(12)	V(12)-O(7)	1.977(14)
V(9)-O(29)#1	1.960(15)	V(10)-O(2)	1.931(13)	V(11)-O(6)#1	1.984(14)	V(12)-O(34)	1.986(14)
V(9)-O(1)	1.997(12)	V(10)-O(11)	2.007(13)	V(11)-O(34)	2.018(15)	V(12)-O(27)#1	2.014(16)
V(13)-O(33)	1.552(14)	V(14)-O(39)	1.600(18)				
V(13)-O(29)	1.898(14)	V(14)-O(41)	1.958(15)				
V(13)-O(32)#2	1.928(13)	V(14)-O(14)	1.958(13)				
V(13)-O(18)#2	1.935(15)	V(14)-O(25)	1.973(14)				
V(13)-O(6)	1.993(14)	V(14)-O(16)#1	2.009(15)				
$Cu(O)(bpy)_2$							
Cu(1)-N(2)#3	2.01(2)	Cu(2)-N(3)	1.69(2)	Symmetry transformations used to generate equivalent atoms:			
Cu(1)-N(2)	2.01(2)	Cu(2)-N(1)	1.859(18)	#1 -x+1/2,y-1/2,-z+1/2	#2 -x+1/2,y+1/2,-z+1/2		
Cu(1)-O(26)#3	2.654(13)	Cu(2)-O(21)	2.205(15)	#3 -x,y,-z+1/2	#4 -x+1/2,-y+5/2,-z		
Cu(1)-O(26)	2.654(13)	Cu(2)-O(42)	2.448(14)	#5 x-1/2,y-1/2,z	#6 x+1/2,y+1/2,z		
				#7 -x,-y+2,-z			

atoms are 1.859(18) Å and 1.690(2) Å for Cu(2)-N(1) and Cu(2)-N(3), respectively. The bond valence sums calculations of the Cu(2) site reveal that Cu(2) is formally divalent with the calculated BVS of 1.99.

Looking at the bpy ligands, there are four crystallographically unique nitrogen atoms, N(1), N(2), N(3) and N(4). This means that there are two crystallographically independent bpy ligands per unit cell as each bpy has two nitrogen atoms per molecule. Besides the expected bond distances between the C-C and N-C atoms within the bpy unit, each bpy also coordinates to copper sites as was mentioned above. Three of the four nitrogen atoms coordinate to copper atoms while one of the nitrogen sites, N(4), seemingly does not coordinate to any additional elements besides the N(4)-N(4) sites, see above Figure 6.8. This strongly suggests that one of the two N(4) sites is protonated and results in hydrogen bonding to the neighboring nitrogen atom to extend the network structure.

Diffuse reflectance UV-vis data were collected on ground single crystals of compound **1**. Kubelka-Munk function was used to convert the reflectance data into absorbance and a Tauc plot was obtained as described in Chapter 2 and according to the reference below.[14] By extrapolating the linear region of the absorption edge energy band gap was obtained. The experimental band gap for compound **1** is 2.26 eV as shown in Figure 6.16. For comparison, the band gap of **V14** starting material was found to be 2.48 eV.

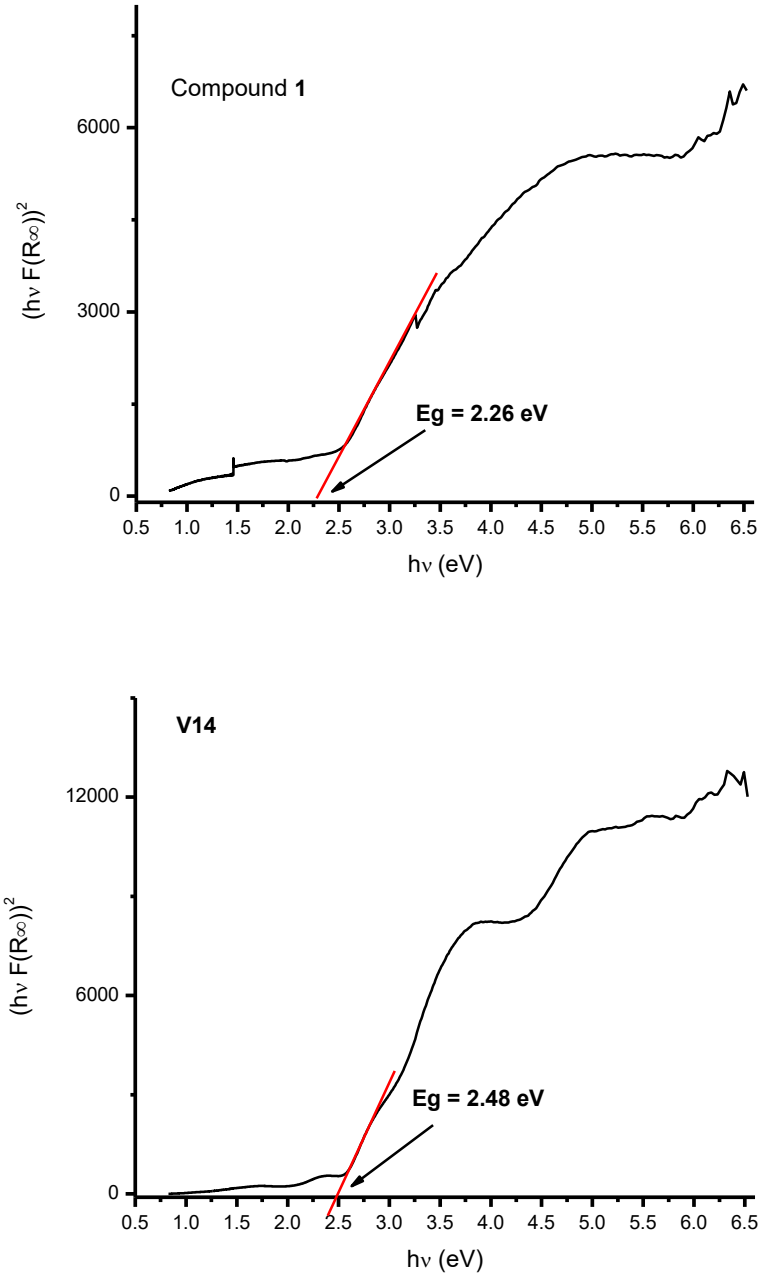

Figure 6.16: Tauc plots for compound **1** and **V14** starting material showing the band gap obtained from UV-vis reflectance data.

Structure of $[Cu(bpy)]_2 \bullet [H_3V_{14}As_8O_{42}Cl]$ (**2**)

Compound **2** crystalizes in the monoclinic crystal system, space group $P\ 2_1/n$ (no.14), Z = 2. The unit cell dimensions are a = 14.233(3) Å, b = 11.490(2) Å, c = 19.568(4) Å, β = 109.83(3) ^{o}. Further crystallographic data and constants can be observed in Table 6.1. The cluster, $(H_3V_{14}As_8O_{42}Cl)^{2-}$, in compound **2** is composed of seven crystallographically unique vanadium sites and four unique arsenic sites. Each vanadium (V^{4+} d^1) site is coordinated to five oxygen atoms in a square pyramidal coordination environment. The four equatorial bonds between the vanadium sites range between 1.894 Å and 2.005 Å. These distances are expected based on the combined crystal radii of 1.88 Å for V^{4+} and O^{2-} being 0.67 Å and 1.21 Å, respectively. The remaining vanadium to oxygen bond is the vanadyl apical bond pointing away from the center of the cluster. The distances between the vanadyl, vanadium to oxygen, bonds range between 1.559 Å and 1.624 Å. Interestingly, the cluster in **2** encloses a chloride, Cl^-, which is spatially disordered along the opposite V(7) atomic sites showing elongated thermal parameters along the line connecting the opposite V(7) atoms. Looking closely at these two V(7) sites, the apical V = O bond distance is the longest, 1.624 Å, among the seven vanadium sites. The reason for the comparatively longer apical oxygen bond for V(7) could possibly be due to the preferential coordination of chloride to V(7) which in turn elongates the apical bond. The bond valence sums parameters of the V(7) atomic site, show the highest BVS parameters among the seven vanadium sites with BVS of 4.28 for V^{4+} and 4.50 for V^{5+} calculations. In addition to the disorder in the chloride anion with preferential coordination to the V(7) site, the cluster itself seems slightly elongated with the V(7) to V(7) distance being 8.174

Å. Comparatively, this is the longest such distance between opposite vanadium atomic sites. The remaining two opposite-vanadium distances are 7.376 Å and 7.488 Å for the V(1) and V(5) opposite atomic sites, respectively. The cluster shape as it compares to the other $(V_{14}As_8O_{42}Cl)^{n-}$ clusters as well as the original cluster in **V14** will be further discussed in a separate section below.

The inter-connectivity between $(H_3V_{14}As_8O_{42}Cl)^{2-}$ clusters in **2**, features the long copper to oxygen distances between the Cu(1)-O(19) and Cu(1)-O(20). These distances are 2.656 Å and 2.647 Å, respectively. Perpendicular to the copper-oxygen connectivity, 4,4'-bipyridine molecules coordinate to Cu(1) through lone pair electrons on the nitrogen sites with distances between Cu(1)-N(1) and Cu(1)-N(2) being 2.150 Å and 2.230 Å, respectively.

The Cu(1) site has a distorted square planar (extremely distorted tetrahedral) coordination with respect to the oxygen and nitrogen coordination sites. Given that Cu(1) is formally monovalent based on the bond valence sums calculations, the square planar coordination is not surprising as Cu^{1+} has a full 3*d* ($3d^{10}$)shell and hence the coordination around copper has less of a transition metallic character.

Copper-bipyridine coordination results in infinite chains running along the *b* crystallographic direction as shown in Fig. 6.18. In compound **2**, one crystallographically unique 4,4'-bipyridine unit with N(1) and N(2) at opposite ends runs along the *b* direction with connectivity to Cu(1) as mentioned above. The 4,4'-bipyridine unit has a slightly twisted orientation with respect to the two pyridine rings. The dihedral angle between the N(1)-containing and N(2)-containing rings is 18°.

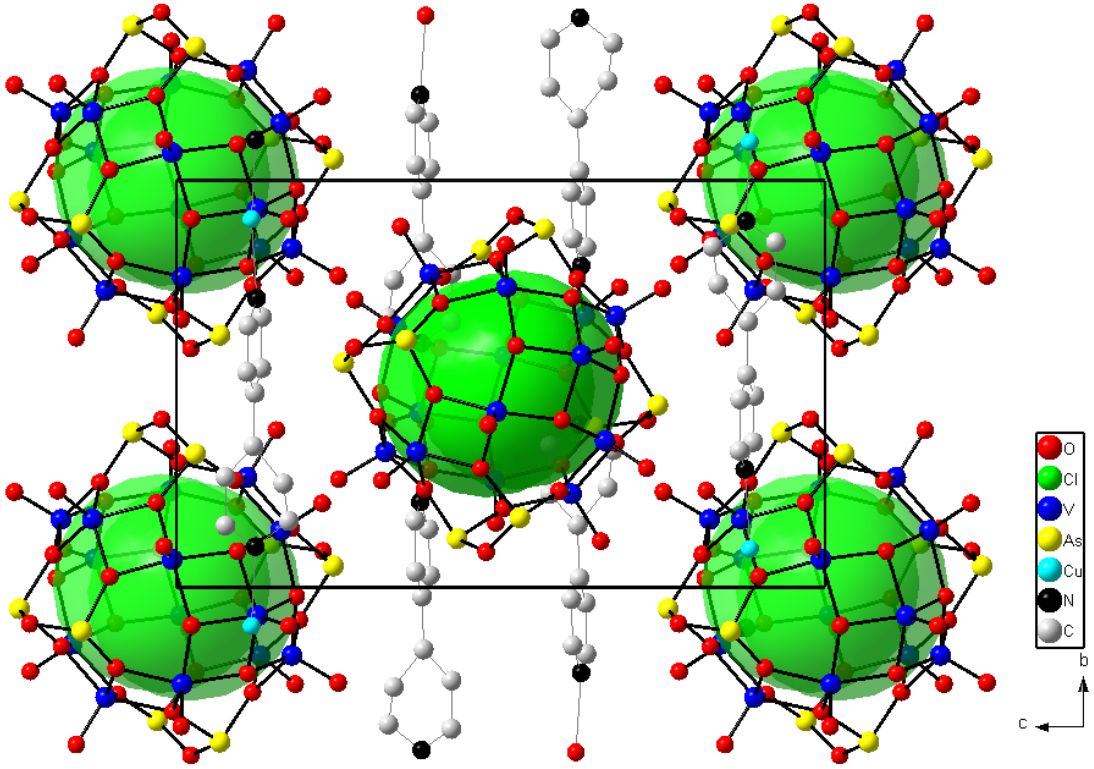

Figure 6.17: Perspective view of the structure of **2** in the *bc* plane.

Table 6.9: Atomic coordinates (x 10^4 Å) and parameters for compound **2**.

Atom	Wyckoff notation	sof	x	y	z
As(1)	4*e*	1.00	5201(2)	3803(2)	673(1)
As(2)	4*e*	1.00	6883(2)	3924(2)	3543(1)
As(3)	4*e*	1.00	8291(2)	4475(2)	2580(1)
As(4)	4*e*	1.00	3387(2)	6719(2)	294(1)
V(1)	4*e*	1.00	7047(3)	1673(3)	1296(2)
V(2)	4*e*	1.00	3112(3)	2378(3)	90(2)
V(3)	4*e*	1.00	10592(3)	3606(3)	3394(2)
V(4)	4*e*	1.00	5185(3)	1670(3)	1778(2)
V(5)	4*e*	1.00	5938(3)	7300(3)	1090(2)
V(6)	4*e*	1.00	7352(3)	5688(3)	4936(2)
V(7)	4*e*	1.00	3279(3)	701(3)	1251(2)
Cu(1)	4*e*	1.00	4389(7)	5953(6)	3828(4)
Cl(1)	4*e*	0.50	4650(13)	104(15)	224(9)
O(1)	4*e*	1.00	5505(11)	2619(12)	-907(6)
O(2)	4*e*	1.00	8560(11)	5802(12)	3113(7)
O(3)	4*e*	1.00	7004(13)	2085(12)	306(7)
O(4)	4*e*	1.00	7379(12)	5260(12)	3977(7)
O(5)	4*e*	1.00	9149(11)	3552(12)	3221(7)
O(6)	4*e*	1.00	3124(11)	-903(12)	948(7)
O(7)	4*e*	1.00	5819(12)	2582(11)	1176(7)
O(8)	4*e*	1.00	7888(11)	3020(11)	4070(7)
O(9)	4*e*	1.00	2384(12)	3420(14)	72(8)
O(10)	4*e*	1.00	6309(14)	6134(14)	1541(10)
O(11)	4*e*	1.00	4565(12)	213(12)	1852(7)
O(12)	4*e*	1.00	7997(12)	2375(14)	1832(7)
O(13)	4*e*	1.00	4288(11)	3043(13)	-48(8)
O(14)	4*e*	1.00	2461(12)	945(13)	233(7)
O(15)	4*e*	1.00	7176(11)	4103(15)	2745(8)
O(16)	4*e*	1.00	3917(11)	2107(12)	1099(7)
O(17)	4*e*	1.00	10812(14)	2938(14)	2753(8)
O(18)	4*e*	1.00	3938(15)	5874(13)	-226(9)
O(19)	4*e*	1.00	6220(12)	6012(15)	4799(9)
O(20)	4*e*	1.00	2584(14)	937(16)	1746(8)
O(21)	4*e*	1.00	5313(14)	2361(16)	2490(9)

Table 6.9: Atomic coordinates (x 10^4 Å) and parameters for compound **2** (continued).

Atom	Wyckoff notation	sof	x	y	z
N(1)	4*e*	1.00	4390(30)	7820(40)	3780(20)
N(2)	4*e*	1.00	4220(20)	4020(30)	3774(18)
C(1)	4*e*	1.00	3550(50)	8370(40)	3660(20)
C(2)	4*e*	1.00	4270(30)	220(50)	3789(18)
C(3)	4*e*	1.00	3510(50)	3440(80)	3300(30)
C(4)	4*e*	1.00	5060(20)	6540(30)	5790(20)
C(5)	4*e*	1.00	5020(20)	2290(30)	4250(15)
C(6)	4*e*	1.00	4260(20)	1490(50)	3818(14)
C(7)	4*e*	1.00	1580(20)	4670(40)	1330(20)
C(8)	4*e*	1.00	9880(40)	4720(60)	1080(20)
C(9)	4*e*	1.00	5070(30)	8500(60)	3910(20)
C(10)	4*e*	1.00	3490(20)	2460(70)	3335(18)

The stacking of the neighboring bpy units occurs through the well-known attractive non-covalent interaction between the aromatic rings due to pi bonds, also known as π-π stacking. The neighboring 4,4'-bipyridine rings stack in a parallel-displaced configuration with distances between the neighboring aromatic pyridine rings of 3.78 Å and 4.00 Å. These π-π stacking distances are comparable to the reported similar systems and are in the range of strong π-π stacking interactions in aromatic systems.[14] Potentially weak anion-π interaction occurs between the oxygen and the aromatic 4,4'-bipyrdine ring. The distance from the center of the ring to the nearest oxygen atoms are 3.324 Å and 3.416 Å. These anion-π interactions are weak at best given that the distances between the pyridine ring and oxygen atoms (O(22) and O20)) are larger than the sum of the van der Waals radii for oxygen and carbon (on 4,4'bipyridine) which is 3.20 Å.[16] Figure 6.19 illustrates the π-π stacking and anion-π interactions in compound **2**.

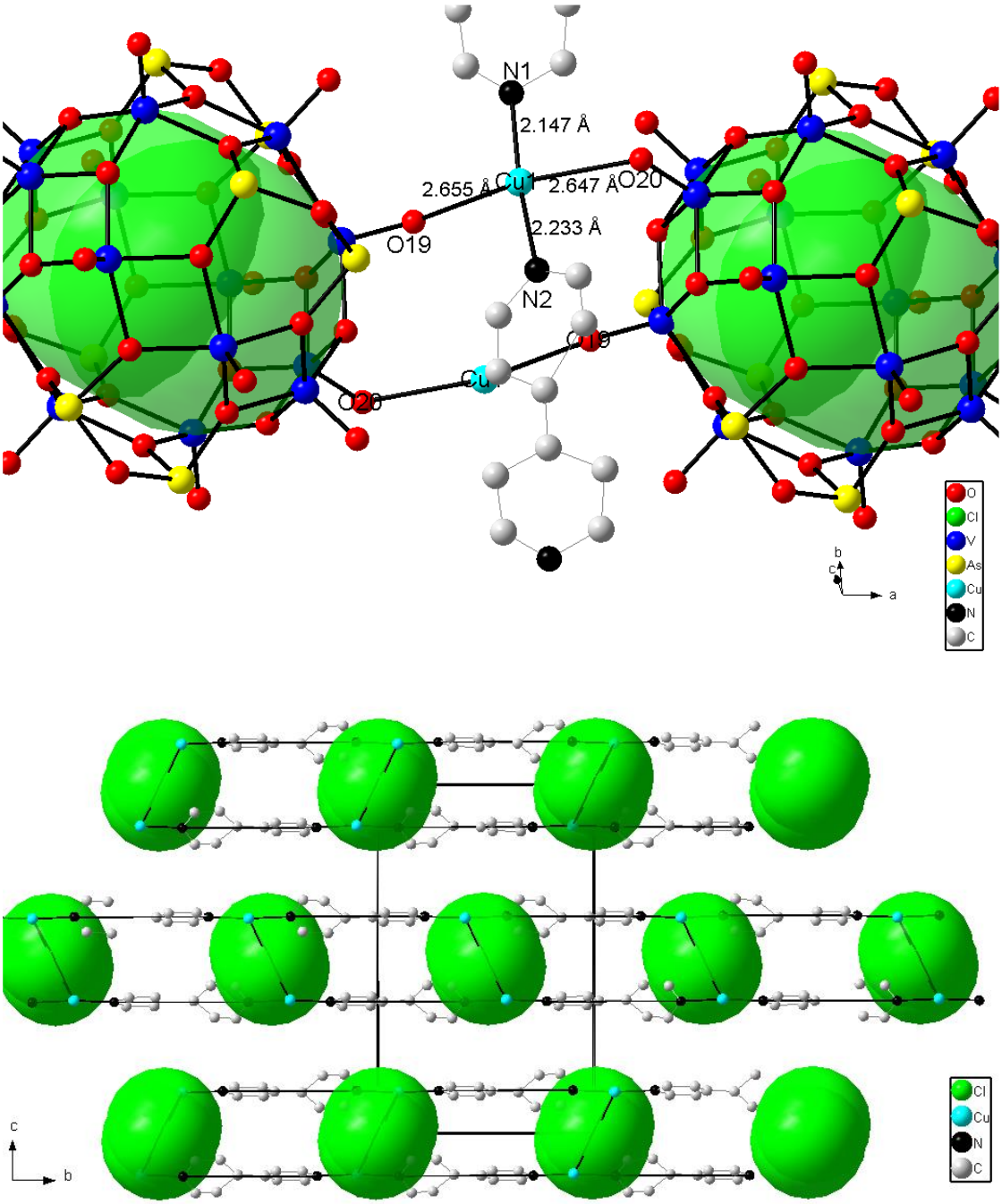

Figure 6.18: (top) Connectivity between the neighboring clusters through copper and oxygen in compound **2** running infinitely along *a* direction. The copper-bipyridine connectivity runs perpendicular to copper-oxygen connectivity and extends infinitely along *b* direction. (bottom) Packing of clusters (represented by central Cl atom) forming layered sheets with copper bipyridine in the *ab* plane.

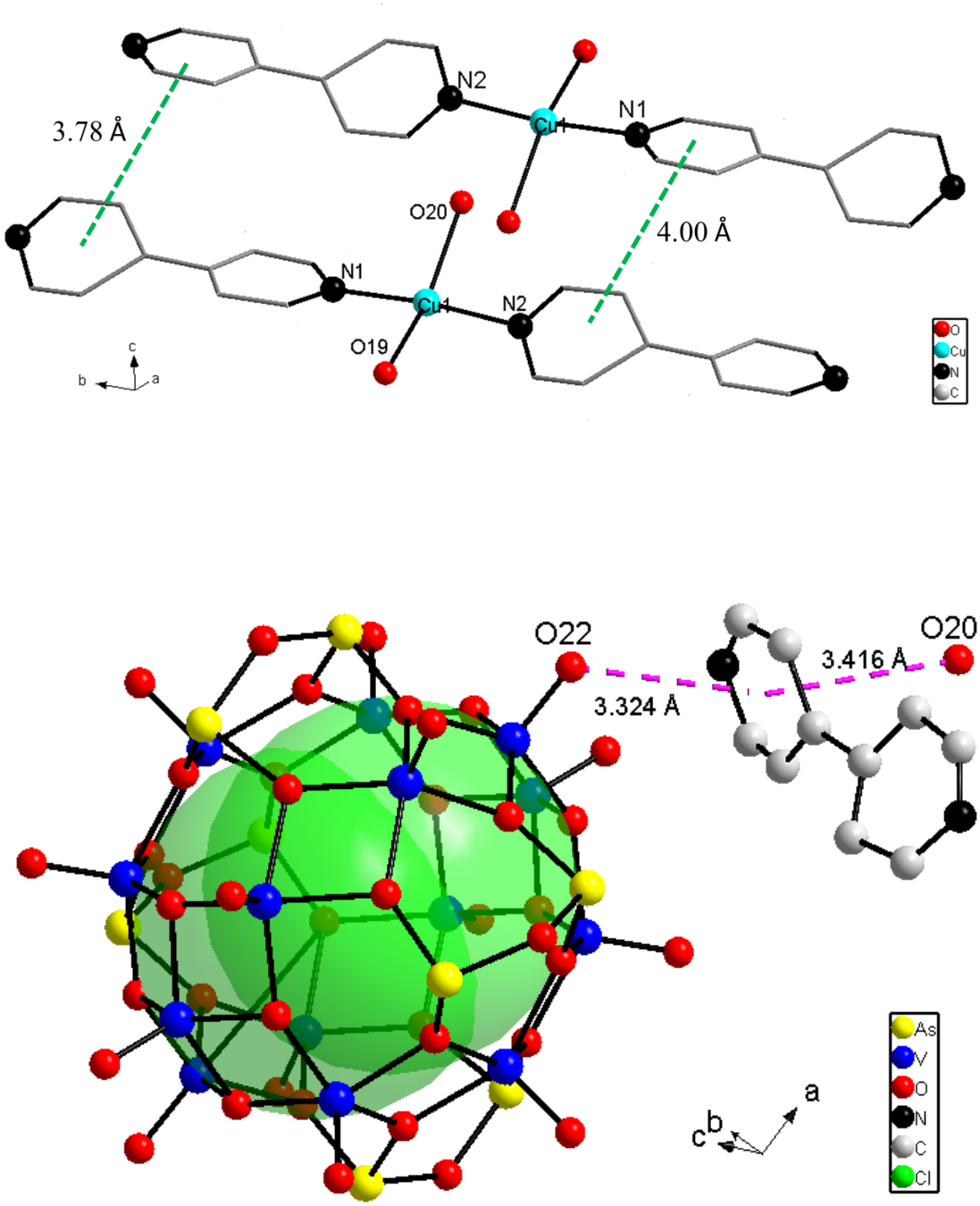

Figure 6.19: (top) π-π stacking in compound **2** between the neighboring 4,4'-bipyridine rings. (bottom) Closest anion-π interaction between the vanadyl oxygen atoms and the 4,4'-bipyridine.

Table 6.10: Anisotropic thermal parameters ($Å^2$ x 10^3) for compound **2**.

Atom	U11	U22	U33	U23	U13	U12
As(1)	73(2)	16(1)	36(1)	-3(1)	8(1)	-2(1)
As(2)	68(2)	26(1)	27(1)	-2(1)	4(1)	-1(1)
As(3)	66(1)	28(1)	21(1)	-3(1)	3(1)	2(1)
As(4)	73(2)	21(1)	33(1)	4(1)	8(1)	-5(1)
V(1)	64(2)	20(2)	23(2)	-2(1)	1(2)	-4(2)
V(2)	63(2)	20(2)	33(2)	-2(1)	6(2)	-2(2)
V(3)	70(2)	31(2)	24(2)	-4(1)	9(2)	9(2)
V(4)	71(2)	25(2)	26(2)	-3(1)	7(2)	-2(2)
V(5)	72(2)	19(2)	27(2)	6(1)	6(2)	-4(2)
V(6)	63(2)	24(2)	25(2)	-4(1)	8(2)	3(2)
V(7)	77(3)	31(2)	29(2)	-4(2)	10(2)	-3(2)
Cu(1)	232(8)	72(4)	146(6)	1(4)	34(5)	1(4)
Cl(1)	96(11)	58(9)	78(10)	12(8)	2(8)	-7(8)
O(1)	68(9)	26(7)	18(6)	3(5)	4(6)	-5(7)
O(2)	60(9)	29(8)	23(6)	-18(6)	-4(6)	-3(7)
O(3)	95(12)	16(7)	25(7)	0(5)	17(7)	-3(7)
O(4)	78(10)	23(7)	23(6)	-8(5)	4(7)	0(7)
O(5)	67(9)	19(7)	27(7)	4(5)	3(6)	2(6)
O(6)	70(9)	20(7)	30(7)	-2(6)	13(7)	-1(6)
O(7)	72(9)	17(7)	28(7)	-4(5)	10(7)	-6(6)
O(8)	66(9)	15(6)	25(6)	0(5)	10(6)	-2(6)
O(9)	73(10)	37(9)	39(8)	4(7)	10(8)	14(8)
O(10)	96(13)	23(8)	57(10)	4(7)	-1(9)	13(8)
O(11)	83(11)	15(7)	32(7)	-9(6)	13(7)	-7(7)
O(12)	74(10)	37(9)	21(6)	-3(6)	-7(7)	-8(7)
O(13)	62(9)	25(8)	43(8)	0(6)	4(7)	0(7)
O(14)	80(10)	24(8)	28(7)	-5(6)	6(7)	-9(7)
O(15)	49(8)	47(10)	45(9)	-6(7)	4(7)	-8(7)
O(16)	63(9)	24(7)	30(7)	-1(6)	-8(7)	-18(7)
O(17)	89(12)	37(9)	37(8)	-9(7)	15(8)	18(8)
O(18)	116(14)	13(7)	48(9)	-2(6)	27(9)	1(8)
O(19)	66(10)	37(10)	62(10)	-2(8)	0(8)	28(8)
O(20)	88(12)	51(11)	30(7)	-9(7)	15(8)	-2(9)
O(21)	88(12)	51(11)	43(9)	-22(8)	18(9)	-14(9)
N(1)	90(20)	180(40)	110(30)	-80(30)	60(20)	-40(30)
N(2)	82(19)	150(30)	90(20)	70(20)	49(17)	40(20)
C(1)	230(60)	100(30)	70(20)	-40(20)	80(30)	-110(40)
C(2)	80(20)	170(50)	52(18)	-60(20)	32(17)	-30(30)
C(3)	160(50)	290(90)	50(20)	100(40)	0(30)	130(60)
C(4)	58(17)	70(20)	130(30)	0(20)	40(20)	-14(16)
C(5)	52(15)	110(30)	48(14)	-1(17)	5(12)	-12(16)
C(6)	70(20)	260(60)	32(14)	-60(30)	38(15)	-60(30)
C(7)	60(18)	160(40)	100(30)	50(30)	35(18)	30(20)
C(8)	120(40)	170(60)	80(30)	50(30)	0(30)	20(40)
C(9)	100(30)	230(70)	70(20)	-60(30)	50(20)	-50(40)
C(10)	33(15)	400(100)	29(16)	70(40)	21(14)	50(30)

Table 6.11: Selected bond distances (Å) for compounds **2**.

AsO_3							
As(1)-O(7)	1.768(14)	As(2)-O(15)	1.760(17)	As(3)-O(5)	1.775(13)	As(4)-O(18)	1.770(17)
As(1)-O(18)#1	1.770(19)	As(2)-O(4)	1.780(14)	As(3)-O(15)	1.775(16)	As(4)-O(3)#1	1.771(14)
As(1)-O(13)	1.788(14)	As(2)-O(8)	1.786(14)	As(3)-O(2)	1.814(13)	As(4)-O(1)#1	1.795(13)
VO_5							
V(1)-O(12)	1.618(14)	V(2)-O(9)	1.577(16)	V(3)-O(17)	1.589(15)	V(4)-O(21)	1.559(16)
V(1)-O(2)#2	1.940(15)	V(2)-O(13)	1.940(17)	V(3)-O(11)#4	1.902(14)	V(4)-O(16)	1.910(14)
V(1)-O(4)#2	1.971(16)	V(2)-O(16)	1.942(13)	V(3)-O(6)#4	1.929(15)	V(4)-O(11)	1.921(15)
V(1)-O(3)	1.974(14)	V(2)-O(14)	1.955(15)	V(3)-O(5)	1.966(16)	V(4)-O(2)#2	1.993(16)
V(1)-O(7)	1.981(16)	V(2)-O(8)#3	1.965(13)	V(3)-O(1)#5	1.995(15)	V(4)-O(7)	2.005(15)
V(5)-O(10)	1.593(16)	V(6)-O(19)	1.587(16)	V(7)-O(20)	1.624(18)		
V(5)-O(1)#1	1.964(16)	V(6)-O(6)#5	1.927(14)	V(7)-O(11)	1.894(16)		
V(5)-O(8)#4	1.983(15)	V(6)-O(4)	1.952(14)	V(7)-O(6)	1.925(14)		
V(5)-O(13)#1	1.993(16)	V(6)-O(14)#5	1.954(15)	V(7)-O(16)	1.925(14)		
V(5)-O(5)#4	2.004(14)	V(6)-O(3)#4	1.983(16)	V(7)-O(14)	1.957(14)		
$Cu(O)_2(bpy)_2$		**N-C and C-C distances in bpy**					
Cu(1)-N(1)	2.15(5)	N(1)-C(9)	1.20(6)	N(2)-C(4)#7	1.26(4)	C(1)-C(7)#8	1.51(7)
Cu(1)-N(2)	2.23(4)	N(1)-C(1)	1.31(7)	N(2)-C(3)	1.31(9)		
Cu(1)-O(19)	2.656(55)						
Cu(1)-O(20)	2.647(39)	C(2)-C(8)#2	1.29(6)	C(3)-C(10)	1.13(11)	C(4)-N(2)#7	1.26(4)
		C(2)-C(7)#9	1.31(5)			C(4)-C(5)#7	1.35(5)
		C(2)-C(6)	1.46(7)				
Symmetry transformations used to generate equivalent atoms:		C(5)-C(4)#7	1.35(5)	C(6)-C(10)	1.62(7)	C(7)-C(2)#8	1.31(5)
#1 -x+1,-y+1,-z #2 -x+3/2,y-1/2,-z+1/2		C(5)-C(6)	1.44(5)			C(7)-C(1)#9	1.51(7)
#3 x-1/2,-y+1/2,z-1/2 #4 -x+3/2,y+1/2,-z+1/2							
#5 x+1/2,-y+1/2,z+1/2 #6 -x+1,-y,-z		C(8)-C(2)#4	1.29(6)	C(9)-C(8)#4	1.39(8)		
#7 -x+1,-y+1,-z+1 #8 -x+1/2,y+1/2,-z+1/2		C(8)-C(9)#2	1.39(8)				
#9 -x+1/2,y-1/2,-z+1/2							

Structure of $[(H_2bpy)]_2 \bullet [V_{14}As_8O_{42}Cl]$ (**3**)

Compound $[(H_2bpy)]_2 \bullet [V_{14}As_8O_{42}Cl]$, **3**, crystallizes in the orthorhombic crystal system in space group *F ddd* (no.70), $Z = 8$, with the unit cell dimensions of $a = 13.481(3)$ Å, $b = 20.265(4)$ Å, $c = 42.808(9)$ Å. The remaining crystallographic constants and data can be seen in Table 6.2. It is worth mentioning that, unlike for compounds **1**, **2**, and **4**, the structure of **3** was solved down to a low *R* value as a result of the collection of data at low temperature (-80 ^{o}C). Due to the high symmetry of the overall crystal system, the $(V_{14}As_8O_{42}Cl)^{4-}$ cluster in **3** is composed of only five crystallographically unique vanadium atoms with V(1), V(2), and V(5) having the multiplicity of two while V(3), V(4) have the multiplicity of four per composition of the cluster or formula unit. As is the case with the clusters in compounds **1** and **2**, the vanadium coordination in compound **3** feature square pyramidal environments with respect to the local oxygen atoms. Based on the sum of the Shannon crystal radii for oxygen and vanadium (1.88 Å),[13] similar to the expected bond distances are observed in the four equatorial bonds between vanadium and oxygen atoms ranging from 1.905 Å to 2.011 Å. The bond valence sums calculations of the five vanadium sites reveal that the oxidation state of vanadium is likely 4+ for all five sites (see Table 6.3). The two crystallographically unique arsenic atomic sites feature somewhat closer than expected bond distances to the oxygen atoms with distances ranging from 1.756 Å to 1.778 Å. Because of these short distances, the bond valence sums calculations of As(1) and As(2) sites are slightly higher than the expected 3+ oxidation state with BVS being 3.18 and 3.19, respectively.

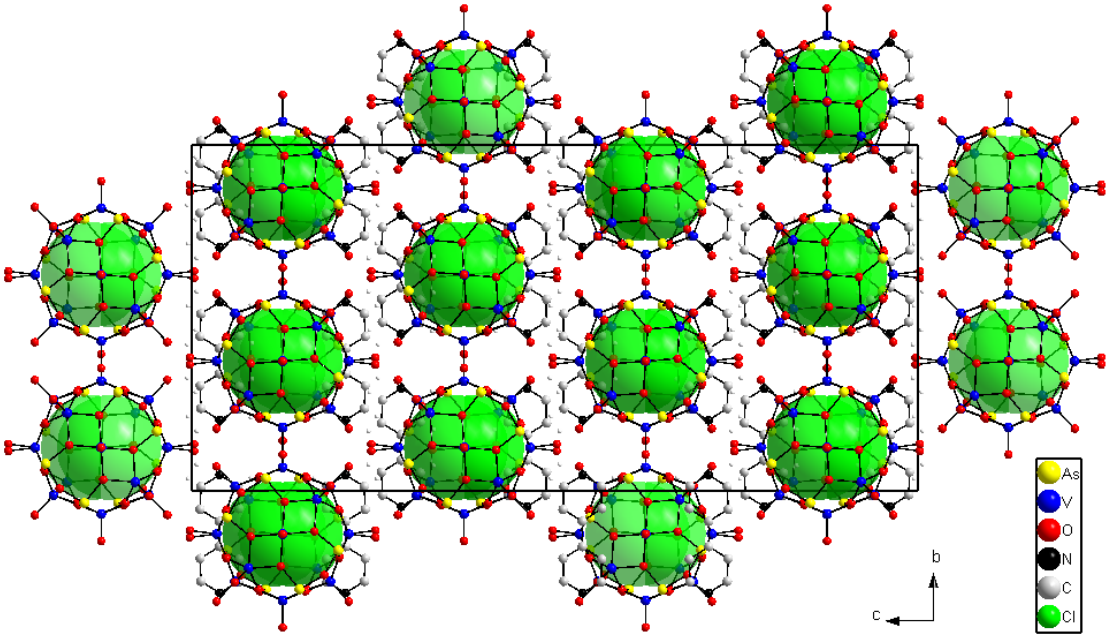

Figure 6.20: Perspective view of the unit cell in compound **3** looking down *a* crystallographic direction.

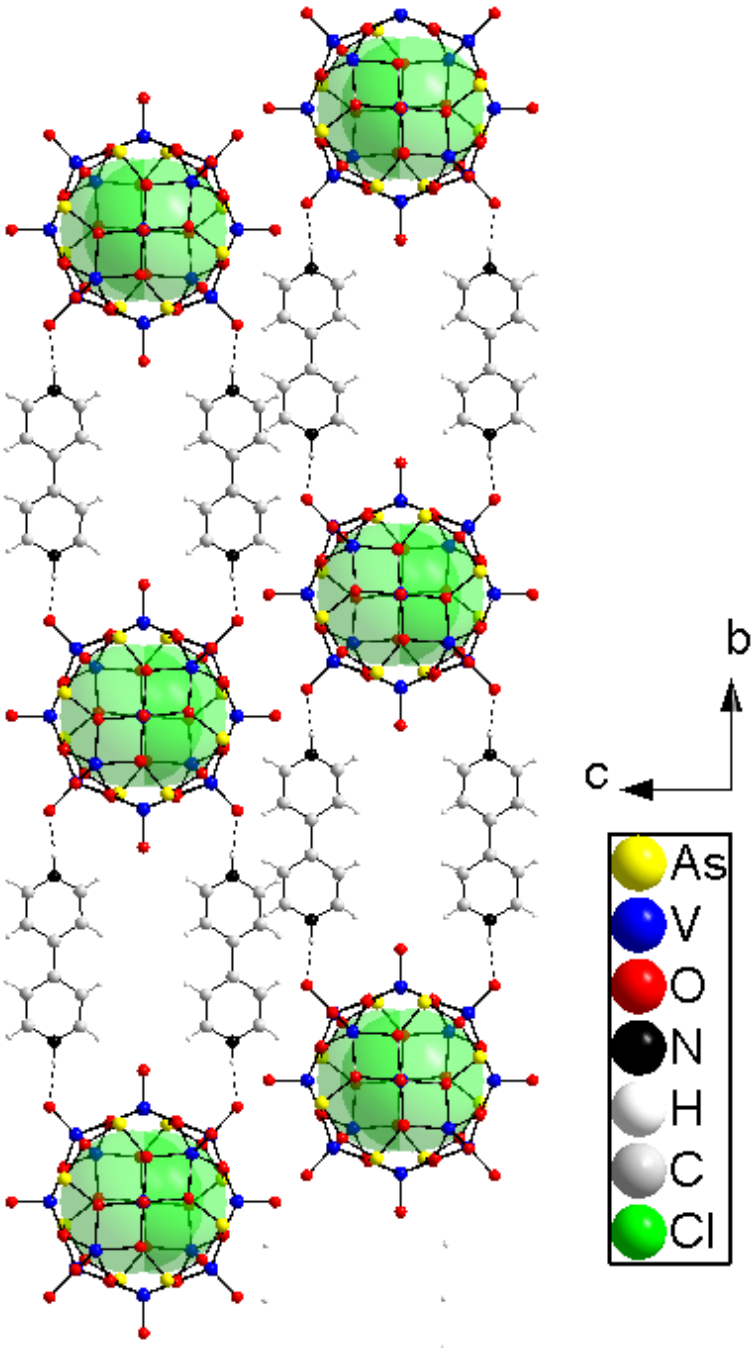

Figure 6.21: Hydrogen bond connectivity between the clusters and the 4,4'-bipyridine molecules making infinite chains along *b* crystallographic direction.

Table 6.12: Atomic coordinates (x 10^4 Å) and parameters for compound **3**.

Atom	Wyckoff notation	sof	x	y	z
As(1)	32*h*	1.00	3955(1)	5778(1)	484(1)
As(2)	32*h*	1.00	3934(1)	4647(1)	1018(1)
V(1)	16*e*	1.00	8954(2)	6250	1250
V(2)	16*f*	1.00	6250	4330(1)	1250
V(3)	32*h*	1.00	6130(1)	4871(1)	595(1)
V(4)	32*h*	1.00	8058(1)	5253(1)	781(1)
V(5)	16*g*	1.00	6250	6250	340(1)
Cl	16*g*	0.50	6250	6250	1140(3)
O(1)	32*h*	1.00	7060(4)	4642(3)	917(1)
O(2)	32*h*	1.00	7098(4)	5542(2)	482(1)
O(3)	32*h*	1.00	5227(4)	5595(3)	471(1)
O(4)	32*h*	1.00	5210(4)	4592(3)	937(1)
O(5)	32*h*	1.00	3948(4)	6321(3)	810(1)
O(6)	32*h*	1.00	6134(5)	4296(3)	337(1)
O(7)	32*h*	1.00	3955(5)	5323(3)	1278(1)
O(8)	32*h*	1.00	3521(5)	5060(3)	677(1)
O(9)	32*h*	1.00	8868(5)	4853(3)	590(2)
O(10)	16*e*	1.00	10125(6)	6250	1250
O(11)	16*f*	1.00	6250	3547(4)	1250
O(12)	16*g*	1.00	6250	6250	-30(2)
N(1)	32*h*	1.00	6084(6)	2953(4)	383(2)
C(5)	32*h*	1.00	6229(6)	1616(4)	380(2)
C(1)	32*h*	1.00	6387(7)	2642(5)	638(2)
C(3)	32*h*	1.00	6436(7)	1983(4)	646(2)
C(2)	32*h*	1.00	5852(9)	2621(5)	125(2)
C(4)	32*h*	1.00	5897(8)	1959(5)	113(2)

Table 6.13: Anisotropic thermal parameters ($Å^2$ x 10^3) for compound **3**.

Atom	U11	U22	U33	U23	U13	U12
As(1)	35(1)	39(1)	30(1)	2(1)	-4(1)	-2(1)
As(2)	41(1)	32(1)	36(1)	2(1)	-1(1)	-8(1)
V(1)	30(1)	36(1)	27(1)	-5(1)	0	0
V(2)	43(1)	26(1)	28(1)	0	-1(1)	0
V(3)	41(1)	27(1)	28(1)	-2(1)	0(1)	-1(1)
V(4)	35(1)	34(1)	30(1)	-3(1)	-1(1)	2(1)
V(5)	36(1)	31(1)	27(1)	0	0	-1(1)
Cl	98(9)	290(20)	68(7)	0	0	-67(12)
O(1)	40(3)	31(3)	32(3)	1(2)	-1(2)	1(2)
O(2)	37(3)	30(3)	28(3)	-5(2)	1(2)	4(2)
O(3)	34(3)	31(3)	31(3)	0(2)	5(2)	0(2)
O(4)	41(3)	36(3)	26(3)	3(2)	-2(2)	-4(2)
O(5)	40(3)	40(3)	27(3)	2(2)	-2(2)	-7(3)
O(6)	64(4)	33(3)	36(3)	-9(2)	-1(3)	6(3)
O(7)	45(3)	33(3)	30(3)	1(2)	-3(2)	0(3)
O(8)	41(3)	42(3)	39(3)	-1(3)	-6(3)	-9(3)
O(9)	44(4)	50(4)	40(3)	-6(3)	6(3)	6(3)
O(10)	31(4)	55(5)	38(5)	-8(4)	0	0
O(11)	68(7)	34(4)	38(5)	0	3(4)	0
O(12)	58(6)	51(5)	33(5)	0	0	-3(4)
N(1)	58(5)	35(4)	39(4)	-1(3)	3(4)	-2(4)
C(5)	33(4)	37(5)	31(4)	1(3)	-2(3)	8(3)
C(1)	50(6)	46(5)	44(5)	-25(4)	2(4)	-6(4)
C(3)	46(5)	39(5)	30(4)	-7(3)	-13(4)	5(4)
C(2)	75(7)	45(5)	35(5)	17(4)	-5(5)	3(5)
C(4)	73(7)	50(5)	30(5)	6(4)	-1(5)	0(5)

Table 6.14: Selected bond distances (Å) for compounds **3**.

AsO_3							
As(1)-O(3)	1.756(6)	As(2)-O(4)	1.759(6)				
As(1)-O(8)	1.770(6)	As(2)-O(7)	1.767(6)				
As(1)-O(5)	1.778(6)	As(2)-O(8)	1.772(6)				
VO_5							
V(1)-O(10)	1.579(9)	V(2)-O(11)	1.586(9)	V(3)-O(6)	1.606(6)	V(4)-O(9)	1.589(6)
V(1)-O(7)#1	1.962(6)	V(2)-O(1)	1.905(6)	V(3)-O(1)	1.919(6)	V(4)-O(2)	1.913(6)
V(1)-O(7)#2	1.962(6)	V(2)-O(1)#1	1.905(6)	V(3)-O(2)	1.946(6)	V(4)-O(1)	1.920(6)
V(1)-O(5)#1	1.964(6)	V(2)-O(4)#1	2.011(5)	V(3)-O(3)	1.978(6)	V(4)-O(5)#2	1.994(6)
V(1)-O(5)#2	1.964(6)	V(2)-O(4)	2.011(5)	V(3)-O(4)	1.999(6)	V(4)-O(7)#1	2.002(5)
V(5)-O(12)	1.583(9)	**N-C and C-C distances in bpy**					
V(5)-O(2)	1.932(5)	N(1)-C(1)	1.327(12)	C(1)-C(3)	1.337(13)	C(5)-C(3)	1.392(11)
V(5)-O(2)#2	1.932(5)	N(1)-C(2)	1.331(12)	C(2)-C(4)	1.344(13)	C(5)-C(4)	1.409(12)
V(5)-O(3)#2	1.995(5)					C(5)-C(5)#4	1.483(16)
V(5)-O(3)	1.995(5)						

Symmetry transformations used to generate equivalent atoms: #1: -x+5/4,y,-z+1/4; #2: -x+5/4,-y+5/4,z; #3: x,-y+5/4,-z+1/4; #4: -x+5/4,-y+1/4,z

However, as discussed above, bond valence sums calculations are not always indicative of the true oxidation state, especially in chemical systems such as polyoxometalates where electrons are easily delocalized between the metal sites. In addition, having mixed-valent atomic sites with multiplicities greater than one complicates things as average oxidation state needs to be taken into account.

Unlike in compounds **1** and **2**, **3** does not feature infinite copper-4,4'-bipyridine connectivity. Instead, the 4,4'-bipyridine units are connected to the oxygen atoms on the ($V_{14}As_8O_{42}Cl$) cluster by means of hydrogen bonds from the protonated nitrogen sites and extend along the *b* crystallographic direction.

Diffuse reflectance UV-vis data were collected on ground single crystals of compound **3**. Kubelka-Munk function was used to convert the reflectance data into absorbance and a Tauc plot was obtained as described in Chapter 2 and according to the reference below.[14] By extrapolating the linear region of the absorption edge energy band gap was obtained. The experimental band gap for compound **3** is 2.27 eV as shown in Figure 6.22. For comparison, the band gap of **V14** starting material was found to be 2.48 eV.

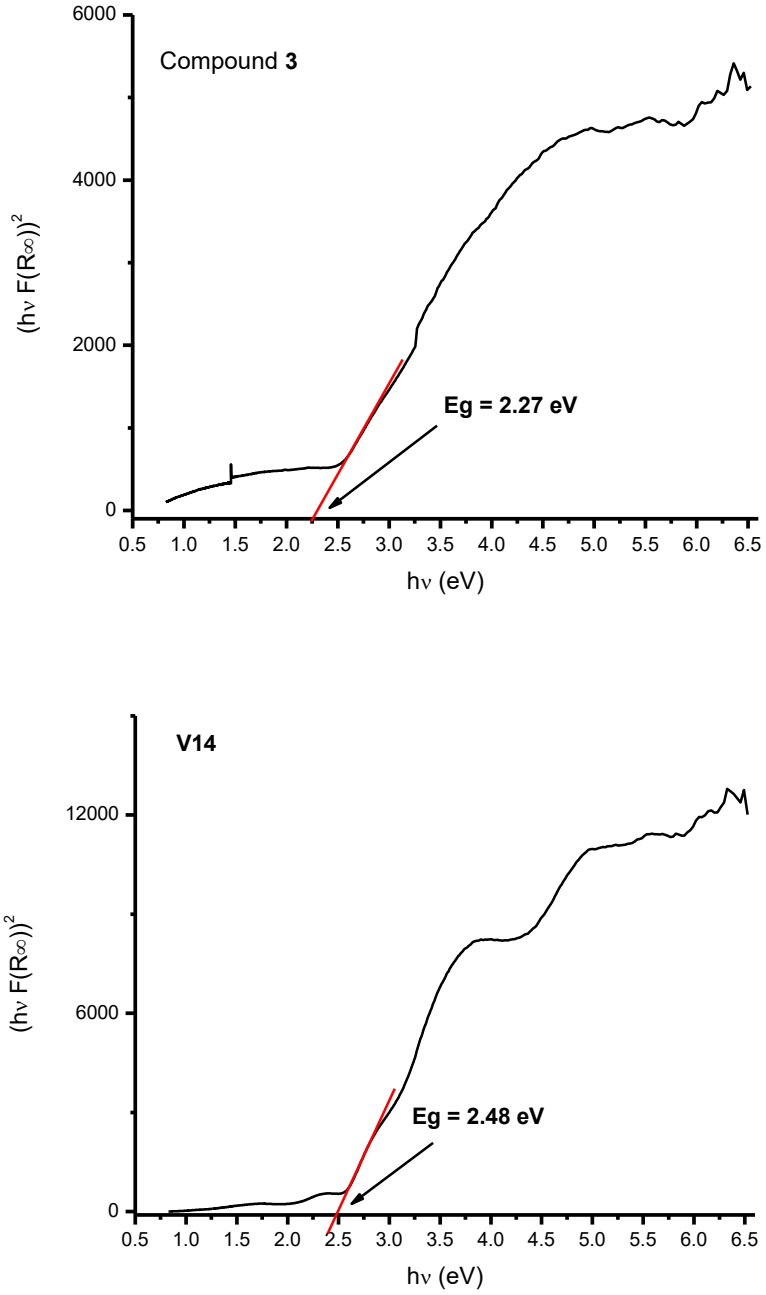

Figure 6.22: Tauc plots for compound **3** and **V14** starting material showing the band gap obtained from UV-vis reflectance data.

Comparison of the $(V_{14}As_8O_{42}Cl)^{n-}$ Clusters in **V14** and **1**~**3**

Looking closely at the structures of each of the $(V_{14}As_8O_{42}Cl)^{n-}$ clusters in compounds **1**~**3** and that in the salt-inclusion solid, **V14** used in the synthesis of **1**~**3**, clear difference in the symmetry and the orientation of atoms can be observed. These differences are illustrated in Figures 6.23 and 6.24. In Figure 6.23, focusing the attention on the four (only two are visible due to eclipsed spheres) arsenic sites (depicted in yellow spheres) on the bottom of the cluster, we can see that these are, more or less, the same for all four clusters. However, looking at the top four (again, some may be eclipsed showing only two) arsenic sites, the difference in these four clusters is evident. The only cluster that is similar to that in the **V14** solid is the cluster featured in compound **3**. The orientation of the arsenic atoms at both the top and the bottom of the clusters in **V14** and in **3** is the same. To better understand the differences in these clusters, rectangles connecting the bottom and the top arsenic sites were drawn as illustrated in Figure 6.23. In addition, vanadium atoms bisecting the arsenic rectangles are drawn for further illustration of the differences in the structures of these four clusters. It should be noted that the oxygen atoms coordinated to arsenic and vanadium atoms were left out for clarity. As is shown in Figure 6.23, in the original **V14** solid and in compound **3**, the orientation of the two (top and bottom from Figure 6.23) arsenic rectangles are staggered at 90^o relative to each other. In addition, the bisecting vanadium arcs are also oriented 90^o relative to each other. In compound **2**, the arsenic rectangles are eclipsed relative to each other with the two bisecting vanadium arcs fusing together and forming an eight-membered ring. In the cluster featured in compound

1, the two arsenic rectangles are staggered with a relative orientation of 45°. The opposite vanadium arcs are also oriented 45° from each other.

Given that the same source of the $(V_{14}As_8O_{42}Cl)^{5-}$ cluster was used in synthesis of all three compounds **1**~**3**, it is somewhat strange that the structures of the clusters in these solids are not the same as that in the **V14** salt-inclusion solid. With clusters in compounds **1** and **2** having significantly different structures than the cluster in **V14**, it is conceivably necessary that the original starting material (**V14**) cluster, instead of a simple twist of bisecting the arsenic rectangle (by as much as 45° a turn), had to undergo bond breaking and bond formation *in situ* in order to form different shapes of clusters in **1** and **2**. Looking at the different orientations of arsenic rectangles and the vanadium arcs, several bonds had to be broken in order to alter the original orientation seen in **V14**. In fact, even in the cluster in compound **1** which has the smallest relative change from the original cluster (**V14**) compared to compound **2** (*i.e*. 45° change vs. 90°), at least eight bonds (four arsenic-oxygen and four vanadium-oxygen bonds) had to be broken to go from the cluster orientation in **V14** to that in the cluster in compound **1**.

Based on literature search, the decomposition and reassembly of polyoxometalates in solution is known. In fact, polyoxometalate clusters are subject to disassembly and reassembly under different pH conditions.[17] It is argued here that the high concentration of H^+, which protonate basic oxygen sites at low pH values, contributes to weakening of metal-oxygen bonds which leads to breaking of metal-oxygen bonds as well as addenda (arsenic in the case of clusters in this chapter) atom oxygen bonds. However, specific conditions of the bond breaking in polyoxometalate clusters are largely unknown. From

the limited number of data points presented in this dissertation, looking at the conditions under which compounds **1**~**3** were synthesized, it can be inferred that the low pH values of the initial cocktail mixture of reactants seemingly lead to greater extent in transformations of the original **V14** cluster. Compound **1** was synthesized under acidic conditions with pH being adjusted to 3 while compound **2** was synthesized under the adjusted pH of 1.5. Comparatively, the cluster in **3,** which showed no apparent change in the orientation of the arsenic rectangles and the vanadium arcs compared to the cluster in **V14,** was synthesized under the pH of 4. In addition, looking at the ($V_{15}O_{36}Cl$) cluster in **4**, which was also synthesized at relatively higher pH value of 4, there seems to be no apparent change in the cluster compared to that in **V15** salt-inclusion solid. These observations indicate that the low pH lead to decomposition or breaking of bonds within the polyoxovanadate clusters used in the synthesis of **1**~**4**.

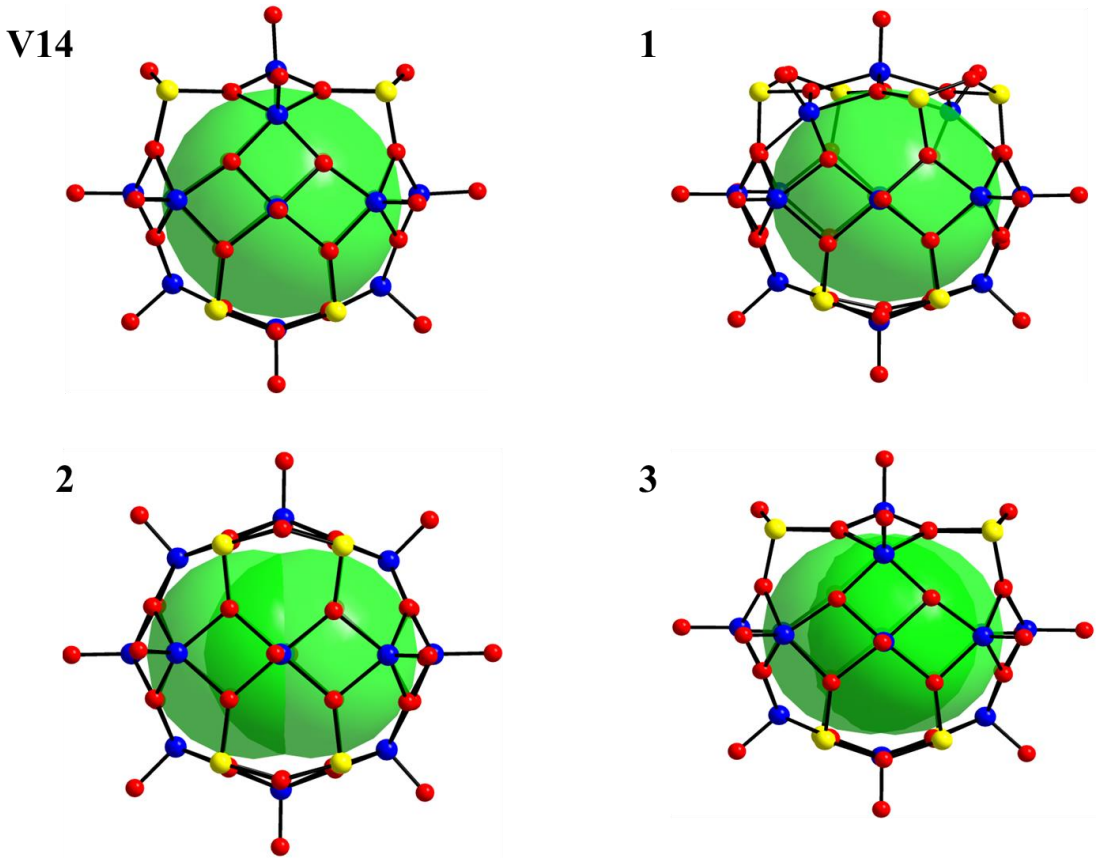

Figure 6.23: Illustration of $(V_{14}As_8O_{42}Cl)^{n-}$ clusters showing the differences in the clusters of **V14** and **1**~**3**.

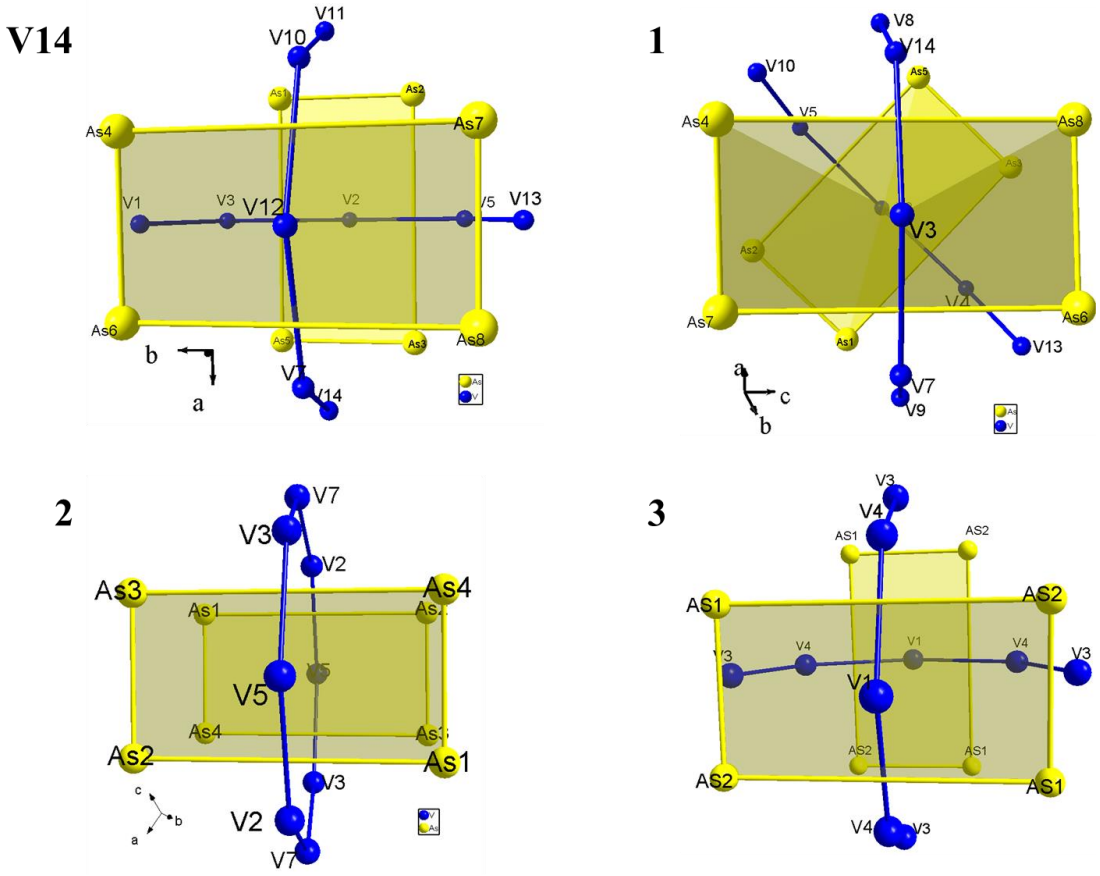

Figure 6.24: Differences in clusters of **V14** and compounds **1**~**3**. Arsenic sites were drawn as planes with each arsenic occupying a corner of the rectangle. Bisecting vanadium arcs are also drawn to illustrate the differences in these clusters. Oxygen atoms were omitted for clarity.

Structure of $[(bpy)_2(H_2bpy)_3(Hbpy)_2]\bullet[V_{15}O_{36}Cl]_2\bullet 4H_2O$ (**4**)

Compound $[(bpy)_2(H_2bpy)_3(Hbpy)_2]\bullet[V_{15}O_{36}Cl]_2\bullet 4H_2O$, **4**, crystalizes in the monoclinic crystals system, space group $P\ 2_1/n$ (no. 14), $Z = 2$ with unit cell dimensions of a = 12.161(2) Å, b = 22.021(4) Å, c = 22.298(5) Å, β = 95.09(3)^o. Unlike compounds **1**~**3** where $(V_{14}As_8O_{42}Cl)^{n-}$ cluster is incorporated in the inorganic-organic hybrid solids described in this chapter, **4** features a different cluster, $(V_{15}O_{36}Cl)^{7-}$. This $(V_{15}O_{36}Cl)^{7-}$ cluster is similar to the cluster in the salt-inclusion solid originally used in the synthesis of **4**.[11] Fifteen crystalographically unique vanadium sites exist with square pyramidal coordination geometry. Four equatorial bonds with close to expected distances (based on the sum of the Shannon radii of O^{2-} and $V^{4+,5+}$ being ~1,88 Å)[13] are observed between the local oxygen atoms and vanadium sites ranging from 1.828 Å and 2.145 Å. The fifth vanadium-oxygen bond is the apical vanadyl, V = O bond pointing away from the center of the cluster with distances ranging between 1.576 Å and 1.640 Å. As is the case with clusters in compounds **1**~**3**, the cluster in **4** features a chloride anion encapsulated inside the 51-atom vanadium-oxygen framework. Figure 6.24 illustrates the high similarity in structures of $(V_{15}O_{36}Cl)^{7-}$ cluster in **4** compared to that in **V15** salt-inclusion solid.[11] Given their anionic charge, the overall charge of the compound is satisfied by the protonated 4,4'-bipyridine units, as discussed above. The connectivity between the cluster and the 4,4'-bipyridine units occurs through hydrogen bonding between the oxygen atoms on the surface of the cluster and the protonated nitrogen sites on the pyridine rings.

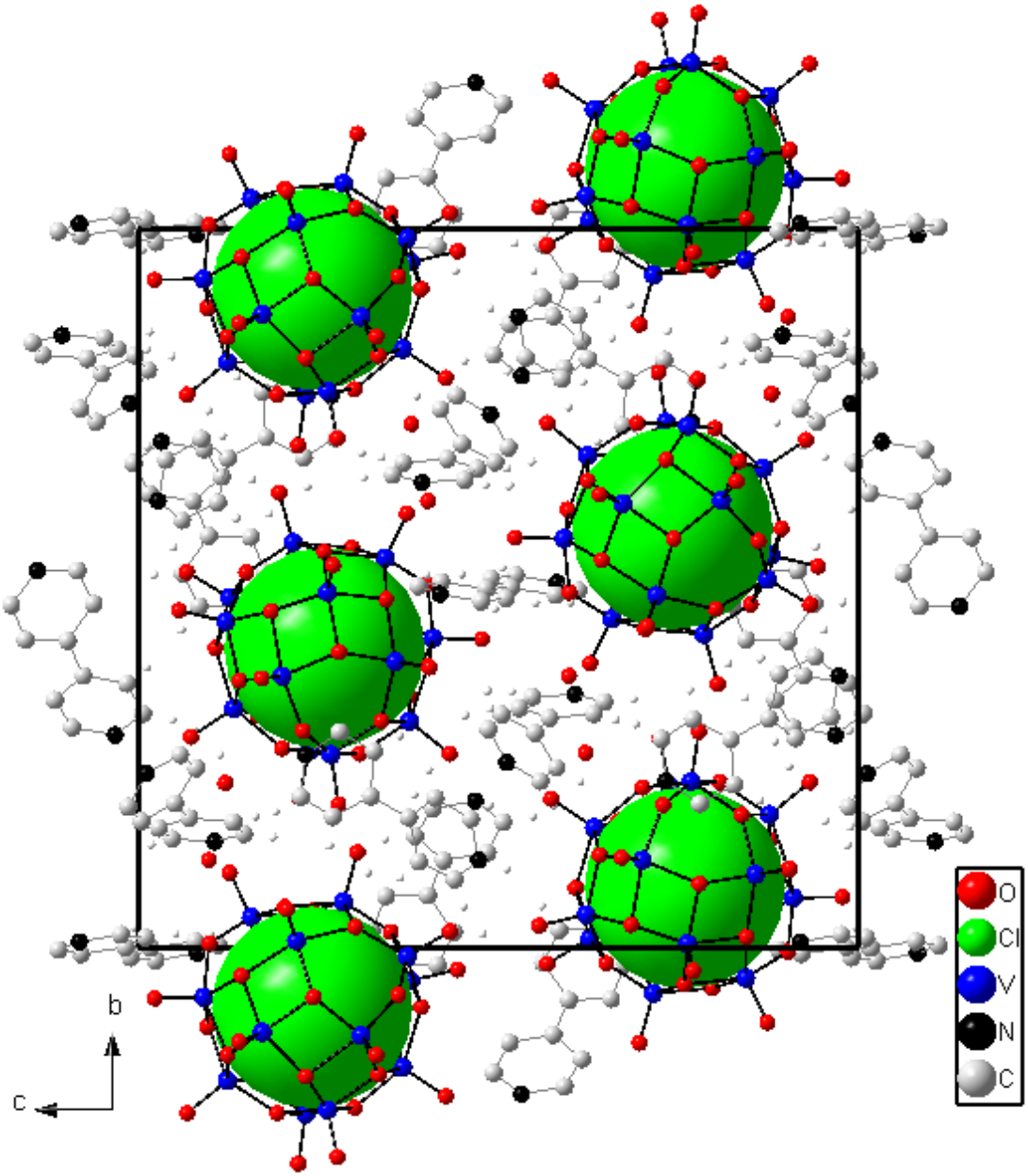

Figure 6.25: Perspective view of compound **4** looking down the *a* crystallographic direction.

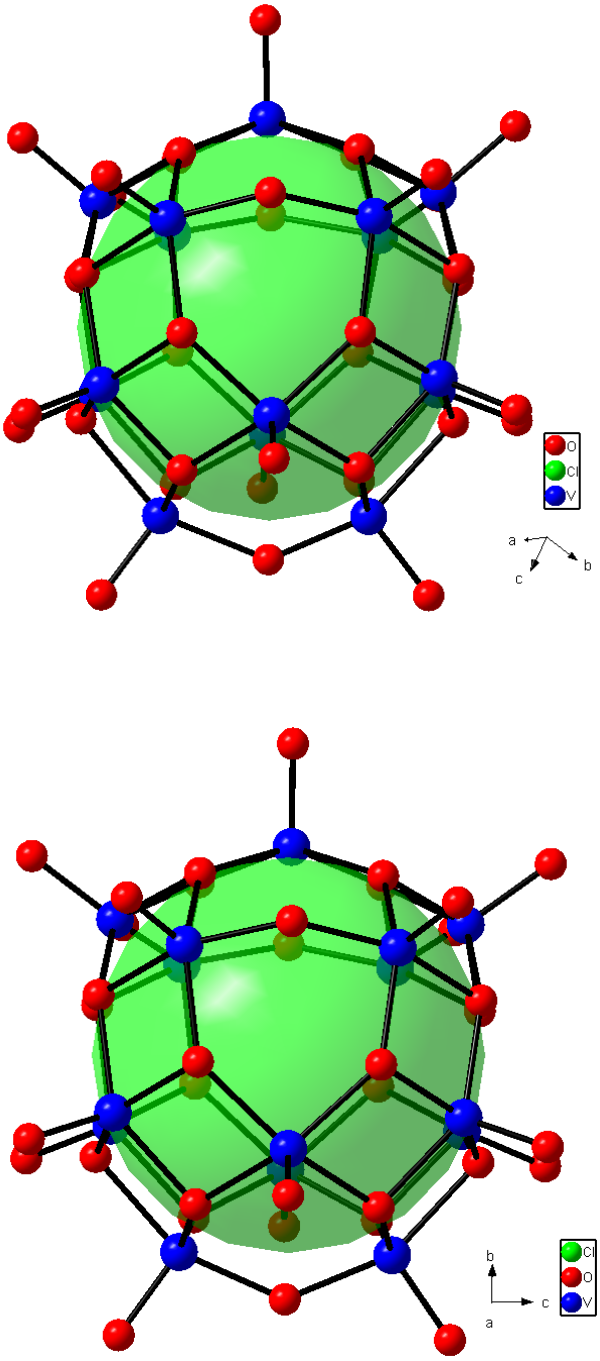

Figure 6.26: Comparison between the cluster in **4** (top) and that in the salt inclusion solid, **V15** (bottom), used in the synthesis of **4**. The cluster in **4** is largely unchanged compared to the cluster in **V15**. (Note, the cluster structure below looks the same.)

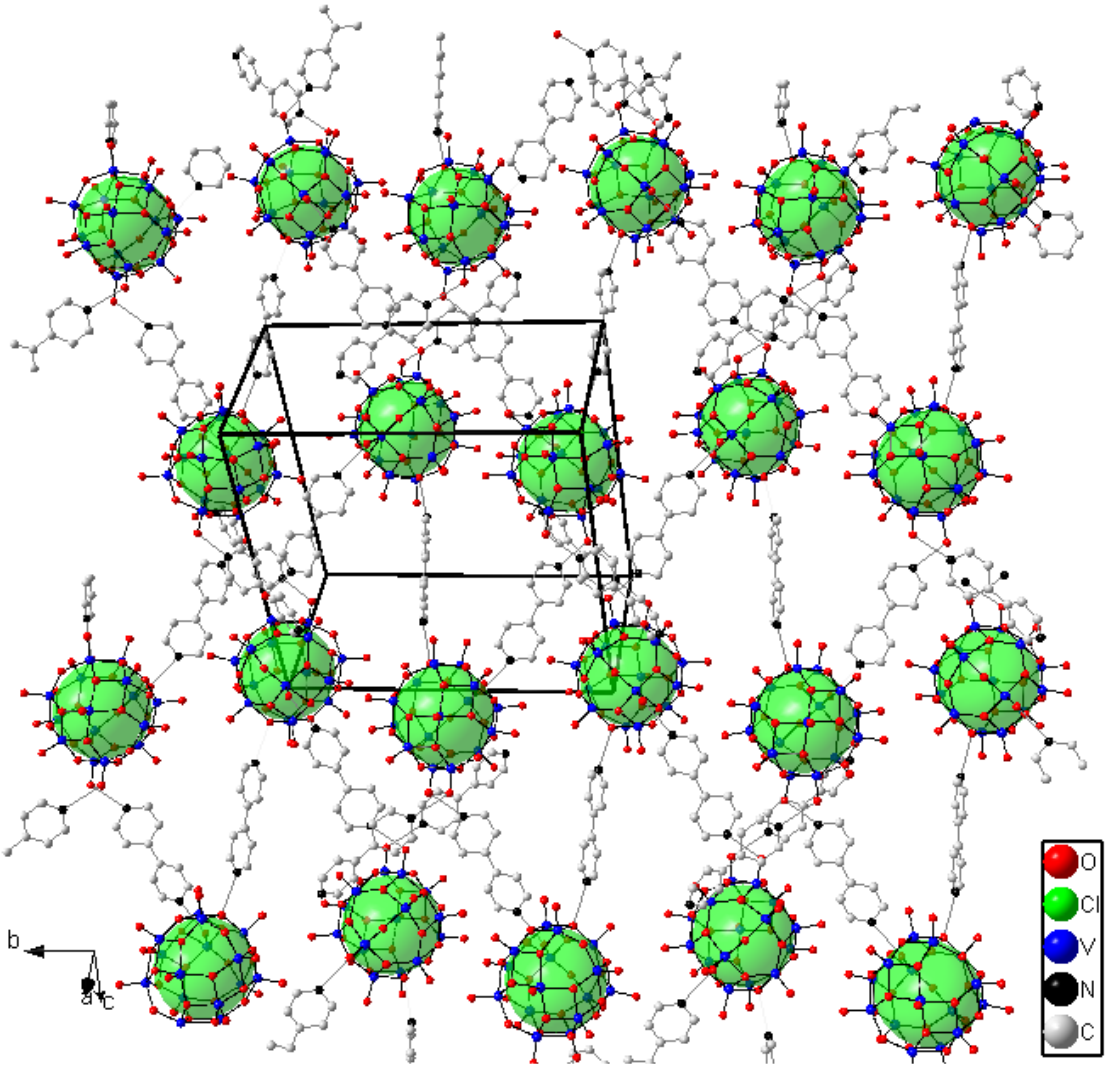

Figure 6.27: A view of one layer of the complex packing and connectivity between the clusters and 4,4'-bipyridine units in **4**.

Table 6.15: Atomic coordinates (x 10^4 Å) and parameters for compound **4**.

Atom	Wyckoff notation	sof	x	y	z
V(1)	4*e*	1.00	2917(2)	6670(1)	1328(1)
V(2)	4*e*	1.00	4292(2)	7257(1)	2372(1)
V(3)	4*e*	1.00	5767(2)	6181(1)	3278(1)
V(4)	4*e*	1.00	859(2)	5055(1)	2625(1)
V(5)	4*e*	1.00	1784(2)	5461(1)	1219(1)
V(6)	4*e*	1.00	1395(2)	6017(1)	3569(1)
V(7)	4*e*	1.00	3276(2)	4363(1)	2150(1)
V(8)	4*e*	1.00	3334(2)	6851(1)	3763(1)
V(9)	4*e*	1.00	5300(2)	4906(1)	2806(1)
V(10)	4*e*	1.00	449(2)	6220(1)	1999(1)
V(11)	4*e*	1.00	5621(2)	6223(1)	1905(1)
V(12)	4*e*	1.00	1981(2)	7314(1)	2677(1)
V(13)	4*e*	1.00	4015(2)	5127(1)	1268(1)
V(14)	4*e*	1.00	2730(2)	4577(1)	3431(1)
V(15)	4*e*	1.00	4282(2)	5692(1)	4094(1)
Cl	4*e*	1.00	3244(3)	5833(1)	2586(2)
O(1)	4*e*	1.00	4472(7)	6765(3)	1665(3)
O(2)	4*e*	1.00	556(7)	5886(3)	2787(3)
O(3)	4*e*	1.00	1846(7)	6846(3)	3375(3)
O(4)	4*e*	1.00	3139(6)	5829(3)	1072(3)
O(5)	4*e*	1.00	2804(7)	7227(3)	1999(3)
O(6)	4*e*	1.00	3580(7)	7302(3)	3071(3)
O(7)	4*e*	1.00	1467(6)	6285(3)	1404(4)
O(8)	4*e*	1.00	3951(7)	4436(3)	2967(3)
O(9)	4*e*	1.00	5486(7)	6793(3)	2675(4)
O(10)	4*e*	1.00	1982(7)	4488(3)	2580(4)
O(11)	4*e*	1.00	1538(7)	5149(3)	3439(3)
O(12)	4*e*	1.00	4626(6)	4712(3)	1987(3)
O(13)	4*e*	1.00	1658(7)	8007(3)	2779(4)
O(14)	4*e*	1.00	5915(7)	5691(3)	2568(3)
O(15)	4*e*	1.00	2607(7)	4780(3)	1498(3)
O(16)	4*e*	1.00	5365(7)	5393(4)	3566(4)
O(17)	4*e*	1.00	2865(7)	6084(3)	4023(3)
O(18)	4*e*	1.00	4807(8)	5706(4)	4773(4)
O(19)	4*e*	1.00	3550(7)	4942(4)	4014(3)
O(20)	4*e*	1.00	4729(7)	6496(4)	3759(4)
O(21)	4*e*	1.00	760(7)	6984(3)	2285(4)
O(22)	4*e*	1.00	-800(7)	6251(4)	1711(4)

Table 6.15: Atomic coordinates (x 10^4 Å) and parameters for compound **4** (contin...).

Atom	Wyckoff notation	sof	x	y	z
O(23)	4*e*	1.00	783(7)	5317(4)	1842(3)
O(24)	4*e*	1.00	1117(7)	5308(4)	567(4)
O(25)	4*e*	1.00	4727(8)	7913(4)	2236(4)
O(26)	4*e*	1.00	-237(7)	4677(4)	2704(4)
O(27)	4*e*	1.00	3329(8)	7303(4)	4321(4)
O(28)	4*e*	1.00	6783(7)	6495(4)	1696(4)
O(29)	4*e*	1.00	5258(7)	5660(4)	1391(4)
O(30)	4*e*	1.00	4253(8)	4774(4)	675(4)
O(31)	4*e*	1.00	6966(8)	6309(4)	3600(4)
O(32)	4*e*	1.00	2782(8)	7069(4)	731(4)
O(33)	4*e*	1.00	6336(8)	4469(4)	2937(4)
O(34)	4*e*	1.00	2362(8)	3958(4)	3730(4)
O(35)	4*e*	1.00	484(8)	6101(4)	4045(4)
O(36)	4*e*	1.00	3260(8)	3672(4)	1957(4)
O(37)	4*e*	1.00	6210(20)	7290(11)	6208(11)
O(38)	4*e*	1.00	4970(12)	3781(8)	4021(6)
N(1)	4*e*	1.00	5635(11)	7959(5)	4680(6)
N(2)	4*e*	1.00	-2095(13)	5247(7)	1403(7)
N(3)	4*e*	1.00	7064(11)	3525(5)	3942(6)
N(4)	4*e*	1.00	7534(12)	7425(6)	5115(6)
N(5)	4*e*	1.00	7399(9)	5079(5)	4185(5)
N(6)	4*e*	1.00	8066(10)	7320(7)	2322(6)
N(7)	4*e*	1.00	866(13)	6218(6)	-276(7)
C(1)	4*e*	1.00	5905(10)	3786(6)	762(6)
C(2)	4*e*	1.00	4513(12)	3065(6)	916(6)
C(3)	4*e*	1.00	6641(11)	4271(6)	978(5)
C(4)	4*e*	1.00	5316(12)	3448(6)	1158(6)
C(5)	4*e*	1.00	5706(12)	3678(6)	153(6)
C(6)	4*e*	1.00	6812(12)	4789(7)	619(7)
C(7)	4*e*	1.00	7174(16)	4286(8)	1563(7)
C(8)	4*e*	1.00	5033(15)	8255(7)	5065(7)
C(9)	4*e*	1.00	-2223(16)	4772(10)	1762(9)
C(10)	4*e*	1.00	7438(19)	5246(10)	845(9)
C(11)	4*e*	1.00	2245(13)	8419(6)	1469(6)
C(12)	4*e*	1.00	1180(14)	8251(6)	1322(6)
C(13)	4*e*	1.00	791(12)	8197(6)	708(6)
C(14)	4*e*	1.00	-795(14)	7504(7)	805(7)
C(15)	4*e*	1.00	2593(13)	8486(6)	469(6)
C(16)	4*e*	1.00	1527(12)	6666(6)	5289(6)

Table 6.15: Atomic coordinates (x 10^4 Å) and parameters for compound **4** (contin….).

Atom	Wyckoff notation	sof	x	y	z
C(17)	4*e*	1.00	332(13)	2990(6)	4491(7)
C(18)	4*e*	1.00	8034(15)	6960(8)	4862(7)
C(19)	4*e*	1.00	-957(14)	6756(7)	5044(6)
C(20)	4*e*	1.00	8157(17)	7682(9)	5581(9)
C(21)	4*e*	1.00	-556(10)	5005(6)	4829(5)
C(22)	4*e*	1.00	-681(11)	4911(6)	4204(6)
C(23)	4*e*	1.00	8281(12)	4969(7)	3892(7)
C(24)	4*e*	1.00	1508(12)	4863(7)	4897(6)
C(25)	4*e*	1.00	2527(12)	4818(7)	5241(6)
C(26)	4*e*	1.00	-1022(13)	7268(6)	3274(7)
C(27)	4*e*	1.00	-115(13)	8190(6)	3756(7)
C(28)	4*e*	1.00	1606(14)	2904(7)	2741(6)
C(29)	4*e*	1.00	1022(14)	3179(7)	2298(7)
C(30)	4*e*	1.00	-702(12)	7897(6)	3227(6)
C(31)	4*e*	1.00	8403(13)	7001(7)	2796(7)
C(32)	4*e*	1.00	709(13)	7916(7)	4121(6)
C(33)	4*e*	1.00	1199(16)	6790(8)	-383(7)
C(34)	4*e*	1.00	64(19)	5951(9)	-607(9)
C(35)	4*e*	1.00	400(16)	3804(8)	1105(9)

Table 6.16: Anisotropic thermal parameters ($Å^2$ x 10^3) for compound **4**.

Atom	U11	U22	U33	U23	U13	U12
V(1)	30(1)	30(1)	26(1)	1(1)	3(1)	-2(1)
V(2)	33(1)	34(1)	33(1)	-2(1)	7(1)	-5(1)
V(3)	31(1)	40(1)	32(1)	-1(1)	1(1)	-4(1)
V(4)	29(1)	33(1)	33(1)	0(1)	4(1)	-2(1)
V(5)	31(1)	33(1)	28(1)	0(1)	1(1)	1(1)
V(6)	33(1)	34(1)	30(1)	-2(1)	9(1)	1(1)
V(7)	32(1)	33(1)	31(1)	0(1)	4(1)	0(1)
V(8)	35(1)	35(1)	29(1)	-4(1)	4(1)	-4(1)
V(9)	34(1)	42(1)	33(1)	2(1)	1(1)	4(1)
V(10)	26(1)	42(1)	36(1)	5(1)	5(1)	3(1)
V(11)	29(1)	47(1)	33(1)	5(1)	5(1)	0(1)
V(12)	41(1)	33(1)	36(1)	1(1)	13(1)	5(1)
V(13)	35(1)	37(1)	27(1)	-2(1)	4(1)	6(1)
V(14)	41(1)	37(1)	31(1)	6(1)	6(1)	4(1)
V(15)	39(1)	45(1)	29(1)	0(1)	1(1)	5(1)
Cl	42(2)	45(2)	44(2)	-1(1)	8(1)	-4(1)
O(1)	35(5)	35(4)	23(4)	-2(3)	2(3)	-3(3)
O(2)	38(5)	35(4)	27(4)	-2(3)	4(4)	2(4)
O(3)	34(5)	26(4)	33(4)	1(3)	4(4)	4(3)
O(4)	30(4)	34(4)	24(4)	-2(3)	7(3)	1(3)
O(5)	42(5)	31(4)	27(4)	-1(3)	9(4)	2(4)
O(6)	45(5)	32(4)	29(4)	-1(3)	11(4)	-6(4)
O(7)	25(4)	30(4)	39(4)	3(3)	2(3)	4(3)
O(8)	38(5)	39(4)	26(4)	0(3)	4(4)	1(4)
O(9)	31(5)	33(4)	39(5)	2(3)	-7(4)	-6(3)
O(10)	27(4)	37(4)	34(4)	-1(3)	4(3)	0(3)
O(11)	35(5)	35(4)	28(4)	-2(3)	0(3)	-3(4)
O(12)	24(4)	39(4)	32(4)	-6(3)	-2(3)	2(3)
O(13)	45(5)	30(4)	48(5)	1(4)	15(4)	7(4)
O(14)	40(5)	35(4)	27(4)	-6(3)	13(4)	2(4)
O(15)	40(5)	29(4)	28(4)	-1(3)	-1(4)	-1(3)
O(16)	30(5)	37(4)	41(5)	6(4)	4(4)	-3(3)
O(17)	43(5)	32(4)	27(4)	-1(3)	7(4)	-7(4)
O(18)	52(6)	62(6)	29(5)	-6(4)	-7(4)	4(5)
O(19)	31(5)	47(5)	28(4)	-3(3)	7(3)	-1(4)
O(20)	38(5)	44(5)	38(5)	-2(4)	4(4)	-1(4)
O(21)	28(4)	37(4)	35(4)	-3(3)	3(4)	-4(3)
O(22)	26(4)	48(5)	40(5)	-4(4)	1(4)	-1(4)
O(23)	28(4)	44(5)	29(4)	-1(3)	3(3)	-4(4)
O(24)	43(5)	42(5)	27(4)	-4(3)	-3(4)	-3(4)
O(25)	49(6)	37(5)	45(5)	-3(4)	8(4)	-4(4)
O(26)	41(5)	37(5)	49(5)	3(4)	7(4)	-7(4)
O(27)	57(6)	45(5)	35(5)	-19(4)	-2(4)	-8(4)
O(28)	26(5)	56(5)	49(5)	-3(4)	11(4)	0(4)
O(29)	27(4)	42(5)	36(4)	3(4)	-4(4)	-3(4)
O(30)	43(5)	58(5)	27(4)	-8(4)	5(4)	9(4)
O(31)	34(5)	63(6)	42(5)	3(4)	-4(4)	-7(4)
O(32)	56(6)	37(4)	27(4)	0(3)	3(4)	2(4)
O(33)	42(6)	52(5)	53(6)	-3(4)	-7(5)	8(4)
O(34)	45(6)	40(5)	43(5)	13(4)	3(4)	-5(4)
O(35)	38(5)	56(5)	40(5)	-12(4)	14(4)	-4(4)

Table 6.16: Anisotropic thermal parameters ($Å^2$ x 10^3) for compound **4** (continued).

Atom	U11	U22	U33	U23	U13	U12
O(36)	51(6)	35(4)	45(5)	-4(4)	9(4)	10(4)
O(37)	180(20)	190(20)	170(20)	-30(17)	54(17)	-20(17)
O(38)	73(10)	166(15)	81(10)	-9(9)	3(8)	49(10)
N(1)	55(8)	54(7)	52(7)	4(6)	4(6)	18(6)
N(2)	77(11)	67(9)	75(11)	5(8)	10(8)	-4(8)
N(3)	64(9)	37(6)	58(8)	-7(5)	9(6)	6(6)
N(4)	64(9)	84(9)	48(7)	-15(7)	-8(7)	20(7)
N(5)	33(6)	60(7)	42(7)	1(5)	7(5)	-3(5)
N(6)	36(7)	89(10)	50(7)	-22(7)	8(6)	-3(6)
N(7)	78(10)	49(7)	77(10)	20(7)	-2(8)	-1(7)
C(1)	30(7)	42(7)	42(7)	-2(5)	2(6)	8(5)
C(2)	44(8)	58(8)	38(7)	-5(6)	12(6)	-5(7)
C(3)	45(8)	57(8)	26(6)	-18(6)	11(6)	-1(6)
C(4)	42(8)	48(7)	49(8)	-15(6)	9(6)	15(6)
C(5)	51(8)	44(7)	31(7)	3(5)	8(6)	-5(6)
C(6)	46(9)	61(9)	47(8)	-9(7)	-5(7)	-14(7)
C(7)	82(12)	75(10)	35(8)	13(7)	-21(8)	-9(9)
C(8)	76(12)	63(9)	48(9)	-1(7)	18(8)	18(8)
C(9)	61(12)	104(15)	70(12)	-28(11)	-13(10)	9(11)
C(10)	112(18)	91(14)	60(12)	9(10)	27(12)	3(13)
C(11)	55(9)	47(8)	38(7)	1(6)	0(7)	10(7)
C(12)	75(11)	41(7)	36(7)	1(6)	11(7)	-5(7)
C(13)	54(9)	35(6)	48(8)	10(6)	10(7)	6(6)
C(14)	60(10)	66(10)	58(10)	20(8)	-16(8)	-29(8)
C(15)	51(9)	56(8)	44(8)	0(6)	7(7)	-6(7)
C(16)	45(8)	48(7)	43(7)	-7(6)	-5(6)	3(6)
C(17)	51(9)	47(8)	57(9)	2(7)	-2(7)	0(7)
C(18)	70(12)	74(11)	49(9)	-24(8)	6(8)	11(9)
C(19)	82(12)	51(8)	36(7)	-18(6)	1(7)	26(8)
C(20)	81(14)	86(13)	84(13)	-33(11)	1(11)	40(11)
C(21)	33(7)	43(6)	32(6)	-3(5)	0(5)	-3(5)
C(22)	35(7)	43(7)	47(8)	-5(6)	16(6)	-6(6)
C(23)	42(8)	64(9)	43(8)	15(7)	2(6)	-10(7)
C(24)	52(9)	64(9)	34(7)	2(6)	16(6)	19(7)
C(25)	36(8)	82(10)	42(8)	3(7)	10(6)	15(7)
C(26)	58(10)	48(8)	51(8)	2(6)	33(7)	2(7)
C(27)	56(9)	39(7)	53(8)	-18(6)	-18(7)	15(6)
C(28)	64(10)	72(10)	31(7)	3(7)	0(7)	-23(8)
C(29)	65(11)	43(8)	62(10)	-1(7)	-3(8)	-11(7)
C(30)	51(9)	44(7)	42(7)	-16(6)	-3(6)	2(6)
C(31)	56(10)	66(10)	52(9)	-16(8)	26(8)	-20(8)
C(32)	61(10)	54(8)	35(7)	-12(6)	-5(7)	18(7)
C(33)	80(13)	80(11)	42(8)	4(8)	-1(8)	-18(10)
C(34)	109(17)	80(13)	96(15)	54(12)	-41(13)	-46(12)
C(35)	79(13)	74(11)	95(14)	40(10)	-24(11)	-50(10)

Table 6.17: Selected bond distances (Å) for compounds **4**.

VO_5							
V(1)-O(32)	1.593(8)	V(2)-O(25)	1.576(9)	V(3)-O(31)	1.592(9)	V(4)-O(26)	1.594(9)
V(1)-O(5)	1.949(8)	V(2)-O(6)	1.850(8)	V(3)-O(20)	1.863(9)	V(4)-O(23)	1.835(8)
V(1)-O(4)	1.962(7)	V(2)-O(9)	1.853(8)	V(3)-O(9)	1.914(8)	V(4)-O(10)	1.859(8)
V(1)-O(7)	1.976(8)	V(2)-O(5)	1.925(9)	V(3)-O(16)	1.927(8)	V(4)-O(2)	1.910(8)
V(1)-O(1)	1.983(8)	V(2)-O(1)	1.943(8)	V(3)-O(14)	1.935(8)	V(4)-O(11)	1.936(8)
V(5)-O(24)	1.635(8)	V(6)-O(35)	1.611(9)	V(7)-O(36)	1.580(8)	V(8)-O(27)	1.594(8)
V(5)-O(15)	1.878(8)	V(6)-O(11)	1.945(8)	V(7)-O(15)	1.847(8)	V(8)-O(20)	1.868(9)
V(5)-O(4)	1.891(8)	V(6)-O(2)	1.961(8)	V(7)-O(12)	1.877(8)	V(8)-O(6)	1.882(8)
V(5)-O(7)	1.908(8)	V(6)-O(3)	1.965(8)	V(7)-O(10)	1.934(8)	V(8)-O(17)	1.890(8)
V(5)-O(23)	1.952(8)	V(6)-O(17)	1.981(9)	V(7)-O(8)	1.936(8)	V(8)-O(3)	1.935(8)
V(9)-O(33)	1.593(9)	V(10)-O(22)	1.597(8)	V(11)-O(28)	1.640(9)	V(12)-O(13)	1.597(8)
V(9)-O(14)	1.975(8)	V(10)-O(21)	1.828(8)	V(11)-O(29)	1.719(8)	V(12)-O(21)	1.807(8)
V(9)-O(12)	1.980(8)	V(10)-O(7)	1.898(9)	V(11)-O(1)	1.879(8)	V(12)-O(3)	1.886(8)
V(9)-O(8)	1.999(9)	V(10)-O(2)	1.900(8)	V(11)-O(14)	1.895(8)	V(12)-O(5)	1.895(8)
V(9)-O(16)	2.001(9)	V(10)-O(23)	2.064(8)	V(11)-O(9)	2.145(8)	V(12)-O(6)	2.062(9)
V(13)-O(30)	1.584(8)	V(14)-O(34)	1.599(8)	V(15)-O(18)	1.590(8)		
V(13)-O(4)	1.907(8)	V(14)-O(19)	1.760(8)	V(15)-O(19)	1.879(9)		
V(13)-O(29)	1.913(8)	V(14)-O(8)	1.911(9)	V(15)-O(17)	1.921(9)		
V(13)-O(12)	1.935(8)	V(14)-O(11)	1.920(8)	V(15)-O(16)	1.957(9)		
V(13)-O(15)	1.984(9)	V(14)-O(10)	2.041(8)	V(15)-O(20)	2.015(9)		

Table 6.17: Selected bond distances (Å) for compounds **4** (continued).

C-N and C-C bond distances							
N(1)-C(8)	1.345(19)	N(2)-C(10)#2	1.32(2)	N(3)-C(11)#3	1.318(19)	N(4)-C(18)	1.340(19)
N(1)-C(2)#1	1.346(17)	N(2)-C(9)	1.33(2)	N(3)-C(15)#3	1.344(18)	N(4)-C(20)	1.36(2)
N(5)-C(25)#4	1.295(17)	N(6)-C(31)	1.30(2)	N(7)-C(34)	1.31(2)	C(1)-C(5)	1.378(17)
N(5)-C(23)	1.325(18)	N(6)-C(28)#1	1.36(2)	N(7)-C(33)	1.35(2)	C(1)-C(4)	1.400(19)
						C(1)-C(3)	1.447(18)
C(2)-N(1)#3	1.346(17)	C(3)-C(7)	1.405(18)	C(5)-C(8)#3	1.35(2)	C(7)-C(9)#5	1.35(2)
C(2)-C(4)	1.364(19)	C(3)-C(6)	1.42(2)	C(6)-C(10)	1.33(2)	C(8)-C(5)#1	1.35(2)
C(9)-C(7)#2	1.35(2)	C(11)-N(3)#1	1.318(19)	C(12)-C(13)	1.415(19)	C(13)-C(16)#6	1.38(2)
C(10)-N(2)#5	1.32(2)	C(11)-C(12)	1.36(2)			C(13)-C(17)#7	1.47(2)
C(14)-C(20)#8	1.39(2)	C(15)-N(3)#1	1.344(18)	C(16)-C(15)#9	1.365(19)	C(17)-C(19)#10	1.35(2)
C(14)-C(17)#7	1.40(2)	C(15)-C(16)#6	1.365(19)	C(16)-C(13)#9	1.38(2)	C(17)-C(14)#11	1.40(2)
						C(17)-C(13)#11	1.47(2)
C(18)-C(19)#5	1.34(2)	C(19)-C(18)#2	1.34(2)	C(20)-C(14)#12	1.39(2)	C(21)-C(24)#10	1.388(18)
		C(19)-C(17)#10	1.35(2)			C(21)-C(22)	1.402(17)
						C(21)-C(21)#10	1.49(2)
C(22)-C(23)#2	1.392(19)	C(23)-C(22)#5	1.392(19)	C(24)-C(21)#10	1.388(18)	C(25)-N(5)#4	1.295(17)
				C(24)-C(25)	1.40(2)		
C(26)-C(31)#2	1.36(2)	C(27)-C(32)	1.374(18)	C(28)-C(29)	1.31(2)	C(29)-C(30)#11	1.35(2)
C(26)-C(30)	1.444(19)	C(27)-C(35)#7	1.438(19)	C(28)-N(6)#3	1.36(2)	C(30)-C(29)#7	1.35(2)
		C(27)-C(30)	1.473(17)				
C(31)-C(26)#5	1.36(2)	C(33)-C(32)#6	1.37(2)	C(34)-C(35)#13	1.32(2)	C(35)-C(34)#13	1.32(2)
C(32)-C(33)#9	1.37(2)					C(35)-C(27)#11	1.438(19)

Symmetry transformations used to generate equivalent atoms:

#1	-x+1,y+1/2,-z+1/2	#2	x-1,y,z	#3	-x+1,y-1/2,-z+1/2	#4	-x+1,-y+1,-z+1
#5	x+1,y,z	#6	x,-y+3/2,z-1/2	#7	-x,y+1/2,-z+1/2	#8	x-1,-y+3/2,z-1/2
#9	x,-y+3/2,z+1/2	#10	-x,-y+1,-z+1	#11	-x,y-1/2,-z+1/2	#12	x+1,-y+3/2,z+1/2
#13	-x,-y+1,-z						

Conclusions

Four new inorganic-organic hybrid polyoxometalate-based solids were synthesized using the solution-based synthesis where soluble pre-synthesized polyoxometalate clusters were used as precursors. This method meant to provide a unique synthetic strategy unlike the commonly used *bottom-up* synthetic approaches in which simple transition metal oxides are used to synthesize polyoxometalates *in situ*. Using the synthetic method described herein, more control can be expected in the formation of desired solids given that the synthesis of polyoxometalate-containing material (*i.e.* soluble salt-inclusion polyoxometalate solids) was done prior to the introduction of organic ligands for formation of polyoxometalate inorganic-organic hybrids.

Compounds **1**~**3** feature $(V_{14}As_8O_{42}Cl)^{n-}$ clusters connected through copper-oxygen, copper-nitrogen, non-covalent hydrogen bonding (compounds **1**~**2**) and non-covalent hydrogen bonding in compound **3**. In addition, a $(V_{15}O_{36}Cl)^{4-}$ cluster was isolated in **4** using similar reaction conditions in which a soluble salt-inclusion polyoxometalate solid, **V15**, was used in the original synthesis.

From the reactions which produced single crystals of **1**~**4**, it can be inferred that the reaction conditions are very sensitive with respect to the amount of organic ligand, 4,4'-bipyridine, used. Having a large ratio of 4,4'-bipyridine ligands compared to the polyoxometalate starting materials seemingly increased the yields as was shown for compounds **1** and **3**. This, of course, could be a kinetic occurrence where excess of 4,4'-bipyridine molecules increased the chance of forming solids with the polyoxometalate anions. In addition, pH of the initial reaction mixture played an important role in terms of

the transformations in cluster shapes for compounds **1**~**3** and potentially for compound **4** as well. Among these four solids, the largest cluster transformations (in reference to the original cluster shape in **V14** and **V15** salt-inclusion solids) was observed in compounds **1** and **2** which were synthesized in the lowest relative pH conditions being 1.5 and 3, respectively. The remaining two solids, **3** and **4**, which were synthesized at relatively higher pH values, 4 and 5, respectively, show no apparent change in the cluster shape compared to those in **V14** and **V15**. It is argued that the protonation of basic oxygen sites on the clusters under highly acidic conditions weaken the metal oxygen bonds in the polyoxometalate clusters and thereby result in breaking of vanadium-oxygen bonds which leads to fragmentation of the polyoxometalate clusters and subsequent rearrangement and rotation of the arsenic rectangle caps in relation to the original clusters in **V14** solid.

Future Work

In regards to the synthesis of hybrid inorganic-organic polyoxometalate-containing solids, it can be envisaged that the new synthetic method described herein, using soluble polyoxometalates as precursors, can lead to new solids with emergent properties relevant to many technologies. However, as was the case with the attempted synthesis of POMOFs which lead to the formation of compounds **1**~**4**, predictability of structures and formation of hybrid polyoxometalate-containing materials under given conditions has yet to be fine-tuned. Several experiments should be done in order to better understand the formation of solids in Chapter 6. Namely, 1) conditions governing the oxidation state change of the polyoxometalate clusters in the final product compared to that in the starting

material should be studied with respect to the pH of the solution 2) In addition, conditions which preserve a given oxidation state of the cluster should be explored by systematically varying the reaction conditions including pH; 3) The role of the transition metal cation used in reactions which did not incorporate these cations should be revealed 4) High yield of all of the compounds presented in Chapter 6 could be obtained by using different solvent systems and temperature conditions.

As far as the synthesis of POMOFs goes, it is evident from the synthesis of **1**~**4**, that 4,4'-bipyridine ligand leads to inter-penetrated networks with small or no porous structures. Using ligands that generally do not lead to inter-penetrated networks, *i.e*. ligands with coordination sites oriented in three dimensions (3D) rather than linear ones, may lead to formation of porous polyoxometalate-containing hybrids.

Finally, given that compounds **1**~**4** are new solids, their physical and chemical properties are unknown. The reduced state of the clusters in **1**~**4** may lead to interesting magnetic and/or electronic properties related to confined electrons within the metal-oxygen cluster framework. Future magnetic susceptibility studies are due which may potentially reveal interesting phenomena associated with these solids. In addition, given their catalytic properties, polyoxovanadate clusters in **1**~**4** may show superior catalytic properties compared to the currently available such catalysts.

Literature Cited

1. (a) Troupis, A.; Triantis, T.; Hiskia, A.; Papaconstantinou, E. *Eur. J. Inorg. Chem.*, **2008**, 5579−5586

   (b) Zhang, G.; Keita, B.; Craescu, C. T.; Miron, S.; Oliveira, P.; Nadjo, L. *J. Phys. Chem. B*, **2007**, 111 (38), 11253−11259.

   (c) Hiskia, A.; Troupis, A.; Antonaraki, S.; Gkika, E.; Kormalip, P.; Papaconstantinou, E. *Intern. J. Environ. Anal. Chem*. **2006**, 86 (3-4), 233−242.

   (d) Lv, H., Geletii, Y., Zhao, C., Vickers, J., Zhu, G., Luo, Z., Song, J., Lian, T., Musaevb, D. & Hill, C. *Chem. Soc. Rev.* **2012**, *41*, 7572–7589.

   (e) Song, Y., & Tsunashima, R. *Chem. Soc. Rev*. **2012,** *41*, 7384-7402.

2. (a) Yamase, T. *Chem. Rev*., **1998**, 98, 307.

   (b) Hill, C. L.; Prosser-McCartha, C. M.; Gratzel, M.; Kalyanasundaram, M. *Photosensitization and photocatalysis using inorganic and organometallic compounds*, Kluwer Academic Publishers, Dordrecht, 1993. pp. 307.

   (c) Papaconstantinou, E. *Chem. Soc. Rev.*, **1989**, 18, 1.

3. Brimblecombe, R.; Dismukes, G. C.; Swiegers, G. F.; Spiccia, L. *Dalton Transactions*. **2009**, 9374-9384.

4. (a) Yaghi, O. M.; Li, G.; Li, H. *Nature.* **1995,** 378, 703-706.

   (b) Yaghi, O. M.; Li, H.; Davis, C.; Richardson, D.; Groy, T. L. *Acc. Chem*. **1998,** 31, 474–484.

   (c) Chen, B.; Liang, C.; Yang, J.; Yaghi, O. M. *Angew. Chem. Int. Ed.* **2006,** 45, 1390-1393.

5. Janiak, C. *Dalton Trans*. **2003**, 14, 2781-2804.

6. Yaghi, O. M.; Rosi, N.L.; Eddaoudi M.;Kim, J; O'Keeffe, M. *CrystEngComm*. **2002**, 4(68), 401–404.

7. Rosi, N.L.; Eckert, J.; Eddaoudi, M.; Vodak, D.T.; Kim, J.; O'Keeffe, M.; Yaghi, O.M. *Science*. **2003,** 300, 1127.

8. Hupp, J. T.; Lee, J.; Farha, O. K.; Roberts, J.; Scheidt, K. A.; Nguyen, S. T. *Chem. Soc. Rev*. **2009**, 38, 1450.

9. Nohra, B.; El Moll, H.; Albelo, L. M. R.; Mialane, P.; Marrot, J.; Mellot-Draznieks, C.; O'Keeffe, M.; Biboum, R. N.; Lemaire, J.; Keita, B.; Nadjo, L.; Dolbecq, A. *J. Am. Chem. Soc.* **2011**, 133, 13363–13374.

10. Queen, W.L.; West, J.P.; Hwu, S.-J.; Tran, T.T.; Halasyamani, P.S.; VanDerveer, D. *Chem. Commun*. **2012**, 48, 1665–1667.

11. Queen, W.L.; West, J.P.; Hudson, J.; Hwu, S.-J. *Inorg. Chem*. **2011**, 50, 11064–11068.

12. Szatylowicz, H. *J. Phys. Org. Chem*. **2008**, *21*, 897-914.

13. Shannon, R.D. *Acta Cryst*. **1976**, *A32*, 751-767.

14. (a) Kubelka, P.; Munk, F. *Z. Tech. Phys*. **1931**, *12*, 593.

    (b) Kubelka, P. *J. Opt. Soc. Am*. **1948**, *38*, 448-457.

15. Sinnokrot, M.O.; Valeev, E.F.; Sherrill, C.D. *J. Am. Chem. Soc*., **2002**, *124* (36), 10887-10893.

16. Robertazzi, A.; Krull, F.; Knapp, E.W.; Gamez, P. *Cryst. Eng. Comm*., **2011**, *13*, 3293-3300.

17. Pradeep, C. P.; Long, D. L.; Streb, C.; Cronin, L. *J. Am. Chem. Soc*. **2008**, *130*, 14946-14947.

CHAPTER SEVEN

CONCLUSIONS AND FUTURE WORK

The main goal of the research presented in this dissertation was the exploratory synthesis and characterization of extended solids featuring electronically reduced polyoxometalate (POM) clusters. The efforts presented in this dissertation produced many new POM containing solids. In addition, the methods used in the synthesis of these new POM materials are unconventional based on the hitherto published literature of POMs. This unique approach to synthesis of POM materials provides a new synthetic method that can open doors to synthesis and isolation of otherwise unattainable POM compounds. The motivation for synthesis of electronically reduced POM materials stems largely from the interesting properties which arise due to unpaired valence *d* electrons in magnetism and electronic properties, for example. The idea of confined electrons in a zero-dimensional (0D) molecular cage has always intrigued researchers in the magnetic communities. This intrigue largely stems from materials that are analogous to POMs (at least with regard to 0D or low dimensionality) in which interesting properties are exhibited by low dimensional magnets such as single molecule magnets (SMMs), single chain magnets (SCMs) and even single ion magnets (SIMs). In theory, POMs are ideal for potential SMM-like behavior due to their molecular nature and the large number of potential magnetic ions incorporated into the structure. Compared to their organic coordination compound counterparts, POMs have some intrinsic advantages: 1) they exhibit robust, stable, all-inorganic structures; 2) they

have multiple metal sites with potential for inclusion of magnetic ions; 3) they possess the ability to accept a number of electrons without a significant change in structure.

Though there were many initial application-based motivations to study reduced POMs, this dissertation is largely concerned with the synthesis of reduced POMs using an unconventional method. Property measurements of these solids were done to a limited extent. Naturally, after the complete synthetic and structural characterization of these solids, which was done to a significant extent in this dissertation, property measurements should follow in the near future. The following paragraphs will highlight the main findings from each chapter and will provide future directions related to each. Finally, overall conclusions will be made.

In Chapter 3, a new salt inclusion solid (*SIS*) containing discrete POM clusters was presented. This new compound has the composition of $Cs_6I_3Na(PMo_{12}O_{40})$ in which the one-electron reduced Keggin-based POM is featured. To the best of my knowledge, this is the first time a Keggin-based polyoxometalate has been isolated using conventional, high-temperature method using molten halide salt as a high-temperature solvent and inevitably, a reactant. From our recent two reports of reduced polyoxovanadates (POVs), and the compounds presented in this dissertation, we have reasons to believe that high temperature synthesis of POMs promotes the isolation of reduced species which is not generally the case with the solution-based low temperature synthetic routes. Upon the investigation of the structure and bonding in compound $Cs_6I_3Na(PMo_{12}O_{40})$, it can be noticed that the Keggin clusters, $(PMo_{12}O_{40})^{4-}$, are linked through a Na^+ ion in a square antiprismatic eight-coordination extending along *c* crystallographic direction. Parallel to the Keggin-Na-

Keggin chains, a $[Cs_2I]_\infty$ antifluorite salt chain runs along *c*. In this salt chain, the neighboring iodine atoms are unusually close in proximity which suggests that there exists a non-covalent I···I interaction between the two neighboring iodine atoms which further stabilizes the overall structure. This additional stabilizing feature is likely related to the large size of iodine atoms and their ability to form halogen bonds. In Chapter 3, this halogen bonding is possibly the reason for insolubility of $Cs_6I_3Na(PMo_{12}O_{40})$ compound in water and its increased solubility in less polar solvents. The TGA data shows that the title compound is thermally stable under N_2 gas flow up to about 200 ^oC and has two sharp weight losses corresponding to about 13% weight loss attributed to the oxidation of iodide, I^-, and loss of iodine, I_2, gas. The relatively low thermal stability (compared to metal-oxide, inorganic compounds) is attributed to the volatility and release of I_2 molecules from the $[Cs_2I]_\infty$ salt lattice. The magnetic susceptibility measurements show distinctive paramagnetic behavior which suggests that any long-range ordering is likely suppressed by the insulating nature of the ionic salt lattices and the large separation of $S = ½$ spins.

In Chapter 4, a series of new salt inclusion solids containing two-electron reduced Keggin polyoxometalate clusters was presented. These new two-electron reduced polyoxometalates, based on $Cs_6X_2Na(PMo_{12}O_{40})$ (where X_2 can be Cl_2, Br_2, and I_2 and ICl), are structurally similar to the one-electron reduced, $Cs_6I_3Na(PMo_{12}O_{40})$ compound presented in Chapter 3. Incorporating a slightly different salt lattice, *i.e.* $[Cs_6X_2]_\infty$ salt chains, compared to the $[Cs_6I_3]_\infty$ lattice in compound described in Chapter 3, resulted in Keggin-based solids where two of the twelve molybdenum atoms are in their formal 5+ oxidation state. The isolation of these Keggin-based solids described in this dissertation

using high-temperature, molten-salt method is, to the best of my knowledge, the first example of high-temperature synthesis of reduced POM Keggin clusters. Using the high-temperature method for synthesis of POMs enabled for isolation of reduced species which otherwise are not easily synthesized using conventional methods due to the oxidative conditions in aqueous and other solvents. The structure of the title series of compounds features isolated covalent metal-oxide Keggin clusters connected *via* square antiprismatic Na^+ cation along the c crystallographic direction. These Keggin-Na-Keggin chains are templated by the $[Cs_6X_2]_\infty$ salt chains running parallel to the cluster chains. The salt chain features halide anions in alternating tetrahedral-octahedral environments with respect to the neighboring Cs atoms. In addition to the coordination of Cs^+ to halide anions, Cs^+ cations also coordinate to oxygen atoms on the Keggin cluster. The distances between the neighboring halides in the $[Cs_6X_2]_\infty$ salt chains are much longer compared to those found in the compound described in Chapter 3. This means that the halide···halide interactions are not present in the compounds $Cs_6X_2Na(PMo_{12}O_{40})$ mainly due to the difference in charge on the Keggin cluster (*i.e.* one electron higher (5- vs 4-) for the compounds described in this Chapter) and hence no additional negative charges in the form of halide anions are necessary to balance the positive charge of the polynuclear salt chain. Unlike compound $Cs_6I_3Na(PMo_{12}O_{40})$, $Cs_6X_2Na(PMo_{12}O_{40})$ compounds are soluble in water up to about 1 mM concentration. The magnetic susceptibility studies revealed that the two electrons, from two Mo^{5+} cations, pair up and interact diamagnetically as was evidenced by the negative magnetic susceptibility values in the χ vs. T plots. As such, these materials may not be particularly be interesting to the magnetic communities. Attempts were made

to study the electronic properties of the aqueous solutions of the title compounds using cyclic voltammetry but due to the poor solubility in water and the limitations of water as the solvent of choice in cyclic voltammetry, these attempts resulted in broad and undefined waves. For this reason, a reaction targeting cation substitution using organic cations, *i.e.* tetrabutylammonium (TBA), to replace the polynuclear cation, $(Cs_6X_2Na)^{5+}$, in order to dissolve the clusters in organic solvents which are commonly used in voltammetry experiments such as dimethylformamide (DMF). Successful substitution of the inorganic polynuclear cation was achieved and resulted in a DMF-soluble solid with the formula of $TBA_4(PMo_{12}O_{40})$. Cyclic voltammetry of the 1 mM solution of $TBA_4(PMo_{12}O_{40})$ shows three distinct quazi-reversible waves as a result of three electron redox processes of the molybdenum cations.

Because of their solubility in aqueous, physiological conditions, and the previous reports showing biomedical activity (antibacterial, antitumor and antiviral) of POMs, the title compounds were tested for effectiveness in bacterial growth inhibition. Minimum Inhibitory Concentration (MIC) values for several bacterial strains including the SA1199 (wild strain) and SA1199B (mutant strain resistant to antibiotics) of the *Staphylococcus* (S.) *aureus* bacteria were obtained using a serial macrobroth dilution assay based on the Clinical Laboratory and Standards Institute (CLSI). The results of the MIC studies showed that the reduced POMs presented in Chapter 4 are not the substrates of the efflux pump which is commonly responsible for bacterial resistance to antibiotics. Comparing the results of the MIC studies of the reduced polyoxometalates (r-POMs) to the commercially available, fully oxidized Keggin-based POMs, it can easily be observed that the r-POMs

are much more effective in the inhibition of bacterial growth with approximately an order of magnitude higher effectiveness. A proposed mechanism of the bacterial inhibition by r-POMs was presented and can be explained by the high surface negative charge of the r-POMs. Previously proposed mechanisms of bacterial growth inhibition of POMs by Yamase and co-workers deals with the reduction of the fully oxidized POMs by the electrons in the electron transport chain in the bacterial cellular membrane and thus slows down a vital cellular process, ATP production. However, given that the r-POMs are already reduces species, likely mechanism of bacterial growth inhibition deals with the interaction of r-POMs with the proton gradient (or proton motive force) required for synthesis of ATP. Presumably, r-POMs being highly charged, interact with protons outside of the cell and by doing so they weaken the proton motive force which results in decreased production of ATP, the cellular energy currency, and eventually this leads to cellular death. The results of the ATP bioluminescence assay are in line with the expected ATP reduction in the presence of r-POMs which shows a significantly reduced production of ATP compared to the control group. This result provides support that the proposed mechanism is valid, however no bold conclusions can be made due to the complexity of biological systems and intricate cellular processes. It should be noted that the simultaneous action of the two above-described mechanisms of bacterial growth inhibition cannot be rejected based on the available data at hand.

In addition to the antibacterial properties, the r-POMs presented in Chapter 4 also show antitumor effects. Based on the preliminary antitumor studies, r-POMs can be used to inhibit tumor cell growth while having significantly lower relative toxicity on the normal

human cells up to certain concentrations. These results are preliminary and further studies, described below, could potentially shed light on the biomedical properties of the r-POMs presented in Chapter 4. Nevertheless, the results thus far show the importance and versatility of using new synthetic methods (high-temperature molten-salt in this case) to produce otherwise inaccessible solids with potentially interesting properties as exemplified by the biomedical results in Chapter 4.

In Chapter 5, several new salt-inclusion solid nanostructures containing discrete polyoxometalate clusters were presented. The general composition of the solids discussed in Chapter 5 is $Cs_6X_2M(PMo_{12}O_{40})$, where X can be Cl, Br, and I; and M can be Ti, V, Mn, and Fe. As was the case for compounds in Chapters 3 and 4, compounds presented in Chapter 5 feature a series of Keggin-based POM compounds synthesized for the first time, hitherto, using high- temperature, molten-salt method. In addition, compounds presented in Chapter 5 feature an unusual square-antiprismatic (D_{4d}) eight-coordination of the first-row transition-metal (M in the general formula above). To the best of my knowledge, this is the first example of an all-inorganic, rigid compound with the square-antiprismatic coordination of a first-row transition-metal complex. Oxo complexes of first-row transition metals with eight-coordination environment are rare due to unfavorable small size of the metals. However, in compounds presented herein, the Keggin cluster with multiple oxygen (four per cluster in the case of compounds presented herein) donors acts as a multidentate ligand seemingly resulting in chelate effect stabilization of the eight-coordinate, first-row transition metals. Originally, because a tetravalent vanadium oxide source (VO_2) was used in the original synthesis of the series of compounds presented in Chapter 5, it was believed

that the eight-coordinate metal site was tetravalent. However, bond valence sums calculations clearly indicate a trivalent state which likely means that the M was reduced *in situ* by MoO_2. Subsequent reactions in which trivalent first-row transition metals (V^{III}, Mn^{III}, Fe^{III}) were used in the synthesis showed successful formation of targeted compounds which is another indication that the M site is trivalent. In addition to the replacement of M, halide anion Cl^- in the salt lattice seems to be easily replaced by other halide anions, *i.e.* Br^- and I^-. To further show the flexibility of the compounds presented in Chapter 5, vanadium was attempted to be inserted in the metal centers of the Keggin cluster (*i.e.* molybdenum sites). It was shown that one molybdenum per twelve in the Keggin cluster can be replaced by a vanadium in both the Cl^- and I^- compounds. However, further substitution of the Mo sites by vanadium was proven to be unsuccessful. Profile refinements of the powder X-ray patterns obtained from stoichiometric reactions of these compounds showed expected linear trend with the increased size of halide anion. Magnetic susceptibility measurements of Ti, V, Mn, and Fe (M in the above formula) derivatives showed that the even number (four) of Mo^{5+} spins in the Keggin cluster tend to pair up which is a common occurrence in similar clusters reduced by an even number of electrons. Based on these preliminary magnetic susceptibility measurements, it seems that the magnetic contributions arise solely from the trivalent first-row transition-metals. Ti, V, and Fe derivatives showed deviation from paramagnetic behavior with indications of antiferromagnetic interactions. Interestingly, compound Mn derivative showed ferromagnetic interactions based on the positive Weiss constant and shape of the χT vs. T curve. It should be said that having single crystal structures of all of the derivatives studied

using magnetic susceptibility measurements would make it easier to predict the interactions between spins and their spin states (*e.g.* d^4 vs. d^5 in Mn site for Mn derivative).

Given that several transition metal derivatives with different *d* valence electron counts were able to be isolated in Chapter 5, this new family of compounds presents a platform to study their magnetic properties as a function of first-row, transition-metal ion.

In Chapter 6, four new inorganic-organic hybrid polyoxometalate-based solids were synthesized using the solution-based synthesis where soluble pre-synthesized polyoxometalate clusters were used as precursors. This method provides a unique synthetic strategy unlike the commonly used *bottom-up* synthetic approaches in which simple transition metal oxides are used to synthesize polyoxometalates *in situ*. Using the synthetic method described in Chapter 6, more control can be expected in the formation of desired solids given that the synthesis of POM-containing materials (*i.e.* soluble salt-inclusion polyoxometalate solids) was done prior to the introduction of organic ligands for formation of POM-based inorganic-organic hybrids.

Compounds presented in Chapter 6 feature $(V_{14}As_8O_{42}Cl)^{n-}$ clusters connected through copper-oxygen, copper-nitrogen, non-covalent hydrogen bonding and non-covalent hydrogen bonding in compound. In addition, a $(V_{15}O_{36}Cl)^{4-}$ cluster was isolated in using similar reaction conditions in which a soluble salt-inclusion POM solid was used in the original synthesis.

From the reactions which produced single crystals of POM-based inorganic-organic hybrid compounds, it can be inferred that the reaction conditions are very sensitive with respect to the amount of organic ligand, 4,4'-bipyridine, used. Having a large ratio of

4,4'-bipyridine ligands compared to the polyoxometalate starting materials seemingly increased the yields of single crystals. In addition, the use of mixed solvent system also increased the yield of single crystals. This, of course, could be a kinetic occurrence due to improved solubility of the organic ligand. In addition to the choice of solvent, pH of the initial reaction mixture played an important role in terms of the transformations in cluster shapes for compounds containing the $(V_{14}As_8O_{42}Cl)^{n-}$ clusters. Among the three solids, the largest cluster transformations (in reference to the original cluster shape in the salt-inclusion solid, $Cs_5(V_{14}As_8O_{42})$) was observed in compounds that were synthesized in the lowest relative pH conditions. It is argued that the protonation of basic oxygen sites on the clusters under highly acidic conditions weaken the metal oxygen bonds in the polyoxometalate clusters and thereby result in breaking of possibly partial vanadium-oxygen bonds which leads to fragmentation of the POM clusters and subsequent rearrangement and rotation of the arsenic rectangle caps in relation to the original clusters.

Future Directions

In regards to the future directions of $Cs_6I_3Na(PMo_{12}O_{40})$ compound from Chapter 3, it would be interesting to see if the solubility of the title compound could essentially be tuned by replacing the large Cs^+ ions with smaller A-site cations, such as Rb^+, K^+, Na^+, which would result in comparably poorer size matching between the large iodine and smaller A-site cations resulting in a relatively more ionic-type interaction. If similar water soluble clusters can be isolated, they could potentially be used as building blocks for conventional solution-based synthesis, as exemplified in Chapter 6, of extended solids

featuring polyoxometalate clusters. In addition, their properties with respect to biological systems could be investigated and compared to those of fully oxidized clusters previously studied. In addition, it is thought that the thermal decomposition of $Cs_6I_3Na(PMo_{12}O_{40})$ results in oxidation of I^- to I_2. A better understanding of the decomposition process could potentially be exploited for synthesis of new similar phases. If the oxidation of I^- is indeed occurring, the likely result is that Mo^{6+} is being reduced which can potentially lead to synthesis of further reduced POM species. The title compound illustrates, once more, the importance of salt-inclusion synthesis and the vast utility of this synthetic method in formation of novel frameworks.

The solids presented in Chapter 4 have the potential to be used in biomedical applications such as antibacterial, antitumor, and antiviral applications. With the preliminary data showing promising results, mainly for antibacterial and antitumor properties, these solids should be further studied to shed light on their use in biomedical applications. The first obstacle of using r-POMs in biomedical applications is their potential toxicity to humans, animals, and the environment. For that reason, thorough toxicity evaluations of these materials are necessary in order to determine their viability for use in various applications. The second obstacle would be their effectiveness related to the currently available materials. For example, the r-POM usage in antibacterial applications would depend on their effectiveness compared to the currently available antibiotics. In the case of antibiotic resistant bacteria such as the SA1199B strain of *Staph. Aureous*, r-POMs would be potential candidates to be used as antibiotics due to their effectiveness of growth inhibition of SA1199B strain.

In regards to the synthesis of new related compounds similar in composition and structure to the $Cs_6X_2Na(PMo_{12}O_{40})$ series, there are several future directions one can take. For example, reducing the cluster even further than the current two-electron reduced state in order to add another data point in the r-POMs series, could potentially be done by doing aliovalent substitutions of the monovalent cations by divalent and trivalent ones. As an example, attempts to replace Cs^+ by a similar size, divalent cation, Ba^{2+} can be done according to the targeted composition of $Cs_{6-y}Ba_yX_2Na(PMo_{12}O_{40})$ where each Cs replaced by Ba would further reduce the cluster by one electron. This could potentially produce compounds with even higher negative surface charge on the cluster which would be interesting to test and see if the higher negative charge of the POM would show improved antibacterial properties.

Given that only the preliminary data for normal human cell toxicity and colon tumor cell toxicity were obtained using *in vitro* cell viability tests in the presence of r-POM **1**, it is foreseeable that in-depth studies of antitumor properties of r-POMs presented in this dissertation will be done in the near future.

For compounds presented in Chapter 5, concerning the synthesis of single crystals, it would be invaluable to have single crystal structures of all of the derivatives described in Chapter 5. This would facilitate the study and interpretation of their properties such as magnetic and or electronic. To try to grow larger single crystals of these compounds, higher temperatures could possibly prove to be successful as was shown to be the case with at least one of the derivatives. In addition, longer cooling times (*e.g.* slower than 0.05 ^oC per minute rate) would aid in growth of larger crystals. Finally, the use of eutectic salt flux

with the high yield products could possibly increase the chance of growing larger crystals due to increased diffusion of reactants as a result of using a high-temperature 'solvent'.

More in depth magnetic studies are needed to reveal any interesting properties of these materials. For example, field-dependent magnetic susceptibility measurements are in line for all of the compounds synthesized especially the compound showing ferromagnetic interactions. In addition, due to potential diamagnetic contribution of the Keggin cluster with an even number of electrons in these compounds, the diamagnetic contribution should be subtracted in all. In order to do this, the diamagnetic contribution of the Keggin cluster with even number of electrons should be measured and subtracted from the magnetic susceptibility measurements. By synthesizing a compound with d^0 electron count in the M site of $Cs_6Cl_2M(PMo_{12}O_{40})$, where there are four Mo^{5+} sites, would be an ideal candidate to measure its diamagnetic contribution due to paired spins of the four Mo^{5+} ions. Given that the M site in the title compounds is trivalent, it would be intuitive to use Sc^{3+} ion as the d^0 ion to replace the paramagnetic ions in the title compounds and measure the magnetic contribution of only the Mo ions in the Keggin cluster.

Finally, because of the 1D metal-oxide connectivity running along the *c* crystallographic direction, possible interesting electronic properties may arise from existence of electron delocalization pathways along *c*. As is the case with the reduced molybdenum 'blue' pseudo one-dimensional (*e.g.* $K_{0.3}MoO_3$) compounds featuring corner shared clusters of octahedra, title compounds may also show interesting electronic properties such as metal-like electronic behavior. Resistivity measurements are in line for all of the derivatives presented herein. In addition, in order to gain more understanding

about potential electronic properties of the compounds presented in Chapter 5, heat capacity and thermoelectric properties should be studied.

As discussed in Chapter 5, due to the flexibility of the structure with respect to the incorporation of different transition metal ions and halide ion replacement, this series of compounds presents an interesting platform to study their properties as a function of different chemical compositions.

As far as the synthesis of POMOFs goes, it is evident from the synthesis of compounds presented in Chapter 6, that 4,4'-bipyridine ligand leads to inter-penetrated networks with small or no porous structures. Using ligands that generally do not lead to inter-penetrated networks, *i.e*. ligands with coordination sites oriented in three dimensions (3D) rather than linear ones, may lead to formation of porous polyoxometalate-containing hybrids.

From the synthesis of hybrid inorganic-organic polyoxometalate-containing solids presented in Chapter 6, it can be envisaged that the new synthetic method described in Chapter 6, using soluble polyoxometalates as precursors, can lead to new solids with possibly interesting properties relevant to many technologies. However, as was the case with the attempted synthesis of POMOFs which lead to the formation of the compounds in Chapter 6, predictability of structures and formation of hybrid polyoxometalate-containing materials under given conditions has yet to be fine-tuned. Several experiments should be done in order to better understand the formation of solids in Chapter 6. Namely, 1) conditions governing the oxidation state change of the polyoxometalate clusters in the final product compared to that in the starting material should be studied with respect to the pH

of the solution 2) In addition, conditions which preserve a given oxidation state of the cluster should be explored by systematically varying the reaction conditions including pH; 3) The role of the transition metal cation used in reactions which did not incorporate these cations should be revealed 4) High yield of all of the compounds presented in Chapter 6 could be obtained by using different solvent systems and temperature conditions.

Finally, other similar methods to isolate POM clusters in solution along with organic ligands should be explored. One recent method is the use of ionic liquids to synthesize extended inorganic-organic hybrid networks. The use of ionic liquids in which cations and anions are readily available in solution, could prove to be effective for the synthesis of POMOFs which was the original goal of reactions in Chapter 6. In order for property measurements to be done on all of these solids, high yields of single crystals or polycrystalline materials will need to be obtained.

Given that Chapter 6 compounds are new solids, their physical and chemical properties are unknown. The reduced state of the clusters in these solids may lead to interesting magnetic and/or electronic properties related to confined electrons within the metal-oxygen cluster framework. Future magnetic susceptibility studies are due which may potentially reveal interesting phenomena associated with these solids. In addition, given their catalytic properties, polyoxovanadate clusters in may show superior catalytic properties compared to the currently available such catalysts.

Overall, the research presented in this dissertation was exploratory in nature. This means that the conditions under which the title compounds formed were previously not known. The research presented herein aimed to reveal some of the reaction conditions

under which electronically reduced polyoxometalate clusters can form. The work presented in this dissertation is significant for several reasons: 1) this opens up a new method for synthesis of POM solids; 2) isolation of electronically reduced POMs is favored using the high-temperature, molten-salt method; 3) this method produced novel POM-based *SIS*s that are otherwise unattainable using conventional methods; 4) unusual structures and local geometry (*e.g.* metal-oxide connectivity along *c* and eight-coordination of transition metals) could give rise to interesting properties, including water-soluble clusters, to be studied in the near future; 5) in regards to the solids synthesized in Chapter 6, a new understanding of the interaction between anionic POV clusters and organic ligands with respect to the nature of bonding is learned; 6) finally, the synthesis of POM *SIS*s illustrated, once more, the versatility and utility of the salt-inclusion synthetic method.

APPENDICES

Appendix A

CheckCIF files for Chapter 3 compound, $Cs_6I_3Na(PMo_{12}O_{40})$

checkCIF/PLATON report

You have not supplied any structure factors. As a result the full set of tests cannot be run.

THIS REPORT IS FOR GUIDANCE ONLY. IF USED AS PART OF A REVIEW PROCEDURE FOR PUBLICATION, IT SHOULD NOT REPLACE THE EXPERTISE OF AN EXPERIENCED CRYSTALLOGRAPHIC REFEREE.

No syntax errors found. CIF dictionary Interpreting this report

Datablock: cd8884a_Cs6I3

```
Bond precision:  Mo- O = 0.0109 A        Wavelength=0.71073

Cell:             a=15.203(2)      b=15.203(2)      c=19.181(4)
                  alpha=90         beta=90          gamma=90
Temperature:      293 K
```

	Calculated	Reported
Volume	4433.3(15)	4433.3(13)
Space group	P 4/n c c	P4/ncc
Hall group	-P 4a 2ac	?
Moiety formula	2(Mo12 O40 P), I6, 12(Cs), 2(Na)	?
Sum formula	Cs12 I6 Mo24 Na2 O80 P2	Cs6 I3 Mo12 Na1 O40 P
Mr	6046.80	3023.36
Dx,g cm-3	4.530	4.524
Z	2	4
Mu (mm-1)	10.367	10.357
F000	5356.0	5349.0
F000'	5261.51	
h,k,lmax	18,18,22	18,18,22
Nref	1975	1966
Tmin,Tmax	0.385,0.484	0.133,0.199
Tmin'	0.226	

```
Correction method= MULTI SCAN

Data completeness= 0.995          Theta(max)= 25.050

R(reflections)= 0.0571( 1743)     wR2(reflections)= 0.1405( 1966)

S = 1.091                 Npar= 155
```

```
The following ALERTS were generated. Each ALERT has the format
      test-name_ALERT_alert-type_alert-level.
Click on the hyperlinks for more details of the test.
```

Alert level A

```
PLAT213_ALERT_2_A Atom O3              has ADP max/min Ratio .....        5.4 prolat
PLAT213_ALERT_2_A Atom O6              has ADP max/min Ratio .....        6.5 prolat
PLAT213_ALERT_2_A Atom O7              has ADP max/min Ratio .....        5.8 prolat
```

Alert level B

```
PLAT213_ALERT_2_B Atom O4              has ADP max/min Ratio .....        4.5 prolat
PLAT213_ALERT_2_B Atom O8              has ADP max/min Ratio .....        4.1 prolat
PLAT220_ALERT_2_B Large Non-Solvent    O     Ueq(max)/Ueq(min) ...        4.4 Ratio
```

Alert level C

```
PLAT068_ALERT_1_C Reported F000 Differs from Calcd (or Missing)...     Please Check
PLAT213_ALERT_2_C Atom O1              has ADP max/min Ratio .....        3.3 prolat
PLAT213_ALERT_2_C Atom O5              has ADP max/min Ratio .....        3.8 prolat
PLAT213_ALERT_2_C Atom O9              has ADP max/min Ratio .....        3.5 prolat
PLAT241_ALERT_2_C High      Ueq as Compared to Neighbors for .....         O5 Check
PLAT242_ALERT_2_C Low       Ueq as Compared to Neighbors for .....        Mo1 Check
PLAT242_ALERT_2_C Low       Ueq as Compared to Neighbors for .....        Mo2 Check
PLAT242_ALERT_2_C Low       Ueq as Compared to Neighbors for .....        Mo3 Check
```

Alert level G

```
PLAT004_ALERT_5_G Polymeric Structure Found with Dimension .......          1 Info
PLAT005_ALERT_5_G No _iucr_refine_instructions_details  in the CIF     Please Do !
PLAT045_ALERT_1_G Calculated and Reported Z Differ by ............       0.50 Ratio
PLAT083_ALERT_2_G SHELXL Second Parameter in WGHT Unusually Large.     207.80
PLAT152_ALERT_1_G The Supplied and Calc. Volume s.u. Differ by ...          2 Units
PLAT199_ALERT_1_G Reported _cell_measurement_temperature ..... (K)        293 Check
PLAT200_ALERT_1_G Reported   _diffrn_ambient_temperature ..... (K)        293 Check
PLAT301_ALERT_3_G Main Residue  Disorder ..... Percentage =          8 Note
```

```
   3 ALERT level A = Most likely a serious problem - resolve or explain
   3 ALERT level B = A potentially serious problem, consider carefully
   8 ALERT level C = Check. Ensure it is not caused by an omission or oversight
   8 ALERT level G = General information/check it is not something unexpected

   5 ALERT type 1 CIF construction/syntax error, inconsistent or missing data
  14 ALERT type 2 Indicator that the structure model may be wrong or deficient
   1 ALERT type 3 Indicator that the structure quality may be low
   0 ALERT type 4 Improvement, methodology, query or suggestion
   2 ALERT type 5 Informative message, check
```

It is advisable to attempt to resolve as many as possible of the alerts in all categories. Often the minor alerts point to easily fixed oversights, errors and omissions in your CIF or refinement strategy, so attention to these fine details can be worthwhile. In order to resolve some of the more serious problems it may be necessary to carry out additional measurements or structure refinements. However, the purpose of your study may justify the reported deviations and the more serious of these should normally be commented upon in the discussion or experimental section of a paper or in the "special_details" fields of the CIF. checkCIF was carefully designed to identify outliers and unusual parameters, but every test has its limitations and alerts that are not important in a particular case may appear. Conversely, the absence of alerts does not guarantee there are no aspects of the results needing attention. It is up to the individual to critically assess their own results and, if necessary, seek expert advice.

Publication of your CIF in IUCr journals

A basic structural check has been run on your CIF. These basic checks will be run on all CIFs submitted for publication in IUCr journals (*Acta Crystallographica*, *Journal of Applied Crystallography*, *Journal of Synchrotron Radiation*); however, if you intend to submit to *Acta Crystallographica Section C* or *E*, you should make sure that full publication checks are run on the final version of your CIF prior to submission.

Publication of your CIF in other journals

Please refer to the *Notes for Authors* of the relevant journal for any special instructions relating to CIF submission.

PLATON version of 18/09/2013; check.def file version of 12/09/2013

Datablock: cd8884a_CsI2 - ellipsoid plot

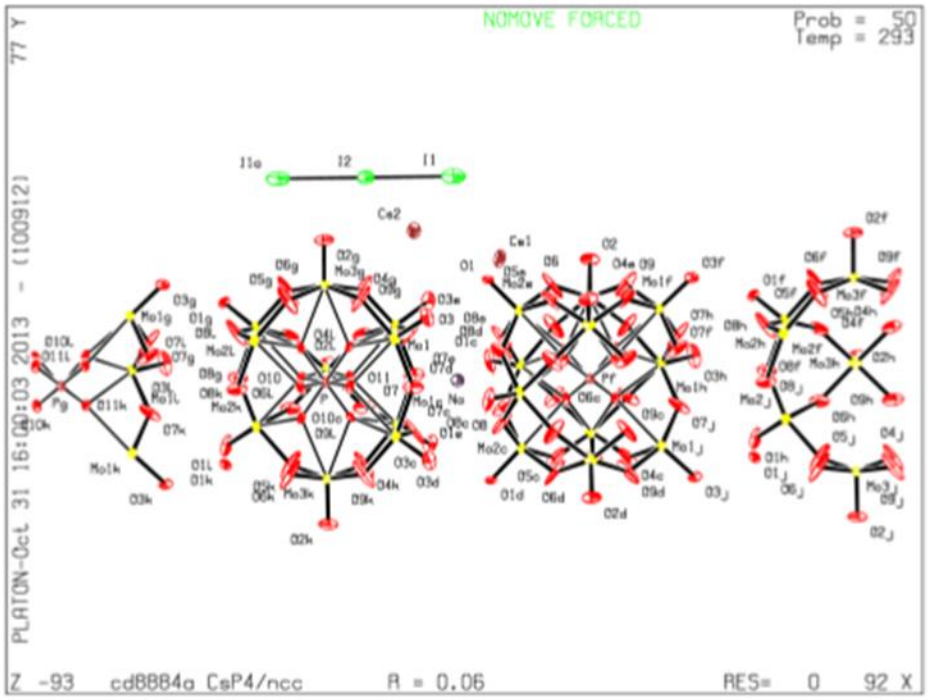

Appendix B

CheckCIF files for Chapter 4 compound, $Cs_6Cl_2Na(PMo_{12}O_{40})$

checkCIF/PLATON report

You have not supplied any structure factors. As a result the full set of tests cannot be run.

THIS REPORT IS FOR GUIDANCE ONLY. IF USED AS PART OF A REVIEW PROCEDURE FOR PUBLICATION, IT SHOULD NOT REPLACE THE EXPERTISE OF AN EXPERIENCED CRYSTALLOGRAPHIC REFEREE.

No syntax errors found. CIF dictionary Interpreting this report

Datablock: cd8973a_Cs6Cl2

```
Bond precision:  Mo- O = 0.0159 A        Wavelength=0.71073

Cell:             a=14.780(2)      b=14.780(2)      c=19.172(4)
                  alpha=90         beta=90          gamma=90
Temperature:      293 K
```

	Calculated	Reported
Volume	4188.1(14)	4188.1(12)
Space group	P 4/n c c	P4/ncc
Hall group	-P 4a 2ac	?
Moiety formula	Mo24 O80 P2, 4(Cl), 12(Cs), 2(Na)	?
Sum formula	Cl4 Cs12 Mo24 Na2 O80 P2	Cl2 Cs6 Mo12 Na1 O40 P
Mr	5427.20	2713.57
Dx,g cm-3	4.304	4.425
Z	2	4
Mu (mm-1)	8.888	8.589
F000	4856.0	2832.0
F000'	4768.08	
h,k,lmax	17,17,22	17,17,22
Nref	1864	1863
Tmin,Tmax	0.165,0.232	0.133,0.199
Tmin'	0.139	

```
Correction method= MULTI SCAN

Data completeness= 0.999          Theta(max)= 25.050

R(reflections)= 0.0718( 1802)     wR2(reflections)= 0.1564( 1863)

S = 1.188                 Npar= 153
```

```
The following ALERTS were generated. Each ALERT has the format
      test-name_ALERT_alert-type_alert-level.
Click on the hyperlinks for more details of the test.
```

Alert level C

```
ABSMU01_ALERT_1_C  The ratio of given/expected absorption coefficient lies
              outside the range 0.99 <> 1.01
           Calculated value of mu =     8.888
           Value of mu given      =     8.589
DENSD01_ALERT_1_C  The ratio of the submitted crystal density and that
           calculated from the formula is outside the range 0.99 <> 1.01
           Crystal density given    =      4.425
           Calculated crystal density =      4.303
PLAT046_ALERT_1_C Reported Z, MW and D(calc) are Inconsistent ....      4.304
PLAT051_ALERT_1_C Mu(calc) and Mu(CIF) Ratio Differs from 1.0 by .      3.48 %
PLAT068_ALERT_1_C Reported F000 Differs from Calcd (or Missing)...     Please Check
PLAT220_ALERT_2_C Large Non-Solvent    O     Ueq(max)/Ueq(min) ...       4.0 Ratio
PLAT241_ALERT_2_C High      Ueq as Compared to Neighbors for .....       O5 Check
PLAT242_ALERT_2_C Low       Ueq as Compared to Neighbors for .....      Mo1 Check
PLAT242_ALERT_2_C Low       Ueq as Compared to Neighbors for .....      Mo2 Check
PLAT242_ALERT_2_C Low       Ueq as Compared to Neighbors for .....      Mo3 Check
```

Alert level G

```
PLAT004_ALERT_5_G Polymeric Structure Found with Dimension .......         1 Info
PLAT005_ALERT_5_G No _iucr_refine_instructions_details  in the CIF     Please Do !
PLAT045_ALERT_1_G Calculated and Reported Z Differ by .............     0.50 Ratio
PLAT083_ALERT_2_G SHELXL Second Parameter in WGHT Unusually Large.    297.36
PLAT152_ALERT_1_G The Supplied and Calc. Volume s.u. Differ by ...         2 Units
PLAT199_ALERT_1_G Reported _cell_measurement_temperature ..... (K)       293 Check
PLAT200_ALERT_1_G Reported   _diffrn_ambient_temperature ..... (K)       293 Check
PLAT301_ALERT_3_G Main Residue  Disorder ..... Percentage =          8 Note
```

```
   0 ALERT level A = Most likely a serious problem - resolve or explain
   0 ALERT level B = A potentially serious problem, consider carefully
  10 ALERT level C = Check. Ensure it is not caused by an omission or oversight
   8 ALERT level G = General information/check it is not something unexpected

   9 ALERT type 1 CIF construction/syntax error, inconsistent or missing data
   6 ALERT type 2 Indicator that the structure model may be wrong or deficient
   1 ALERT type 3 Indicator that the structure quality may be low
   0 ALERT type 4 Improvement, methodology, query or suggestion
   2 ALERT type 5 Informative message, check
```

It is advisable to attempt to resolve as many as possible of the alerts in all categories. Often the minor alerts point to easily fixed oversights, errors and omissions in your CIF or refinement strategy, so attention to these fine details can be worthwhile. In order to resolve some of the more serious problems it may be necessary to carry out additional measurements or structure refinements. However, the purpose of your study may justify the reported deviations and the more serious of these should normally be commented upon in the discussion or experimental section of a paper or in the "special_details" fields of the CIF. checkCIF was carefully designed to identify outliers and unusual parameters, but every test has its limitations and alerts that are not important in a particular case may appear. Conversely, the absence of alerts does not guarantee there are no aspects of the results needing attention. It is up to the individual to critically assess their own results and, if necessary, seek expert advice.

Publication of your CIF in IUCr journals

A basic structural check has been run on your CIF. These basic checks will be run on all CIFs submitted for publication in IUCr journals (*Acta Crystallographica*, *Journal of Applied Crystallography*, *Journal of Synchrotron Radiation*); however, if you intend to submit to *Acta Crystallographica Section C* or *E*, you should make sure that full publication checks are run on the final version of your CIF prior to submission.

Publication of your CIF in other journals

Please refer to the *Notes for Authors* of the relevant journal for any special instructions relating to CIF submission.

PLATON version of 18/09/2013; check.def file version of 12/09/2013

Datablock cd8973a_Cs6Cl2 - ellipsoid plot

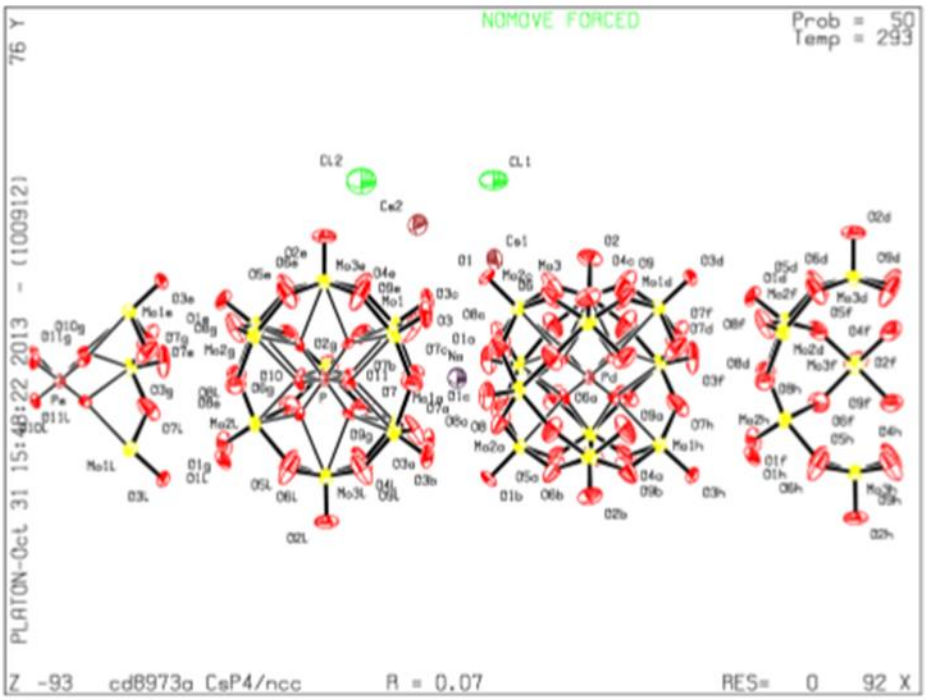

Appendix C

CheckCIF files for Chapter 4 compound, $Cs_6ICl Na(PMo_{12}O_{40})$

checkCIF/PLATON report

You have not supplied any structure factors. As a result the full set of tests cannot be run.

THIS REPORT IS FOR GUIDANCE ONLY. IF USED AS PART OF A REVIEW PROCEDURE FOR PUBLICATION, IT SHOULD NOT REPLACE THE EXPERTISE OF AN EXPERIENCED CRYSTALLOGRAPHIC REFEREE.

No syntax errors found. CIF dictionary Interpreting this report

Datablock: cd9010b_Cs6ICl

Bond precision: Mo- O = 0.0113 A Wavelength=0.71073

Cell: a=15.026(2) b=15.026(2) c=19.145(4)
alpha=90 beta=90 gamma=90
Temperature: 293 K

	Calculated	Reported
Volume	4322.6(15)	4322.5(12)
Space group	P 4/n c c	P4/ncc
Hall group	-P 4a 2ac	?
Moiety formula	Mo24 O80 P2, 2(I), 2(Cl), 12(Cs), 2(Na)	?
Sum formula	Cl2 Cs12 I2 Mo24 Na2 O80 P2	Cl1 Cs6 I1 Mo12 Na1 O40 P
Mr	5610.10	2805.02
Dx,g cm-3	4.310	4.310
Z	2	4
Mu (mm-1)	9.264	9.265
F000	5000.0	5000.0
F000'	4909.69	
h,k,lmax	17,17,22	17,17,22
Nref	1923	1918
Tmin,Tmax	0.187,0.273	0.133,0.199
Tmin'	0.158	

Correction method= MULTI SCAN

Data completeness= 0.997 Theta(max)= 25.050

R(reflections)= 0.0613(1675) wR2(reflections)= 0.1828(1918)

S = 1.118 Npar= 153

The following ALERTS were generated. Each ALERT has the format
test-name_ALERT_alert-type_alert-level.
Click on the hyperlinks for more details of the test.

Alert level C

```
PLAT213_ALERT_2_C Atom O6              has ADP max/min Ratio .....      3.7 prolat
PLAT214_ALERT_2_C Atom Na      (Anion/Solvent) ADP max/min Ratio        4.7 prolat
PLAT220_ALERT_2_C Large Non-Solvent    O     Ueq(max)/Ueq(min) ...      3.3 Ratio
PLAT241_ALERT_2_C High      Ueq as Compared to Neighbors for .....      O5 Check
PLAT242_ALERT_2_C Low       Ueq as Compared to Neighbors for .....      Mo1 Check
PLAT242_ALERT_2_C Low       Ueq as Compared to Neighbors for .....      Mo2 Check
PLAT242_ALERT_2_C Low       Ueq as Compared to Neighbors for .....      Mo3 Check
```

Alert level G

```
PLAT004_ALERT_5_G Polymeric Structure Found with Dimension .......        1 Info
PLAT005_ALERT_5_G No _iucr_refine_instructions_details  in the CIF    Please Do !
PLAT045_ALERT_1_G Calculated and Reported Z Differ by .............     0.50 Ratio
PLAT072_ALERT_2_G SHELXL First  Parameter in WGHT Unusually Large.      0.12
PLAT083_ALERT_2_G SHELXL Second Parameter in WGHT Unusually Large.     34.94
PLAT152_ALERT_1_G The Supplied and Calc. Volume s.u. Differ by ...        3 Units
PLAT199_ALERT_1_G Reported _cell_measurement_temperature ..... (K)      293 Check
PLAT200_ALERT_1_G Reported   _diffrn_ambient_temperature ..... (K)      293 Check
PLAT301_ALERT_3_G Main Residue  Disorder ............. Percentage =       8 Note
```

```
   0 ALERT level A = Most likely a serious problem - resolve or explain
   0 ALERT level B = A potentially serious problem, consider carefully
   7 ALERT level C = Check. Ensure it is not caused by an omission or oversight
   9 ALERT level G = General information/check it is not something unexpected

   4 ALERT type 1 CIF construction/syntax error, inconsistent or missing data
   9 ALERT type 2 Indicator that the structure model may be wrong or deficient
   1 ALERT type 3 Indicator that the structure quality may be low
   0 ALERT type 4 Improvement, methodology, query or suggestion
   2 ALERT type 5 Informative message, check
```

It is advisable to attempt to resolve as many as possible of the alerts in all categories. Often the minor alerts point to easily fixed oversights, errors and omissions in your CIF or refinement strategy, so attention to these fine details can be worthwhile. In order to resolve some of the more serious problems it may be necessary to carry out additional measurements or structure refinements. However, the purpose of your study may justify the reported deviations and the more serious of these should normally be commented upon in the discussion or experimental section of a paper or in the "special_details" fields of the CIF. checkCIF was carefully designed to identify outliers and unusual parameters, but every test has its limitations and alerts that are not important in a particular case may appear. Conversely, the absence of alerts does not guarantee there are no aspects of the results needing attention. It is up to the individual to critically assess their own results and, if necessary, seek expert advice.

Publication of your CIF in IUCr journals

A basic structural check has been run on your CIF. These basic checks will be run on all CIFs submitted for publication in IUCr journals (*Acta Crystallographica*, *Journal of Applied Crystallography*, *Journal of Synchrotron Radiation*); however, if you intend to submit to *Acta Crystallographica Section C* or *E*, you should make sure that full publication checks are run on the final version of your CIF prior to submission.

Publication of your CIF in other journals

Please refer to the *Notes for Authors* of the relevant journal for any special instructions relating to CIF submission.

PLATON version of 18/09/2013; check.def file version of 12/09/2013

Datablock cd9010b_CsEICl - ellipsoid plot